An investigation into the mechanisms of Progressive Myoclonic Epilepsy and Ataxia

Jenna Colette Carpenter

A thesis submitted to University College London for the degree of Doctor of Philosophy

Department of Clinical and Experimental Epilepsy
UCL Queen Square Institute of Neurology
Queen Square
London
WC1N 3BG

Declaration

I, Jenna Carpenter, confirm that the work presented in this thesis is my own. Where information has been derived from other sources, I confirm that this has been indicated in the thesis. Where others have contributed to this work, I confirm that this has been clearly indicated.

Abstract

Progressive myoclonic epilepsy (PME) is a rare and severe epilepsy syndrome that is caused by mutations in a diversity of genes. The syndrome is characterised by core symptoms of myoclonus (muscle jerks), epilepsy and progressive neurological dysfunction, occurring after a period of apparently normal brain development. Although the genetic causes of PME have been well studied, the underlying mechanisms remain poorly understood. In particular, it is not known how mutations in a wide range of genes, of apparently unrelated function, give rise to a distinct epilepsy syndrome. This thesis aimed to characterize the neuronal effects of mutations recently identified in *KCNC1* ($K_v3.1$) and Golgi SNARE receptor complex member 2 (*GOSR2*) that have been shown to cause PME with ataxia. $K_v3.1$ is a voltage-gated potassium channel important for high frequency neuronal firing. A recurrent p.Arg320His mutation in $K_v3.1$ had been previously found to be a loss-of-function with a dominant negative effect. I selectively overexpressed $Kv3.1^{R320H}$ in interneurons *in vitro* and found that it rapidly induced a reduction in dendritic length and neurotoxicity. Repeating these experiments using a lentiviral-based overexpression strategy, I again observed morphological defects as well as alterations in firing. Using an oocyte expression system, we excluded omega currents through the voltage-sensor domain of the channel as a potential mechanism of toxicity.

The second mutation studied was a p.G144W loss-of-function mutation in GOSR2, an essential protein required for ER-Golgi transport. In primary cortical cultures, I found that overexpression of $GOSR2^{G144W}$ resulted in a significant reduction of miniature excitatory post-synaptic currents, which was not caused by a reduction in excitatory synapse number. I also characterised the effects of this mutation on dendritic outgrowth in Purkinje cells of the mouse cerebellum. Overall, I suggest that the pathological effects of these two distinct PME mutations converge on dendritic dysfunction, which may generally apply across the PMEs.

Impact Statement

Progressive myoclonic epilepsy (PME) is a very rare and severe form of epilepsy caused by genetic mutations. PME is characterised by uncontrollable muscle jerks, problems with coordinating movements and seizures. It also features progressive neurodegeneration and can be fatal. PME increases in severity over time and symptoms are highly disabling, often leaving patients wheelchair bound. Unfortunately, no specific treatments currently exist for this rare form of epilepsy.

Much of what we understand about how seizures are caused in people with epilepsy has been learnt by studying rare epilepsies that have an identifiable genetic cause. Many of these mutations affect genes that encode ion channels, which are proteins that regulate the activity of neurons. Recently, for the first time, a mutation in an ion channel, $K_V3.1$, was discovered to cause PME. I expected that the mutation would change the activity of a particular group of neurons that fire at high frequencies in the brain. However, surprisingly, I found this mutation to interface between life and death decisions faced by the cell and to cause shrinkage of neuronal processes. This unexpected finding uncovers a novel, potentially important mechanism for seizure generation.

A second mutation in a non-ion channel gene, *GOSR2*, leads to a form of PME that is very similar in its clinical features. GOSR2 is an essential protein involved in trafficking of cargo in neurons. Fruit flies with mutations in *GOSR2* have previously been shown to display neuronal defects including synaptic development and dendritic outgrowth. Our work shows that mammalian neurons also have synaptic deficits. These synaptic deficits may also be common to other forms of PME that feature dementia.

The correct development of the neuron and their synaptic contacts is required to ensure that neurons are correctly wired into brain circuits. Through our research I have potentially uncovered dendritic dysfunction as a novel and convergent disease mechanism in PME. Our findings are important because they will facilitate further investigation into the neuronal circuits underlying myoclonus, epilepsy and ataxia in PME. This is based on our hypothesis that cells of the cerebellum, such as Purkinje cells, and interneurons of the motor cortex are likely to be particularly vulnerable to the dendritic and synaptic effects of PME mutations. By uncovering common disease mechanisms, I not only provide insights into epilepsy and neurodegeneration, but may also help instruct the development of novel therapeutics for this devastating disease.

Acknowledgments

I would firstly like to thank my supervisor, Professor S. Schorge, for her support and encouragement throughout my PhD and for providing me with many opportunities for scientific development. You have helped me to develop the independence and confidence that I have today.

I would also like to thank Dr G. Lignani for his valued mentorship and friendship throughout my PhD and Dr R. Männikkö, Dr J. Jepson and Dr E. Clayton for their collaboration. Thanks also T. Turner and J. Heneine for being brilliant students and for contributing to this work.

I would like to thank the Wellcome Trust for funding this research and the Wellcome committee at UCL for providing me with this opportunity. During my PhD and rotation projects I met some outstanding scientists and consider myself very lucky to have had the opportunity to work at such a word-class university.

I would like to say thank you to my Trashbears for their friendship throughout my PhD. Grazie alla mia polpettina, Eleonora, Gareth, Yichen, Erica and Marco! Thanks also to Marisol for her help with the oocyte project, Bao Luen for being a friendly presence into the late hours of the night and Albert for writing the Python scripts used in this thesis. Finally, thanks to all my other wonderful colleagues in the Department of Clinical and Experimental Epilepsy for their help and support over the years.

Last, but by absolutely no means least, I would like to thank my beautiful family and friends. I would like to thank my parents, Freddie and my sister, Nadine, for their unwavering love and support, upon the foundation of which, this PhD thesis rests. I would also like to thank Charlotte, Ally, Lizzie, Emily, Hannah, Rachael and Jo for their continued support and valued friendship. #hotforknowledge

Abbreviations

AAV	Adeno-associated virus
AED	Anti-epileptic drug
AHP	Afterhyperpolarisation
AMPAR	α-amino-3-hydroxy-5-methyl-4-isoxazolepropionic acid receptor
AMRF	Action Myoclonus Renal Failure Syndrome
AP	Action potential
BMP-4	Bone morphogenic protein 4
CC-3	Cleaved caspase 3
CLN#	Neuronal ceroid lipofuscinoses
CNS	Central nervous system
COPI	Coat protein complex I
COPII	Coat protein complex II
cPPT-CTS	Central polypurine tract-central termination sequence
CRISPR	Clustered Regularly Interspaced Short Palindromic Repeats
Cas9	CRISPR associated protein 9
cRNA	Copy RNA
CSPα	Cysteine string protein α
CSTB	Cystatin B
DAPI	4′,6-diamidino-2-phenylindole
DIV	Days in vitro
DNA	Deoxyribonucleic acid
dNTP	deoxyribonucleotide
DRPLA	Dentato-rubro-pallido-luysian atrophy
DSB	Double stranded break
dscGFP	Destabilised green fluorescent protein
EEG	Electroencephalogram
EF-1α	Elongation factor-1 alpha
EGFP	Enhanced green fluorescence protein
ELISA	Enzyme-linked immunosorbent assay
EMG	Electromyography
EPSP	Excitatory post-synaptic potential
ER	Endoplasmic reticulum
ERGIC	ER-Golgi-intermediate compartment

FLEx	Flip excision switch
GA	Golgi apparatus
GAD67	Glutamic acid decarboxylase isoform 67
GABA	γ-Aminobutyric Acid
GEFS+	Generalised epilepsy with febrile seizures plus
GOI	Gene of Interest
GOSR2	Golgi SNAP Receptor Complex Member 2
GTCS	Generalised tonic-clonic seizures
HDR	Homology directed repair
HEK	Human embryonic kidney
HITI	Homology-independent targeted integration
HOMER1	Homer protein homolog 1
HR	Homologous recombination
hSyn	Human synapsin promoter
IFU	Infectious units
Indel	Insertion/deletion
ILAE	International League against epilepsy
IPSC	Inhibitory postsynaptic current
JME	Juvenile Myoclonic Epilepsy
KD	Knock-down
KO	Knock out
LAMP1	Lysosomal-associated membrane protein 1
LB	Lafora Body
LBD	Lafora Body Disease
LICI	Long-interval cortical inhibition
LIMP2	Lysosome membrane protein 2
LJP	Liquid junction potential
LLR	Long-loop transcortical reflex
LQTS	Long QT syndrome
LTR	Long terminal repeat
LV	Lentivirus
MCS	Multiple cloning site
mDlx	Mouse distal-less homeobox
MEAK	Myoclonic epilepsy and ataxia caused by potassium channel mutation
MERRF	Myoclonic epilepsy with ragged red fibers
mEPSC	Miniature excitatory post-synaptic current

MGE	Medial ganglionic eminence
mIPSC	Miniature inhibitory post-synaptic current
MOI	Multiplicity of Infection
MRI	Magnetic Resonance Imaging
NAF	Nuclear area factor
NCL	Neuronal ceroid lipofuscinosis
NF-H	Neurofilament heavy chain
NHEJ	Non-homologous end joining
NMDAR	N-methyl-D-aspartic acid receptor
NMJ	Neuromuscular junction
NS-PME	North-Sea progressive myoclonic epilepsy
oChIEF	Codon optimized ChIEF
PAM	Protospacer adjacent motif
PBS	Phosphate Buffered Solution
PBS-T	Phosphate Buffered Solution with Triton
PCP	Planar cell polarity
PCP2	Purkinje Cell Protein 2
PCR	Polymerase Chain Reaction
PGK	Phosphoglycerate kinase
PI	Propidium Iodide
PLV	Presynaptic lysosome related vesicles
PMA	Progressive Myoclonus Ataxia
PME	Progressive Myoclonic Epilepsy
P0	Postnatal day 0
PRICKLE1	RILP for REST/NRSF interacting LIM domain protein
PTG	Polycistronic-tRNA-gRNA
PV	Parvalbumin
RRE	Rev response element
RNA	Ribonucleic acid
SCA	Spinocerebellar Ataxia
SCARB2	Scavenger Receptor Class B Member 2
SDM	Site-directed mutagenesis
sgRNA	Short guide ribonucleic acid
SICI	Short-interval cortical inhibition
SNAP-25	Synaptosomal nerve-associated protein 25
SNARE	Soluble *N*-ethylmaleimide-sensitive factor Attachment protein REceptor

SST	Somatostatin
SSEP	Somatosensory evoked potential
SV	Synaptic vesicle
T2A	*Thosea asigna* virus 2A self-cleaving peptide
T7E1	T7 Endonuclease I
TEVC	Two-electrode voltage clamp
TGN	Trans-Golgi network
TMS	Transmagnetic stimulation
TUNEL	Terminal deoxynucleotide transferase dUTP nick end labelling
t-SNARE	target-SNARE
ULD	Unverricht-Lundborg disease
UTR	Untranslated region
VGAT	Vesicular GABA transporter
VGIC	Voltage-gated ion channel
VGKC	Voltage-gated potassium channel
VGLUT1	Vesicular glutamate transporter 1
VSD	Voltage sensor domain
v-SNARE	Vesicle-SNARE
VSVg	Vesicular stomatitis virus G
WPRE	Woodchuck hepatitis virus posttranscriptional regulatory element
WT	Wild-type

Table of Contents

List of Tables

List of Figures

Chapter 1

Introduction

Epilepsy is a neural network disease, characterized by paroxysmal attacks of neuronal hyperexcitability and hypersynchronicity that are marked by temporary losses of consciousness, convulsions or sensory disturbances (seizures) (Fisher et al., 2013). The epilepsies are diverse in aetiology and clinical presentation, with over 50 recognised syndromes affecting around 1% of the population (ILAE, 2018; Ngugi et al., 2010). Epilepsy is therefore one of the most common neurological disorders with a significant associated socio-economic burden. While many anti-epileptic drugs (AEDs) are available as first-line treatments, they are ineffective in around 30% of cases and can have significant side-effects (Devinsky et al., 2018). The development of targeted therapeutics, guided by specific mechanistic insights, is therefore essential for improving the treatment of these life-limiting, often devastating, group of diseases.

1.1 Classification of the epilepsies

A person has epilepsy if 1) they have two or more unprovoked seizures over 24 hours apart or 2) if they are determined to have a very high risk of seizure recurrence (60-90%) following a single unprovoked seizure (Fisher et al., 2014). The type of seizure a patient has is used to diagnose an epileptic disorder according to the International League Against Epilepsy (ILAE) Classification Framework (**Figure 1.1**) (Fisher et al., 2017; Scheffer et al., 2017). Seizures are classified as generalised, focal or unknown (Fisher et al., 2017). Generalised seizures originate in both cerebral hemispheres and can manifest as bilateral jerks if motor areas are involved. Focal seizures, however, initially affect only one hemisphere of the brain. Some patients may have both generalised and focal seizures. Alternatively, when the origin of the seizure cannot be confidently established, the epilepsy type is classified as ‘unknown’ (Fisher et al., 2017).

The aetiology, or cause, of the seizures is also used to classify the epilepsies. Epilepsy can be described by 6 main aetiologies: genetic, structural, immune, infectious, metabolic, or unknown (**Figure 1.1**) (Scheffer et al., 2017) . The aetiology of the epilepsy, and an assessment of associated comorbidities, is used in order to provide a final diagnosis of an epilepsy type or syndrome (Devinsky et al., 2018). An epilepsy syndrome, therefore, is the combined occurrence of specific features, such as clinical presentation, age of onset, seizure types and electroencephalogram (EEG) findings, informed also by neuroimaging and a consideration of any associated comorbidities

(**Figure 1.1**) (Devinsky et al., 2018). Over 50 epilepsy syndromes are recognised. Examples include Dravet syndrome, generalised tonic-clonic epilepsy and progressive myoclonic epilepsy (ILAE, 2018).

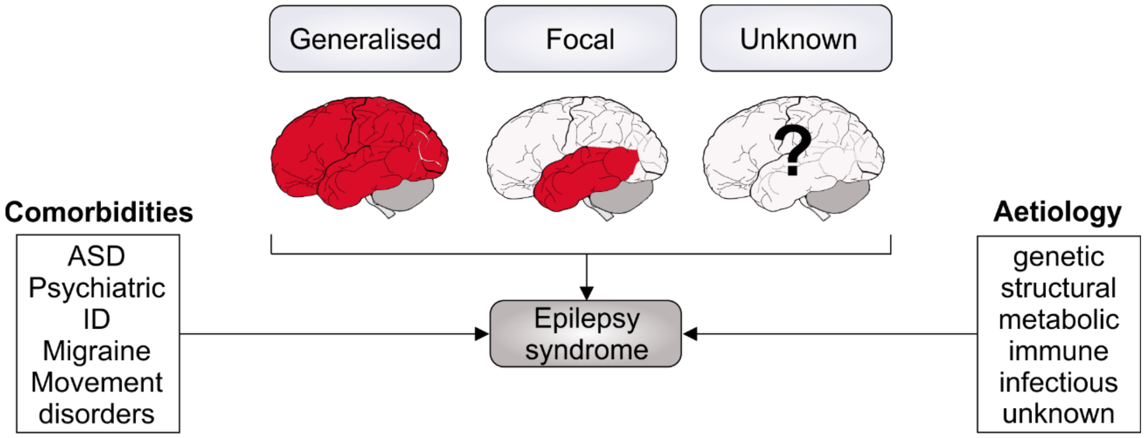

Figure 1.1. Framework for the classification of epilepsy syndromes. Seizures are classified as generalized, focal or unknown (patients can also have a combination of generalised and focal). The aetiology of the epilepsy and associated comorbidities also instruct the diagnosis of an epileptic syndrome. ASD: autism spectrum disorder; ID: intellectual disability.

1.2 Genetic Epilepsies

It is becoming increasingly apparent that many diverse epilepsy syndromes have a suspected or known genetic component. Early gene discoveries in epilepsy were initially made for more common familial epilepsies because large family sizes afforded the investigation of genetic linkage (Oyrer et al., 2018). One of the first epilepsy genes discovered was *SCN1A* in 2000, causative for Dravet syndrome or generalised epilepsy with febrile seizures plus (GEFS+) (Escayg et al., 2000). Since then, over 1000 mutations have been identified in this gene, including a high proportion of *de novo* mutations (mutation is absent in both parents) representing 75-80% of all mutations (Gataullina & Dulac, 2017). *De novo* mutations are an increasing trend in the rare epileptic encephalopathies, likely due to the advent of cheaper deoxyribonucleic acid (DNA) sequencing technologies that require less statistical power to confirm pathogenicity (Appenzeller et al., 2014; Epi4K Consortium et al., 2013; Torkamani et al., 2014).

Another emerging area of genetic epilepsy is somatic mosaicism. Somatic mosaicism is where an individual carries at least two populations of cells with different genotypes, one population of which harbours a pathogenic variant that has arisen by random mutation at some point during brain development (Poduri et al., 2013). If the individual is mosaic in the germline, offspring can become affected by the disease, whilst the parent remains unaffected. For example, a parent that has <45% mosaicism for an *SCN1A* mutation may be unaffected, whereas their offspring develops Dravet syndrome (Depienne et al., 2010).

Somatic mosaicism usefully demonstrates the dose response element of epilepsy gene mutations on seizure thresholds. In the case of Dravet syndrome, mutational load dictates the degree of SCN1A haploinsufficiency and reveals the extent by which homeostatic mechanisms in gene and neural networks can buffer the effects of $Na_V1.1$ loss-of-function. This principle applies to more common epilepsies that are suspected to have a more complex (non-Mendelian) genetic inheritance. In these cases, it is predicted that multiple susceptibility alleles are inherited and combined to reduce seizure threshold and result in epilepsy (Symonds & Zuberi, 2018). It has been highly debated whether a large number of variants make small contributions to an overall reduced seizure threshold or whether a small number of rare variants make large contributions (League Against Epilepsy Consortium on Complex Epilepsies, 2014). Recent research into genetic generalised epilepsy (GGE), a syndrome with complex genetic inheritance, suggests that the latter case applies, as many patients with GGE were found to harbour rare chromosomal microdeletions or a number of ultra-rare variants in known epilepsy genes (Epi4K Consortium, Epilepsy Phenome/Genome Project, 2017). Furthermore, even focal epilepsies that are caused by macroscopic structural abnormalities, such as focal cortical dysplasia, have been found to carry a significant genetic component (Epi4K Consortium, Epilepsy Phenome/Genome Project, 2017; Iffland & Crino, 2017).

Over the past two decades, over 500 genes have been identified in association with epilepsy (Devinsky et al., 2018). Initially, in the instance of rare monogenic epilepsies, mutations were found to predominate in ligand- or voltage-gated ion channels (VGICs), leading to the designation of the genetic epilepsies as a group of neuronal ‘channelopathies’ (Kullmann, 2002; Reid, Berkovic, & Petrou, 2009). The search for pathogenic variants in ion channel genes was largely hypothesis driven, following decades of pharmacological experiments that established the idea that imbalances in excitatory and inhibitory conductances give rise to seizures (Staley, 2015). It was predicted that gain-of-function of excitatory conductances (Na^+ or Ca^{2+}) and loss-of-function of inhibitory conductances (K^+ or Cl^-) would result in neuronal hyperexcitability and therefore seizure phenotypes. Whilst this is generally the trend, it has become increasingly apparent, as more variants are identified in candidate genes, that genotype-phenotype relationships are complex and can be strongly influenced by modifier genes and environmental factors (Carpenter & Schorge, 2018).

Since the advent of the neuronal channelopathies, many epilepsy associated genes have been identified that encode proteins that are not ion channels. In particular, a large number of epilepsy mutations have been found in synaptic proteins and genes controlling the synaptic vesicle cycle (EuroEPINOMICS-RES Consortium, Epilepsy Phenome/Genome project, Epi4K Consortium, 2014). In addition to this, the advancement of genome sequencing technologies and the adoption of hypothesis-free approaches to gene discovery, has led to the identification of mutations in genes that implicate a wide range biological pathways, such as metabolism, Ca^{2+} homeostasis, apoptosis and cell migration (Myers & Mefford, 2015). Overall, the genetic data suggest that the molecular and cellular changes that transform a normal neural network into an epileptic neural network (epileptogenesis) are highly heterogeneous, especially for cases in which the genes involved do not directly imply imbalanced excitation and inhibition. However, while the discovery of diverse epilepsy genes has led to suggested paradigmatic shifts in epilepsy genetics, mutations in ion channels still represent around 25% of all epilepsy mutations (Oyrer et al., 2018).

1.2.1.1 Mechanistic insights from the neuronal channelopathies

The study of the neuronal channelopathies has afforded insights into how the molecular, cellular and network changes caused by ion channel dysfunction lead to epilepsy. Furthermore, the study of the neuronal channelopathies have also provided an investigative framework for other non-ion channel mutations and is already informing the development of new treatments (**Figure 1.2**) (Carpenter & Schorge, 2018).

1.2.1.1.1 Determining pathogenicity

When a new epilepsy gene or gene variant is discovered, there are a number of factors to consider before pathogenicity can be determined:

1) Can genetic linkage be determined for the mutation?
2) Is the mutation absent from control databases?
3) Does the mutation recur in unrelated families?
4) Does the mutation occur in highly conserved residues or structures?

In silico predictions of pathogenicity might also consider observed or predicted mutation rates in healthy populations. If the mutation appears to have arisen *de novo*, then increased attention must be paid to points 2-4 listed above. In relation to point 4, after decades of research into the channelopathies it has been found that a surprising number of non-truncating mutations, such as missense mutations, encode functional channels (Cannon, 2010). Missense mutations often occur in mutational ‘hot-spots’; locations in the coding sequence where pathogenic variants are found to cluster (Symonds & Zuberi, 2018). These hot-spots tend to encode important functional parts of the channel, such as the voltage-sensor domain (VSD), ligand-binding domains or pore forming domain and therefore have low tolerance to mutation (Symonds & Zuberi, 2018). Channel gating (opening or closing) is most commonly affected by missense mutations (Cannon, 2010). Alternatively, a mutation may affect the ability of the channel to form functional homomeric channels or may result in the dominant negative suppression of wild-type (WT) channel function when forming heteromers.

The most definitive method for determining the pathogenicity of a novel gene variant, however, is an *in vitro* functional assay (**Figure 1.2**). For ion channel mutants, electrophysiological analysis carried out in heterologous expression systems, such as *Xenopus laevis* oocytes or human embryonic kidney cells (HEKs), is the gold-standard (Oyrer et al., 2018). These expression systems present the advantage of being able to functionally characterise the mutant channel of interest in the absence of other active conductances and are compatible with relatively high-throughput experiments. However, not all aspects of channel dysfunction are likely to be faithfully reproduced using these types of expression systems. Examples of this include: the modulation of channel activity, subcellular targeting to specialised membrane compartments and estimates of cell surface expression levels - all of which are likely to have a significant impact on neuronal excitability.

1.2.1.1.2 Cell-type specific dysfunction

Investigating the effects of ion channel mutants on neuronal excitability is essential for understanding mechanisms of epileptogenesis. Interestingly, when the effects of individual mutations are studied at the neuronal level, many have been found to exert cell-type specific effects (Asinof et al., 2015; Boillot *et al.,* 2014, 2016; Dutton et al., 2013; Rossignol et al., 2013). Impaired excitability of inhibitory neurons or the hyperexcitability of excitatory neurons selectively imposed by a gene mutation can lead to imbalances in excitation and inhibition, which is thought to be the primary ictogenic (seizure generating) mechanism underlying most epilepsies (Jiang et al. 2016 ; Goldberg & Coulter 2013). Certainly, the vast majority of identified epilepsy mutations, including those that do not encode membrane conductances, have been found to impair GABAergic interneurons

(Noebels, 2015). For example, mutations in $Na_V1.1$, that underlie Dravet syndrome, are generally loss-of-function and so it seemed paradoxical that a loss of sodium current would result in seizures. However, when expressed in different neuronal subtypes, it was found that *SCN1A* mutations disproportionately impaired interneuron firing (Yu et al., 2006). Dravet syndrome might therefore be caused by the 'inhibition of an inhibitor'.

The idea of cell-type specific dysfunction in neurological disease is not new. Neurodegenerative diseases, for example, are characterized by the selective degeneration and death of specific neuronal populations, such as motor neurons in Amyotrophic Lateral Sclerosis or dopaminergic neurons in Huntington's disease (Han et al., 2010; Saxena & Caroni, 2011; Shaw & Eggett, 2000). The selective vulnerability of different groups of neuron is generally thought to reflect the functional specialization of different cell-types, which presumably render them intolerant to certain perturbations, such as the expression of mutant protein in a tightly regulated pathway (Hardy *et al.,* 2016). The diversity and highly specialised functions of interneurons in the brain would suggest that selective dysfunction of specific interneuronal subtypes might also exist and contribute towards epileptogenesis (Jiang et al., 2016). For example, the selective deletion of $Na_V1.1$ in parvalbumin-positive (PV) or somatostatin-positive (SST) interneurons was found to increase susceptibility to thermally induced seizures in mice, replicating a key disease phenotype in Dravet syndrome (Rubinstein et al., 2015). Furthermore, dysfunction of specific interneuron subtypes has been reported to underlie different disease phenotypes in Dravet syndrome. The deletion of $Na_V1.1$ in PV interneurons was found contribute towards autistic-like behaviours, whereas impaired SST function was found to cause hyperactivity (Rubinstein et al., 2015). Cell-type specific dysfunction therefore emerges an important theme in epilepsy (Goldberg & Coulter, 2013).

1.2.1.1.3 Mouse models of epilepsy

The generation of transgenic mouse models is essential in order to test hypotheses that have been generated from studying the effects of ion channel mutations *in vitro*. Mouse models allow for the impact of epilepsy mutations to be assessed at the circuit level and thus facilitate investigation into how an epilepsy mutation leads to excitatory-inhibitory imbalances (Staley, 2015). Furthermore, with the advent of Clustered Regularly Interspaced Short Palindromic Repeats (CRISPR)/Cas9 genome editing technology, pathogenic variants can be 'knocked-in' to the genome, allowing for expression at physiologically relevant levels and developmental stages, as well as the production of multiple splice isoforms.

Mouse models should ideally recapitulate most aspects of the human disease, such as spontaneous seizures, and should be based on clinically relevant human genetic mutations. Often gene knockouts are used to model autosomal recessive, loss-of-function conditions, however, one should be cautious if inferring complete loss-of-function from gene mutations that truncate the encoded protein, as often these proteins will be partially translated and can have dominant negative effects on WT channels (Oyrer et al., 2018). Furthermore, it has been recently found that truncating mutations can trigger the expression of related genes via the induction of nonsense mediated decay (el-Brolosy et al., 2019; Ma et al., 2019). As a result, gene knockouts may not be the most appropriate model for loss-of-functions resulting from missense mutations or reduced gene expression and may, surprisingly, result in less severe disease phenotypes than gene knock-down.

Mouse models also allow for preclinical testing of therapeutics. The development of effective therapeutics, aimed at the specific molecular or cellular basis of the disease, can eventually be used back in the clinic to treat the patient, thus closing the loop between basic science and translational research (Oyrer et al., 2018; Wykes & Lignani, 2018).

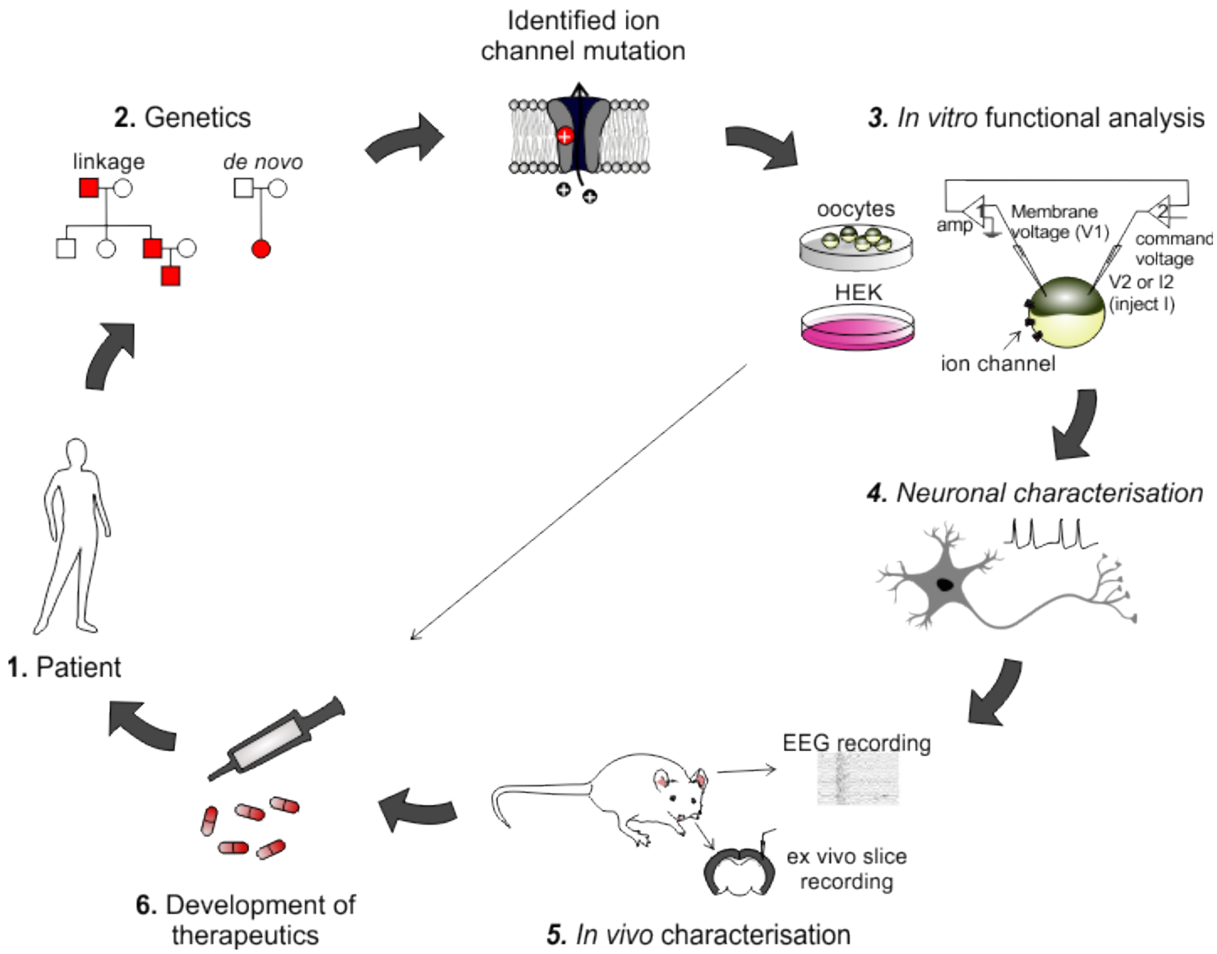

Figure 1.2. Gene discovery in epilepsy and the pathway towards targeted therapeutics. A patient with epilepsy of suspected genetic cause will have their DNA sequenced in an attempt to identify a candidate gene mutation. If the mutation is not detected in the parents then it is said to have arisen *de novo*. *In vitro* functional analysis of ion channel mutants is carried out in heterologous expression systems such as *X.laevis* oocytes using electrophysiological recording such as two-electrode voltage clamp. The effect of the mutation is assessed using transgenic mice, behavioural assessments and EEG recording to monitor central nervous system (CNS) activity.

1.3 The Progressive Myoclonic Epilepsies

Progressive myoclonic epilepsy (PME) is a rare and severe epilepsy syndrome that is caused by mutations in a diverse number of different genes and accounts for 1% of all cases of epilepsy. PME is characterised by the core symptoms of myoclonus (muscle jerks), epilepsy and progressive neurological dysfunction that appear after a period of apparently normal brain development (Marseille Consensus Group, 1990; Minassian, 2014). The PMEs vary widely with regards to the progressive nature of the disease and thus prognosis/clinical outcomes. In some PME cases, neurodegeneration is a prominent disease feature and patients rapidly become cognitively impaired, severely disabled and have reduced life expectancies. In other cases, cognition is relatively preserved and, with the provision of appropriate care, life expectancy can be normal. However, progressive neurological dysfunction may still exist, most commonly in the form of ataxia. Thus, the PMEs may be broadly subdivided into PME with or without dementia.

1.3.1 PME with dementia

PME with dementia largely exhibits an autosomal recessive form of inheritance (Coppola et al., 2005; Ramachandran et al., 2009). The most common PMEs with dementia include Lafora Body disease (LBD), the sialidoses and the neuronal ceroid lipofuscinoses (NCLs). With the exception of LBD, most autosomal recessive PME with dementia are lysosomal storage disorders (Ramachandran et al., 2009). All autosomal recessive PMEs with dementia are, however, characterised by the presence of intracellular inclusion bodies, which in the case of LBD, are strongly associated with neuronal loss (Duran et al., 2014; Ortolano et al., 2014; Turnbull et al., 2011) . Rarer forms of PME with dementia include dentatorubral-pallidoluysian atrophy (DRPLA) and myoclonic epilepsy with ragged red fibres (MERRF), which display autosomal dominant or mitochondrial modes of inheritance, respectively (DiMauro, 2004; Tsuji, 2012).

1.3.1.1 Lafora Body disease (LBD)

LBD is the most common form of PME with dementia, affecting approximately over 250 patients and/or families worldwide (Turnbull et al., 2016). LBD presents during adolescence and has an unrelenting disease course, with death typically occurring within 10 years of disease-onset (Minassian, 2001). LBD is characterised by the presence of intracellular inclusion bodies, or Lafora bodies, that are formed of aggregated polyglucosans. LBs are found in organs throughout the body and diagnosis is typically made via biopsy from the sweat glands (Carpenter & Karpati, 1981). However, despite being a multi-system disease, LBD mainly results from neurological dysfunction.

The majority of cases of LBD result from mutations in the genes *EPM2A* "EPM2A glucan phosphatase" and *NHLRC1* "NHL repeat containing E3 ubiquitin protein ligase 1", which encode the enzymes laforin and NHLRC1 (previously named malin) respectively, both of which function within glycogen metabolism pathways (Chan et al., 2003; Minassian et al., 1998). Laforin binds glycogen and polyglucosans and has a dual-specificity phosphatase domain and NHLRC1 is an E3 ubiquitin ligase that has laforin and glycogen-debranching enzyme as disease relevant substrates (Cheng et al., 2007;

Gentry et al., 2005; Minassian et al., 1998). Mutation of these proteins results in the accumulation of polyglucosans that are insufficiently branched and therefore insoluble (Tagliabracci et al., 2007). The accumulation of insoluble polyglucosans results in the formation of LBs in the neuronal perikarya and dendrites, the simple presence of which is thought to drive neurodegeneration (Duran et al., 2014; Turnbull et al., 2011).

1.3.1.2 Neuronal Ceroid Lipofuscinoses (NCL)

The NCLs are a group of at least 14 neurodegenerative diseases that are characterised by the intracellular accumulation of autofluorescent storage material (ceroid lipofuscin) in neurons of the CNS and in many other organs of the body (Mole & Cotman, 2015). These diseases feature myoclonus, epilepsy, visual failure, psychomotor delay and early death (Nita et al., 2016). Before the genomic era, the NCLs were classified as: infantile; late-infantile; juvenile and adult according to the age of onset, initial symptom manifestations, disease course and the nature of the autofluorescent storage material (Haltia & Goebel, 2013; Nita et al., 2016). Since then, more than 500 mutations have been identified in 13 genes, giving rise to 14 genetically defined NCL subtypes (a genetic cause is suspected, but has yet to be discovered, for CLN9) (UCL mutations database; Mole & Cotman, 2015). NCL genes encode lysosomal proteins (CLN1, 2, 5, 10, 13), as well as a protein of the secretory pathway (CLN11), transmembrane proteins of varied subcellular localization (CLN3, 6, 7, 8, 12) and cytoplasmic proteins that peripherally associate with membranes (CLN4 and CLN14) (Mole & Cotman, 2015). Following post-genomic classification schema, not all NCL subtypes can be considered a PME. The NCLs with PME phenotypes are CLN1, 2, 4, 5, 6, 7, 8, and 14. Of these, CLN4, CLN8 and CLN14 have the most distinctive, or ‘pure’, PME phenotypes.

1.3.1.2.1 CLN4

CLN4, also known as ‘Parry disease’ or Kufs disease, is a rare adult-onset form of NCL and is the only NCL that has an autosomal dominant mode of inheritance (Mole & Cotman, 2015). CLN4 is caused by mutations in a single gene, *DNAJC5* “DnaJ heat shock protein family (Hsp40) member C5” but can present with two different disease phenotypes: Kufs, type A, that is characterised by prominent PME symptoms of myoclonus, epilepsy, dementia and ataxia or Kufs, type B, that features behavioural changes, dementia and facial dyskinesia and that would not be considered a form of PME (Berkovic et al., 1988; Nita et al., 2016). *DNAJC5* encodes cysteine-string protein alpha (CSPα) (Nosková et al., 2011). CSPα is a synaptic vesicle associated protein that acts as a chaperone for protein folding (Donnelier & Braun, 2014). CSPα has been shown to regulate synaptic vesicle exo- and endocytosis and is neuroprotective (Burgoyne & Morgan, 2015; Chandra et al., 2005).

1.3.1.2.2 CLN8

Over 24 mutations in *CLN8* “CLN8 transmembrane ER and ER-Golgi intermediate (ERGIC) protein” have been found in association with NCL (Mole & Cotman, 2015). *CLN8* mutations can result in progressive epilepsy with mental retardation, otherwise known as Northern Epilepsy, or a late-infantile NCL phenotype (Ranta et al., 1999). *CLN8* encodes a transmembrane protein that is localized to endoplasmic reticulum (ER) and ER-Golgi intermediate (ERGIC) compartments, but is also predicted to have other subcellular localisations (Lonka et al., 2000; Lonka et al., 2004; Vantaggiato et al., 2009). The function of CLN8 is largely unknown, but is thought to be involved in the biosynthesis and transport of lipids, such as glycosphingolipid trafficking and ceramide synthesis (Jalanko & Braulke, 2009).

1.3.1.2.3 CLN14

CLN14 is caused by mutations in *KCTD7* “potassium channel tetramerization domain-containing protein 7”, that has also been found to cause ataxia (Kousi et al., 2012; Krabichler et al., 2012; Van Bogaert et al., 2007). KCDT7 is a soluble cytoplasmic protein that is also associated with the cell surface membrane and has been shown to regulate K^+ conductance and the resting membrane potential in neurons (Azizieh et al., 2011; Moen et al., 2016; Staropoli et al., 2012). KCTD7 has been found to be expressed in cortical neurons, hippocampal granule cells and pyramidal cells and cerebellar Purkinje cells, of the mouse brain (Azizieh et al., 2011; Staropoli et al., 2012)

1.3.1.3 Type I Sialidoses

The sialidoses are lysosomal storage disorders that cause PME with dementia. The disease is caused by mutation of *NEU1* “neuraminidase 1”, which encodes alpha-neuraminidase (Bonten et al., 1996). There are two clinically distinct forms of sialidosis, Type I and Type II, which are classified according to the age of disease onset and severity. Type I sialidosis, is a late-onset form of the disease and has a milder disease course than Type II sialidosis. Patients present with worsening generalized myoclonic epilepsy, particularly action myoclonus, in the second or third decade in life with ataxia and seizures co-occurring in over 50% of cases (Franceschetti & Canafoglia, 2016). Patients may also have a characteristic macular ‘cherry red spot’ caused by accumulation of storage material in the ganglionic cells of the eye, hence the disease also being known as ‘cherry red spot-myoclonus syndrome’ (Rapin et al., 1978). Type II sialidosis is of infantile onset and follows a more severe disease course. Patients with Type II sialidosis do not have PME and instead display dysmorphic features, hepatomegaly, dysostosis multiplex and developmental delay (Franceschetti & Canafoglia, 2016). Generally, patients with Type II sialidosis carry mutations that severely reduce or eliminate NEU1 activity, whereas patients with Type I sialidosis carry mutations that have less of a severe impact on enzymatic activity (Khan & Sergi, 2018).

Alpha-neuraminidase is a lysosomal enzyme that exists as part of a multi-enzyme complex with cathepsin A, beta-galactosidase and N-acetyl-galactosamine-6-sulfate sulfatase (Pshezhetsky & Potier, 1996). When part of the lysosomal enzyme complex, alpha-neuraminidase catalyses the removal of terminal sialic acid molecules from oligosaccharides, glycoproteins and glycolipids. Deficiency of alpha-neuraminidase results in an accumulation of siaylated macromolecules in the cell. Pathological signs of sialidosis are therefore the intracytoplasmic presence of lipofuscin-like pigment in neurons and vacuolation of the cytoplasm (Franceschetti & Canafoglia, 2016). The disease is diagnosed by the presence of siaylated oligosaccharides in the urine as well as sialidase enzymatic activity assessment in cultured patient fibroblasts to confirm alpha-neuraminidase deficiency, which is especially important in milder disease cases (Canafoglia et al., 2014; Schene et al., 2016).

1.3.2 PME without dementia

The PMEs without dementia feature a less severely progressive disease course than PMEs with dementia. The paradigmatic disorder for PME without dementia is Unverricht-Lundborg disease (ULD), which was first described by Heinrich Unverricht in 1891 and later by Herman Lundborg in 1903 and from whom the disorder takes its name (Genton et al., 2016). ULD is caused by mutations in *CSTB* “cystatin B” and is considered to be one of the more ‘pure’ forms of PME, in that the disease features mainly myoclonus, epilepsy and ataxia without any major additional abnormalities (Minassian, 2014). ULD is the most common form of PME and is also the best characterised. Historically, PME patients exhibiting PME without dementia have been clinically stratified as ‘ULD-like’ even if they did not have a mutation in *CSTB*. The genomic era has since allowed for the molecular bases of ULD-like PMEs to be solved. ULD and the genes that give rise to similar clinical phenotypes will be discussed in this section (**Table 1**).

1.3.2.1 Unverricht-Lundborg disease (ULD)

The average age of onset of ULD is 12-13 years with patients typically presenting with generalised tonic-clonic seizures (GTCS) (Kälviäinen et al., 2008). Patients quickly develop myoclonus that is highly action and stimulus sensitive and may also display signs of ataxia (Kälviäinen et al., 2008). An important feature of ULD is that, although some neurodegeneration does occur as part of the disease course, cognition is relatively preserved and symptoms stabilize over time (Magaudda et al., 2006). Self-limited disease progression is a defining feature of ULD and contrasts with the relentlessly progressive nature of other forms PME with dementia, previously described. Indeed, with appropriate seizure management, life expectancy in ULD can be normal (Khiari et al., 2009).

ULD is an autosomal recessive disease caused by mutations in *CSTB*. A dodecamer repeat expansion in the 5' untranslated (UTR) promoter region of *CSTB* is responsible for over 90% of cases of ULD and results in a decrease in promoter activity and deficiency of CSTB protein (Joensuu et al., 2008). ULD patients are typically homozygous for the dodecamer repeat expansion mutation, however some patients are compound heterozygous for the expansion and carry a rare missense, nonsense or splice site mutation in the other *CSTB* allele (Kälviäinen et al., 2008). CSTB is a protease that inhibits the activity of papain family cysteine proteases, otherwise known as cathepsins. CSTB has been shown to inhibit the activity of the lysosomal cathepsins B, H, L and S and a reduction in the levels of CTSB has been shown to result in an increase in activity of cathepsins B, L and S in patient-derived lymphoblast cells (Rinne et al., 2002). CTSB is also predicted to have substrates other than cathepsins, such as beta-spectrin, protein kinase C receptor and neurofilament light polypeptide (Di Giaimo et al., 2002). The subcellular localization of CSTB is controversial, and results of studies differ according to the cell type/line used (Kälviäinen et al., 2008). However, CSTB has been found in the nucleus, cytoplasm and peripherally associated with lysosomes (Brannvall et al., 2003). Loss of lysosomal association has been reported for some CSTB mutants and may contribute to disease pathogenesis (Alakurtti et al., 2005; Joensuu et al., 2008). However, pathophysiology of ULD cannot simply be explained by increased cathepsin activity because complementation studies involving knockout of cathepsin genes, on a *Cstb*$^{-/-}$ background, did not rescue any aspects of disease phenotypes (Houseweart et al., 2003). Only knockout of cathepsin B was disease modifying, resulting in a reduction of cerebellar granule cell apoptosis, however, this had no effect on ataxia or seizure phenotypes in these mice (Houseweart et al., 2003).

1.3.2.2 Recently described ULD-like PME genes

1.3.2.2.1 SCARB2/LIMP2 and Action Myoclonus with or without Renal Failure

Mutations occurring in the *SCARB2* “scavenger receptor class B member 2” gene have been identified in autosomal recessively inherited cases of PME with or without renal failure (AMRF) (Berkovic et al., 2008; Dibbens et al., 2009). AMRF patients present initially with tremor, followed by action myoclonus, GTCS, ataxia and dysarthria (Berkovic et al., 2008). AMRF patients develop kidney failure later in the disease course, and most patients die within 7-15 years of disease onset from kidney failure, aspiration pneumonia or multi-organ failure (Berkovic et al., 2008). Other accompanying symptoms are listed in **Table 1** (Berkovic et al., 2008). Recently, mutations in *SCARB2* have been found to be causative for unsolved cases of ULD-like PME *without* renal failure (Dibbens et al., 2009). The clinical presentation for these patients is similar to those with AMRF with regards to the prevalence of myoclonus and seizure frequency, however it appears that two classes of patients exist according to the age of onset, with a juvenile age of onset featuring more severe epileptic phenotype, with poor seizure control, whilst adult age of onset follows a milder disease course. Interestingly, dementia features in SCARB2-PME without renal failure, whereas it is remarkably absent in AMRF, where cognition is relatively preserved until late disease stages (Dibbens et al., 2009).

PME-linked *SCARB2* mutations comprise a range of splice site, nonsense and missense mutations (Berkovic et al., 2008; Dibbens et al., 2009). Patients are mostly homozygous for specific *SCARB2* mutations, however, compound heterozygous cases are also documented. *SCARB2* encodes LIMP2 “lysosomal integral membrane protein type 2”. LIMP2 is localized to lysosomal membranes in the brain and the kidneys and plays a role in lysosome/endosome size and biogenesis. LIMP2 is also thought to play a role in lipid transport, and has also been shown to be required for the trafficking of beta-glucocerebrosidase through the secretory pathway (Neculai et al., 2013; Reczek et al., 2007). Interestingly, mutations in GBA “glucosylceramidase beta” that encodes beta-glucocerebrosidase cause Gaucher’s disease, a lysosomal storage disorder characterised by an accumulation of the glycosphingolipid, glucosylceramide, in the lysosome (Zunke et al., 2016). *SCARB2* mutations have been shown to result in the retention of LIMP2 in the ER which has been shown to result in the extracellular secretion of beta-glucocerebrosidase (Dibbens et al., 2016). It is unclear whether aberrant transport of beta-glucocerebrosidase applies for all LIMP2 mutants and whether it contributes to disease pathogenesis.

1.3.2.2.1 PRICKLE1 and Progressive Myoclonus Epilepsy and Ataxia syndrome

A missense mutation in *PRICKLE1* “prickle planar cell polarity protein 1” has been identified in three families as causative for an autosomal recessive ULD-like form of PME (Bassuk et al., 2008). In all three pedigrees, patients presented with ataxia at around 4-5 years of age and went on to develop myoclonus and epilepsy (Bassuk et al., 2008). *PRICKLE1*-based PME is clinically similar to ULD; patients have relatively normal cognitive functioning and brain MRI appears normal (Bassuk et al., 2008).

PRICKLE1 is a planar cell polarity (PCP) gene that acts in the non-canonical PCP/Wnt signaling pathway, which establishes cell polarity and regulates morphogenesis during development (Simons & Mlodzik, 2008). The p.R104Q missense mutation in PRICKLE1, which causes PME, occurs within the highly conserved PET (Prickle, Espinas, and Testin) domain of the protein that is important for interactions with REST “RE1-silencing transcription factor”, a regulator of neuronal gene expression (Bassuk et al., 2008). The p.R104Q mutation has been shown to disrupt interactions with REST, resulting in an alteration of its subcellular localisation (Liu et al., 2013). Knock-down of PRICKLE1 in hippocampal neurons *in vitro*, which would model PRICKLE1 haploinsufficiency, has been shown to result in defects in dendritic and axonal outgrowth (Liu et al., 2013). It is therefore likely that *PRICKLE*1-based PME represents a neurodevelopmental disorder.

1.3.2.2.2 GOSR2 and North Sea Progressive Myoclonus Epilepsy

Mutations in *GOSR2* “Golgi SNARE receptor complex member 2” have been shown to cause a form of PME known as “North Sea Progressive Myoclonus Epilepsy” (NS-PME) or, rather ambiguously, “Rhamsay-Hunt Syndrome”. NS-PME is so-called in recognition of founder effects for this disease, whereby patient birthplaces cluster around coastal regions of the North Sea (Boissé Lomax et al., 2013). NS-PME is autosomal recessive disease and most patients are homozygous for a G144W missense mutation in the soluble *N*-ethylmaleimide-sensitive factor attachment protein receptor (SNARE) domain of the protein. One patient has, however, been identified as compound heterozygous for the G144W mutation and carries a ΔK164 mutation on the other allele (Praschberger et al., 2015). NS-PME is discussed in detail later in this chapter (**Section 1.6**).

1.3.2.2.3 KCNC1 and Myoclonus Epilepsy and Ataxia Due to a Potassium Channel mutation (MEAK)

Recently, a recurrent, *de novo* mutation in *KCNC1*, which encodes $K_V3.1$, was discovered as a novel cause of ULD-like PME (Muona et al., 2014). Since the discovery of the mutation, and a more thorough characterisation of genotype-phenotype relationships, *KCNC1*-based PME has been termed “Myoclonic epilepsy and ataxia caused by mutation of K^+ channel” or (MEAK) (Oliver et al., 2017). MEAK is one of the few forms of PME that exhibits an autosomal dominant mode of inheritance and the only form of PME identified to date that is caused by a mutation in an ion channel. The disease is very similar at presentation to ULD but differences in clinical phenotype become apparent as the disease evolves (Oliver et al., 2017). MEAK is discussed in detail later in this chapter (**Section 1.5**).

1.3.3 Brief summary of the PMEs

The PMEs are caused by mutations in a large number of different genes with diverse cellular functions. Despite this, all the PMEs feature the triad of epilepsy, myoclonus and ataxia as their core symptoms. The PMEs diverge considerably with respect to the severity of these symptoms, particularly with regards to the extent of neurodegeneration and historically have been broadly subdivided into PME with or without dementia. Lysosomal storage disorders are highly represented in PME with dementia. In PME without dementia, such as the paradigmatic ULD, disease progression is more limited and ataxia features prominently. Over the last decade, novel gene variants have been identified for ULD-like PME. The elucidation of the neuronal effects of these novel genes promises to provide further insights into the PME disease mechanisms.

Table 1.1: ULD-like PME genes

Disease	Gene and protein	Mutation	Inheritance	Clinical symptoms			References
				Age of onset	Core	Non-obligatory	
ULD (EPM1) **MIM: 254800**	*CSTB* encoding cystatin B	Dodecamer repeat expansion in *CSTB* promoter (90% cases)	AR	12-13, GTCS/ Myoclonus	• Ataxia • Myoclonus • Seizures: - GTCS - Absence - Tonic-clonic • Photosensitivity	• Depression	Magaudda et al., 2006; Kälviäinen et al., 2008
SCARB2 (EPM4) **MIM: 254900**	*SCARB2* encoding LIMP2	Missense, frameshift, splice-site, nonsense	AR	15-25, Tremor	• Ataxia • Myoclonus • Seizures - GTCS - Absence • Photosensitivity	• Renal failure • Dilated cardiomyopathy • Sensorimotor neuropathy	Berkovic et al., 2008 Dibbens et al., 2009
PRICKLE1 (EPM1B) **MIM: 608500**	*PRICKLE1* encoding prickle-like protein 1	Missense: p.R104Q	AR	4-5, Ataxia	• Ataxia • Myoclonus • Seizures • Photosensitivity (some) • Impaired upgaze	• Mild sensory neuropathy • Dysmetria • Extensor plantar reflexes • Tremor	Bassuk et al., 2008
North-Sea PME (EPM6) **MIM: 614018**	*GOSR2* encoding GOSR2	Missense: p.G144W p.ΔK164	AR	1-3, Ataxia	• Ataxia • Myoclonus • Seizures: - GTCS	• Syndactly • Areflexia • Scoliosis	Corbett et al., 2011; Lomax et al., 2013; Van Egmond et al., 2014.

					- Absence - Drop-attack - Tonic-clonic • Photosensitivity (all)	• Sensory neuropathy • Elevated creatine kinase levels	
MEAK (EPM7) **MIM: 176258**	*KCNC1* encoding $K_V3.1$	Missense: p.R320H	AD	3-15, Ataxia/ GTCS/ Myoclonus	• Ataxia • Action myoclonus • Seizures - GTCS (19/20) - Absence (some) • Photosensitivity (some)	---	Muona et al., 2014; Oliver et al., 2017
AR: autosomal recessive; AD: autosomal dominant; EPM; epilepsy progressive myoclonic; MIM: phenotype Mendelian Inheritance of Man (MIM) number							

1.4 PME disease mechanisms

1.4.1 Overview of PME genes

Although the genetic causes of PME have been well studied, the underlying disease mechanisms remain poorly understood. This is likely due to the immense genetic and clinical diversity of this syndrome. PME genes are highly heterogeneous and are involved in a wide range of cellular processes including: lysosomal function (CLN1, CLN2, CLN5, CLN10, CLN13, Type I sialidosis, SCARB2-PME and ULD); the secretory pathway (NS-PME, CLN11, CLN8); synaptic function (CLN4); neurodevelopment and transcriptional regulation (PRICKLE1, DRPLA); mitochondrial function (MERRF); the regulation of potassium conductance (MEAK, CLN14) and glycogen metabolism (LBD) (**Figure 1.3**). In addition to these known roles, based on the primary localisation of these gene products, the physiological roles of many individual PME genes have not been completely characterised, and so mutation of individual PME genes is likely to have additional unpredictable effects on neuronal function. Furthermore, PME gene products often participate in more than one biological pathway and likely impact other genes and processes via mechanisms of homeostatic plasticity. Often it is unclear whether observed neuronal phenotypes are a cause or consequence of disease.

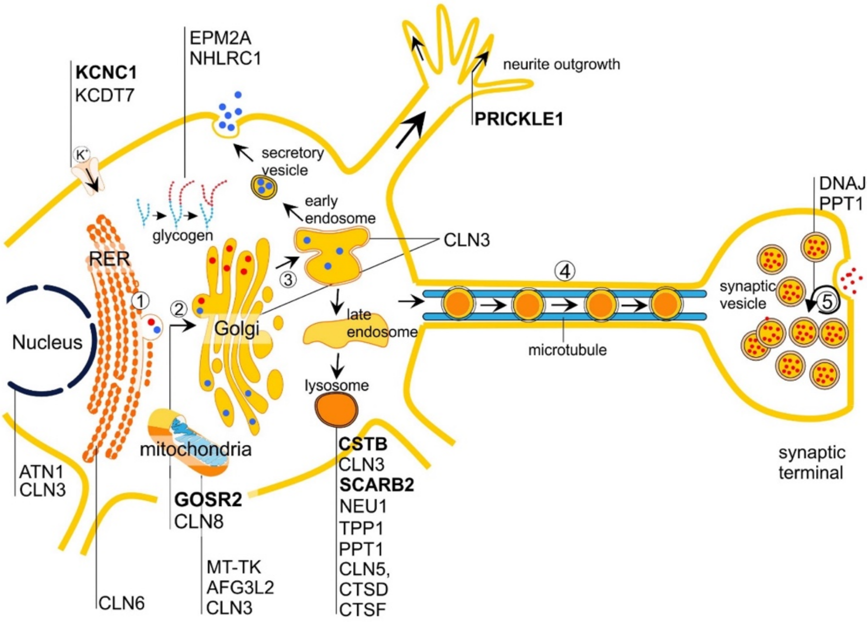

Figure 1.3. Functional roles of PME genes based on their primary function or localisation. RER: rough endoplasmic reticulum; *AFG3L2*: ATPase family gene3-like 2; *ATN1*: atrophin 1; *CLN3*: battenin; *CLN5*: intracellular trafficking protein; *CLN6*: CLN6 transmembrane ER protein; *CLN8:* CLN8 transmembrane ER and ERGIC protein; *CTSD*: cathepsin D; *CTSF*: cathepsin F; *MT-TK*: mitochondrially encoded tRNA-Lys (AAA/G); *PPT1*: palmitoyl-protein thioesterase 1;

TPP1: tripeptidyl peptidase1. In **Bold** are the genes that cause PME without dementia or 'ULD-like' PME.

1.4.2 Myoclonus in PME

Myoclonus is the cardinal feature of PME. Myoclonus is a term used to describe brief, shock-like muscle jerks that are caused by the sudden and involuntary contraction (positive myoclonus) or relaxation (negative myoclonus or asterixis), of both agonist and antagonist muscles simultaneously (Cassim & Houdayer, 2006). Typically, myoclonus is caused by short bursts of electromyographic (EMG) activity, lasting around 100 ± 50 ms, followed by a period of inactivity (Avanzini et al., 2016a; Zutt et al., 2018). In the case of negative myoclonus, muscle jerks result from the sudden cessation of muscle activity, which is then resumed. Negative myoclonus is caused by a mechanism of supraspinal inhibition and lasts around 100 – 500 ms (Avanzini et al., 2016a). Most PME patients will show a combination of both positive and negative myoclonus (Avanzini et al., 2016b).

Many different approaches have been taken to classify myoclonus, however, myoclonus is most frequently described according to its neuroanatomical origin (Eberhardt & Topka, 2017). Myoclonus can be broadly classified as cortical, subcortical (reticular) or spinal (Eberhardt & Topka, 2017). In PME, myoclonus is cortical in origin and is stimulus sensitive (Avanzini et al., 2016a). Patients with PME are therefore said to have 'cortical reflex myoclonus'. Subcortical involvement in myoclonus in PME is also likely, but has yet to be established (Carr, 2011; Faught, 2003).

1.4.2.1 Neurophysiological signs of cortical reflex myoclonus

The neurophysiological signs of cortical reflex myoclonus have been investigated using simultaneous EEG and EMG recordings and by measuring cortical responses to peripheral stimulation (Grosse et al., 2002; Zutt et al., 2018). Such tests are also used to diagnose the neuroanatomical origin of myoclonus and may help in the differential diagnosis of myoclonic disorders. EEG correlates of cortical myoclonus include the presence of spike/spike-wave complexes that occur 20-25 ms before the EMG myoclonus (when recording from the hand); a time-delay in accordance with cortico-spinal signal transduction (Shibasaki & Kuroiwa, 1975; Shibasaki & Thompson, 2011). In most cases of PME, however, the EEG correlate of myoclonus is much smaller in amplitude, with time-locked spike/spike-wave depolarisations observed only for large biphasic jerks (myoclonus simultaneously involving muscles on both sides of the body) (Faught, 2003). The technique of jerk-locked back averaging is particularly helpful in the diagnosis of cortical myoclonus in PME because it helps to distinguish small cortical depolarisations preceding myoclonus from spontaneous EEG background activity (Avanzini et al., 2016; Shibasaki & Kuroiwa, 1975). Sometimes, the EEG can be rhythmic, and myoclonus can occur at regular intervals, as has been observed for SCARB2-based PME and some storage disorders (Berkovic et al., 2008; Rubboli et al., 2011). In these cases, myoclonus may begin to approximate epileptic cortical tremor (Ikeda et al., 1990).

Cortical reflex myoclonus is also characterised by the presence of enlarged responses of the sensori-motor cortex to peripheral stimulation. In PME, giant somato-sensory evoked potentials (SSEPs) in response to peripheral stimulation are frequently described (Shibasaki et al., 1985). Cortical reflex myoclonus may also be diagnosed by the presence of the C-reflex, a long-loop transcortical reflex (LLR) in response to somatosensory stimuli (Sutton & Mayer, 1974). Whilst all three of these physiological abnormalities have been observed in PME, not all three have to be present for diagnosis. Indeed, it is often the progressive nature of the clinical abnormalities, as well as the age of onset, that are used to distinguish PME from the milder, but similar epilepsy syndromes, such as Juvenile myoclonic epilepsy (JME) (Eberhardt & Topka, 2017).

1.4.2.2 Stimulus sensitivity in myoclonus

PME phenomenology appears relatively similar across the different genetic conditions. In general, cortical reflex myoclonus in PME tends to be multi-focal; arrhythmic and variable in amplitude, with many small jerks frequently involving the muscles of the face and distal (upper) limbs (Eberhardt & Topka, 2017; Faught, 2003; Hallett, 1985). Myoclonus in PME is also stimulus sensitive. Myoclonic jerks may be precipitated by sensory stimuli, movement (action myoclonus) or may occur spontaneously at rest (Faught, 2003). Most patients will exhibit a combination of these stimulus sensitivities that present to varying degrees. Action myoclonus, where myoclonus is initiated by movement or the intention to move, is the most common stimulus sensitivity in PME and is often the most disabling disease feature (Avanzini et al., 2016a; Laura Canafoglia et al., 2011). In other forms of PME, such as ULD and rare cases of NCL, photosensitive myoclonus may feature prominently (Faught, 2003; Guellerin et al., 2012). In cases of photic myoclonus, intermittent photic stimulation has been shown to lead to poly-spike wave discharges in the visual cortex that are correlated with large amplitude myoclonic jerks. Sustained stimulation can result in massive myoclonic jerks and further photic stimulation can result in a generalised seizure (Avanzini et al., 2016a). The predominance of one form of stimulus sensitivity can also change over the course of the disease. LBD, for example, presents with marked photosensitivity, whereas action myoclonus and spontaneous myoclonus predominate in the later disease stages (Canafoglia et al., 2004).

1.4.3 Epilepsy in PME

Myoclonus in PME is classified as 'epileptic myoclonus', meaning that myoclonus occurs in the setting of an epilepsy syndrome (Marsden & Hallett, 1981). This definition is straightforward and serves to differentiate the aetiology of epileptic myoclonus from physiological myoclonus, essential myoclonus (idiopathic and of autosomal dominant inheritance) and symptomatic myoclonus (Kojovic et al., 2011). The term 'epileptic myoclonus' is useful also, because it acknowledges cortical hyperexcitability as the singular underlying cause of both myoclonus and epilepsy. In the case of PME, it is sensorimotor cortical hyperexcitability that is thought to underlie seizure generation and myoclonus (Canafoglia et al., 2004; Reutens et al., 1993)

GTCS seizures are the most common type of epilepsy in PME (Shahwan et al., 2005). Other forms of epilepsy occurring in PME include absence, tonic and, in rare cases, focal seizures - such as the visual seizures that occur in LBD (Minassian, 2001). Photosensitivity is a prominent feature of PME and occurs in around 90% of cases, including MERRF and Gaucher's disease (Silva & Leal, 2017). Photosensitivity does not, however, feature in sialidosis (Franceschetti & Canafoglia, 2016). Seizure frequency varies dramatically in PME, ranging from once a day to very rarely (Canafoglia et al., 2017). Indeed, extreme variation in seizure frequency can also exist within genetically stratified groups of patients, where, in rare cases, epilepsy may not feature at all (Kälviäinen et al., 2008; Magaudda et al., 2006). The variability in seizure frequency observed in PME may be a feature typical of the genetic epilepsies. For example, in Dravet syndrome, members of families sharing the same genetic mutation may have febrile seizures in infancy with no later manifestation or may develop Dravet syndrome, a severe epileptic encephalopathy where there are no normal epochs of brain activity and frequent seizures (Brunklaus & Zuberi, 2014).

1.4.3.1 Pharmacological treatments for PME

Treatment of seizures in PME remains symptomatic. Valproate is a first-line treatment option, except in cases of mitochondrial disease (MERRF) (Ferlazzo et al., 2017). Levetiracetam and clonazepam are recommended add-on treatments (Ferlazzo et al., 2017; Genton et al., 2004). Perampanel and zonisamide have recently been shown to be promising alternatives, particularly in the treatment of refractory cases of sialidosis, LBD and DRPLA (Crespel et al., 2017; Goldsmith & Minassian, 2016; Hu et al., 2018; Shiraishi et al., 2017; Vossler et al., 2008). Drugs that aggravate myoclonus, such as phenytoin and carbamazepine, should be avoided (Ferlazzo et al., 2017). Responsiveness to AEDs varies across the PMEs. Often, in the more severe cases of PME with dementia, epilepsy is poorly controlled by AEDs. In LBD, for example, death usually occurs 5-10 years after disease onset, due to respiratory failure during status epilepticus (Minassian, 2001). In other conditions, such as ULD, seizures are well controlled with AEDs and many patients will achieve seizure freedom (Roivainen et al., 2014). Such differences in seizure control likely reflect the varying degrees of neurodegeneration that occur across the different genetic pathologies.

1.4.4 Mechanisms of myoclonus and epilepsy in PME

1.4.4.1 Impaired inhibition in the sensorimotor cortices

Despite high genetic diversity, PME phenomenology appears relatively similar across the different genetic conditions, suggesting that common neurological circuits might be impaired across the PMEs. The core symptom of PME is cortical myoclonus, which might originate from hyperexcitability of the sensorimotor cortices. Transcranial magnetic stimulation (TMS) studies performed on PME patients have found a reduction in short intracortical inhibition (SICI), implicating impaired inhibition as a cause of cortical hyperexcitability in PME (Canafoglia et al., 2010; Nardone et al., 2018). Evidence suggests that SICI is mediated by the activation of interneurons and their signalling via $GABA_A$ receptors (Ziemann, 2004). A reduction in SICI therefore implies an impairment of cortical interneuron function. Indeed, it has been previously shown that GABA levels are reduced in the cerebrospinal fluid of PME patients (Airaksinen & Leino, 1982). Significantly, the AED, valproate, currently the most effective treatment for PME (Wheless & Sankar, 2003), augments GABA action in the brain. Furthermore, $GABA_A$ antagonists administered via the lateral ventricles in otherwise healthy rats have been shown to generate myoclonic jerks, further implicating impaired GABA signalling in the pathogenesis of cortical myoclonus (Matsumoto et al., 2000).

1.4.4.2 Interneuronal pathology in mouse models of PME

The role of interneurons in the pathogenesis in PME has been studied using sporadic and engineered animal models of PME. Mouse models that faithfully recapitulate the majority of PME phenotypes have been generated for ULD, LBD and a large number of the CLNs. While significant neuronal death was generally observed in all PME mouse models, the loss of interneurons was consistently found to be disproportionately greater than the loss of glutamatergic neurons. In ULD (*Cstb*$^{-/-}$) transgenic mice, cell loss was shown to be most severe in the thalamus and cortices, occurring to a lesser extent in the hippocampus (Franceschetti et al., 2007). *Ex vivo* slice recordings found the hippocampus to be hyperexcitable, as evidenced by an increased number of population spikes and lower latency to epileptiform activity following kainic acid challenge (Franceschetti et al., 2007). Immunolabelling for interneuronal markers in the hippocampus revealed a reduced number of GABAergic interneurons that likely contributes to hippocampal hyperexcitability (Franceschetti et al., 2007). Furthermore, a dramatic reduction in the number of GABAergic synaptic terminals, as evidenced by vesicular GABA transporter (VGAT) immunolabelling, has been observed in the somatosensory cortices of ULD mice (Buzzi et al., 2012). In contrast, the number of vesicular glutamate transporter (VGLUT) positive terminals was only slightly reduced compared to WT mice (Buzzi et al., 2012).

Progressive interneuron pathology has also been observed in mouse models of LBD (*Epm2a*$^{-/-}$) where loss of interneurons occurs after just one month of age (Ortolano et al., 2014). Interestingly, also at one month of age, the number of cortical GABAergic neurons in *Epm2a*$^{-/-}$ mice is found to be already half that of age-matched WT controls, implicating early development abnormalities of GABAergic interneurons in LBD (Ortolano et al., 2014). The intraneuronal presence of LBs is strongly associated with neuronal death (Turnbull et al., 2016). In the *Epm2a*$^{-/-}$ mouse, at three months of age, the majority of LBs in the brain were found to be localized to GABAergic interneurons, foretelling further loss of this cell type during disease progression (Duran et al., 2014; Ortolano et al., 2014; Turnbull et al., 2011). PV^{+} interneurons may be particularly vulnerable in LBD. A 75-85% reduction in the number of PV^{+} cortical interneurons was found in LBD brain biopsies and the remaining PV^{+} cells were found to have degenerating processes (Sharma et al., 2013).

Interneuron pathology has also been observed in the NCLs. In a mouse model of CLN8 (*mnd/mnd*), early accumulation of autofluorescent lipopigment was found to be most pronounced in subpopulations of cortical and hippocampal GABAergic interneurons (PV, SST and Calbindin-positive) and was predictive of later GABAergic neuronal loss (Cooper et al., 1999). Hypertrophy and thickening of the dendrites of remaining PV^{+} interneurons was also observed at 9 months (Cooper et al., 1999).

1.4.4.3 Interneurons and disease progression in PME

Taken together, the data from PME mouse models suggest that interneurons are highly vulnerable to the cellular perturbations brought about by mutation of PME genes. Significantly, loss of GABAergic neurons has been observed in human tissue samples from PME patients with different genetic pathologies, highlighting the translational relevance of these findings (Buzzi et al., 2012; Sharma et al., 2013). Given that PME can be considered in part a neurodegenerative disorder, death of interneurons as a cause of epilepsy and myoclonus becomes an obvious hypothesis. However, the mechanisms by which interneurons are especially vulnerable to the effects of PME mutations are largely unknown and are likely to be multifaceted. Furthermore, more complex network dysfunction is expected to underlie PMEs with dementia because interneuron death occurs in the context of global neurodegeneration. This is evidenced in TMS studies of patients with LBD where a reduction in long cortical inhibition (LICI) is observed in addition to a reduction in SICI (Canafoglia et al., 2010). Contrastingly, LICI is normal in ULD.

It remains possible, however, that pathological alterations in interneurons occur as a common early event in PME pathogenesis that promotes further neurodegenerative changes. Developmental abnormalities of interneurons, or interneuron loss that occurs early in the disease course, would be expected to predispose an otherwise normal neural network to one that is capable of supporting spontaneous and recurrent seizures. Evidence of early interneuronal abnormalities, that precede pathological changes in principle cells, has been observed in models of ULD (Buzzi et al., 2012). For PME with dementia, the various intracellular inclusions that are the pathological hallmarks of the different diseases are first observed in interneurons. The concept that ‘seizures beget seizures’ may be particularly relevant to the PMEs. For example, CSTB is thought to be protective against cellular damage and apoptosis during periods of intense neuronal activity. In models of epilepsy, CSTB levels are increased during epileptic seizures (D'Amato et al., 2000). Thus, when seizures begin to occur in ULD, resulting primarily from interneuron functional abnormalities, more cells die, further predisposing the network to the generation of seizures. Indeed, with AED treatment, seizures can be well controlled in ULD, with some patients even achieving seizure freedom and life span can be normal (Khiari et al., 2009).

A similar scenario might exist for LBD. Recently, it has been found that malin loss of function results in a reduction in the levels of glutamate transporter 1 in the cell membranes of astrocytes (Muñoz-Ballester et al., 2016). Astrocytes are known to play an important role in glutamate uptake at synapses in the brain and help to prevent excitotoxicity during periods of intense neuronal signalling (Yi & Hazell, 2006). Excitotoxicity is one well known mechanism by which cell loss occurs in epilepsy. It is possible that once seizures start, e.g. due to early interneuron death, more cells start to degenerate due to lack of neuroprotective mechanisms, resulting in a destructive feedback loop.

1.4.5 Ataxia in PME

Ataxia is also a major part of PME symptomology. Ataxia is a term used to describe impaired coordination of voluntary movements that arise from dysfunction of the cerebellum (Ashizawa & Xia, 2016). Ataxia features in all PME cases, occurring either early or late in the disease course (**Table 1**). MRI studies of patients with different types of PME often reveal mild-moderate cerebellar atrophy, while histopathological analysis of post-mortem brain tissue has also found focal neurodegenerative changes, namely loss of Purkinje cells and cerebellar gliosis (Boissé Lomax et al., 2013; Buzzi et al., 2012; Corbett et al., 2011; Oliver et al., 2017; Turnbull et al., 2016).

Neurodegenerative changes in the cerebellum have also been observed in mouse models of PME. In ULD, substantial apoptosis of cerebellar granule cells is observed, which is hypothesized to be due to impaired resistance to oxidative stress. A reduction in the number of GABAergic synapses onto Purkinje cells with a concomitant reduction of miniature inhibitory post-synaptic currents (mIPSCs) was also observed (Shannon et al., 2002; Lehtinen et al., 2009; Joensuu et al., 2014). However, while cerebellar granule cell apoptosis is a major histopathological feature of $Cstb^{-/-}$ mice, in humans, severe focal degeneration of Purkinje cells is mainly observed. Indeed, cerebellar granule cell apoptosis can be rescued by crossing $Cstb^{-/-}$ mice with cathepsin B knockout mice but has no effect on ataxic phenotypes, suggesting that dysfunction of other types of cerebellar neuron might be contributing to ataxia in these mice (Houseweart et al., 2003). In mouse models of LBD, a striking accumulation of LBs is observed after two months of age in the dendrites of Purkinje cells. Mild focal degenerative changes in Purkinje cells were also observed, which was shown to worsen over the course of the disease (Turnbull et al., 2016).

It would therefore appear that ataxia in PME, is driven by focal degenerative changes in the cerebellum, with Purkinje cell involvement. Interestingly, when ULD patients were historically treated with the AED phenytoin, symptoms of ataxia and myoclonus were found to worsen to the extent that the treated patient cohort were considered to have a different underlying genetic aetiology associated with greater disease severity (Iivanainen & Himberg, 1982). *In vitro*, phenytoin has been shown to cause Purkinje cell degeneration such that it is possible that the use of phenytoin in ULD patients exacerbated existing Purkinje cell dysfunction leading to worsening ataxia (Tauer et al., 1998). Indeed, it has been found in a cohort of patients with epilepsies that do not feature ataxia as a comorbidity, that long-term treatment with phenytoin resulted in the development of irreversible cerebellar ataxia in 40% of cases and that a reduction in cerebellar volume was still observed in many cases that did not show ataxic phenotypes (Shanmugarajah et al., 2018).

1.4.5.1 The concept of Progressive myoclonus ataxia (PMA)

We have seen how myoclonus is an essential feature in the PMEs, while epilepsy and ataxia feature prominently, but to varying degrees. Recently, the concept of progressive myoclonus ataxia (PMA), formerly ‘Rhamsay Hunt syndrome’, has developed (van der Veen et al., 2018). PMA is defined as progressive myoclonus and ataxia with infrequent epilepsy (no more than 6 seizures per year and well controlled by AEDs) that is of known or suspected genetic origin (van der Veen et al., 2018). While the two syndromes are initially difficult to distinguish because they share core symptomology, PME can be differentiated by more severe epilepsy and dementia (**Figure 1.4**). Indeed, to date, the only clinical demarcation that has existed for the PMEs has drawn the distinction between PME with and without dementia, indicating that redefining ‘PME without dementia’ (or ‘ULD-like’) as PMA represents a natural subdivision.

The PME disorders: NS-PME, MEAK, PME1B due to *PRICKLE1* mutation and AMRF can be well described as PMA (**Table 1**). Ataxia features prominently in these epilepsies and is often the presenting symptom, while seizures are generally well controlled (Bassuk et al., 2008; Lomax et al., 2013; Oliver et al., 2017). Severe and progressive action myoclonus is often the most disabling disease feature. Where the data are available, many of these epilepsies exhibit progressive cerebellar atrophy.

The genetic and clinical heterogeneity of PME, has somewhat hindered efforts aimed at identifying common underlying disease mechanisms. By studying a more clinically homogeneous group of PME disorders, such as PMA, the likelihood of uncovering common disease mechanisms is increased. However, *SCARB2* and *PRICKLE1*, are mutations found in only single or few families. Furthermore, *SCARB2* KO mice do not recapitulate PME phenotypes for AMRF (Gamp et al., 2003). In contrast, whilst still both comparatively rare, MEAK and NS-PME represent a significant number of families carrying identical recurrent disease mutations (GOSR2 p.G114W and Kv3.1 p.R320H) (Lomax et al., 2013; Oliver et al., 2017). Furthermore, the *Drosophila melanogaster* model of NS-PME, features abnormal motor phenotypes and reduced threshold to electroconvulsive tests and the *GOSR2* KO mouse results in locomotor deficits in the heterozygous condition (it is homozygous lethal) (Praschberger et al., 2017; Meehan, Conte et al., 2017) . No relevant disease models currently exist for MEAK, nor have the effects of this mutation been characterised in neurons. MEAK and NS-PME therefore represent excellent gene candidates to study PME mechanisms.

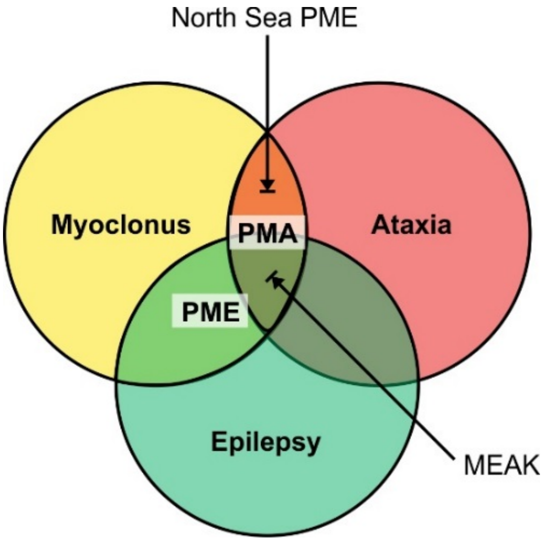

Figure 1.4. Overlapping PME and PMA phenotypes. Both NS-PME and MEAK are well described as PMA. NS-PME prominently features ataxia and myoclonus with rare seizures. Ataxia and myoclonus are also the major disease features of MEAK, however seizures are more common than for NS-PME.

1.5 *KCNC1* (K_V3.1) and MEAK

1.5.1 The genetic and clinical features of MEAK

Recently, a recurrent, *de novo* mutation in the *KCNC1* gene, which encodes the voltage-gated potassium channel (VGKC), K_V3.1, was discovered as a cause of PME, now termed MEAK (Muona et al., 2014; Oliver et al., 2017). 20 patients from 16 unrelated families have been identified as heterozygous for the identical c.959.G>A mutation in the *KCNC1* gene that results in the substitution of a highly conserved arginine residue with a histidine residue at amino acid position 320 (p.R320H) in the VSD of the channel (**Figure 1.5**) (Muona et al., 2014; Oliver et al., 2017). MEAK has an autosomal dominant mode of inheritance and one instance of somatic mosaicism has been observed (Kim et al., 2018; Muona et al., 2014).

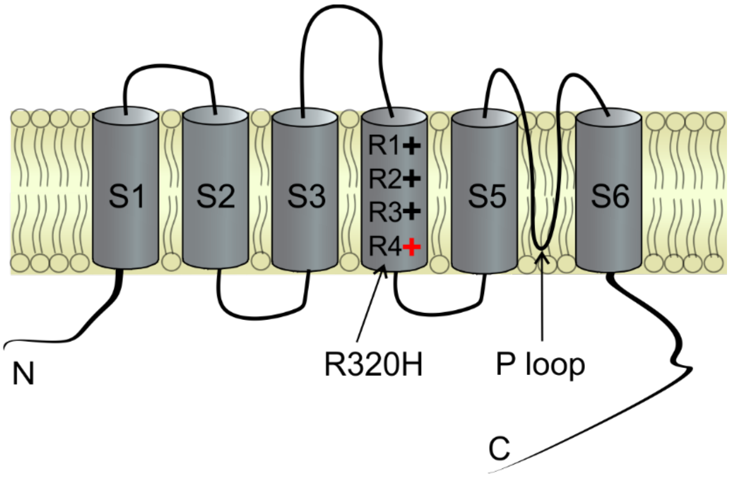

Figure 1.5. K_V3.1 channel topology. The R320H mutation associated with MEAK occurs in the fourth arginine of the S4 voltage-sensor.

Patients with MEAK present between 3-15 years of age most commonly with cortical myoclonus, ataxia or GTCS (Oliver et al., 2017). Action myoclonus is the most severe and disabling symptom in MEAK, occurring frequently and progressively worsening over time, to the extent that patients are often wheelchair-bound 10 years after disease onset (Muona et al., 2014; Oliver et al., 2017). Myoclonus has been found to be at its worst upon awakening and is exacerbated by stress, anxiety, startle or menses. Simultaneous EEG-EMG recordings and neurophysiological testing have showed signs of cortical reflex myoclonus, typical of PME (Oliver et al., 2017).

Ataxia features prominently in MEAK (19/20 patients) and appears early in the disease course (Oliver et al., 2017). Patient brain MRI scans often reveal symmetrical cerebellar atrophy of moderate severity (**Figure 1.6**). In two patients, progressive cerebellar atrophy was observed. Other MRI features of note are an enlarged 4th ventricle and a prominent corpus callosum.

GTCS are rare in MEAK and were absent in one case (Oliver et al., 2017). GTCS were more frequent during adolescence. Photosensitivity was also present in some patients and one patient also had focal occipital epileptiform discharges (Oliver et al., 2017). Seizures are however, generally well controlled by combinatorial AED therapy with valproate being most commonly administered (Oliver et al., 2017). Severe dementia is not present in MEAK and most patients do not have cognitive deficits, although around 50% of patients show signs of cognitive decline over the disease course. With respect to seizure frequency and the stabilization of symptoms in mid-life, MEAK is very much similar to ULD in its clinical presentation.

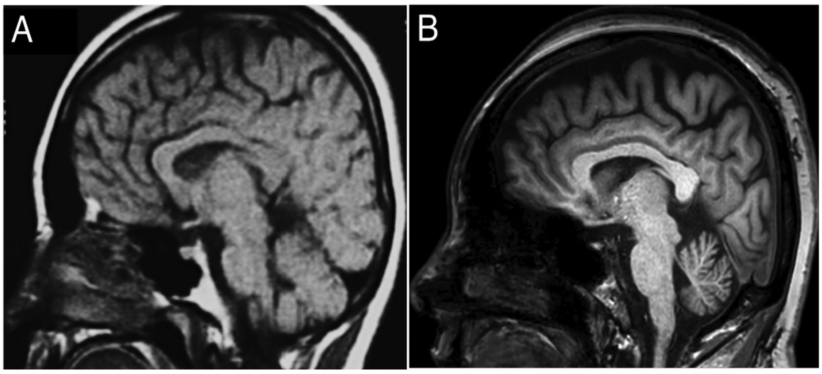

Figure 1.6. MRI of a patient with MEAK displaying cerebellar atrophy. MRI at 16 years of age **(A)** and MRI at 44 years of age **(B)** shows interim progression of cerebellar atrophy from mild to moderate and prominence of cerebellar folia. Some mild cerebral atrophy is also present. Adapted from Oliver et al., 2017.

1.5.1.1 Biophysical characterization of $K_V3.1^{R320H}$ channel mutants

The p.R320H mutation in $K_V3.1$ ($K_V3.1^{R320H}$) has been functionally characterised in two different heterologous expression systems; *X.laevis* oocytes and human embryonic kidney (HEK) cells (Munch et al., 2018; Muona et al., 2014; Oliver et al., 2017). The first study to describe the c.959G>A/p.R320H mutation in $K_V3.1$, expressed the $K_V3.1^{R320H}$ channel in *X.laevis* oocytes and found the mutation to be a loss-of-function, with the channel rendered insensitive to changes in transmembrane voltage (Muona et al., 2014). The R320H mutation was also found to induce a loss-of-function when expressed in HEK cells, however, the measured currents were much larger than those reported in oocytes ($K_V3.1^{R320H}$ expressed 24% of WT current in HEK cells whereas K^+ currents were virtually undetectable in oocytes) (Munch et al., 2018; Muona et al., 2014).

The R320H mutation has also been found to exert a dominant negative effect on WT $K_V3.1$ channel function. When the mutant channel was co-expressed with $K_V3.1^{WT}$ at a 1:1 ratio in oocytes, the mutant channel caused a reduction in current amplitude at +40 mV as well as a hyperpolarizing shift in the voltage-dependence of activation (Muona et al., 2014). Similar results were obtained when $K_V3.1^{R320H}$ was transiently expressed in HEK cell lines stably expressing $K_V3.1^{WT}$ (Oliver, et al., 2017). This study also found impaired channel inactivation for $K_V3.1^{WT+R320H}$ at higher temperatures, a property that the authors suggest results in alleviation of PME symptoms during fever (Oliver et al., 2017). However, another study that expressed $K_V3.1^{R320H}$ in HEK cells, in isolation or with $K_V3.1^{WT}$ at a 1:1 ratio, obtained conflicting results (Munch et al., 2018). In this study, the authors reported significantly slower kinetics of activation and deactivation for the mutant channel but did not find any significant differences in the voltage dependency of channel activation or the voltage dependency of half maximal activation ($V_{0.5}$) for homo/heteromeric $K_V3.1^{R320H}$ channels (Munch et al., 2018).

The functional effects of the R320H mutation in $K_V3.1$ have yet to be characterised in neurons. In order to predict what affects the mutation might have on neuronal excitability one must first consider the physiological roles of the channel.

1.5.2 Voltage gated potassium channels

Potassium channels are the largest and most diverse group of ion channels in the mammalian genome (Yu & Catterall, 2004). Potassium channels are transmembrane proteins with a central aqueous pore that allows for the highly selective passage of K^+ ions across the membrane down their electrochemical gradient. VGKCs are a major group within the K^+ channel family that couple changes in transmembrane voltage to the opening and closing (gating) of the central ion-conductive pore (Hodgkin & Huxley, 1952). VGKC are critical regulators of neuronal excitability and act to shape the action potential waveform, set the resting membrane potential, influence firing patterns and regulate of neurotransmitter release (Coetzee et al., 1999).

The VGKC superfamily is formed of 40 different genes that are grouped into 12 evolutionary and functionally related families (K_V1-12) (Attalli et al., 2019). Further diversity can be generated within these families by alternative splicing, the formation of heteromultimers and RNA editing (Coetzee et al., 1999). Despite their diversity in voltage-dependency and kinetics, VGKCs ubiquitously perform three essential functions

1) K^+ ion conduction through the central pore 2) permeation controlled by gating and 3) gating controlled by voltage (Islas, 2016). Mutagenesis, structural biology and electrophysiological studies have helped us to understand how this is achieved at a molecular level and has led to a deeper appreciation of structure-function relationships.

1.5.2.1 Structure and function of VGKCs

All VGKCs are assemblies of four homologous subunits (α-subunits) that come together to form the main ion-conductive pore of the channel (α-pore). Each α-subunit is formed of 6 transmembrane domains, S1-S6, that are connected by a series of alternating intracellular and extracellular loops, with intracellular amino (N-terminal) and carboxyl termini (C-terminal). The ion-conducting pore region of the channel is formed from the tetrameric assembly of S5 and S6 domains and the pore loop (P-loop) - a re-entrant extracellular loop that connects S5 and S6 and that confers K^+ selectivity. The VSD of the channel is formed of the tetrameric assembly of transmembrane domains S1-S4.

1.5.2.1.1 Structure-function relationships of the VSD

The function of the VSD is to detect changes in transmembrane voltage and to translate this energy into the opening or closing of the main ion-conductive pore. Changes in transmembrane voltage are detected by highly conserved, positively charged arginine residues located on the S4 helix. Upon membrane depolarisation, the S4 helix is driven upwards by electrostatic repulsion resulting in the opening or closing of the ion pore (Starace & Bezanilla, 2001). The movement of the positive charges (gating charges) on the S4 helix from one side of the membrane to the other can be detected as a very small, transient 'gating current' that precedes the K^+ current through the main pore (Figure 1.7B) (Armstrong & Bezanilla, 1973; Keynes & Rojas, 1974).

The contribution of S4 arginine residues to the gating current has been best studied for Shaker, the Drosophila orthologue of $K_V1.1$. Although every third residue in the S4 domain is positively charged, only 4 arginine residues (commonly denoted R1-R4) contribute to the gating charge (Islas & Sigworth, 1999). Of these gating charges, it has been shown using histidine scanning mutagenesis that only R2, R3 and R4 transverse the membrane during voltage sensor transitions and thus contribute towards the gating current (Starace & Bezanilla, 2001). Later studies using molecular dynamics simulations have confirmed that the gating charge is carried entirely by the S4 domain and that only R2-R4 participate (Jensen et al., 2012).

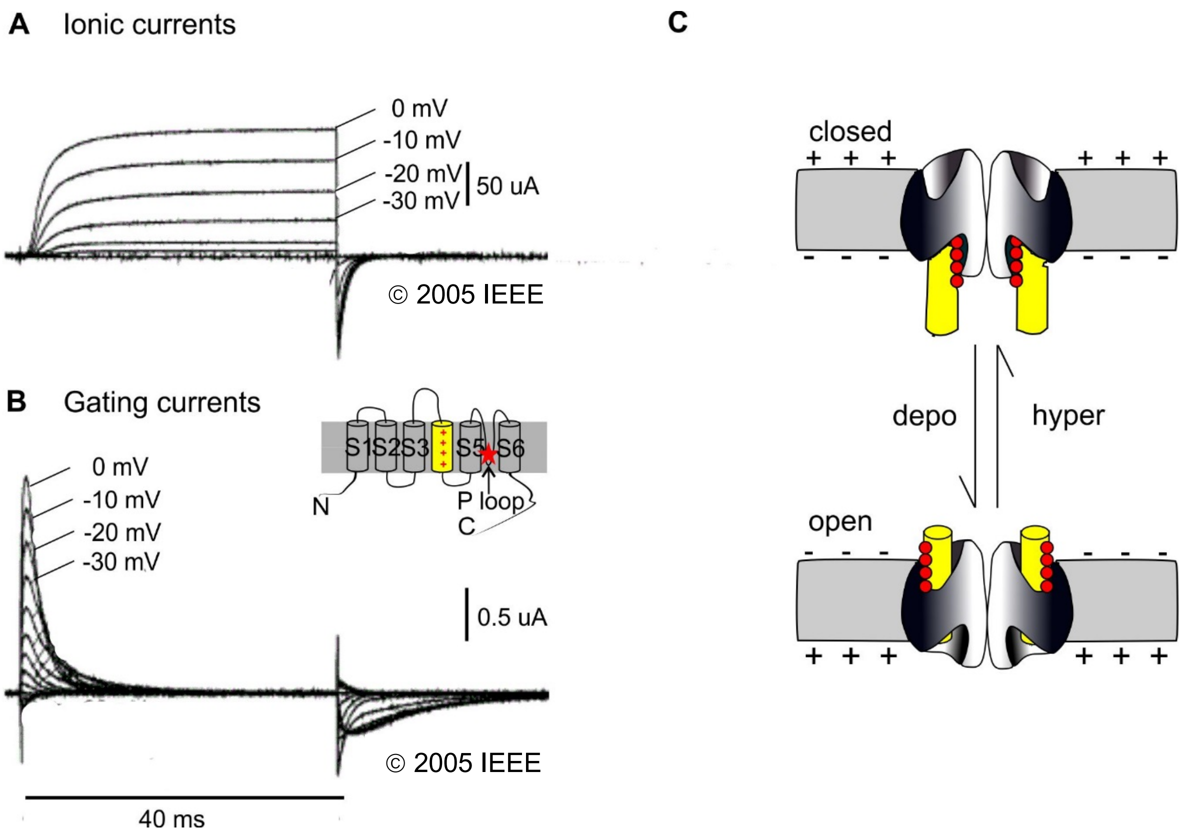

Figure 1.7. Shaker voltage sensor domain transitions upon membrane depolarisation. A) Shaker K^+ currents elicited by depolarizing voltage steps. **B)** Shaker gating currents recorded in the absence of α-pore currents shown in A. An engineered mutation in the P-loop of Shaker blocks K^+ currents through the α-pore. **C)** The helical-screw model of voltage-sensor transitions. Upon depolarization, the S4 helix rotates and translocates towards the external face of the membrane and the solvent accessibility of R1-R4 moves from inside to outside. The movement of charges R1-R4 can be observed as a gating current, as shown in B. Yellow helix: S4 helix, red star: P loop mutation, red circles/crosses: positive gating charges, R1-R4. Adapted from Bezanilla, 2005, Figures 4a & 7a.

1.5.2.2 Gating pore currents as a pathogenic mechanism relevant to the voltage-gated channelopathies

Histidine scanning mutagenesis of R1-R4 in the S4 domain of Shaker unexpectedly revealed that mutation of R371 (R4) to a histidine results in the formation of a proton-conductive pore in the VSD of the channel (Starace & Bezanilla, 2001). Histidine scanning mutagenesis is a method in which arginine residues of the S4 voltage sensor are systematically substituted with histidine residues in order to investigate which arginine residues transverse the membrane during channel gating. Histidine is a small residue with a titratable group, such that, if an S4 arginine residue (replaced by a His) originally crossed the membrane during a S4 voltage sensor transition, it will be detected as a pH-dependent gating current. Mutation of R2 and R3 to histidine residues was found to result in proton transport (whereby a proton is carried from the inside of the cell to the outside of the cell) during voltage sensor transitions, depending on the H$^+$ electrochemical gradient (pH) (Starace & Bezanilla, 2001). Mutation of R4, on the other hand, was found to result in the formation of a proton pore, whereby a voltage-dependent proton current could be detected upon channel activation (Starace & Bezanilla, 2001).

The voltage-dependent proton currents generated by the R371H mutation in Shaker was the first demonstration that mutation of an S4 Arginine - a common type of mutation in the voltage-gated channelopathies – could result in the formation of a pore in the VSD (gating pore). The pathological significance of this was revealed soon after when gating pore currents were detected for pathogenic variants in Na$_V$1.4 and Ca$_V$1.1 in association with hypokalameic (R1 & R2) and normokalaemic (R3) periodic paralysis (Jurkat-Rott et al., 2009; Sokolov et al., 2007). Mutation of R1 & R2 was found to introduce a cation leak in the resting state of the channel whereas mutation of R3 introduced a cation leak in both activated and inactivated channel states for both Na$_V$1.4 and Ca$_V$1.1 (Sokolov et al., 2007; Struyk & Cannon, 2007; Wu et al., 2012). It appears that the loss of the guanidium group that occurs when voltage-sensing arginines are substituted for smaller residues results in the creation of an aqueous path through the VSD of voltage-gated ion channels (Jensen et al., 2012; Tombola et al., 2005). Gating pore currents have also been detected in cardiac arrhythmias and dilated cardiomyopathy and peripheral hyperexcitability (Moreau et al., 2018). A role for gating pore currents has also been suggested, but not demonstrated, in epilepsy, LQTS, familial episodic pain and hemiplegic migraine (Jurkat-Rott et al., 2012).

1.5.3 The K$_V$3 family of voltage-gated potassium channels

K$_V$3.1 belongs to the K$_V$3 family of voltage-gated potassium channels that contain 4 distinct K$_V$3 genes that are abundantly expressed in the CNS (*KCNC1-4* encoding K$_V$3.1-3.4) (Coetzee *et al.,*1999; Rudy *et al.*,1999). Each K$_V$3 family member has a unique expression pattern in the brain, yet individual neurons can express more than one subtype (Brooke et al., 2004). K$_V$3.1-3.3 are highly expressed in restricted subpopulations of neurons, generally of the fast-spiking type, whereas K$_V$3.4 is expressed more diffusely throughout the brain and is also expressed in astrocytes, the spinal cord, the heart and muscle (Boscia et al., 2017; Brooke et al., 2004; Gaborit et al., 2007). K$_V$3 family members are distinguished from other VGKCs by their high voltage of activation (activating from -20 mV) and their rapid deactivation kinetics (Coetzee et al., 1999). K$_V$3.1 and 3.2 are fast delayed-rectifiers that show minimal inactivation, whereas

K_V3.3 and 3.4 produce a fast inactivating A-type current due to rapid N-type inactivation by the N-terminus (Labro 15; Coetzee *et al.,* 1999). K_V3 channels are able to form heteromultimeric channels within the family, which can increase functional diversity (Coetzee *et al.,* 1999). Functional diversity is also achieved by alternative splicing and the differential subcellular targeting of K_V3 homo/heteromultimers (Joho & Hurlock, 2009).

1.5.3.1 Cellular and subcellular localization of K_V3.1 channels

Alternative splicing of the *KCNC1* gene results in the production of two splice isoforms, K_V3.1a and K_V3.1b, which have identical biophysical properties, differing only in the length of their C-termini (Gu et al., 2012; Luneau et al., 1991). The C-termini of K_V3 family members have been shown to be important for subcellular targeting and for the differential modulation of channel properties via intracellular signalling pathways (Chang et al., 2007; Y. Gu et al., 2012; Ozaita et al., 2002; Trimmer, 2015). *In vitro*, K_V3.1a is preferentially targeted to the dendrites, whereas K_V3.1b is mainly detected in the axon (Xu et al., 2007). Polarised targeting of the two splice isoforms has been shown to be due to a conditional interaction between a C-terminal axon targeting motif, common to both K_V3.1a and K_V3.1b and Ankyrin G (Xu et al., 2007). The longer C-terminus in K_V3.1b has been shown to increase the affinity of the interaction of the axon targeting motif with Ankyrin G, facilitating trafficking through the axon initial segment, whereas the axon targeting motif is typically masked in K_V3.1a, resulting in a predominantly dendritic localization (Gu et al., 2012).

K_V3.1b and K_V3.1a also have differing subcellular localisations *in vivo*, although their targeting is not as strictly polarised as is described *in vitro*. *In vivo*, K_V3.1b is found in the proximal dendrites, soma, axons and synaptic terminals, whereas K_V3.1a is mainly axonal, and is typically absent from dendrites (Ozaita et al., 2002; Sekirnjak et al., 1997; Weiser et al., 1995). This pattern of differential expression of the two splice isoforms is generally the trend throughout the brain, with the main exception being in the olfactory bulb, where K_V3.1a is found to be dendritic and K_V3.1b is only weakly expressed. K_V3.1b is the dominant splice isoform in the adult brain, whereas K_V3.1a is expressed more highly during embryonic development (Liu & Kaczmarek, 1998; Perney et al., 1992a).

The expression pattern of K_V3.1b in the adult mouse or rat brain has been extensively studied. K_V3.1b is most highly expressed in the cerebellum, where it is found in granule cells, interneurons and within neurons of the deep cerebellar nuclei (Ozaita et al., 2002)

(**Figure 1.8**). K_V3.1b mRNA has also been detected in Purkinje cells, however K_V3.1b immunoreactivity has been difficult to detect for this cell type (Weiser et al., 1994, 1995). In the neocortex, K_V3.1b has a scattered expression pattern, corresponding to restricted expression in parvalbumin-positive (PV^+) interneurons (**Figure 1.8**). K_V3.1b is absent in SST neurons and is expressed at a low level, if at all, in pyramidal neurons (Chow et al., 1999; Du et al., 1996; Perney et al., 1994; Martina et al., 1998; Perney et al., 1992a; Weiser et al., 1994). K_V3.1b immunoreactivity has also been observed in the reticular thalamus nucleus, globus pallidus, brain stem nuclei, hippocampus and auditory nuclei (Ozaita et al., 2002).

The distribution of K_V3.1 protein in the human brain has not been as extensively studied as it has been for the rodent. At the protein level, western blot analysis has found K_V3.1b to be expressed at a low, but significant, level in the neocortex and cerebellum (Yanagi et al., 2013). Channel protein was, however, undetectable in subcortical grey matter regions such as the hippocampus, thalamus, caudate nucleus and nucleus accumbens (Yanagi et al., 2013). At the mRNA level, in-situ hybridisation studies (Allen Brain Atlas) show a scattered expression pattern for *KCNC1* in the neocortex, which might correspond to restricted expression in interneurons - as has been well documented in the rodent brain. However, whilst multiple immunohistochemical studies in the rodent brain have shown a clear delineation of K_V3.1b expression in interneurons and not in principle cells, in the macaque, prominent expression of K_V3.1b has also been observed in large principle cells of the motor cortex (Soares et al., 2017).

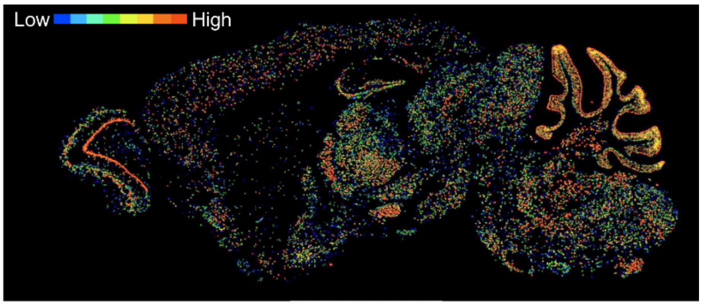

Figure 1.8. The expression pattern of K_V3.1 in the mouse brain. An expression mask image of RNA fluorescent in-situ hybridisation for K_V3.1 mRNA in the C57BL/6J mouse brain at p56, using a heat-map colour scale from low/blue to high/red. The scattered expression of K_V3.1 transcripts in the cortex correspond to restricted expression in PV^+ interneurons. Note also that K_V3.1 is highly expressed in the cerebellum and deep cerebellar nuclei. Image obtained from the Allen Brain Atlas.

1.5.3.2 Neurophysiological roles of $K_V3.1$

1.5.3.2.1 $K_V3.1$ channels and the generation of high frequency firing

The biophysical properties of $K_V3.1$ have been shown to be important for the expression of high frequency firing phenotypes in neurons (Rudy & McBain, 2001). The high voltage of activation of $K_V3.1$ means that $K_V3.1$-mediated K^+ currents predominate during the repolarization phase of the action potential (AP) and do not compromise the peak of the AP (Rudy & McBain, 2001). $K_V3.1$ channels also have a large unitary conductance that aids rapid AP repolarisation, while the fast deactivation kinetics of $K_V3.1$ promote a fast after-hyperpolarisation (AHP) that supports the rapid recovery of voltage-gated sodium channels from inactivation (Rudy et al., 1999). During long depolarisations (< 1 second) $K_V3.1$ channels display very little inactivation, which helps to ensure high channel availability during prolonged periods of neuronal activity (Rudy & McBain, 2001).

The fast deactivation kinetics of $K_V3.1$ might, however, be expected to be disadvantageous in the context of very brief membrane depolarisations, such fast APs of duration <1 ms. This is because the membrane potential remains more positive than the activation threshold for $K_V3.1$ (-10 mV) for only a short period of time, which might result in premature channel closure. One way in which this could be compensated for would be for the neuron to express $K_V3.1$ at very high levels. Recently, however it has been shown that $K_V3.1$ channels express “resurgent” K^+ currents that help to secure AP repolarisation during brief depolarisations (Labro et al., 2015). This phenomenon results from the kinetic properties of the VSD of the channel, which displays relaxation before channel opening only during brief depolarisations that is associated with a deceleration of the deactivation kinetics of the channel. Slowed channel deactivation results in a significant hooked K^+ tail current (resurgent current) upon channel closure that contributes ~25% of the total K^+ current (Labro et al., 2015). $K_V3.1$ channels thus facilitate the generation of narrow, non-adapting APs with fast, but limited, AHPs; important prerequisites for high frequency firing (Rudy et al., 1999; Rudy & McBain, 2001).

$K_V3.1$ channels appear to be kinetically tuned to support high frequency neuronal firing. $K_V3.1$ channels are highly expressed in PV^+ interneurons of the fast-spiking phenotype, cerebellar granule cells and auditory nuclei, where neurons can fire APs at rates of > 600 Hz (Chow et al., 1999; Ozaita et al., 2002; Wang et al., 1998). *Kcnc1* is also found in gene expression clusters correlating fast-spiking electrophysiological phenotypes with the expression of PV and correlating fast-spiking electrophysiological phenotypes with ion channel expression; genes included *Kcnc1/Kcnc2* (K_V3.1/3.2), *Scn1a/Scn8a* (Na_V1.1/1.6) and *Kcna1* (K_V1.1) (Saunders et al., 2018; Toledo-Rodriguez et al., 2004). The expression of PV and K_V3.1 also appears to be developmentally co-regulated, with the expression of both proteins appearing *in vivo* at 14 days in vitro (DIV) (Du et al., 1996).

As well as correlative evidence for K_V3 expression and high frequency firing, there is also strong causal evidence for K_V3.1 expression influencing this type of electrical behaviour (Gu et al., 2012; Lien & Jonas, 2003). Overexpression of K_V3.1 in hippocampal neurons has been shown to transform the spiking phenotype of young excitatory hippocampal neurons from slow to fast-spiking (Gu et al., 2012). Similar effects have been observed using dynamic clamp experiments, whereby the injection of K_V3.1 model conductances into regular spiking pyramidal neurons and CA1 oriens-alveus interneurons in hippocampal slices allowed these cells to fire at high frequencies (Lien & Jonas, 2003).

1.5.3.2.2 K_V3.1 and dendritic integration

Aside from facilitating high frequency firing at the axon, K_V3.1 conductances also influence the excitability of other neuronal compartments. K_V3 currents in the dendrites have been shown to accelerate the rate of decay of excitatory post-synaptic potentials (EPSPs), which is suggested to narrow the time window for temporal summation (Hu et al., 2010; 2014). Rapid EPSPs are also thought to bias summation of spatially separated synaptic inputs arriving across the dendritic tree, which might represent one mechanism by which PV interneurons are able to respond to specific patterns of principle cell activity and regulate their activity via feedforward inhibition (Hu et al., 2010).

1.5.3.2.3 K_V3.1 and the regulation of neurotransmitter release

At the terminals, K_V3 channels act to limit the duration of the presynaptic AP, thereby limiting Ca^{2+} influx and directly impacting on neurotransmitter release (Goldberg et al., 2005). K_V3.1 channels appear to be present throughout the terminal bouton, but are much less present in the active zones, an observation that would be consistent with a ‘gatekeeper’ function of K_V3.1, whereby K_V3 channels limit Ca^{2+} entry into the bouton (Sekirnjak et al., 1997; Weiser et al., 1995). The presence of K_V3.1 is likely to be of functional relevance at PV synapses that are highly specialised to transmit information at high frequencies. At these synapses, K_V3.1 is thought to limit Ca^{2+} entry and release probability, thus influencing short-term plasticity and the efficacy of these synapses (Goldberg et al., 2005).

1.5.3.3 K_V3 channels and human neurological disease

1.5.3.3.1 K_V3.1 variants result in intellectual disability and MEAK

To date, only two mutations in the *KCNC1* gene have been identified in association with human neurological disease. Recently, a nonsense mutation, c.1015.C>T (p.R339*) in *KCNC1* was identified in three affected individuals of one family with intellectual disability (Poirier et al., 2017). The mutation is predicted to result in K_V3.1 haploinsufficiency due to nonsense-mediated decay of the *KCNC1* transcript (Poirier et al., 2017). Conversely, the c.959G>A (p.R320H) missense mutation in *KCNC1*, identified in 20 patients, represents a partial loss-of-function with a dominant negative effect and causes the epilepsy syndrome, MEAK (Munch et al., 2018; Muona et al., 2014; Oliver et al., 2017).

The different disease phenotypes associated with human K_V3.1 mutations are akin to the phenotypic differences observed for single or double *Kcnc1/Kcnc3* knock-out mice (*Kcnc1*$^{-/-}$ or *Kcnc1/Kcnc3*$^{-/-}$). Homozygous *Kcnc1* single knockout mice exhibit mild motor deficits and reduced seizure thresholds, but are overall phenotypically similar to WT littermates (Ho et al., 1997). This is similar to human disease cases of intellectual disability caused by K_V3.1 haploinsufficiency, where patients have relatively mild phenotypes and do not have seizures or myoclonus (Poirier et al., 2017). Double knockout of K_V3.1 and K_V3.3, on the other hand, results in a much more severe disease phenotype, where mice feature myoclonus, reduced seizure threshold, severe ataxia, tremor, hyperactivity and sleep disturbance (Espinosa et al., 2001). The differences in phenotypic severity for single and double knock-out mice likely reflect functional redundancy within the K_V3 family. The more severe disease phenotypes in MEAK, where patients exhibit seizures, myoclonus and severe motor impairment, is likely due to dominant negative effects of the K_V3.1 mutant channel on other K_V3 channels, reducing the ability of healthy K_V3 channels to functionally compensate for K_V3.1 loss-of-function.

1.5.3.3.2 K_V3.3 channel mutations cause spinocerebellar ataxia

Mutations in *KCNC3* (K_V3.3) have been shown to cause autosomal dominant spinocerebellar ataxia type 13 (SCA13). The spinocerebellar ataxias are a heterogenous group of neurodegenerative disorders that primarily involve the cerebellum. Patients with SCA exhibit progressive cerebellar atrophy, ataxia and motor incoordination, although extracerebellar features may also occur. SCA13 occurs at a rate of 1% of all autosomal dominant cerebellar ataxias (Figueroa et al., 2011).

Although mutations in *KCNC3* are rare, they are recurrent and involve highly conserved residues in different positions throughout the channel, including selected voltage-sensing arginine residues of the S4 domain. Mutations in *KCNC3* generally result in two forms of SCA13; early-onset ataxia which often features seizures or intellectual disability or late-onset ataxia that represents a more 'pure' cerebellar syndrome (Zhang & Kaczmarek, 2016b). The functionally characterised R420H and R423H mutations have been shown to both result in non-functional channels that have strong dominant negative effects on WT $K_v3.3$ channels (Figueroa et al., 2011; Waters et al., 2006). Both channel mutants are retained in the Golgi, degraded more rapidly with respect to WT channels and feature aberrant glycosylation (Duarri et al., 2015; Gallego-Iradi et al., 2014; Zhao et al., 2013). Remarkably, despite both causing arginine to histidine substitutions and exhibiting similar functional deficits, $K_v3.3^{R420H}$ results in adult-onset SCA13, whereas $K_v3.3^{R423H}$ results in the early-onset form of the disorder (Figueroa et al., 2011). Other mutations in SCA13 alter the activation (F448L) and/or inactivation (G592R and P583_585Del) kinetics of the channel (Khare et al., 2018; Waters et al., 2006).

1.5.3.3.3 K_V3 family members and other disease associations

In addition to disorders directly caused by mutations in $K_V3.1$ and $K_V3.3$ there is some evidence, as with many genes, that these channels are dysregulated in neurodegenerative disorders and schizophrenia (Angulo et al., 2004; Boscia et al., 2017; Pratt et al., 2008; Yanagi et al., 2014).

1.6 North Sea PME

1.6.1 Clinical and genetic description of North Sea PME

In 2011, molecular diagnosis was achieved for a subset of PME patients presenting with early ataxia and severe and evolving action myoclonus, without dementia (Corbett et al., 2011). These patients were found to be homozygous for a missense mutation, c.430G>T/p.G144W, in *GOSR2* "Golgi SNAP receptor complex 2 protein", which is involved in cis to trans trafficking through the Golgi apparatus (GA). To date, 18 patients from 17 families have been found to carry the missense mutation in *GOSR2*, which displays an autosomal recessive mode of inheritance (Lomax et al., 2013; Corbett et al., 2011; van Egmond et al., 2014). A single patient has also been identified as compound heterozygous for the G144W mutation and a novel c.491_493DelAGA/p.ΔK164 mutation on the other disease allele (Praschberger et al., 2015). Founder effects have been established for the G144W mutation and so *GOSR2*-based PME is also known as 'North Sea' PME (NS-PME) because the ancestral origins of the disease cluster around the coastal regions of countries that border the North Sea, extending up to Norway (Lomax et al., 2013).

NS-PME is remarkably homogeneous in its clinical presentation. In all cases, ataxia is the presenting symptom, occurring between 2-3 years of age (Lomax et al., 2013; van Egmond et al., 2014). Ataxia is followed by stimulus-sensitive myoclonus (action, photo and stress) around the age of 6.5 years which may appear alongside tremor or absence seizures. Typically, seizures manifest during early adolescence, and are a mixture of GTCS, myoclonic status and drop attacks. Photosensitivity is present in all patients. In addition to these prominent CNS signs, patients also exhibit non-obligatory features of areflexia (loss of reflexes); scoliosis; skeletal abnormalities, such as syndactyl and elevated creatine kinase levels in the absence of muscular abnormalities (Lomax et al., 2013; van Egmond et al., 2014). In patients with areflexia, EMG findings suggest that they have sensory neuropathy with chronic anterior horn cell involvement (van Egmond et al., 2014). The disease course is progressive and can result in a reduced life expectancy (Lomax et al., 2013). MRI appears normal for most patients and cognition is well preserved until late in the disease course. The MRI of 3 patients have shown cerebellar atrophy (Lomax et al., 2013; Corbett et al., 2011; Praschberger et al., 2015). The post-mortem study of one deceased patient showed a loss of Purkinje cells in the cerebellum and gliosis in cerebellar vermis (Corbett et al., 2011). The brain weight was also relatively reduced. Abnormal histological features such as intracellular or extracellular inclusion bodies were absent.

1.6.2 *GOSR2* and its role in the secretory pathway

GOSR2, also known as Membrin or GS27, is a SNARE protein that is required for ER-Golgi transport in the early secretory pathway (Lowe et al., 1997). In order to predict how mutations in *GOSR2* might cause NS-PME, one must first consider the roles of the ER, Golgi and SNARE proteins in the context of the secretory pathway.

1.6.2.1 The role of the Golgi apparatus in the secretory pathway

The secretory pathway is the route taken by newly synthesized lipids and proteins that are destined for the cell membrane, endosome, lysosome or secretion. Transport through the secretory pathway relies upon the trafficking of cargo-laden vesicles through the complex endomembrane system of the cell, which delineates functionally specialized organelles that sort and perform post-translational modifications of substrates. Proteins encoded by over a third of eukaryotic genes traffic through this pathway (Dancourt & Barlowe, 2010). The ER and GA are organelles that mediate early steps of the secretory pathway. The ER receives nascent polypeptide chains from ER-associated ribosomes and promotes protein folding with the help of resident chaperone proteins (Yeagle, 2016). The ER is also the site of lipid synthesis and early post-translational modifications of newly synthesised proteins and lipids (Yeagle, 2016). Following quality-control checks, proteins and lipids are then transported to the GA.

The GA is the central sorting hub of the secretory pathway (Morre & Mollenhauer, 2009) (**Figure 1.9**). The GA consists of flattened stacks of folded membrane compartments, or cisternae, which encompass three modules: the cis Golgi network, which is orientated towards, and receives output from, the ER; the cis- medial- and trans-cisternae and the trans Golgi network (TGN) that faces the plasma membrane (Huang & Wang, 2017). Golgi cisternae in mammalian cells are also linked by tubular structures, giving rise to structures called ‘Golgi ribbons’ (Klumperman, 2011). Proteins and lipids are trafficked through the stacks, from the cis- to the trans- face of the Golgi, via pathways and mechanisms that are still being debated (Glick et al., 2013). Within the lumen of each stack, proteins and lipids undergo extensive post-translational modifications that are important for their function and subcellular targeting (Nakamura et al., 2012). The structural and functional compartmentalization of the Golgi is essential in ensuring the fidelity of these modifications. For example, to attain the full cellular complement of glycan structural modifications, the activity of around 700 proteins that include glycosyltransferases, glycosidases and nucleotide sugar transporters, must be sequentially coordinated, which can be controlled in part, by the segregation of different enzymes in the stack (Zhang & Wang, 2016). Once secretory cargoes have been trafficked through the stacks to reach the TGN, they are sorted to the plasma membrane, endosomes or lysosomes (**Figure 1.9**).

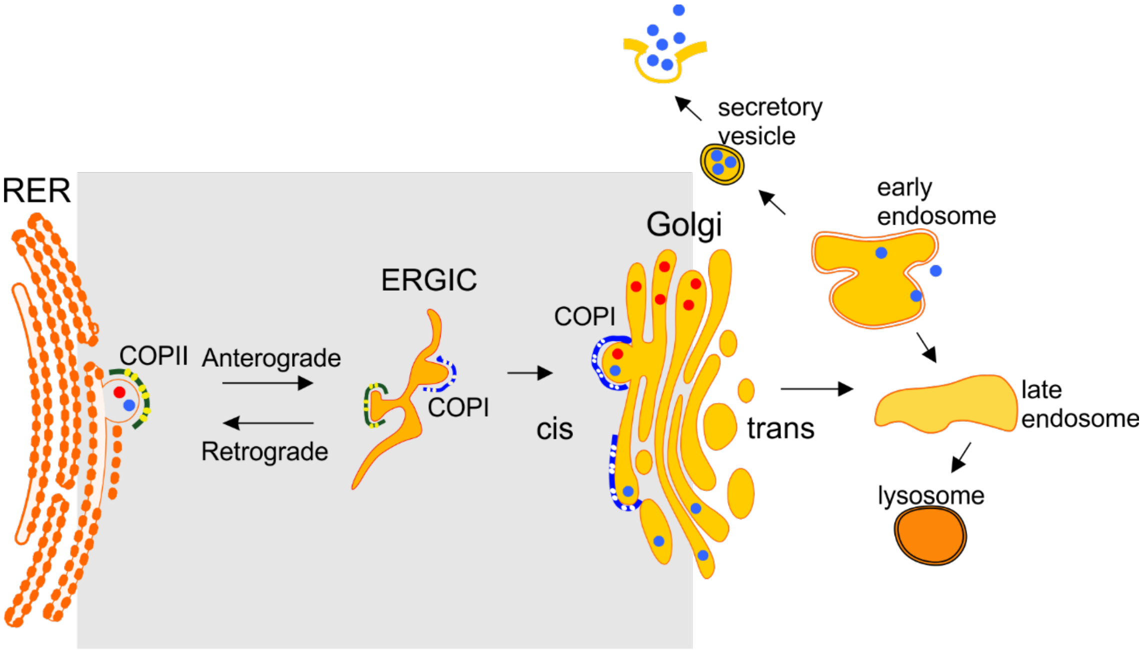

Figure 1.9. The secretory pathway. Proteins and lipids leaving the ER are packaged into COPII coated vesicles that bud from the ER membrane. COPII vesicles fuse together to form the ERGIC which then moves along microtubules towards the cis Golgi network. Vesicles to be recycled back to the ER (retrograde transport) from the ERGIC or Golgi are COPI coated. Secretory cargo is then transported from the cis to the trans face of the Golgi. At the trans Golgi network, secretory cargoes are transported onwards to the cell membrane and early endosomes and lysosomes via recycling pathways. The grey box highlights the process of ER-Golgi transport, an early step within the secretory pathway within which GOSR2 participates.

1.6.2.2 Vesicle trafficking through the secretory pathway requires SNARE proteins

Trafficking of cargo through the secretory pathway critically relies upon the fusion of transport vesicles with their acceptor membranes, which in turn relies on the concerted action of evolutionarily conserved SNARE proteins (Kloepper et al., 2007). SNAREs are single-pass transmembrane proteins that associate with membrane-enclosed transport vesicles (v-SNAREs) or target organelle membranes (t-SNAREs) and interact in specific combinations to drive membrane fusion (Cohen & Melikyan, 2004; Gao et al., 2012). Each SNARE contains 1 or 2 defining SNARE motifs of ~60 amino acids in an 8 heptad repeat structure that are joined to the C-terminal transmembrane domain of the SNARE by a short linker of ~10 amino acids (Südhof & Rothman, 2009). *In vitro* liposome fusion assays have uncovered strict rules for SNARE assembly, whereby only 1 v-SNARE can interact with a specific t-SNARE complex comprised of 2 or 3 polypeptides (Fukuda et al., 2000; McNew et al., 2000; Parlati et al., 2000). SNAREs therefore not only drive membrane fusion, but can also guide the specificity of fusion events.

Interaction of a v-SNARE with its cognate t-SNARE results in the formation of a parallel four-helix bundle, or SNAREpin, which is functionally required for membrane fusion (Hayashi et al., 1994a; Sutton et al., 1998). Each helix in the bundle is contributed by a SNARE motif, which adopts a coiled-coil secondary structure (Fasshauer, 2003). At the core of the SNAREpin are 15 layers of hydrophobic amino acids and one middle layer of ionic amino acids (Kloepper et al., 2007). The ionic layer is formed of 3 glutamine (Q) residues and 1 arginine (R) residue, each contributed by 4 different SNARE motifs (Fasshauer et al., 1998). The composition of the ionic layer is virtually unchanged throughout the SNARE family and SNAREs are principally categorised as Qa, Qb, Qc or R SNAREs (QabcR-complex) according the position and identity of the amino acid residue contributed by their SNARE motif (Fasshauer et al., 1998; Kloepper et al., 2007). Crystal structures of SNAREpins reveal high structural conservation across different SNARE complexes (Antonin et al., 2002; Jahn & Scheller, 2006; Sutton et al., 1998).

High structural conservation of SNAREpins implies a highly conserved process of SNARE assembly. For all SNARE complexes studied, SNARE assembly begins with the slow association of N-terminal domains, the passage through half-zippered intermediate states, followed by fast zippering of SNAREs towards their membrane-associated C-termini (Gao et al., 2012; Zorman et al., 2014). The energy released upon SNARE assembly is used to overcome the energy barrier of membrane fusion; indeed, the energy of interaction is highest towards the C-termini of SNAREs, where the repulsion between the two membranes is the highest (Zorman et al., 2014). Whilst, SNARE assembly is highly stereotyped for different SNARE complexes, differences lie in the energy released upon the last step of SNAREpin formation (Zorman et al., 2014). The differing energies of interaction for different SNARE complexes are thought to translate into varying rates of membrane fusion (Zorman et al., 2014).

The high degree of structural and functional conservation of SNARE proteins implies an essential role in membrane fusion for all eukaryotes throughout evolution (Südhof & Rothman, 2009). The specificity of interactions between SNARE proteins also implies the existence of functionally conserved SNARE units that catalyse specific steps of membrane fusion in the secretory pathway. Indeed, evolutionary analysis has found there to be 20 SNARE subclasses, which can be assigned to the main routes of vesicle trafficking within the eukaryotic cell and that form basic SNARE units according to the structural QabcR rule (**Figure 1.10**) (Kloepper et al., 2007). The conservation of these SNARE units throughout evolution thus also implies the conservation of these trafficking steps. Interestingly, SNAREs of the ER, Golgi and TGN secretory routes were found to exhibit the fewest gene duplication and divergence events, implying that it is a highly conserved and regulated transport step in all eukaryotes (Kloepper et al., 2007).

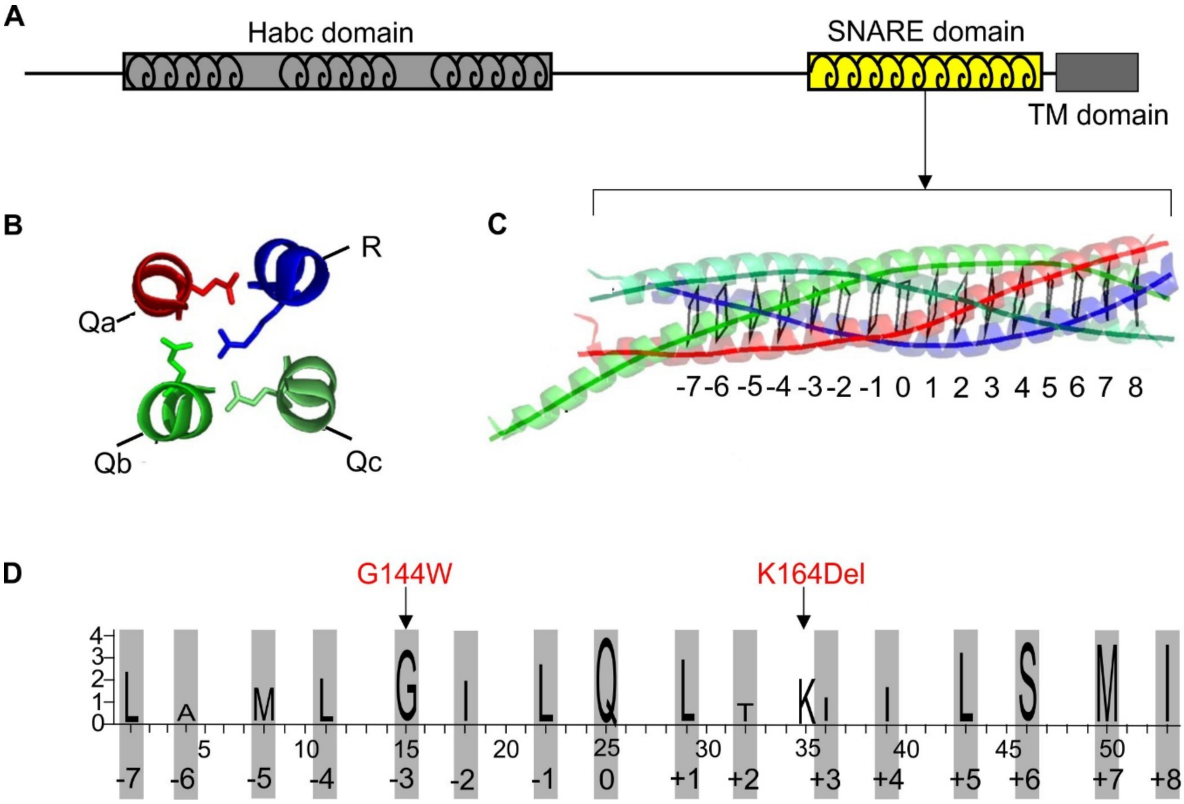

Figure 1.10. Structure of a Qb-SNARE. A) Domain structure of a Qb-SNARE such as GOSR2. **B)** The arrangement of Qa, b, c or R amino acids in the zero layer of the quaternary SNARE complex. **C)** The 3D structure of the quaternary SNARE complex. The colour of helices corresponds to the colour of the zero layer amino acid in B. Numbers denote the position of the core internal layers of the SNARE complex. **D)** The amino acid sequence of the highly conserved SNARE domain of GOSR2. Grey bars indicate the amino acid at one of the SNARE layers. The size of the letter corresponds to the degree of conservation of that residue. The position of the mutations occurring within the SNARE domain that are associated with PME are indicated. **TM**: transmembrane. Panels A, B and C are adapted from Kloepper et al., 2008, Figure 1. Panel D is adapted from Völker et al., 2017, Figure 1.

1.6.2.3 GOSR2 is a SNARE protein required for ER-Golgi transport

GOSR2, is a Qb-type, t-SNARE that is predominantly localized to the cis Golgi network and is required for ER-Golgi trafficking (Volchuk et al., 2004). ER-Golgi trafficking is bidirectional and occurs via the ERGIC, a tubulovesicular membrane structure that acts as an intermediate sorting and transport station (Lee et al., 2004) (**Figure 1.9**). Anterograde transport between the ER and Golgi requires COPII (coat protein complex

II) coated vesicles, whereas retrograde transport relies more on COPI vesicles (Bannykh et al., 1996). Fusion of COPII vesicles with the ERGIC or cis Golgi is catalysed by the formation of a SNARE complex involving the COPII v-SNARE, bet-1 and a t-SNARE, comprised of GOSR2, syntaxin-5 and sec22 (Hay et al., 1998; 1997).

GOSR2 is also implicated to a certain extent in intra-Golgi transport, although a different SNARE unit containing GS28, a closely related Qb-SNARE, has been more strongly associated with this role (Fusella et al., 2013). Indeed, GOSR2 and GS28 show a differential localization in the Golgi stack, with GOSR2 localised predominantly to the cis Golgi network whilst GS28 is found in the medial and trans Golgi compartments (Fusella et al., 2013). Interestingly, both GOSR2 and GS28 have been found in Golgi vesicles. The role of Golgi vesicles in Golgi transport is unclear, largely because a unifying model of intra-Golgi transport has not been agreed upon and the multiple proposed models in existence involve Golgi vesicles to different extents (or not at all) (Glick et al., 2013). It has been proposed, however, that the partitioning of Golgi Qb-SNAREs into Golgi vesicles helps to regulate intra-Golgi transport: extraction of Qb-SNAREs into vesicles blocks Golgi transport whereas fusion of vesicles with the Golgi is associated with active intra-Golgi transport (Fusella et al., 2013). Thus, a tentative role for GOSR2 in the regulation of intra-Golgi transport emerges. Indeed, GOSR2 appears to be dynamically distributed in the Golgi stack whereas syntaxin-5, a cognate SNARE, is stably present throughout the stack (Volchuk et al., 2004).

Furthermore, GOSR2 may play a role in Golgi retrograde transport. GOSR2 has been shown to interact with ARF1, a small GTPase that regulates the binding and polymerization of COPI on membrane vesicles (Honda et al., 2005). Given the similar distribution of ARF1 and GOSR2 within the GA, and the ability of GOSR2 to partition into COPI Golgi vesicles, it is possible that GOSR2 is able to recruit ARF1 to the cis Golgi (Fusella et al., 2013; Honda et al., 2005).

1.6.3 Structural and functional effects of GOSR2 mutants

Both the G144W and K164Del PME mutations in GOSR2 occur within the highly conserved SNARE domain of the protein and would therefore be predicted to have deleterious effects on SNARE assembly or function (**Figure 1.10**). Homology modelling and molecular dynamics simulations have shown that both GOSR2-G144W and -ΔK164 mutants, and homologous mutations in the yeast orthologue, Bos1, are able to assemble into SNARE complexes that are of comparable stability to WT complexes (Völker et al., 2017). The G144W mutant was, however, found to disrupt the packing of side chains in the hydrophobic core of the four-helix bundle and to increase the solvent accessibility of residues adjacent to the tryptophan substitution due to steric hindrance introduced by the large side chain (Völker et al., 2017). The ∆K164 mutation, on the other hand, was surprisingly well tolerated within the four-helix bundle structure and did not alter the solvent accessibility of residues contributing to the formation of the hydrophobic core. The ∆K164 mutation, does, however, lead to a secondary structural alterations and a slight impairment of hydrogen bonding between GOSR2 (Qb-SNARE) and Qa-SNARE helices (Völker et al., 2017). These structural findings suggest that the ∆K164 mutation is less severe than the G144W mutation.

Alterations in the kinetics of SNARE assembly for both GOSR2 mutants would be predicted to negatively impact upon rates of membrane fusion because SNARE assembly provides much of the driving force for membrane fusion. As predicted, rates of membrane fusion were found to be reduced for both GOSR2 mutants during *in vitro* liposome fusion assays using donor liposomes reconstituted with Bet1 and acceptor liposomes reconstituted with Bos1 mutants, Sec22 and Sed5 (Praschberger et al., 2017). Interestingly, rates of liposome fusion were most reduced for the ∆K164 mutant compared to G144W and WT, a finding at odds with previous studies that suggested that this mutant was less severe than G144W (Völker et al., 2017). The predicted functional impact of G144W induced structural alterations were, however, corroborated in the results of liposome fusion assays that showed that impaired N-terminal association, the first step in SNARE assembly, reduced membrane fusion rates because reconstitution with the C-terminal half of Bet1 SNARE domain restored membrane fusion rates (Praschberger et al., 2017). Incubation of SNAREs overnight restored rate of fusion also, but did not for the deletion mutation.

Overall, a reduced rate of fusion is likely to be the major functional impact of the G144W mutant, which would be predicted to result in impaired ER-Golgi trafficking provided that G144W mutant was still able to localize to the cis Golgi (**Figure 1.11**). Both the ∆K164 and G144W were found to localize to the cis Golgi when overexpressed in control patient fibroblasts, and when probed for in mutant patient fibroblasts (Praschberger et al., 2017). However, the overlap coefficient with the cis Golgi marker was significantly reduced for G144W, both in patient fibroblasts and when overexpressed, suggesting that loss of GOSR2 availability might have a role in the disease. A previous study that initially characterised the mutation in yeast, showed a complete mislocalisation for the G144W mutant (Corbett et al., 2011). Partial mis-localisation of GOSR2-G144W may therefore contribute towards trafficking defects in the disease.

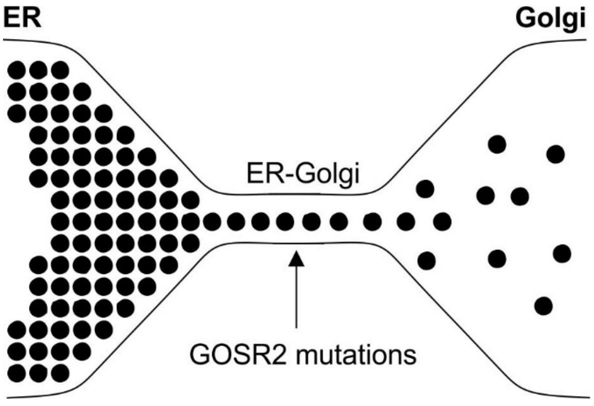

Figure 1.11. Mutations in GOSR2 introduce a trafficking bottleneck in the early secretory pathway. Impaired ER-Golgi transport is likely to have a downstream impact on the rate of flux through the secretory pathway.

1.6.4 Impact of GOSR2 mutants on the nervous system

GOSR2 is an essential Qb-SNARE that is required for ER-Golgi transport and is highly evolutionarily conserved (Kloepper et al., 2007). Homozygous knock-out of *GOSR2* has been shown to be lethal in organisms of increasing complexity, including yeast, flies and mice (Meehan et al., 2017; Praschberger et al., 2017; Shim et al., 1991). Both the G144W and ΔK164 mutations in GOSR2 have been shown to induce partial loss-of-function of varying severity and are therefore largely compatible with organismal viability (Praschberger et al., 2017; Völker et al., 2017). However, what is remarkable is that GOSR2 is a ubiquitous protein expressed throughout cells of the body, yet the effects of these mutations manifest primarily in the nervous system. Furthermore, patients with GOSR2 mutations appear to have relatively normal brain development; preserved cognition and the very specific PMA disease phenotype, which is similar in its presentation to other molecularly defined cases (Lomax et al., 2013; Van der Veen et al., 2018). This would suggest that not all neurons of the CNS are equally as affected by GOSR2 loss-of-function.

In order to understand how a mutation in a ubiquitous and essential protein could lead to a largely restricted neurological phenotype, Praschberger *et al.,* generated a fly model of GOSR2-based PME, by introducing the homologous G144W/ΔK164 mutations (G147W and ΔK166) into the fly orthologue, Membrin (Praschberger et al., 2017). Flies overexpressing Membrin mutants on a null background were found to be weaker, uncoordinated and displayed reduced locomotion (Praschberger et al., 2017). Overexpression of Membrin mutants selectively in neurons was found to phenocopy whole organism expression of Membrin, emphasizing that these phenotypes are caused by nervous system pathology (Praschberger et al., 2017). Interestingly, no defects in secretory trafficking were observed in patient fibroblasts, suggesting that increased secretory demands unique to the nervous system precipitate loss-of-function phenotypes (Praschberger et al., 2017).

1.6.4.1 Secretory pathway deficits in neurons impact dendritic development

The lack of disease phenotypes when Membrin mutants are expressed outside of the CNS suggests that neurons place unique demands on the secretory pathway. Given the early age of onset of NS-PME, Praschberger et al., reasoned that secretory pathway deficits caused by Membrin loss-of-function could impact neurite outgrowth. As hypothesised, Membrin mutants were shown to impair dendritic outgrowth and arborisation when overexpressed in ddaC sensory neurons of the larval fly wall, chosen as a model neuron because they have highly elaborate dendritic trees (Praschberger et al., 2017). Importantly, null mutations engineered into other proteins involved in ER-Golgi transport, such as (*ARF1*) “ADP-ribosylation factor 1” and protein kinase D, have previously been shown to impair dendritic outgrowth in this cell type, highlighting the sensitivity of this developmental process to perturbations within the early secretory pathway (Horton et al., 2005).

The sensitivity of dendritic development to early secretory pathway deficits may be due, in part, to the fact that the development of the neuronal dendritic tree requires significant plasma membrane expansion, which in turn heavily depends on the biosynthesis and trafficking of lipid and protein components. The subservience of the dendrites by the Golgi is evidenced by the polarized orientation of the GA towards the apical dendrite *in vivo*, which biases the direction of anterograde flux into the dendrite with the highest biosynthetic needs (Horton et al., 2005). Furthermore, the secretory pathway in neurons is organised in such a way that lipid and protein synthesis does not solely occur in the perinuclear ER, but also occurs in the dendrites near structures called Golgi “outposts”. (Horton et al., 2005; Horton & Ehlers, 2003). Golgi outposts, defined by their mini-stack structure and immunoreactivity for the Golgin GM130, are localised to dendritic branchpoints and have been found to be important for dendritic arborisation (Jan & Jan, 2010). The number of Golgi outposts in a neuron is positively correlated with longer and more complex dendrites, whereas the depletion or laser damage of Golgi outposts has been shown to result in the shrinkage of dendrites and a reduction in dendritic arborisation (Horton et al., 2005; Ye et al., 2007). Axons, on the other hand, appear to lack satellite secretory pathways, such as Golgi outposts (Ye et al., 2007).

Whereas dendritic outgrowth was found to be significantly impaired in Drosophila overexpressing Membrin mutants, axonal outgrowth appeared to be relatively unaffected; axons derived from ddaC neurons overexpressing Membrin mutants were able to reach their relatively distant targets in the ventral nerve cord (Praschberger et al., 2017). The relative preservation of axonal length in NS-PME flies may reflect a differential sensitivity of axonal and dendritic outgrowth (and maintenance) on ER-Golgi/post-Golgi trafficking. Indeed, a genetic screen performed in Drosophila, aimed at identifying mutants that reduced ddaC neuron dendritic arborisation but not axonal growth, found that the majority of mutations occurred in genes encoding key regulators of the early secretory pathway (Ye et al., 2007). In a separate study, blockade of post-Golgi secretory trafficking by mutation of protein kinase D was found to selectively reduce dendritic growth but not axonal growth (Horton et al., 2005). Taken together, these data suggest that axonal and dendritic outgrowth and maintenance may be differentially regulated by the secretory pathway, likely both spatially and temporally, which may confer a differential sensitivity to Membrin loss-of-function.

1.6.4.2 The effects of Membrin mutants on synapse form and function at the Drosophila neuromuscular junction

Whilst axonal outgrowth appears to be unaffected in fly neurons overexpressing Membrin mutants, abnormalities in presynaptic morphology and function have, however, been observed (Praschberger et al., 2017). Membrin-G147 and ΔK166 expressing synaptic terminals at the fly neuromuscular junction were found to exhibit morphological defects, such as abnormal axonal protrusions that lacked regularly shaped, rounded synaptic boutons, as well as signs of synaptic retraction, possibly caused by local presynaptic cytoskeletal abnormalities (Praschberger et al., 2017).

GOSR2-PME flies were also found to have functional synaptic deficits. The presynaptic expression of G147W and ΔK166 Membrin mutants was found to result in the reduction of miniature excitatory endplate potentials. Furthermore, whilst the amplitude and waveform of single evoked EPSPs were not found to be significantly different from WT controls, striking EPSP abnormalities were instead revealed during trains of stimuli. The delivery of 5 stimuli at 10Hz was found to result in broader, partially merging EPSPs and the occurrence of multiple peaks for a single stimulus, compared to WT (Praschberger et al., 2017). Morphological and functional presynaptic abnormalities in NS-PME fly models are likely due to defects in axonal trafficking (Praschberger et al., 2017).

1.7 Conclusions

Genotype-phenotype relationships in PME remain poorly understood despite a known genetic cause having been discovered in the majority of PME cases. However, similarities in clinical presentation suggest that common underlying circuits might be impaired in PME. TMS studies in PME patients have revealed a reduction in cortical inhibition, likely as a result of interneuron dysfunction. Mouse models of the different genetic pathologies have added to this evidence, finding interneurons to be somewhat selectively vulnerable to the effects of PME mutations early in the disease course. However, the majority of available PME mouse models are for the PME subtypes that heavily feature neurodegeneration. Global neurodegeneration complicates efforts to identify specific disease circuits in PME as it becomes uncertain whether seizures are causing cell loss and vice versa. Furthermore, the genes that cause PME are often ubiquitously expressed and have poorly characterised functional roles. As a result, most studies to date have limited their focus to the cell biology mechanisms of the individual PME genes and histopathological characterisation of disease models.

Another complication in understanding PME disease mechanisms is that, although PME is defined as progressive myoclonus, epilepsy and ataxia, the full extent of these criteria is not delimited. This means that many ‘PMEs’ feature non-obligatory features such a peripheral neuropathies, myopathy and progressive demyelination that might also contribute to disease phenotypes. The PMEs are also very rare, as such it is can be difficult for clinicians to diagnose the specific movement disorder or reach a consensus on patient clustering. Furthermore, the broad diagnosis of PME does not consider the fact that neurodegeneration and seizure severity can vary dramatically across the different conditions, which might indicate that different epileptogenic mechanisms are at play. Perhaps in recognition of this, initial attempts to stratify patients focused on the presence or absence of dementia. Recently, however, the concept of PMA has emerged that might supersede the use of the descriptor, ‘ULD-like’. Patients with PMA prominently feature myoclonus and ataxia with infrequent or absent seizures. PME caused by mutations in *KCNC1* (MEAK) and *GOSR2* (NS-PME) are well described by PMA. Furthermore, mutations in the closely related VGKC, *KCNC3* ($K_V3.3$) causative for SCA13/14, have also been found to cause PMA phenotypes (van der Veen et al., 2018). Patients carrying *GOSR2*, *KCNC1* and certain *KCNC3* mutations form a rather homogenous PMA group, which are more likely to share common underlying disease mechanisms.

MEAK is the first example of an ion channel mutation causing PME. Up to now, the pathogenic effects of this mutation have not been investigated. The R320H mutation in $K_V3.1$ is distinguished from other PME mutations in that the physiological role and CNS expression pattern of this channel has been extensively characterised. $K_V3.1$ is an important regulator of dendritic integration, high frequency firing and neurotransmitter release and so mutations in $K_V3.1$ would be predicted to significantly alter the input-output properties of expressing neurons. $K_V3.1$ is highly expressed in fast-spiking interneurons and neurons of the cerebellum and deep cerebellar nuclei. In view of existing evidence for interneuron dysfunction in PME pathogenesis and the prominence of ataxic phenotypes across the spectrum of genetic aetiologies, I hypothesise that *KCNC1*-based PME embodies interneuron dysfunction and represents a rare chance to rationally dissect the contribution of different neuronal subtypes to the pathogenesis of PME.

Data from the fly model of GOSR2 PME also suggest that selective neuronal populations are affected in PME. Given the essential role of ER-Golgi transport, and the fact that GOSR2 is expressed in every cell in the body, it was surprising to find that *GOSR2* mutations predominantly result in a CNS disorder with a highly specific PME phenotype. This would suggest firstly, that neurons are a cell type that place significant demands on the secretory pathway, and secondly, that selective sub-types of neuron are more affected than others by deficits in secretory pathway flux. I hypothesise that neurons that are more likely to be vulnerable to the effects of *GOSR2* mutation are those with large and complex dendritic arbours or neurons that rely on the fast recycling of synaptic vesicle pools in order to sustain a high rate of synaptic transmission, such as fast-spiking interneurons.

1.8 Aims and objectives

1.8.1 Aim 1

I first aimed to characterize the pathogenic effects of the p.R320H mutation in $K_V3.1$, which is causative for MEAK, in interneurons. My first objective was to characterise the biophysical properties of the mutant channel in *X.laevis* oocytes (**Chapter 3**). My second objective was to investigate the neurophysiological effects of mutant $K_V3.1b$ channels in cortical interneurons *in vitro* (**Chapter 3**). My third objective was to generate a CRISPR/Cas9 based knock-in model of KCNC1-based PME in order to investigate the neuronal effects of the mutation when expressed at physiological levels *in vitro* and *in vivo* (**Chapter 4**).

1.8.2 Aim 2

My second aim was to investigate the neuronal effects of the G144W and ΔK164 mutations in GOSR2, which are causative for NS-PME (**Chapter 5**). My first objective was to express GOSR2 mutants in murine cortical neurons *in vitro* and to characterize the effects of these mutations on synaptic function. My second objective was to express the G144W mutant in Purkinje cells *in vivo* in order to test the hypothesis that neurons with large dendritic trees are highly vulnerable to the effects of PME mutations.

Chapter 2

Materials and Methods

2.1 Gene and protein nomenclature

2.1.1 Gene

The nomenclature used for gene names and symbols is in accordance with HUGO Gene Nomenclature Committee guidelines. The nomenclature used for mouse gene names and symbols are in accordance with the current policies outlined by the International Committee for Standardised Genetic Nomenclature for Mice.

2.1.2 Protein

The nomenclature used for protein names and symbols is in accordance with International Protein Nomenclature Guidelines.

2.2 Animal care and procedures

2.2.1 Animal care

All animal work was carried out according to the Animals (Scientific Procedures) 1986 Act. WT mice and Cre-driver lines were bred in a dedicated facility.

2.2.2 Mouse lines

The following mouse lines were used in this thesis:

- 129P2-Pvalb$^{tm1(cre)Arbr}$/J (PV Cre)
- Sst$^{tm2.1(cre)Zjh}$/J (SST Cre)
- Cg-Tg(Camk2a-cre)T29-1Stl/J (CAMKII Cre)
- Cg-Gt(ROSA)26Sor$^{tm9(CAG-tdTomato)Hze}$/J (Ai9)
- C57BL/6J (WT)

2.2.3. Breeding and maintenance

Transgenic mice were maintained as homozygous for the Cre recombinase gene on a C57BL/J background. To generate PV^{Cre}/Ai9 mice, mice homozygous for the PV^{Cre} allele were mated with mice homozygous for the Ai9 allele, generating offspring that were heterozygous for PV^{Cre} and Ai9. Pups were collected at P0-P2 for cultures, and killed in a humane manner for tissue collection.

2.2.4 Animal procedures

2.2.4.1 Intracranial injection of neonatal mice

Bilateral injection of adeno-associated virus 9 (AAV9) into the lateral ventricles was performed in p0 mice. The entire litter to be injected was removed from the mother and placed in a 32°C incubator within a lined container. Left and right lateral ventricles were manually injected at a depth of 3 mm with 2.5 µL of viral supernatant (containing around 10^{13} transforming units ml^{-1}) per hemisphere using a 5 µL Hamilton syringe (Hamilton, 87930) with a 12 mm, 32 gauge needle (Hamilton, 7803-04) (Kim et al., 2013). Pups injected with different viral vectors were identified by tattooing of forelimbs (Solong Imp & Exp Co., Light Green ink tattoo) using a 0.5 mL insulin syringe (U100). After recovery, pups were returned to their mother and maintained and weaned as normal.

2.2.4.2 *X.laevis* oocyte collection

Ovarian lobes were obtained from adult female *Xenopus laevis* within UCL, in line with procedures approved by UCL Biological Services and the UK Home Office.

2.3 Molecular Biology Methods

2.3.1 General Molecular Biology methods

2.3.1.1 Genomic DNA extraction

Genomic DNA extraction was performed using the PicoPure™ DNA extraction kit (Arcuturus™, KIT0103). Adherent P19 cells grown in a T25 flask were rinsed 1X in Phosphate Buffered Saline (PBS) and then detached from the culture vessel surface by incubation with 1 mL of 0.05% Trypsin-EDTA (Gibco®, 25300) for 5 mins (T25 flask). Trypsin was neutralized by the addition of 5 mL of P19 media and cells were centrifuged at 2000 rpm for 5 min at 22°C. 155 µL of ice-cold Reconstitution Buffer with Proteinase K was added to a pellet of approximately 10^5-10^6 cells, and gently vortexed at ≤ 1000 rpm. The reaction mixture was incubated at 65°C for 3 hrs in a thermoblock with gentle mixing at 100 rpm, and pulsed using a bench-top ultracentrifuge every 30-40 min. Proteinase K was then heat-inactivated at 95°C for 10 min. The genomic DNA samples were stored at -20°C or used immediately in PCR.

2.3.1.2 Polymerase chain reaction (PCR)

The following were combined on ice in a 0.2 mL flat-capped PCR tube on ice to achieve a total reaction volume of 50 µL: 1 µL each of the relevant forward and reverse primers, both at 10 µM (Eurofins Genomics); 1 µL of the DNA template at 100 ng μL^{-1}; 22 µL of molecular biology grade H_2O and 25 µL of PfuUltra II Hotstart 2X PCR master mix (Agilent, 600850). The reaction was placed within a thermocycler and subjected to the temperature cycle outlined in **Table 2.1**. The PCR product was purified using the Wizard® SV Gel and PCR Clean-Up System (Promega, A9281) prior to further downstream reactions. The identity of the PCR product was then confirmed by agarose gel electrophoresis.

Table 2.1. PCR thermocycling conditions

Stage	Number of cycles	Temperature	Duration (vector)	Duration (genomic)
Initialisation	1	95°C	1 min	2 min
Denaturation	30	95°C*	20 s	10 s
Annealing		Primer Tm - 5°C	20 s	5 s
Extension		72°C	15 s / kb	1 min/kb
Hold	1	72°C	3 min	3 min
Hold	1	4°C	∞	∞
* 98°C for genomic PCR				

2.3.1.2.1 Genomic PCR

Genomic PCR primers were designed using NCBI Primer-BLAST software (Ye et al., 2012). The genomic reference sequence for the *Mus musculus Kcnc1* locus was accessed using Ensembl Genome Browser 92 and based on the genome assembly, GRCm38:CM001000.2, for the C57BL/6 mouse strain. Genomic PCR was performed using a high-fidelity (mutation rate of < 0.005%) DNA polymerase (PrimeSTAR Hot-start Takara, #R010A). The reaction was composed of the following components: 15 pmol each of the forward and primers, 100 ng of genomic DNA, 10 µL 5X PrimeStar buffer (Takara), 4 µL deoxyribonucleotides (dNTPs), 0.5 µL DNA polymerase and H_2O to a total volume of 50 µL. The reaction was prepared on ice to prevent degradation of dNTPs. Thermocycling conditions are outlined in **Table 2.1**. For primer sequences refer to **Appendix**, **Table 2.11**.

2.3.1.3 Site-directed mutagenesis

Site directed mutagenesis was carried out using Qiagen Quick Change mutagenesis kit (Agilent Technologies) according to manufacturer's instructions. In every instance, the entire length of the modified transgene was verified by Sanger Sequencing (Section

2.2.1.10). For sequences of mutagenic primers used in this thesis, refer to (**Appendix, Table 2.12**).

2.3.1.4 DNA Transformation

50 µL of Stbl3™ chemically competent *E.coli* cells (Invitrogen) were transformed using 500 ng of circularised plasmid DNA or 2.5 µL of a ligation reaction. Cells were incubated with DNA on ice for 30 min and then heat-shocked at 42°C for 30 s in a water bath, before being placed back on ice for a further 2 min. Cells were allowed to recover for 45 min at 37°C, shaking at 250 rpm in 250 µL of S.O.C media (Invitrogen). 50 µL of the bacterial suspension was streaked onto an agar plate containing the appropriate selective antibiotic (imMedia™ agar, ampicillin or kanamycin) and grown for 20-24 hr at 37°C. Isolated transformant colonies were picked and used to inoculate 3 mL of sterile LB broth, supplemented with the appropriate antibiotic (imMedia™). Cultures were incubated for 18-20 hr at 37°C, shaking at 180-220 rpm.

2.3.1.5 Restriction digest reactions

Restriction digests were carried out using restriction enzymes and reaction buffers from New England BioLabs® (NEB), using High Fidelity® enzymes where available. Restriction digests were carried out using 10-15 units of restriction enzyme per µg of DNA, the appropriate restriction enzyme buffer at 1X concentration and molecular biology grade H_2O (W3500) for a total volume of 40 µL at 37°C for 45 min, unless manufacturer guidelines stated otherwise. Reaction products were purified and isolated using agarose gel electrophoresis or the Wizard® SV Gel and PCR Clean-Up System (Promega, A9281).

2.3.1.6 DNA backbone dephosphorylation

5'-ends of linearized vector DNA were dephosphorylated to prevent vector recircularization via the direct addition of 5 units of Antarctic phosphatase per pmol of DNA (NEB #M0289), 2 µL of Antarctic phosphatase Reaction Buffer (10X, NEB) and H_2O to the un-purified restriction digestion reaction for a final volume of 50 µL. The reaction was incubated at 37°C for 30 min, followed by incubation at 80°C for 2 min to heat-inactivate the phosphatase. Dephosphorylated DNA vectors were purified prior to downstream applications.

2.3.1.7 Agarose gel electrophoresis and gel extraction

1% agarose gels were prepared using an agarose-TAE blend (Sigma, A6236) and 0.01% (v/v) SYBR™ safe DNA gel stain (Invitrogen™). Samples were run alongside 10-20 µL of a Quick-Load® 100bp or 1kb DNA ladder (NEB, N0467S or N0468S). Gel electrophoresis was carried out in a gel tank with 1X TAE buffer, with 100 V applied voltage and 400 mA of constant current. DNA bands of the correct size were identified using a blue-light transilluminator and subsequently gel extracted using the Wizard® SV Gel and PCR Clean-Up System (Promega, A9281) according to the manufacturer's protocol. The purified DNA was eluted in molecular biology grade H_2O (W3500) and concentrated in a final volume of 10 µL using PureLink™ PCR Purification kit (Invitrogen, K310001) prior to subsequent DNA ligation reactions.

2.3.1.8 DNA ligation reactions

DNA ligation reactions were prepared on ice by combining the following in a 0.2 mL PCR tube: 100 ng vector DNA (V); a variable amount of insert DNA (I) in order to achieve a 3:1 or a 5:1 ligation ratio (**Equation 1**); 1 µL T4 DNA ligase reaction buffer (10X, NEB, B0202S); 1 µL T4 DNA ligase (NEB, M0202S) and molecular biology grade H_2O (W3500) to achieve a final volume of 10 µL. Ligation reactions were carried out for 14-18 hr at 16°C in a thermocycler.

$$I\ (ng) = \frac{V\ (ng)\ x\ kb\ size\ of\ I}{kb\ size\ of\ V}\ x\ molar\ ratio\ \frac{I}{V} \qquad \textbf{(Eq.1)}$$

2.3.1.9 DNA purification and quantification

Endotoxin-free plasmid DNA stocks, used for transfection or lentiviral synthesis, were prepared using the NucleoBond® Endotoxin-Free maxiprep kit (Macherey-Nagel). Plasmids pertaining to cloning intermediates that were not used for previously stated applications were purified using the GeneElute™ plasmid miniprep kit (Sigma-Aldrich). DNA concentration and quality were assessed using a Nanodrop™ 2000 spectrophotometer.

2.3.1.10 DNA sequencing

The critical regions of all plasmids used in transfection or lentiviral synthesis were sequence verified. DNA sequencing was carried out using a Sanger Sequencing service provided by Source Bioscience. Sequencing primers were designed using Primer3web version 4.1.0 (Primer3.ut.ee) and obtained from Eurofins Genomics.

2.3.3 DNA vector design and Synthesis

2.3.3.1 DNA constructs used in Results Chapter 3

2.3.3.1.1 Lentiviral vectors for interneuronal targeting of KCNC1 transgenes

The mouse distalless homeobox (mDlx) promoter/enhancer was based on published sequences (Dimidschstein et al., 2016). A DNA fragment of 1777bp, comprising of the mDlx promoter element, a chimeric intron, destabilised green fluorescent protein (dscGFP), a Thoseaasigna virus 2A (T2A) signal peptide sequence and a Multiple Cloning Site (MCS), was commercially synthesised (GeneArt, Invitrogen). The synthesised insert was subcloned into a third-generation pCCL lentiviral transfer plasmid (Dull et al., 1998) between the central polypurine tract (cPPT/CTS) and the Woodchuck Hepatitis *Virus* (WHP) Posttranscriptional Regulatory Element (WPRE) using EcoR1 and Sal1 restriction sites in order to generate the control construct, pCCL-mDlx-dscGFP. The human *KCNC1* transgene encoding the $K_V3.1b$ isoform was codon optimized for expression in murine cells and commercially synthesised (Thermofisher, GeneArt). The c.959G>A mutation was introduced into the *KCNC1* gene using site-directed mutagenesis (**Section 2.2.1.3, Table 2.12**). WT and mutant *KCNC1* transgenes were amplified in a PCR and subcloned into the pCCL-mDlx-GFP plasmid using Nhe1 and Sal1 restriction sites, resulting in the following constructs: pCCL-mDlx-GFP; pCCL-mDlx-GFP-T2A-$K_V3.1b^{WT}$ and pCCL-mDlx-GFP-T2A-$K_V3.1b^{R320H}$.

2.3.3.2 DNA constructs used in Results Chapter 4

2.3.3.2.1 Cre-dependent vectors for optogenetic experiments

A **Fl**ip-**ex**cision (FLEx) switch DNA insert comprising: Cre recombinase responsive loxP and lox2272 sites, the murine phosphoglycerate kinase (PGK) promoter, internal multiple cloning sites (MCS) and a T2A sequence, in the reverse orientation, was commercially synthesised (DNA2.0). The FLEx switch was subcloned into a pCCL lentiviral transfer plasmid between the cPPT/CTS and WPRE elements using EcoR1 and Sal1 restriction sites to generate the intermediate construct, pCCL-Flex-MCS. Prior to this, a second EcoR1 site, 3' of the WPRE element, was destroyed using site directed mutagenesis (**Table 2.12**). Codon optimized ChIEF (oChIEF), C-terminally tagged with mCitrine, was amplified from AAV-oChIEF-citrine, a gift from Roger Tsien (Addgene plasmid # 50974) in a PCR and subcloned into the pCCL-Flex-MCS vector in the inverse orientation using Nhe1 and Mlu1 restriction sites (**Table 2.13**). WT and mutant *KCNC1* transgenes were subcloned downstream of the T2A sequence in the inverse orientation using Xba1 and Sbf1 sites. Constructs containing the human synapsin (hSyn) promoter in place of the

PGK promoter were generated subsequently. The hSyn promoter was amplified by PCR from an AAV transfer vector (Addgene plasmid # 50974) and subcloned into the pCCL backbone using BamH1 and EcoR1 sites. For primer sequences used in the above reactions refer to **Appendix**, **Table 2.13**.

2.3.2.3 DNA constructs used in Results Chapter 5

2.3.2.3.1 pCCL-PTG reporter vectors for gene knock-in events

The pCCL-U6-PTG-EF1α-tdTomato-T2A-EGFP reporter plasmid (referred to in text as pCCL-PTG) for gene knock-in events was constructed via multiple subcloning reactions. EF1α-tdTomato was amplified by PCR from a vector (obtained in-house) and subcloned upstream, and in-frame with, a T2A-EGFP sequence located in a separate transfer plasmid (also obtained in-house) using Xho1 and BstB1 restriction sites (**Appendix, Table 2.14**). The resulting construct was digested with EcoR1 and Nhe1 restriction enzymes and the EF1α-tdTomato-T2A-EGFP insert was subcloned into a pCCL lentiviral backbone using EcoR1 and Nhe1 restriction sites. The U6-PTG gene was commercially synthesised (GeneArt, Thermofisher) and subcloned into the pCCL-EF1α-tdTomato-T2A-EGFP intermediate construct using EcoR1 and Xho1 restriction sites. The design of the PTG gene was based upon a tRNA-gRNA-tRNA-gRNA tandem gene structure using the rice plant tRNA^{GLY} gene (Xie et al., 2015). The gRNA sequences used for targeting EGFP were based on previously published sequences (**Appendix**, **Table 2.15**) (Hu et al., 2018).

2.3.2.4 DNA constructs used in Results Chapter 6

2.3.2.4.1 Constructs for the expression of GOSR2 transgenes using the PGK promoter

An intermediate lentiviral transfer vector containing the PGK promoter was generated by subcloning a dscGFP-T2A-KCNA1 DNA insert from a separate lentiviral transfer vector (Snowball et al., 2019) into the pCCL-FLEx vector, described above, using EcoR1 and BamH1 restriction sites. pcDNA3.1 plasmids containing N-terminally FLAG-tagged human GOSR2 transgenes were obtained in-house (Dr. Roman Praschberger and Dr James Jepson). FLAG-tagged GOSR2 gene variants (WT, ΔK164 and G144W) were amplified using PCR, and subcloned into the pCCL-PGK-dscGFP-T2A-KCNA1 vector downstream of the T2A sequence using Nhe1 and Sal1 restriction sites in order to replace the KCNA1 transgene (**Appendix, Table 2.16**). In total 4 constructs were synthesised: PCCL-GFP; pCCL-PGK-GFP-T2A-GOSR2.WT; pCCL-PGK-GFP-T2A-GOSR2.G144W and pCCL-PGK-GFP-T2A-GOSR2.ΔK164.

2.3.2.4.2 Constructs for the expression of GOSR2 transgenes using the PCP2 promoter
The sequence of the human Purkinje cell protein 2 (PCP2) promoter was based on the sequence given for Ple155, the minimal PCP2 promoter identified as part of the Pleiades (Ple) MiniPromoters project (De Leeuw et al., 2016). The PCP2 promoter was amplified by PCR from pEMS1424, a gift from Elizabeth Simpson (Addgene plasmid # 29220) and subcloned into an AAV2 backbone (Weston et al., 2018) using EcoR1 and BamH1 restriction sites (**Appendix, Table 2.17**). DscGFP and *GOSR2* transgenes were subcloned downstream of the PCP2 promoter via a two-step process. Firstly, pCCL-PGK-dscGFP-T2A-GOSR2 plasmids, described previously, were digested with BamH1 and Sal1. Two fragments were generated due to the presence of a BamH1 site in the GOSR2 gene: BamH1-dscGFP-T2A-NtGOSR2 and CtGOSR2-Sal1. The two DNA fragments were isolated and the BamH1-CtGOSR2-Sal1 DNA fragment subsequently subcloned into the pAAV2-PCP2 vector that had been digested with BamH1 and Sal1. The resulting construct was digested again with BamH1, and the BamH1-CtGOSR2-Sal1 DNA fragment was subcloned 3' of the dscGFP gene and T2A sequence. The correct orientation of the insert and the sequence of the entire expression cassette was verified by Sanger sequencing. For the pAAV2-PCP2-dscGFP control construct, dscGFP was isolated from pCCL-PGK-dscGFP by digestion with BamH1 and Sal1 and subcloned into pAAV2-PCP2 using the same compatible sites. The following 3 constructs were generated: pAAV2-PCP2-dscGFP-T2A-GOSR2.WT; pAAV2-PCP2-dscGFP-T2A-GOSR2.G144W and pAAV2-PCP2-dscGFP.

2.3.4 Molecular Biology methods for CRISPR/Cas9 applications

2.3.4.1 Design and cloning of short guide RNAs

4 short guide RNAs (sgRNAs) targeting the *Kcnc1* genomic locus were designed using an online CRISPR design tool (http://crispr.mit.edu/, Zhang lab, MIT 2013). Off-target effects were assessed using the off-target finder software, *Cass-OFFinder* (http://www.rgenome.net/cas-offinder/). Candidate sgRNA sequences were subcloned into a pKLV-U6-(BbsI)-PGK-puro-2A-BFP plasmid that was a gift from Hiroshi Ochiai (Addgene plasmid, #62348) using the BbsI site. Complementary single-stranded DNA oligonucleotides (oligos) (Eurofins Genomics) were annealed to generate dsDNA inserts with single-stranded 5' and 3' DNA overhangs complementary to BbsI restricted ends in the target vector (**Appendix, Table 2.18**). ssDNA oligonucleotides were first 5' phosphorylated by combining the following in a 10 µL reaction volume: 1 µL of sense

oligonucleotide at 100 µM, 1 µL of antisense oligonucleotide at 100 µM, 1 µL T4 polynucleotide kinase (NEB), 1 µL T4 polynucleotide kinase buffer (10X, NEB), and 6 µL of H_2O. The reaction was incubated at 37°C for 30 min and then at 65°C for 20 min to heat-inactivate the kinase. The oligonucleotides were annealed in a thermocycler according to the following protocol: 1. Incubation at 95°C for 5 min 2. Ramp cooling to 25°C at a rate of -6°C min^{-1} 3. Hold at 25°C for 5 min and 4. Hold at 4°C. Oligonucleotides were diluted to 1 ng uL^{-1} and 7 µL of annealed oligonucleotides were used in a ligation reaction with 100 ng of BbsI digested and dephosphorylated backbone DNA, according to the standard protocol (**Section 2.2.1.8**). The sgRNA sequence for each resulting pKLV construct was verified by Sanger sequencing.

2.3.4.2 T7E1 enzyme mismatch assay for the assessment of sgRNA efficiency

A T7 Endonuclease I (T7E1) mismatch cleavage assay was performed using the Engen® Mutation Detection Kit (NEB, #E3321S). P19 cells were co-transfected with Lenti-Cas9-2A-Blast, a gift from Jason Moffat (Addgene plasmid # 73310) and pKLV-U6-sgRNA(1-4)PGK-puro-2A-BFP plasmids (**Section 2.2.2.3.1**). P19 genomic DNA was extracted 48hr later (**Section 2.2.1.1**). The genomic region surrounding the edited *Kcnc1* locus was amplified using PCR primers described in **Appendix**, **Table 2.11**. The T7E1 assay was then carried out as follows: 250 ng of genomic PCR product was combined with 2 µL Buffer 2 (10X, NEB) and H_2O to a total volume of 19 µL. The PCR amplicon was then denatured and annealed in a thermocycler according to the programme outlined in **Table 2.2**. Digestion of the resulting heteroduplexes was achieved by incubation of the reaction mixture with 1 µL of EnGen T7E1 at 37°C for 15 min. T7E1 was then inactivated by incubation with 1 µL of Proteinase K for 5 min at 37°C. The resulting digested PCR amplicons were then stored at -20°C or used immediately for fragment analysis.

Table 2.2. Thermocycling conditions for heteroduplex formation in T7E1 mismatch assay

Cycle step	Temperature (°C)	Ramp rate (°C s^{-1})	Time (min)
Initial denaturation	95		5
Annealing	95-85	- 2	
	85-25	- 0.1	
Hold	4		

DNA fragments were analysed using a 2% agarose gel. 4 µL of Gel Loading dye (6X, NEB) was added to the un-purified T7E1 assay reaction products and the whole reaction mixture was loaded onto the gel, alongside 20 µL of Quick-Load® 100 bp DNA ladder

(NEB, N0467S). DNA bands were imaged using a UV transilluminator. The integrated intensity of each band product was analysed using Image J and the insertion/deletion (indel) frequency was calculated according to **Equation 2**, where ‘a’ is the integrated intensity of the undigested PCR amplicon and ‘b’ and ‘c’ are the integrated intensities of each cleavage product.

$$Indel\ \% = 100\ x\ 1 - \frac{(1-(b+c))}{(a+b+c)^{0.5}} \qquad (\textbf{Eq. 2})$$

2.4 Synthesis and titration of viral vectors

2.4.1 Synthesis of second-generation lentiviruses

VSVg pseudotyped lentiviral particles were generated according to local protocols. HEK-293T cells (ATCC) were cultured in DMEM high glucose + GlutaMAX™ + pyruvate (Gibco®); 1% Penicillin Streptomycin (100x; Invitrogen) and 10% HI-Fetal Bovine Serum (LifeTechnologies, USA origin, 10082147) for no more than 15 passages and seeded prior to transfection in T500 flasks (ThermoScientific, Nunclon delta surface) to reach 80-90% confluence after 48hr. HEKs were co-transfected at 48hr with 50 µg of the transfer vector, 80 µg of the packaging vector (pCMVdR8.74^{D64V}, gag/pol expressor) and 40 µg of the envelope vector (pMD.G, VSV.G expressor) in OptiMEM (Gibco®) and Lipofectamine® 2000 transfection reagant (Thermofisher Scientific, 11668019). The pMDG-VSV.G and pCMVdR8.74^{D64V} plasmids were gifts from the laboratory of Waseem Qasim (UCL Institute of Child Health). Lentivirus-containing supernatant was harvested 48hr after transfection. Cellular debris were pelleted by centrifugation at 1500 rpm, at room temperature for 3 minutes and filtered through 45 µm filters (Millex®-HV (33 mm) sterile filter unit with Durapore® PDVF® membrane, Merck Millipore Ltd.) and transferred into pre-sterilised ultracentrifugation tubes (50 mL Oak Ridge centrifuge Tube PC, ThermoScientific). Lentiviral particles were concentrated by centrifugation at 48,298 g for 2 hr at 4°C in an ultracentrifuge (Beckman, J2-2IM/E, JA20 rotor). After centrifugation, the viral pellet was re-suspended in an appropriate volume of ice-cold 1X Dulbecco’s Phosphate Buffered Saline (Gibco®); aliquoted into sterile deoxyribonuclease (DNase), RNase, pyrogen DNA/RNA-free 0.2 mL tubes, snap-frozen in liquid nitrogen and stored long-term at -80°C. In the instance where lentiviral particles were not synthesised in-house, viral packaging was outsourced to VectorBuilder Inc.

2.4.2 AAV synthesis

All AAVs used in this thesis were synthesised by VectorBuilder Inc.

2.4.3 Determination of lentiviral titres

2.4.3.1 p24 enzyme-linked immunosorbent assay (ELISA) titration method

Viral titres for pCCL-Flex-ChIEF lentiviruses synthesised in-house (**Table 2.3**) were determined by the p24 enzyme-linked immunosorbent assay (ELISA) method (Lenti-X™ p24 Rapid Titer Kit, Takara, Clontech). Briefly, a p24 standard curve was generated by adsorbing a range of p24 standards (200 – 12.5 pg mL^{-1}) onto a microtitre ELISA plate and measuring the absorbance at 450 nm using a FLUOstar Omega plate reader (BMG Labtech). Lentiviral supernatants were diluted in HEK cell media so that their p24 content was in the range of the standard curve (typically a 1 in $1x10^5$ to a 1 in $7x10^5$ dilution was required) and assayed in duplicate. Lentiviral titers were found by calibrating the absorbance values of diluted lentiviral supernatants to p24 antigen concentration using a standard curve. The number of Infectious units (IFU) mL^{-1} were found from the concentration of p24 antigen (pg mL^{-1}) present in the sample using **Equation 3**, where DF is the dilution factor.

$$IFU\ mL^{-1} = \frac{[p24]\ x\ DF}{8x10^{-2}} \qquad \textbf{(Eq.3)}$$

Table 2.3. Titers for FLEx-ChIEF lentiviruses

Lentiviral construct	Size of insert (Kb)**	Promoter	Titre (IFU mL^{-1})	Titre Method	MOI
In house synthesis					
FLEx-ChiEF	4.6	PGK	1.6x10^{10}	p24 ELISA	5
		hSyn	5.7x10^{8}	p24 ELISA	5
FLEx-ChiEF-T2A-KCNC1(WT)	6.4	PGK	2.3x10^{8}	p24 ELISA	5
		hSyn	3.0x10^{8}	p24 ELISA	5
FLEx-ChiEF-T2A-KCNC1(959.G>A)	6.4	PGK	2.0x10^{8}	p24 ELISA	5
		hSyn	3.9x10^{8}	p24 ELISA	5
Commercial synthesis					
FLEx-ChiEF	4.6	hSyn	2.07x10^{9}	qPCR	5
FLEx-ChiEF-T2A-KCNC1(WT)	6.4	hSyn	2.01x10^{9}	qPCR	5
FLEx-ChiEF-T2A-KCNC1(959.G>A)	6.4	hSyn	2.14x10^{9}	qPCR	5

All lentiviruses listed are third-generation lentiviruses created using pCCL transfer vectors.
** When measured between the 5' and 3' Long-Terminal-Repeats (LTRs)
IFU: infectious units; MOI: multiplicity of infection; ELISA: enzyme-linked immunosorbent assay; qPCR: quantitative PCR

2.4.3.2 Fluorescence-based methods of lentivirus titering

Functional lentiviral titers were calculated for constructs containing constitutive promoter sequences driving a fluorescent reporter protein. 10^5 HEK293-T cells were plated in 2 mL of HEK cell media onto 22 mm glass coverslips, within a 6-well plate. 24 hr later, 2 mL of HEK culture medium was entirely replaced by 1 mL of serially diluted lentiviral supernatant using dilution factors in the range of 10^{-2} to 10^{-6}. HEK cells were fixed 48 hr after infection, and mounted onto glass slides according to standard protocols, (**Section 2.6.2**). HEK cells infected with varying concentrations of viral supernatant were imaged using an epifluorescent microscope using the 20X objective. The number of GFP$^+$ HEK cells for each serial dilution were counted using the ImageJ *Cell Counter* plugin. The total number of HEK cells was calculated using the 4′, 6-diamidino-2-phenylindole (DAPI) channel, and automatic cell counting so that the % of GFP$^+$ cells could be calculated. Lentiviral titers were found according to **Equation 4**.

$$\text{TU}\ mL^{-1} = \frac{proportion\ infected\ cells\ x\ DF}{Volume\ of\ virus} \qquad \textbf{(Eq.4)}$$

Table 2.4. Titers for GOSR2 and K$_V$3.1 lentiviruses

Lentivirus	**Size of insert (bp)***	**Titre (TU mL^{-1})**	**Titre Method**	**MOI**
PGK-dscGFP	3514	7.22 x 10^7	Fluorescence	5
PGK-dscGFP-GOSR2 (WT)	4264	3.06 x 10^7	Fluorescence	5
PGK-dscGFP-GOSR2 (G144W)	4264	4.11 x 10^8	Fluorescence	5
PGK-dscGFP-GOSR2 (ΔK164)	4261	2.48 x 10^8	Fluorescence	5
mDlx-K$_V$3.1 Lentiviruses				Volume of virus/ well**
mDlx-dscGFP	3954	Not calculated	Fluorescence on neurons	0.2 µL
mDlx-dscGFP-T2A-KCNC1(WT)	5703	Not calculated	Fluorescence on neurons	1 µL
mDlx-dscGFP-T2A-KCNC1(959G.A)	5703	Not calculated	Fluorescence on neurons	2 µL
All lentiviruses listed here are third-generation lentiviruses created using the pCCL backbone. * When measured between 5' and 3' Long-Terminal-Repeats (LTRs). IFU: infectious units ** Volume used to transduce 120K neurons/ 13 mm coverslip in a 24-well plate				

2.5 Oocyte recordings

2.5.1 Transgenes and plasmids used for oocyte recordings

The Shaker clone used as the coding sequence background for the introduction of the R371H mutation was the non-conducting (W434F), fast-inactivation removed (IR, Δ6–46) Shaker H4 K$^+$ channel (accession number: NM_167595.3) that was a gift of Fredrik Elinder. The p.R371H mutation was introduced by site-directed mutagenesis (**Appendix, Table 2.12 & Section 2.2.1.3**). Transgenes encoding K$_v$3.1b^{WT}, K$_v$3.1b^{R320H} (**Section 2.2.3.1**) Shaker^{WT} or Shaker^{R371H} were digested with Sal1 and Nhe1 and inserted into a pSGEM oocyte expression vector (a gift of Dr M.Hollman, Göttingen Germany) using compatible Xba1 and Nhe1 restriction sites. Sequence alignment of Shaker and K$_V$3.1b was performed using the *Clustal Omega* sequence alignment tool. The W392F α-pore mutation was introduced into $K_v3.1b^{WT}$ and $K_v3.1b^{R320H}$ using site-directed mutagenesis to generate $K_v3.1b^{W392F.WT}$ and $K_v3.1b^{W392F.R320H}$ (**Appendix, Table 2.12)**.

2.5.2 cRNA synthesis for channel expression in oocytes

Copy RNA (cRNA) was synthesised for $K_v3.1b$ channel variants using T7 RNA polymerase in an *in vitro* transcription reaction with Nhe1-linearised template DNA (mMESSAGE mMACHINE™ T7 Transcription Kit, Ambion, AM1344). cRNA for Shaker clones was generated using HindIII-linearised template DNA. The *in vitro* transcription reaction consisted of the incubation of the following reagants for 2hrs at 37°C: 2 µL buffer (X10), 10 µL of NTPs (X2), 6 µL of linearized DNA and 2 µL of T7 enzyme mix (all Ambion, AM1344). The DNA template was then digested by incubation with 1 µL of DNase at 37°C for fifteen minutes. cRNA precipitation was performed overnight at -20°C following the addition of 1.5 volumes of RNase-free H_20 and 1.5 volumes of LiCl. The RNA pellet was isolated by centrifugation at 13,200 rpm for 30 minutes at 4°C and washed by the addition of 0.5 mL of RNase-free 100% ethanol. The RNA pellet was isolated again by centrifugation at 13,200 rpm for 10 minutes at 4°C and left to dry for 15 minutes at room temperature before resuspension in 30 µL RNase-free H_2O (Ambion). RNA was stored long-term at -20°C.

2.5.3 Oocyte preparation and injection

X.laevis oocytes, stage V-VI, were enzymatically defolliculated by incubation in 2mg mL^{-1} of Collagenase A (Roche diagnostics) in a calcium-free Ringer solution (OR-2, **Table 2.5**) at room temperature for 90 min. Following defolliculation, oocytes were washed three times in OR-2 solution and once in Modified Barth's saline (MBS) solution (**Table 2.5**). Healthy oocytes were manually selected and injected using Nanoject (Drummond). Sharps were pulled using PC-10 puller (Narishige) and broken to create a sharp edge for oocyte impaling. Pipettes were backfilled with mineral oil and the cytoplasm of each oocyte was injected with 50 nL of 50 ng of cRNA. Oocytes were maintained in filtered MBS solution supplemented with penicillin (50 U mL^{-1}) and amikacin (100 µg mL^{-1}) at 14-18°C.

Table 2.5. Solutions used in the defolliculation and maintenance of oocytes.

Solution	OR-2	MBS
pH*	7.5 – 7.6	7.4
Chemical	Concentration (mM)	
NaCl	82.5	87.1
KCl	2.0	1.0
HEPES	5.0	10.0
$MgCl_2$	1.0	-
$MgSO_4$	-	1.7
$NaNO_3$	-	0.9
$NaHCO_3$	-	2.4
$CaCl_2$	-	0.9
*pH values adjusted using NaOH		

2.5.4 Oocyte recordings

Currents were recorded from injected oocytes using the two-electrode voltage clamp (TEVC) recording configuration. Currents were acquired using GeneClamp 500B amplifier and digitised using Digidata 1200 digitiser and pCLAMP™ software (Molecular Devices). Signals were filtered at 1 kHz using a Bessel low-pass filter and sampled at a rate of 5 kHz. For all recordings, electrodes were filled with 3M KCl internal solution (pH 7.4) and had a resistance of 0.1-0.5 MΩ. All recordings were carried out at room temperature, 2-3 days after oocyte injection.

2.5.4.1 Recording of K^+ currents

K^+ currents were recorded using a 120 mM $NaMeSO_4$ external solution at pH 7.4, (**Table 2.6**). Oocytes were held at -80 mV and exposed to a series of voltage steps ranging from -100 mV to +60 mV (Δ10 mV) for 250 ms, followed by a step to -30 mV for 250 ms to facilitate the analysis of tail currents. Recordings were carried out using the P/4 leak subtraction protocol.

2.5.4.2 Recording of gating pore currents

Gating pore currents were recorded using 120 mM $NaMeSO_4$ solution at pH 7.4, pH 5.5 or 120 mM Guanidium sulphate solution at pH 7.4 (**Table 2.6**). Oocytes were perfused with external recording solutions in the following order: 1. $NaMeSO_4$ at pH 7.4; 2. $NaMeSO_4$ at pH5.5 and 3. 50% Guanidium Sulphate at 50% $NaMeSO_4$ at pH 7.4. Oocytes were held at -80 mV and exposed to a series of voltage steps ranging from -

100 mV to +60 mV (Δ10 mV) for 250 ms, followed by a step to -30 mV for 250 ms. Gating pore currents were recorded in the absence of online leak subtraction.

Table 2.6. Solutions used in TEVC recordings of oocytes

External solution		
Solution	$NaMeSO_4$	$GnSO_4$
pH	7.4 or 5.5	7.4
Chemical	Concentration (mM)	
CH_3SO_3Na	120.0	-
Guanidium Sulphate salt	-	120.0
$CaSO_4$	1.8	1.8
HEPES	10.0	10.0

2.5.5 Data analysis

Current traces were analysed using Clampfit 10.7 (Molecular Devices), GraphPad Prism 6 (GraphPad Software Inc) and Origin Pro 64-bit 2018 (OriginLab). Steady-state K^+ current amplitudes were measured at the end of each 250 ms test pulse and obtained after plotting an I-V curve for each recorded oocyte. Relative current amplitudes were calculated by normalising the values obtained for $K_v3.1b^{R320H}$ and $K_v3.1b^{R320H}+^{WT}$ at +40 mV to the average current amplitude obtained for oocytes expressing $K_v3.1b^{WT}$ recorded at +40 mV on the same day. Steady-state channel activation was analysed by measuring the amplitude of the tail currents recorded at -30 mV for each pre-pulse test voltage. Each current-voltage relationship (I-V) was then fit by a single Boltzmann function, **Equation 5**, where $V_{0.5}$ is the potential of half-maximal activation, A2 is the maximum tail current amplitude for a test voltage, A1 is the minimum tail current amplitude, X is the test voltage and the slope is the derivative of the fitting at $V_{0.5}$. The Boltzmann asymptotes obtained after fitting were used to normalise current amplitude for channel expression, **Equation 6**, where I is normalised current, x is recorded current, A2 is the minimum asymptote, A1 is the maximal asymptote.

$$I(V) = \mathrm{A2} + \frac{A1-A2}{1+exp^{\left(\frac{V0.5-X}{Slope}\right)}} \qquad \textbf{(Eq. 5)}$$

$$I = (x - A2)/(A1 - A2) \qquad \textbf{(Eq. 6)}$$

Gating pore currents were analysed by generating an I-V curve for each cell recorded for each clone, using steady-state current amplitudes. An average I-V curve was then plotted for each pH value for each clone. Kv3.1b^{WT} pH7.4 and pH5.5, Kv3.1b^{R320H} pH 7.4 and Shaker^{WT} traces were fit with a linear regression line, **Equation 7**, where Y is current, a is the intercept, b is the slope factor and X is voltage.

$$Y = a + bX \qquad \textbf{(Eq. 7)}$$

2.6 Culture and transfection of primary neuronal cultures

2.6.1 Preparation of primary dissociated cortical neuronal cultures

Cortices were dissected from postnatal day 0-2 (P0-2) mice. Cortices were diced, washed in Buffer 1 (HBSS and 5mM HEPES, 1M, pH7.4; Sigma-Aldrich and Gibco®) and trypsinised in 2.5 mL of trypsin solution (0.25% trypsin, Gibco®; 10 mg ml^{-1} DNase from bovine pancreas, Sigma D5025, 137 mM NaCl; 5 mM KCL; 7 mM Na_2HPO_4; 25 mM HEPES, Gibco®) for 10 minutes at 37°C. Trypsinised tissue was neutralised in Buffer 2 (20% HI-FBS, Gibco® in Buffer 1) and washed twice in Buffer 1. Tissue was gently dissociated in Buffer 3 (12 mM $MgSO_4$, 10 mg ml^{-1} DNAse in Buffer 1) and the cell suspension centrifuged for 5 minutes, 2000 rpm, 21°C. The cell pellet was re-suspended in 1 mL Neurobasal A complete medium (Neurobasal A; Glutamax; B27, 50X serum free, all supplied by Gibco®). Viable cells were counted using a haemocytometer and the trypan blue exclusion method. Cells were plated at a density of 7540 cells/cm^2 onto coverglass (No.0, 13 mm, VWR) coated with poly-L-lysine hydrobromide (1 mg mL^{-1}, 30,000-70,000 kDa Sigma-Aldrich, in borate buffer, 0.1 M, titrated to pH 8.5 using sodium tetraborate). One third of the media was changed every 7 days and cultures were maintained in 5% CO_2 at 37°C for up to 4 weeks.

2.6.1.1 Treatment of cortical cultures with bone morphogenic protein 4 (BMP4)

One hour after plating, the media was changed to complete Neurobasal A media containing 20 ng µL^{-1} of BMP4 (R&D systems). Neurons were incubated in BMP4 for 4 DIV. The media was completely replaced with preconditioned media from a 'sacrificial' well with untreated neurons. Cultures were then maintained as normal.

2.6.2 Magnetofection of primary neuronal cultures

Magnetofection (Vlaskou et al., 2007) was performed at 4-5 DIV. Prior to transfection, preconditioned culture media was saved and completely replaced by 400 µL serum-free

Neurobasal A. In separate tubes, 50 µL of Opti-MEM reduced serum medium (Gibco®) was combined with 1 µL of NeuroMag (OZBiosciences) and 50 µL of Opti-MEM was combined with 100 ng of DNA for 5 min. The NeuroMag solution was then combined with the DNA-containing solution for 20 minutes at room temperature. 100 µL of the resulting transfection solution was added per well and the cells were incubated in the transfection medium, on top of a magnet for 10 min. After 10 min, the magnet was removed and cells were further incubated in the transfection solution for 30 min. The media was then completely removed and replaced with pre-conditioned media. Cells were maintained for a maximum of 7 days post-transfection. Amounts are given for cortical neurons plated at high density on 13 mm coverglass in a 24-well plate.

2.6.3 Lentiviral infection of primary neuronal cultures

Primary neuronal cultures were infected with lentivirus at 1-3 DIV. Two-thirds of the pre-conditioned culture media was removed, saved and replaced with one third fresh Neurobasal A complete media containing lentivirus at the appropriate MOI. After 20 hr, all virus containing media was completely removed and disposed of in line with safety procedures and replaced with two thirds of preconditioned media and one third fresh Neurobasal A complete medium. Cultures were then maintained using standard protocols.

2.6.4 Culture and transfection of mammalian cell lines

2.6.4.1 HEK293-T cells

HEK293-T cells (ATCC) were cultured in complete DMEM solution (DMEM high glucose with GlutaMAX™ and pyruvate, Gibco®; 1% Penicillin Streptomycin, 100x Invitrogen and HI-Fetal Bovine Serum, USA origin, Cat#: 10082147, Gibco®) in 75 cm^2 cell culture flasks (Falcon®, Corning, #353136). Cells were kept for no more than 15 passages and maintained in 5% CO_2, at 37°C.

2.6.4.1.2 Subculture of HEK293-T cells

Adherent HEK cells were washed 1X in PBS and then detached by incubation in an appropriate volume of 0.05% Trypsin-EDTA (Gibco® # 25300062) solution for 3 min at 37°C. The trypsin solution was neutralised using 1.5 volumes of HEK cell media and the cell suspension was centrifuged at 1500 rpm for 5 min at room temperature to obtain a cell pellet. The cell pellet was gently re-suspended in 1 mL of fresh HEK media and an appropriate fraction of the cell suspension was used to seed a new culture flask containing fresh HEK media.

2.6.4.2 P19 cells

P19 cells (ATCC® CRL-1825™) were cultured in α-Minimal Essential Medium (MEM) with ribonucleosides and deoxyribonucleosides and Glutamax (Gibco®, #32571036) supplemented with 7.5% bovine serum (Heat-inactivated, New Zealand origin, Thermofisher Scientific, #26170043) and 2.5% fetal bovine serum (Heat-inactivated, US origin, Thermofisher Scientific, #16140071). Cells were subcultured at a ratio of 1:10 every 2-3 days and P19 media was replaced every 48hr. Cells were maintained in an atmosphere of 5% CO_2, at 37°C.

2.6.4.2.1 Selection of P19 cells

An antibiotic kill curve was generated in order to determine the concentration of blasticidin that would kill ~100% of P19 cells within 48 hr. P19 cells were seeded onto 22 mm coverglass and incubated overnight. When cells were at 50% confluency, P19 media was replaced with selective media containing varying concentrations of Blasticidin-S-hydrochloride (Sigma-Aldrich, #: 15205). 48 hr after selection, the number of surviving cells were counted for three fields of view per condition using ImageJ. % cell death was plotted as a function of antibiotic concentration and was fit with a Boltzmann sigmoidal, **Equation 8**. The concentration of blasticidin found to be effective in P19 selection was 35 µg mL^{-1}.

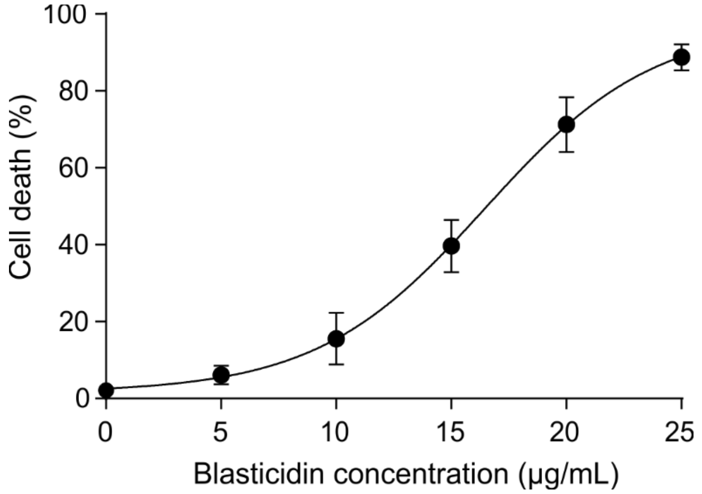

Figure 2.1. Blasticidin kill curve in P19 cells

$$Y = Bottom + \frac{(Top - Bottom)}{1 + exp\frac{V_{0.5} - X}{Slope}} \qquad \textbf{(Eq.8)}$$

2.6.4.2.2 Transfection of P19 cells

P19 cells were cultured in T25 flasks and transfected when at 50-60% confluency. 2 µg of plasmid DNA encoding Cas9 and 2 µg of either pKLV-U6-sgRNA or pCCL-PTG plasmid DNA were combined in a sterile 1.5 mL Eppendorf with 400 µL of Opti-MEM™ (Gibco™, #31985062). The DNA solution was combined with 12 µL of Turbofect transfection reagent (Thermo Fisher Scientific, R0531) and incubated at room temperature for 15-20 min. Old P19 culture media was replaced with 4 mL of fresh P19 medium, followed by the drop-wise addition of the transfection solution. The media was gently mixed over the cells to avoid toxicity and the cells returned to 5% CO2, 37°C culturing conditions. 24 hr post-transfection, the P19 media was replaced with selective media containing 2 µg mL^{-1} of puromycin dihydrochloride (Sigma-Aldrich, #: 15205) – when cells had been transfected with pKLV-U6-sgRNA plasmids - and 35 µg mL^{-1} of blasticidin. 48 hr post-transfection, selected P19 cells were harvested for genomic DNA extraction or split onto coverglass for immunofluorescence assays.

2.6.4.2.3 Subculture of P19 cells

Adherent P19 cells were washed 1X in PBS and then detached by incubation in an appropriate volume of 0.05% Trypsin-EDTA solution for 3 min at 37°C (# 25300062). The trypsin solution was neutralised using 1.5 X volumes of P19 media. P19 cells in suspension were then added to fresh P19 media in a new culture vessel at a 1:10 ratio.

2.7 Imaging

2.7.1 Immunohistochemistry

2.7.1.1 Brain Slice preparation

1 month old mice that had be intracranially injected with AAV9-PCP2 viruses at p0 were terminally anaesthetised with sodium pentobarbital (Euthatal, Merial) and transcardially perfused with 4% PFA in PBS (Affymetrix USB). Brains were harvested and post-fixed in 4% PFA for 24 hr at 4°C and then washed 3X in PBS. 70 µm sagittal brain slices were prepared using a vibratome (Leica) and stored short-term in PBS at 4°C.

2.7.1.2 Immunohistochemistry

Immunohistochemistry was performed on free-floating brain sections. Brain slices were first washed 4X 10 min in PBS and then permeabilised via 2X 10 min washes in PBS-T (0.1% Triton X-100 in PBS). Slices were blocked for 1 hr at room temperature in PBS-T with 5% goat serum (Sigma Aldrich). Slices were then incubated in primary antibody solution (Rabbit-anti-TurboGFP, 1:500) for 18-24 hr at 4°C. Slices were washed 3X 10 min with PBS-T and then incubated with the secondary antibody Alexa Fluor®-488 (goat-anti-rabbit in PBS-T and 5% normal goat serum) for 2 hr at room temperature. Slices were washed 4X 10 min in PBS-T, transferred onto glass microscope slides to air dry and then mounted using Prolong^{TM} Gold antifade reagent with DAPI (Invitrogen) and borosilicate cover-glass. Slides were dried overnight at room temperature and then stored at -20°C. The details of antibodies used in this thesis are given in **Table 2.7**.

2.7.2 Immunocytochemistry

Cells plated on coverglass (VWR borosilicate coverglass, thickness number 0, #6310148) were fixed in 4% Paraformaldehyde (PFA) solution in Phosphate Buffered Saline (PBS) (Affymetrix USB) for 15 min at room temperature. Cells were washed 3X for 5 min in 1X PBS and processed immediately for fluorescence imaging applications or stored at 4°C. Cells were permeabilised and blocked in 5% Normal Goat serum (NGS) in PBS with 0.1% TritonX-100 (PBS-T) for 30 min at room temperature. Cells were then incubated with 200 µL primary antibody solution (2% NGS in PBS-T) overnight at 4°C. The cells were washed 3X in PBS to remove unbound primary antibody and then incubated in 200 µL solution containing fluorescently-conjugated secondary antibodies (2% NGS in PBS-T) for 1 hr at room temperature. Cells were washed 3X in PBS to remove non-specifically bound secondary antibody and mounted onto glass slides (VWR) using Prolong^{TM} Gold antifade reagent with DAPI (Invitrogen). Slides were left to set overnight and were sealed the next day using nail varnish. Slides were stored at 4°C prior to imaging. A list of antibodies used in this thesis are given in **Table 2.7**.

Table 2.7. Primary and secondary antibodies used for immunocytochemistry

Antibody	Species	Dilution	Reference
Primary antibodies			
α-GFP	Chicken	1:1000	Abcam
α-TurboGFP	Rabbit	1:5000 (ICC & WB) 1:500 (IHC)	Evrogen
α-Parvalbumin	Rabbit	1:500	Swant
α-K_v3.1b	Rabbit	1:500	Alomone Labs
α-cleavedcaspase3	Rabbit	1:500	Cell Signalling
α-GM130	Mouse	1:500	Abcam
α-DYKDDDDK (Flag tag)	Rat	1:1000	BioLegend®
α-VGLUT1	Guineapig	1:1000	Millipore, AB5905
α-HOMER1	Rabbit	1:1000	Synaptic systems
α-NF-H (SMI-31)	Mouse	1:1000	SMI-31 (NE1022) BioLegend®
α-MAP2	Guineapig	1:1000	Synaptic Systems, Cat # 188004
α-GAD67	Mouse	1:500	Merck Millipore (MAB5406)
Secondary antibodies			
α -Rabbit IgG (H+L) HCA Alexa Fluor 488	Goat	1:1000	Invitrogen
α-Rabbit IgG (H+L) HCA Alexa Fluor 555	Goat	1:1000	Invitrogen
α-Mouse IgG (H+L) HCA Alexa Fluor 555	Goat	1:1000	Invitrogen
α-Mouse IgG (H+L) HCA Alexa Fluor 647	Goat	1:1000	Invitrogen
α-Rat IgG (H+L) Alexa Fluor 647	Goat	1:1000	Invitrogen
α-Guineapig IgG (H+L) HCA Alex Fluor 647	Goat	1:1000	Invitrogen
α-Chicken-488	Goat	1:1000	Invitrogen

ICC: immunocytochemistry; WB: western blot; IHC: immunohistochemistry; VLGUT1: vesicular glutamate transporter 1; NF-H: Purified anti-Neurofilament H (NF-H), Phosphorylated Antibody; MAP2: microtubule associated protein 2; GAD67: Glutamate decarboxylase 67; HCA: highly cross-adsorbed

2.7.3 Image acquisition

Immunofluorescent images were acquired using an inverted LSM 710 (Zeiss) confocal laser scanning microscope (ZEN software, 2009) with X40 and X63 EC Plan-Neofluar oil-immersion objectives (Zeiss).

2.7.4 Image analysis

All image analysis was performed using ImageJ, version 1.51 u.

2.7.4.1 Sholl analysis

Dendritic Sholl analysis was performed using ImageJ. Before analysis the axon was identified based upon Neurofilament heavy-chain (NF-H) immunolabelling and pixels pertaining to GFP fluorescence from the axon were deleted, leaving only the dendritic tree and cell soma. Images were automatically thresholded using *Yen* to obtain a binary image for Sholl analysis. Sholl analysis was performed by marking the centre of the Sholl radius as the cell soma and using a 3 µm Sholl radius. Sholl curves were obtained by plotting the number of intersections against distance from the soma (µm).

2.7.4.2 Neurite tracing

Axons were identified by NF-H immunoreactivity and traced using NeuronJ Plugin. Total axonal length was calculated from NDF files of traced axons.

2.7.4.3 Calculation of synaptic number per unit dendrite length

For synaptic imaging experiments, neurons were plated at a density of 60K neurons/13 mm coverslip and fixed at 14 DIV. Images of dendrites were acquired using X63 oil immersion objective and 2X digital zoom. A Z projection image of average intensity was created for all colour channels. For calculations of synaptic number per unit dendrite length, a rectangular region of interest (43.5 x 10.7 µm) was drawn around a linear portion of dendrite and pixels pertaining to surrounding fluorescence were deleted. Colour channels corresponding to VGLUT1 and homer protein homolog 1 (HOMER1) puncta were automatically thresholded using *IsoData* and puncta were counted using the *Analyse Particles* option where ‘puncta’ were defined as being greater than 5 grouped pixels. The number of synapses were calculated by multiplying by the overlap coefficient for VGLUT1 and HOMER1 by the number of HOMER1 puncta counted along the dendrite of interest. The number of puncta counted were then divided by the length of the ROI (43.5 µm).

2.7.4.4 Colocalisation analysis for the calculation of synapse number

Colocalisation analysis was performed using the *Just Another Colocalisation Plugin* (JaCoP) in ImageJ. Images of VGLUT1 and HOMER1 puncta were automatically thresholded using the Plugin and the overlap coefficient was obtained using Mander's analysis to obtain Mander's coefficients (M1 & M2) for the overlap of VGLUT1 and HOMER1 puncta (Bolte & Cordelieres, 2006). The overlap coefficient for VGLUT1 and HOMER1 was then used to obtain the number of HOMER1 puncta co-localising with VGLUT1 (defining a synaptic connection).

2.7.4.5 Analysis of nuclear area factor

Nuclei of transfected neurons were outlined and nuclear area factor (NAF) was calculated according to **Equation 9**. Circularity is defined in **Equation 10**, where a circularity value of 1.0 corresponds to a perfect circle.

$$NAF = circularity\ x\ area \qquad \textbf{(Eq.9)}$$

$$Circularity = 4\pi\left(\frac{area}{perimeter^2}\right) \qquad \textbf{(Eq. 10)}$$

2.8 Western Blotting

2.8.1 Preparation of protein lysates

Dissociated cortical neurons were plated in a 6-well plate coated with Poly-D-lysine at a density of 360K cells per well. Protein lysates were prepared at 14-16 DIV as follows: cells were gently washed in ice-cold PBS; lysed in 400 µL ice-cold radioimmunoprecipitation assay (RIPA) buffer supplemented with one cOmplete™ mini protease inhibitor tablet (Roche) and then detached using a cell scraper. Protein lysates were incubated with 1 µL of benzonase for 30 min at 4°C with constant agitation and then centrifuged at 12,000 rpm for 20 min to pellet cellular debris. Proteins were denatured via the addition of Bolt™ LDS sample buffer (X4, Thermo Fisher Scientific) and DTT (to a final concentration of 100 mM) followed by incubation at 65°C for five min. Protein samples were then aliquoted and stored at -80°C.

2.8.2 Sodium dodecyl sulfate (SDS)-Polyacrylamide-gel electrophoresis (PAGE) and immunoblotting

Proteins were separated using SDS-PAGE. 30 µL of protein sample was loaded onto a 4-12% Bis-Tris polyacrylamide Gel (NuPAGE™, Novex, NP0321) alongside 5 µL of SeeBlue® Plus2 Prestained protein standard (Invitrogen, LC5925). The gel was run at

200 V with 400 mA constant current in MOPS SDS Running buffer (Novex, NP0001) for 40 min. Following separation, proteins were transferred onto a 0.2 μm nitrocellulose membrane using a Trans-Blot Turbo Transfer pack (BioRad, Cat#: 170-4159) with the Trans-Blot Turbo transfer system (BioRad), 17 V and 2.5 A for 15 minutes. The membrane was blocked in 5% milk (w/v) (Skimmed milk powder, Oxoid, LP0031) in 0.05**%** PBS-Tween for 1 hr at room temperature to prevent non-specific antibody binding. The membrane was incubated in 5 mL of primary antibody solution (1% Bovine Serum Albumin, w/v, in 0.05% PBS-Tween) for 2 hr at room temperature according to the dilutions outlined in **Table 2.8**. The membrane was washed 3X for 10 min in 0.05% PBS-Tween and then incubated in 10 mL of secondary antibody solution according to the combinations and dilutions outline in **Table 2.9** for 1 hr. The membrane was then washed 3X for 10 min in 0.05% PBS-Tween. Proteins were detected using Odyssey CLx Near-Infrared Fluorescence Imaging System (LI-COR Biosciences). Signal intensities of protein bands were calculated using LI-COR image analysis.

Table 2.8. Primary antibody solutions used in immunoblotting

Protein	MW (kDa)	Species	Dilution	Antibody References
GOSR2	24.2	Rabbit	1:1000	Synaptic Systems (Cat: 170 003)
SNAP-25	23	Mouse	1:5000	Synaptic Systems (Cat: 111 111)
Loading controls				
βIII-Tubulin	50	Mouse	1:10,000	Proteintech (Cat: 66240)
GAPDH	37	Rabbit	1:10,000	Sigma (Cat: 69545)

Table 2.9. Secondary antibodies used in immunoblotting

Antibody	Dilution	Reference
Goat anti-Rabbit IR-dye® 680RD	1:10,000	LI-COR Biosciences (Cat: 926-68071)
Goat anti-Rabbit IR-dye® 800CW	1:10,000	LI-COR Biosciences (Cat: 926-32211)
Goat anti-Mouse IR-dye® 680LT	1:10,000	LI-COR Biosciences (Cat: 926-68020)
Goat anti-Mouse IR-dye® 800CW	1:10,000	LI-COR Biosciences (Cat: 926-32210)

2.9 Optogenetics

For optogenetic experiments a colliminated mounted light emitting diode (LED) with 470 nm nominal wavelength (M470L3, ThorLabs) was mounted to the epifluorescent port of an Olympus IX17. The LED was triggered from the computer via TTL inputs. Protocols written in WinWCP (Strathclyde electrophysiology software) were used to control the frequency and duration of the optical stimulus. The level of light intensity was set manually using an LED driver (DC2100). The maximum power of the LED at the level of the coverslip, when focused through a 40X objective, was measured using a photodiode (Thor Labs, PM100D) and was found to be 4.95 mW.

2.10 Electrophysiological recordings of primary neuronal cultures

2.10.1 General recording details

Electrophysiological recordings were acquired using a MultiClamp 700B amplifier and digitised using a digital-to-analogue converter (National Instruments). Unless stated otherwise, signals were filtered at 10 kHz using a Bessel filter and sampled at a rate of 20 kHz using WinWCP. Recording electrodes were microfabricated from thin-walled borosilicate glass (GC150-F, Clark) and had a resistance of 4-6 MΩ. Unless stated otherwise, the internal solution used in most recordings contained: 148 mM potassium gluconate; 4 mM NaCl; 1 mM $MgSO_4$; 0.02 mM $CaCl_2$; 0.1 mM BAPTA; 15 mM glucose; 5 mM HEPES; 3 mM ATP and 0.1 mM GTP. The external solution contained: 2 mM $CaCl_2$; 140 mM NaCl; 1 mM $MgCl_2$; 10 mM HEPES; 4 mM KCl and 10 mM glucose, at pH 7.3 (adjusted with 1 M NaOH solution). The liquid junction potential (LJP) was found to be 15 mV using the Junction Potential Calculator in Axon™ pClamp™. The osmolarity of the internal solution was ~295 mOsm and the external solution was ~320 mOsm. In all cases, recordings were discarded if the resting membrane potential (RMP) was < 55 mV (unadjusted for the LJP), if the holding currents > -200 pA at -70 mV, if the series resistance was > 15 MΩ or if bridge balance was > 10 MΩ. All recordings were carried out at room temperature (~23°C) in a static bath, unless stated otherwise.

2.10.1.1 Drugs used in electrophysiological experiments

The following drugs were used in electrophysiological recordings where indicated in this methods section (**Table 2.10**).

Table 2.10: Drugs used in electrophysiological recordings

Abbreviation	Name	Supplier	Target
NBQX	2,3-Dioxo-6-nitro-1,2,3,4-tetrahydrobenzo[f]quinoxaline-7-sulfonamide disodium salt	Tocris Bioscience, Cat # 0373	AMPA receptor
APV	DL-2-Amino-5-phosphonovaleric acid	Tocris / ChemCruz®, sc-201503A	NMDA receptor
PTX	picrotoxin	Tocris Bioscience, Cat # 1128	$GABA_A$ receptor
TTX	Tetrodotoxin citrate	Cayman Chemical Company (CAY14964)	Sodium channels

2.10.2 Visualisation of virally transduced neurons

Fluorescent neurons were identified using an LED (all Thor Labs) of an appropriate nominal wavelength mounted to the epifluorescent port of an inverted IX17 (Olympus, Japan) microscope. GFP-positive neurons were identified using a 470 nm LED and RFP-positive neurons were identified using a 560 nm LED (GFP filter: cube U-MWB, excitation filter, 450-480 nm; dichroic mirror, 500 nm and barrier filter, 515 nm; RFP filter: cube U-MWG; excitation filter 510-550 nm; dichroic mirror, 570 nm and barrier filter, 590 nm). $mCitrine^+$ neurons (excitation, 515 nm; emission, 525 nm) were identified using a 505 nm LED in combination with the AT- Enhanced yellow fluorescent protein/Venus/Citrine filter set (#39003, Chroma).

2.10.3 Whole-cell current-clamp recordings

Voltage-clamp was used to obtain the gigaohm seal and to obtain a whole-cell recording. Once stable, the amplifier was switched to the current-clamp recording configuration and the cell was held at -70 mV. Cells were discarded if the holding current was > - 200 pA or if the bridge balance was > 15 MΩ. Neurons were injected with current steps, ranging from –20 pA to +300 pA (Δ20 pA) for 1 s. To investigate cellular firing frequencies (from 10 to 100 Hz), neurons were injected with 10 current pulses at 110% of the AP current threshold (supra-threshold) using a 5 ms stimulus. The current threshold was found by iteratively injecting neurons with 5 ms depolarising steps (Δ10 pA) until an action potential was fired. The spike success rate was calculated as the average number of action potentials recorded at different stimulation frequencies for three sweeps. Cells were discarded if the holding current was > -200 pA or if the bridge balance was > 15 MΩ. For neurons transduced with FLEx-ChiEF lentiviruses, recordings were carried out at 25-26 DIV. For neurons transduced with mDlx-$K_V3.1$ lentiviruses, recordings were carried out 14-16 DIV at 32°C with continuous perfusion, at a rate of 5 mL min^{-1}. In this case an extracellular recording solution containing the following was used: 119 mM NaCl, 25 mM $NaHCO_3$, 11 mM glucose, 2.5 mM KCl, 1.25 mM NaH_2PO_4, 2.5 mM $CaCl_2$ and 1.3 mM $MgCl_2$. In both cases, recordings were carried out in the presence of blockers of synaptic transmission (50 µM APV, 10 µM NBQX, 30 µM PTX) (**Table 2.10**).

2.10.4 Whole-cell voltage-clamp recordings

2.10.4.1 Recording of inhibitory synaptic currents (IPSCs)

The intracellular solution for whole-cell voltage clamp recordings of optically induced IPSCs, in **Section 3.7.3.2**, was a KCl-based solution containing: 130 mM KCl; 10 mM Hepes; 0.2 mM EGTA; 2 mM Mg-ATP; 0.3 mM Na_2GTP; 20 mM sodium phosphocreatine; 50 U mL^{-1} phosphocreatine kinase and 5 mM QX-314.Cl, at pH 7.25. Inhibitory currents were recorded from a holding potential of -70 mV that was adjusted for the LJP of 6 mV, calculated using the Junction Potential Calculator in Axon™ pClamp™. For later recordings of optically induced IPSCs, a potassium-gluconate internal solution was used, as earlier described. The external solution contained: 2 mM $CaCl_2$; 140 mM NaCl; 1 mM $MgCl_2$; 10 mM Hepes ; 4 mM KCl ; 10 mM glucose pH 7.3, and 10 µM NBQX and 50 µM APV. Cells were discarded if the access resistance was >20 MΩ or if the access resistance increased more than 10% during course of the recording.

2.10.4.2 Recording of miniature excitatory postsynaptic currents (mEPSCs)

mEPSCs from GOSR2 lentivirus infected neurons were recorded at a holding potential of -70 mV at room temperature (~23°C) at 14-16 DIV. Recordings were obtained using a potassium gluconate-based internal solution and a HEPES-based extracellular solution (earlier described) containing 30 µM PTX, 50 µM APV and 1 µM TTX. mEPSCs were recorded for a total of 5 min but only the last 3 min of the trace was analysed. Signals were filtered at 3 kHz using a Bessel filter and acquired with a sampling rate of 10 kHz.

2.10.5 Data analysis

Electrophysiological signals were analysed using ClampFit software (Clampex, Molecular Devices) or a custom Python script (created with the help of Dr A. Snowball), and graphs were made using GraphPad Prism. An AP was defined as a spike crossing 0 mV with a rising slope >20 V s^{-1}. AP shape parameters have been extracted using a phase-plane plot implemented in the custom python script. Rising slope was defined as the highest V s^{-1} value; voltage threshold as the first voltage point where the derivate was >20 V s^{-1}; AP peak as the highest voltage value (mV) reached and AP half width as the Δt half-way between the AP peak and voltage threshold. Passive properties were calculated as following: input resistance as the slope of a line passing by 3 points calculated at -20 pA, -10 pA and 10 pA current injection as ΔV/current injected; capacitance as tau/input resistance where tau was calculated by fitting a single exponential between the baseline and the plateau voltage obtained by a -20 pA current injection; resting membrane potential was found manually using the I=0 configuration of the Multiclamp amplifier. Miniature events were detected using a custom template fitting procedure in Clampfit (Clements & Bekkers, 1997). Only the last three minutes of a total recording duration of five minutes was analysed.

2.11 Statistical analysis

All recordings and analysis were carried out with the experimenter blinded to the experimental groups. Data are plotted as scatter plot, representing single data points. The mean ± standard error of the mean (s.e.m) is shown in all the figures and quoted within the main text. The statistical analysis performed is shown in each figure legend. Deviation from normal distributions was assessed using a D'Agostino-Pearson's test, and the F-test was used to compare variances between two sample groups. Student's two-tailed *t*-test was used to compare means. Paired *t*-test was used in Figures 3.10 & 5.3 assuming ratio between paired values was consistent. One-way ANOVA was used to compare three groups and was followed by a post-hoc test to correct for multiple comparisons. To compare two groups at different time points a two-way repeated measure ANOVA, followed by a post-hoc test in order to correct for multiple comparisons, was used. Statistical analysis was carried out using Prism (GraphPad Software, Inc., CA, USA) setting $\alpha = 0.05$.

2.12 Appendix

Table 2.11. PCR primers for the amplification of the edited *Kcnc1* genomic locus

Primer	Sequence (5’ → 3’)	Target site
5F	AGAACACACCCCTCGTATGG	Intron 1 of the *Kcnc1* gene
5R	CTTGTTGGGGCAGAAGACGA	Exon 2 of the *Kcnc1* gene

Table 2.12. Primers used in site-directed mutagenesis experiments

Primer	Sequence (5’→3’)
Shaker362-F	GTCCTTGGCAATATTACACGTGATACGATTAGTTCG
Shaker362-R	CGAACTAATCGTATCACGTGTAATATTGCCAAGGAC
Shaker371-F	CGATTAGTTCGAGTATTTCACATATTTAAGTTATCTAGGC
Shaker371-R	GCCTAGATAACTTAAATATGTGAAATACTCGAACTAATCG
Kv3.1W392-F	CATCCCCATCGGATTTTTTTGGGCCGTCGTGACC
Kv3.1W392-R	GGTCACGACGGCCCAAAAAAATCCGATGGGGATG
Kv3.1959G.A-F	TCGTGCGGATCCTGCACATCTTCAAGCTGAC
Kv3.1959G.A-R	GTCAGCTTGAAGATGTGCAGGATCCGCACGA

Table 2.13. PCR primers used in the generation of Cre-dependent vectors

Primer name	Sequence (5’->3’)	Description
EcoR1-hSyn-F	ACAGCGGAATTCGAGTGCAAGTGGGTTTTAGG	For amplification of the hsyn promoter and the introduction of an EcoR1 site
Bamh1-hSyn-R	ACAGCGGGATCCAATTCGACTGCGCTCTCAG	For amplification of the hsyn promoter and the introduction of a BamH1 site
Nhe1-ChIEF-F	ACAGCTAGCATGGTGAGCAGAAGACC	For amplification of ChIEF-mCitrine and the introduction of a 5’ Nhe1 site
Mlu1-CitrineChIEF-R	ACAACGCGTCCTACTTGTACAGCTCGTCC	For amplification of ChIEF-mCitrine and the introduction of a 3’ Mlu1 site and stop codon

Table 2.14. PCR primers used in the generation of the pCCL-PTG reporter plasmid

Primer name	Sequence (5’-3’)	Notes
Xho1-EF1α-F	ACACTCGAGAATTTAAATGCGGCCGCG	For amplification of the EFIα-tdTomato and the introduction of 5’-Xho1 site
BstB1-tdtom-R	ACATTCGAACTTATACAGCTCATCCATGCC	For amplification of the EFIα-tdTomato and the introduction of 3’-BstB1 site

Table 2.15. SgRNA sequences used in the targeting of EGFP

sgRNA	Sequence (5’-3’)
sgRNA2 GFP	GTGGTCACGAGGGTGGGCCA
sgRNA5 GFP	GTGGTGCAGATGAACTTCAG

Table 2.16. PCR Primers used in the generation of pCCL-PGK-GOSR2 vectors

Primer name	Sequence (5’→3’)	Description
Mod1-Nhe1-F	ACAGCTAGCATGGACTACAAAGAC GATGACGACAAGGATCCC	Amplification GOSR2 from pcdna3.1, introduction of 5’ Nhe1 site for subcloning into pCCL
Mod1-Sal1-GOSR2-R	ACAGTCGACTCATGTCAGGTACTG CACCACGAGG	Amplification GOSR2 from pcdna3.1, introduction of 3’ Sal1 site for subcloning into pCCL

Table 2.17. PCR primers used for subcloning of the PCP2 promoter

Primer name	Sequence (5’→3’)	Reason
EcoR1PCP2	GCGGAATTCAGACTCACT CGTTAATTAGG	Amplification of PCP2 promoter and for the introduction of a 5’ EcoR1 site
BamH1PCP2	ACAGGATCCTGGACTCC AGTCACTTTTC	Amplification of PCP2 promoter from pEMS1424 and for the introduction of a 3’ BamH1 site

Table 2.18. Oligonucleotide sequences for sgRNA subcloning.

Oligo	Sequence (5' → 3')
sgRNA1F	CACCGATAGCATGGCATGTCGGCTTGT
sgRNA1R	TAAAACAAGCCGACATGCCATGCTATC
sgRNA2F	CACCGAGAAACCTGGAGAGCCTCGCGT
sgRNA2R	TAAAACGCGAGGCTCTCCAGGTTTCTC
sgRNA3F	CACCGCATGTCGGCTTAGGCTGTGTGT
sgRNA3R	TAAAACACACAGCCTAAGCCGACATGC
sgRNA4F	CACCGGATGCAGGATTTACTATCCGT
sgRNA4R	TAAAACGGATAGTAAATCCTGCATCC
When the sequence did not start with a G, a G was added to the 5' end as the U6 promoter prefers a G at the transcription start site.	

Chapter 3

Investigating the pathogenic mechanisms underlying MEAK

3.1 Introduction

Myoclonus epilepsy and ataxia caused by a potassium channel mutation (MEAK) is an autosomal dominant form of PME caused by mutation of the *KCNC1* gene, which encodes the voltage-gated potassium channel, K_V3.1. All patients identified with MEAK have a recurrent c.959G>A point mutation in the *KCNC1* gene, which results in the substitution of the fourth voltage-sensing arginine for a histidine (R320H) in the S4 segment of the VSD of the channel (Muona et al., 2014; Oliver et al., 2017). Patients with MEAK exhibit core symptoms of epilepsy, myoclonus and ataxia (Oliver et al., 2017). Neurodegeneration does not appear to feature prominently in MEAK and symptoms stabilise over time, however patient MRI scans frequently reveal cerebellar atrophy (Oliver et al., 2017). The pathogenic mechanisms underlying MEAK have yet to be elucidated.

K_V3.1 belongs to the K_V3 family of voltage-gated potassium channels that includes K_V3.2-K_V3.4 (Coetzee *et al.,* 1999; Rudy *et al.*, 1999). K_V3.1 is a fast-delayed rectifier that has a high voltage of activation, fast activation and deactivation kinetics and shows minimal inactivation (Coetzee *et al.,* 1999). There are two splice isoforms of the channel, K_V3.1a and K_V3.1b, of which Kv3.1b is the predominant isoform expressed in the adult brain (Liu & Kaczmarek, 1998; Perney et al., 1992a). These splice isoforms have been reported to have identical biophysical properties, differing only in their C-termini, which is thought to be important for subcellular targeting (Gu et al., 2012). Thus far, biophysical characterisation has been carried out for K_V3.1a and K_V3.1b in oocytes and HEK cells respectively (Munch et al., 2018; Muona et al., 2014). The consensus between these studies is that the R320H mutation in K_V3.1 is a loss-of-function mutation and that mutant channels exert a dominant negative effect on WT channel currents.

K_V3.1 channels are kinetically tuned to support high frequency firing (Rudy & McBain, 2001). In the rodent brain, K_V3.1 channels are most highly expressed in fast-spiking neurons such as PV$^+$ interneurons, as well as neurons of the cerebellum, suggesting that these cell types are most severely affected in patients with MEAK. Given the essential role of K_V3.1 channels in determining high frequency firing, reduced excitability of neurons that express these channels appears as an obvious functional consequence of channel mutation. However, the story is likely to be complicated by the possible dominant negative effects that this channel may exert on other K_V3 family members due to the ability to form heteromultimers.

3.2 Aims

The overall aim of this chapter was to investigate the neuronal effects of the R320H mutation in $K_V3.1$.

1. I first aimed to characterise the functional effects of the R320H mutation in $K_V3.1b$ channels ($K_V3.1b^{R320H}$). The choice to study the effects of this mutation in the b isoform was taken because it is the major splice isoform expressed in the adult brain and is expressed in the axons and terminals of neurons in culture (Gu et al., 2012). During the time of experimentation, the functional consequences of the R320H mutation had not been characterised for $K_V3.1b$.
2. My second aim was to express mutant $K_V3.1b$ channels in cortical interneurons *in vitro*, using primary neuronal cultures. My specific objective was to characterise the effects of this mutation on neuronal excitability, in particular on firing phenotypes.

3.3 Characterisation of the functional consequences of the R320H mutation in $K_V3.1b$

3.3.1 $K_V3.1b^{R320H}$ is a partial loss-of-function

The R320H mutation in $K_V3.1a$ has been previously shown using an *X.leavis* oocyte expression system to be loss-of-function with a dominant negative effect (Muona et al., 2014). I wanted to confirm that the R320H mutation also induces a loss-of-function in the $K_v3.1b$ splice isoform. Oocytes were injected with 50 ng each of $Kv3.1b^{WT}$, $Kv3.1b^{R320H}$ or $K_v3.1b^{WT}$ + $K_v3.1b^{R320H}$ cRNA at a 1:1 ratio. Oocytes expressing $K_V3.1b$ channels were then subjected to 200 ms depolarising steps ranging from -100 to +60 mV (**Figure 3.1A**, recordings performed by MSc J.Heneine). A significant reduction in the relative steady-state current amplitude for $K_v3.1b^{R320H}$ (0.65 ± 0.11, n = 9) compared to $K_v3.1b^{WT}$ (1.00 ± 0.08, n = 7) at +40 mV was observed (p = 0.03, **Figure 3.1B**). Interestingly, the currents recorded for $K_V3.1b^{R320H}$ were much greater than those observed for $K_V3.1a^{R320H}$, as it was previously found that mutant $K_V3.1a$ channels are virtually insensitive to changes in transmembrane voltage (Muona et al., 2014). Oocytes expressing both $K_v3.1b^{R320H}$ + $K_v3.1b^{WT}$ also appeared to display a reduced current amplitude at +40 mV (n = 2), which suggested a dominant negative effect of this channel, however the sample size is too low to perform statistical analysis (**Figure 3.1B**). The R320H mutation in $K_V3.1b$ therefore appears to be a partial loss-of-function with a potential dominant negative effect. The findings are in agreement with a recent study, published while this work was being carried out, which functionally characterised $K_V3.1b^{R320H}$ in HEK cells and also found this channel to be a partial loss-of-function with a dominant negative effect on WT channel function (Munch et al., 2018).

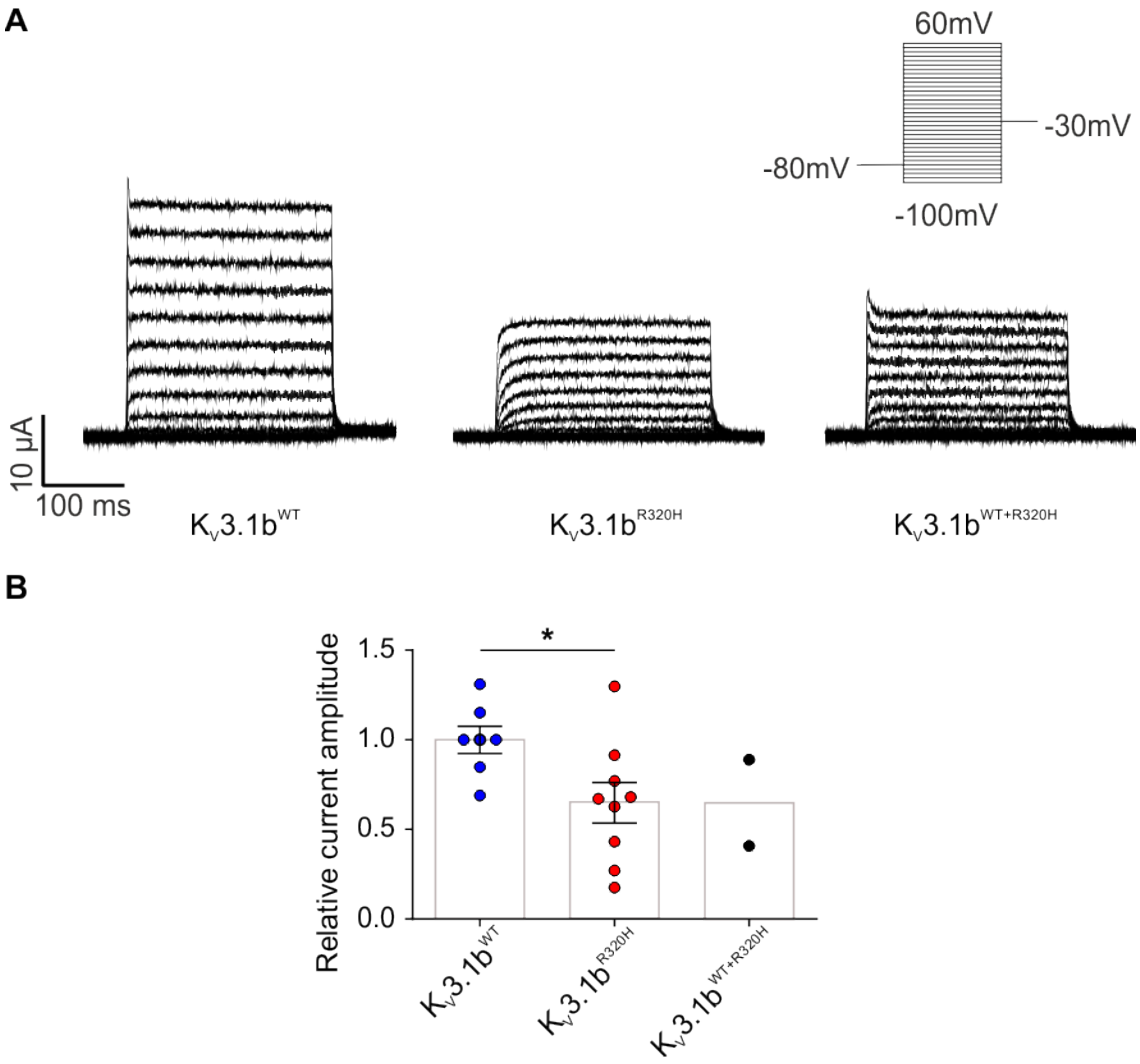

Figure 3.1. Functional characterisation of $K_V3.1b^{R320H}$ channels. A) Representative TEVC recordings of oocytes expressing $K_V3.1b^{WT}$ or $K_V3.1b^{R320H}$ channels in isolation, or at a 1:1 ratio (HET). **B)** Steady-state current amplitudes of $K_V3.1b^{R320H}$ and $K_V3.1b^{R32\ +WT}$ channels at +40 mV, relative to the mean current amplitude for $K_V3.1b^{WT}$ channels recorded on the same day. A significant reduction in current amplitude is observed for $K_V3.1b^{R320H}$ with respect to WT (Student's

t-test, * p = 0.03). Data are presented as means ± s.e.m. Oocyte recordings performed by an MSc student, Jana Heneine, under my supervision.

3.3.2 No change in steady-state channel activation for $K_V3.1b^{R320H}$

Previously, the R320H mutation in $K_V3.1a$ had been found to induce a leftward shift in the voltage-dependence of channel activation (Muona et al., 2014). However, another study that expressed the mutation in the $K_V3.1b$ splice variant in HEK cells, found no differences in channel activation (Munch et al., 2018). I therefore wished to investigate whether the R320H mutation changes the activation properties of $K_V3.1b$. To characterise changes in steady-state channel activation, oocytes were stepped from -100 mV to +60 mV (Δ10 mV) and then to -30 mV for 250 ms. Current amplitudes were measured at the tail voltage of -30 mV, fitted to a single Boltzmann function and then normalised to account for differences in channel expression. Normalised current values were plotted as a function of voltage (**Figure 3.2**). Contrary to what was found for $K_V3.1a$, we observed no significant differences in the voltage of half-activation ($V_{0.5}$) for $K_V3.1b^{R320H}$ (-3.1 ± 3.3 mV, n = 9) compared to $K_V3.1^{WT}$ (-7.9 ± 3.0 mV, n = 10; p = 0.29). There were also no significant differences in the slope factor k (WT: 14.4 ± 0.81; R320H: 16.3 ± 0.63; p = 0.08). The discrepancies in the activation properties of the mutant channel for different splice isoforms may reflect, in part, the fact that Muona et al., studied the activation properties of $K_V3.1a^{WT+R320H}$ heteromeric channels because $K_V3.1a^{R320H}$ expressed in isolation gave negligible currents (Muona et al., 2014). It is worth noting that the $V_{0.5}$ may be underestimated in our data set because $K_V3.1b^{R320H}$ does not appear to be reaching maximal activation. Whilst future studies would require additional data points above +50 mV to obtain a plateau in the current-voltage relationship, I will not repeat this experiment as our findings are in accordance with recently published findings for the $K_V3.1b$ isoform (Munch et al., 2018).

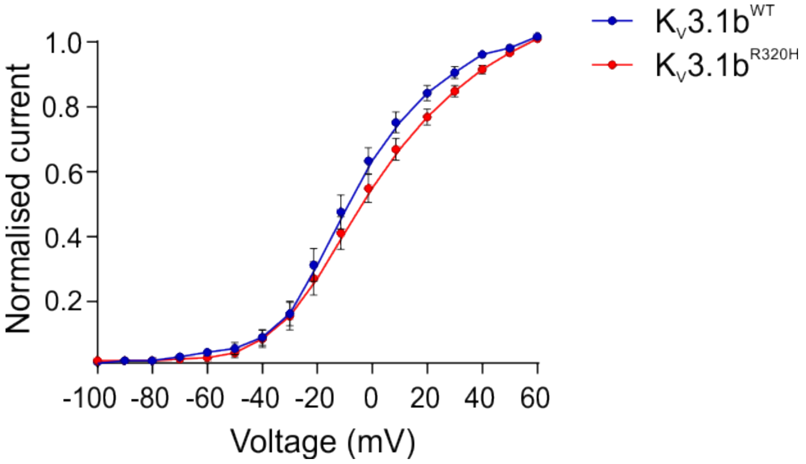

Figure 3.2. Voltage-current relationship for $K_V3.1b^{R320H}$. Lines are fits of a Boltzmann function. The $V_{0.5}$ and slope factor k for $K_V3.1b^{R320H}$ and $K_V3.1b^{WT}$ are not significantly different (Student's *t*-test, p = 0.29 and p = 0.08, respectively). Data is presented as means ± s.e.m. Oocyte recordings performed by an MSc student, Jana Heneine, under my supervision.

3.4 The neuronal expression of $K_V3.1b^{R320H}$ mutant channels triggers morphological changes and cell death

3.4.1 $K_V3.1b$ expression can be targeted to interneurons using the mDlx promoter

Following the validation of our channel clones using electrophysiology, I sought to investigate the effects of mutant $K_V3.1$ channels on neuronal function. Given the role of $K_V3.1b$ channels in high frequency firing, I chose to target transgene expression to interneurons in primary cortical cultures using the recently described mouse distalless homeobox (mDlx) promoter/enhancer element (Dimidschstein et al., 2016). *In situ*, the mDlx enhancer drives expression of Dlx5 and 6 (Dlx5/6) genes which are exclusively expressed in cells of the Dlx5/6 lineage from the telencephalon (Zerucha et al., 2000). When used ectopically as a promoter element, the mDlx promoter can drive the specific postnatal expression of transgenes in forebrain GABAergic interneurons (Dimidschstein et al., 2016).

With the view to use a lentiviral-strategy to overexpress $K_V3.1$ channels in neurons in culture, I generated lentiviral transfer vectors containing GFP, to act as a reporter for cell transfection/transduction, and WT or mutant *KCNC1* transgenes (**Figure 3.3A**). I inserted the mDlx enhancer alongside a chimeric intron upstream of dscGFP, or dscGFP linked to *KCNC1* via a T2A element within a lentiviral backbone. The chimeric intron was included as a cis-acting element in order to enhance expression of downstream transgenes (Powell et al., 2015). In order to assess the strength of GFP expression and the cell-type specificity of the mDlx promoter, I synthesised a GFP control lentivirus using the mDlx-dscGFP lentiviral transfer vector and transduced primary cortical neuronal cultures at DIV 1. At 7 DIV, I found 39 ± 3% of neurons in culture were positive for the pan-interneuron marker, glutamic acid decarboxylase isoform 67 (GAD67). When GFP expression was assessed at 7 DIV, I found that 93% of GFP^+ neurons co-expressed GAD67. I therefore confirmed that the mDlx enhancer element is capable of driving robust and highly specific expression of transgenes in cortical GABAergic interneurons in primary neuronal culture (**Figure 3.3B**).

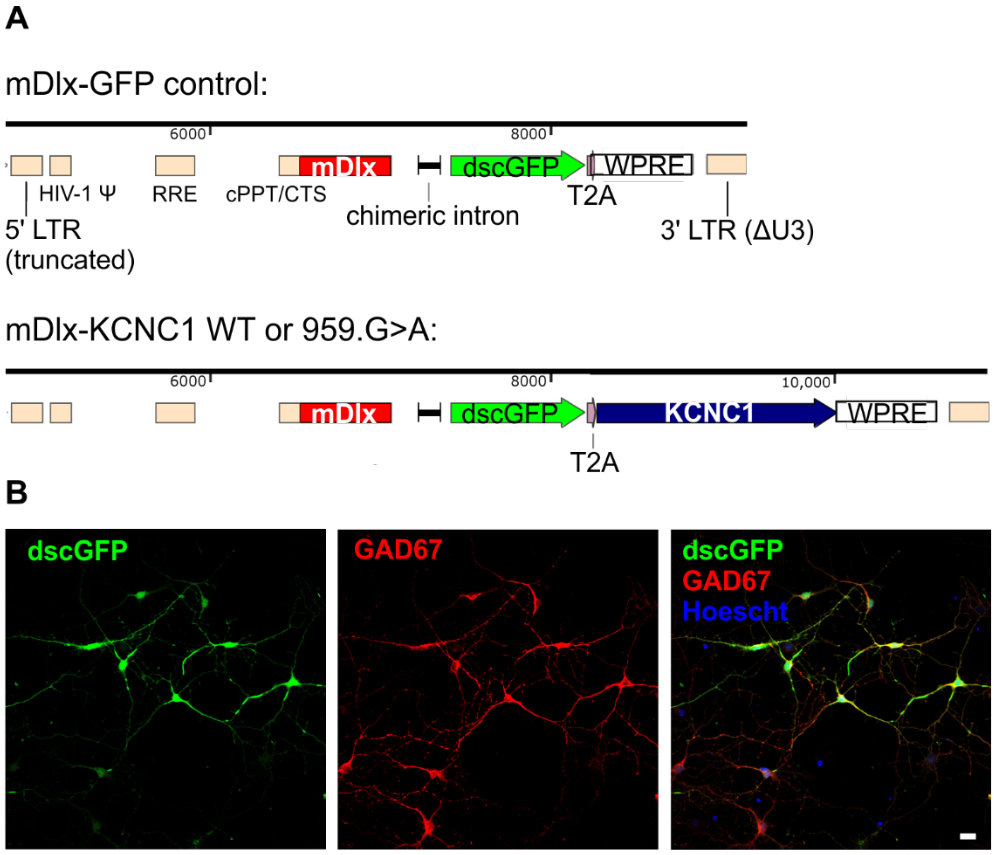

Figure 3.3. Targeting interneurons using the mDlx promoter element. A) Lentiviral transfer vectors containing the mDlx promoter element for targeting interneurons. Important elements of the lentiviral backbone are indicated. LTR: long terminal repeat; RRE: Rev response element; cPPT/CTS: central Polypurine tract. **B)** Representative images from an immunofluorescence assay for GFP and GAD67 colocalisation in murine cortical neuronal cultures at 7 DIV. Scale bar is 20 µm.

3.4.2 $K_V3.1b^{R320H}$ has toxic effects when overexpressed in young cortical neurons

3.4.2.1 $K_V3.1b^{R320H}$ channels induce pro-apoptotic changes in nuclear morphology

Our initial aim was to express mutant and WT $K_V3.1$ channels in neurons using lentiviral vectors. However, early attempts at synthesising lentiviruses expressing $K_V3.1^{R320H}$ channels resulted in extremely low titers, which suggested that the channel was inducing toxicity of producer HEK cells. Indeed, it has recently been shown using transfected HEK cells that trafficking of $K_V3.1^{R320H}$ channels to the cell surface membrane is impaired, which is likely to place the cell under more stress during lentiviral production (Munch et al., 2018). Interestingly, mutation of the analogous arginine residue in $K_V3.3$ (R423H) results in an early-onset form of the neurodegenerative condition, spinocerebellar ataxia 13 (SCA13). This channel was found to be neurotoxic when expressed in Purkinje cells in culture (Irie et al., 2014). I therefore wished to investigate the effects of $K_V3.1b^{R320H}$ channels on neuronal survival.

I elected to use naked DNA to investigate the effects of mutant $K_V3.1b$ channels on neuronal survival. Murine cortical neuronal cultures were transfected with mDlx-GFP, mDlx-$K_v3.1b^{WT}$ or mDlx-$K_v3.1b^{R320H}$ lentiviral expression plasmids at 4 DIV and fixed 24 and 48 hr after transfection. At 48 hr I found that neurons transfected with $K_v3.1b^{R320H}$ channels exhibited what appeared to be pro-apoptotic changes in their nuclei compared to GFP and WT controls (**Figure 3.4A**). Nuclei of cells undergoing apoptosis typically become condensed and more irregularly shaped, which can be quantified as a decrease in nuclear area factor (NAF). I found the NAF to be significantly reduced for $K_v3.1b^{R320H}$ at 48hr (48.0 ± 4.9, n = 6) compared to 24 hr post-transfection (71.6 ± 0.8, n = 6) indicating that pro-apoptotic nuclear changes are triggered within a 24 hr time period ($p < 0.001$, **Figure 3.4B**). I confirmed that these nuclear changes were induced by $K_V3.1b$ mutant channels and not toxicity of transfection by comparing the NAF of $K_V3.1b^{R320H}$ at 48 hr with that of $K_V3.1b^{WT}$ (68.3 ± 4.6, n = 5) and GFP (67.2 ± 5.2, n = 5) controls and found them to be significantly different (GFP vs. R320H $p = 0.014$; WT vs. R320H $p = 0.008$, **Figure 3.4B**). Note that ‘n’ corresponds to the average NAF of three nuclei per coverslip and each coverslip was treated separately.

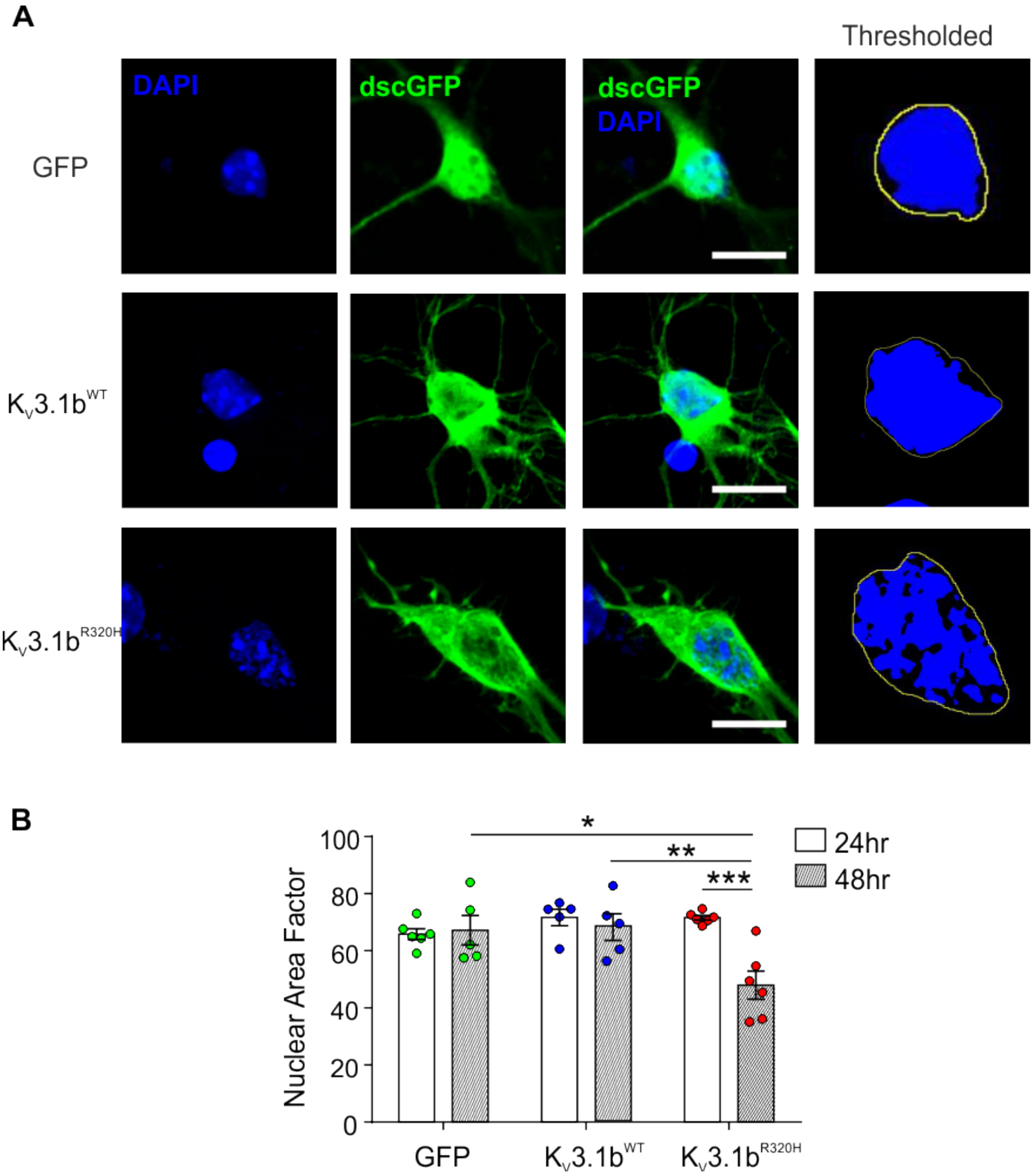

Figure 3.4. $K_V3.1^{R320H}$ induces pro-apoptotic changes in nuclear morphology 48hr post-transfection. A) Representative immunofluorescent images of cortical interneurons 48 hr post-transfection with mDlx-GFP, mDlx-$K_V3.1^{WT}$ or mDlx-$K_V3.1^{R320H}$ plasmids. The RHS panel displays binary images of nuclei following demarcation of the nucleus as a ROI and thresholding of the DAPI staining. Note that neurons expressing $K_V3.1^{R320H}$ channels display dystrophic neurites. **B)** Quantification of NAF 24 and 48 hr post-transfection. A significant reduction in NAF is observed for $K_V3.1b^{R320H}$ between 24 and 48 hr. **24 hr:** GFP vs. R320H p = 0.987; WT vs. R320H p > 0.999; GFP vs. WT p = 0.990. **48 hr:** GFP vs. R320H *p = 0.014; WT vs. R320H **p = 0.008; GFP vs. WT p > 0.999. **24 hr vs. 48 hr**: GFP vs. GFP p > 0.999; WT vs. WT p > 0.999; R320H vs. R320H ***p < 0.001. Two-way ANOVA followed by Bonferroni’s multiple comparisons test. Data are from two independent neuronal preparations and are shown as means ± s.e.m.

3.4.2.2 Caspase-3 activation is not observed in neurons expressing $K_V3.1b^{R320H}$

The visual changes I observed in nuclear morphology for neurons overexpressing $K_v3.1b^{R320H}$ were suggestive of early stage apoptosis. I next wanted to investigate whether neurons expressing the mutant channel were dying via an apoptotic pathway by investigating the presence of cleaved-caspase 3 (CC-3). Caspase-3 is a master executioner of apoptosis and its activation by proteolytic cleavage marks the start of an irreversible cascade of caspase activation that condemns the cell to death. Caspase-3 translocates to the nucleus after activation and plays an important role in inducing the changes in nuclear morphology that occur in apoptotic cells (Kamada et al., 2005). Given that I observed changes in nuclear morphology at 48 hr and not at 24 hr and that CC-3 has a short half-life, I chose to assay for CC-3 immunoreactivity 36 hr post-transfection (**Figure 3.5A**). As a positive control, I also treated cortical neuronal cultures at 4 DIV with 0.1 µM of staurosporine, a kinase inhibitor that is known to induce caspase-dependent apoptosis, and examined CC-3 immunoreactivity 36 hr later (**Figure 3.5B**). I did not observe CC-3 immunoreactivity in neurons expressing $K_v3.1b^{R320H}$ channels 36 hr after transfection (**Figure 3.5A**). In contrast, I observed many apoptotic cells in the staurosporine control condition that were highly reactive for CC-3 (**Figure 3.5B**). Interestingly, I found that neurons that were the most highly reactive for CC-3 in the staurosporine condition were those whose nuclei were highly condensed and fragmented (**Figure 3.5B**). I reasoned that perhaps I would observe CC-3 immunolabelling in our transfected neurons at 72 hr post-transfection, after the nuclei had become more condensed. However, I still did not observe CC-3 at 72 hr (data not shown).

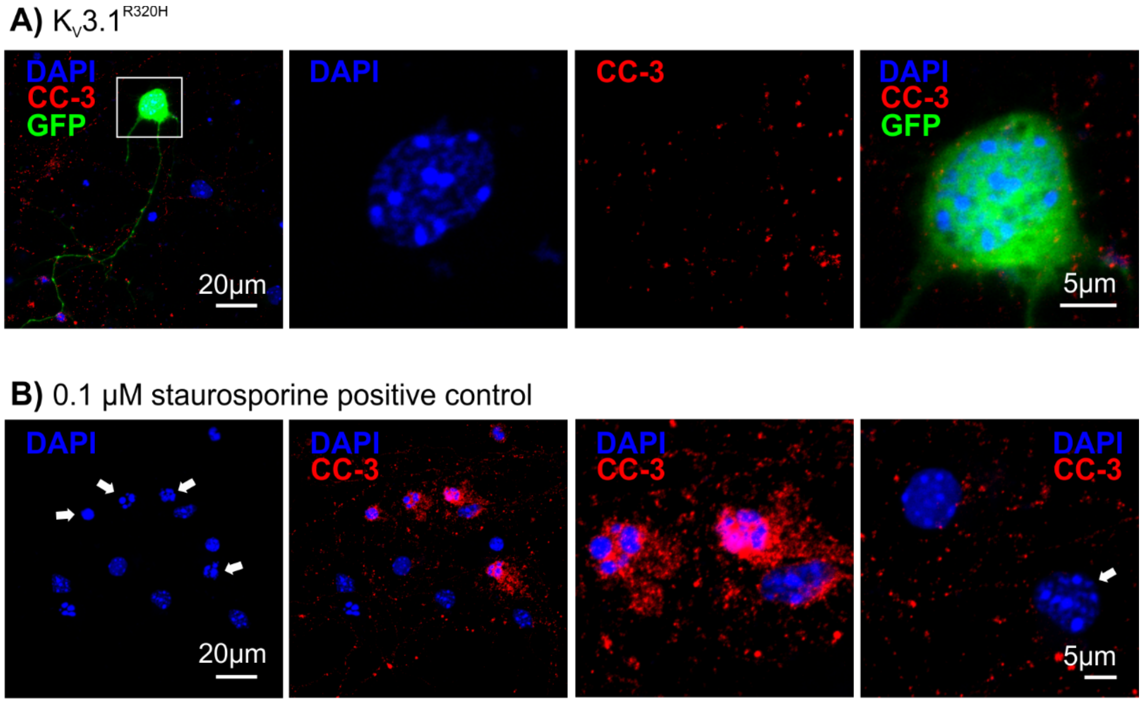
A) $K_V3.1^{R320H}$

B) 0.1 μM staurosporine positive control

Figure 3.5. CC-3 is not detectable in neurons expressing $K_V3.1b^{R320H}$. **A)** CC-3 immunoreactivity is not detectable in neurons expressing $K_V3.1b^{R320H}$ (GFP^+) 36 hr post-transfection (5.5 DIV) despite visible changes in nuclear chromatin and cell morphology. **B)** CC-3 immunoreactivity is clearly detectable in neurons that were treated with 0.1 μM staurosporine for 36 hr. Generally, cells with highly condensed nuclei (white arrows, far LHS panel) are positive for CC-3 immunolabelling (third panel from the left), whereas cells undergoing what appears to be early pro-apoptotic nuclear changes are negative for CC-3 (indicated nucleus in far RHS panel).

3.4.2.3 Neurons remain viable 24 hr after $K_V3.1b^{R320H}$ channel expression

The absence of CC-3 immunolabelling at 36 and 72 hr in neurons expressing $K_V3.1b^{R320H}$ channels suggested that these cells were not dying via a caspase-dependent apoptotic pathway. To have a secondary measure of cell death I therefore performed a live/dead assay of neurons 24 hr after transfection. For this assay I used the vitality stain, propidium iodide (PI), a membrane impermeant dye that is normally excluded from live cells. Upon changes in membrane permeability, such as those that occur during cell death, PI is able to enter the cell and bind to DNA in the nucleus. Upon binding to DNA, PI fluoresces red, thus cell death can be estimated as the proportion of neurons with nuclei positive for PI staining. An estimate of neuron vitality was calculated by imaging 4 GFP^+ neurons per coverslip and calculating the percentage of neurons that were positive for PI fluorescence (this represented an 'n' of 1). I found no significant differences in neuronal viability for neurons transfected with GFP (7.7 ± 2.8%, n = 7), $K_V3.1^{WT}$ (5.5 ± 1.7% n = 9) or $K_V3.1^{R320H}$ (5.5 ± 4.3% n = 9; GFP vs. WT, $p > 0.99$; GFP vs. R320H, $p = 0.86$; WT vs. R320H, $p = 0.85$, **Figure 3.6**). I have therefore confirmed that neurons expressing $K_V3.1b^{R320H}$ channels are still alive after 24 hr and are not necrotic. These neurons still may, however, be undergoing early-stage apoptosis as membrane permeability is highest during late stage apoptosis (Zhang et al., 2018).

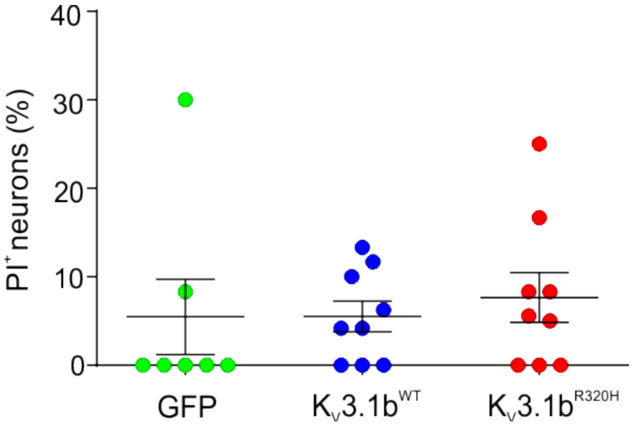

Figure 3.6. Neurons expressing $K_V3.1b^{R320H}$ channels remain viable after 24hr. A PI vitality assay was performed 24 hr after transfection for interneurons expressing GFP only, $K_V3.1b^{WT}$ or $K_V3.1b^{R320H}$ channels. No significant differences in the % of neurons positive for PI staining was found between the groups (GFP vs. WT, $p > 0.99$; GFP vs. R320H, $p = 0.86$; WT vs. R320H, $p = 0.85$, One-way ANOVA followed by Bonferroni's multiple comparisons test). Data are from three independent neuronal preparations and are shown as means ± s.e.m.

3.4.3 Overexpression of $K_V3.1b^{R320H}$ induces changes in neuronal morphology

3.4.3.1 The developmental expression of mutant $K_V3.1b$ channels results in a reduction in dendritic length

I noticed that neurons expressing $K_V3.1b^{R320H}$ channels exhibited dystrophic neurites as well as changes in nuclear morphology (**Figure 3.5A**). In order to delineate the effects of mutant $K_V3.1b$ channels on the axon and dendrites I transfected neurons at 4 DIV with GFP, $K_V3.1b^{WT}$ or $K_V3.1b^{R320H}$ channels and immunolabelled neurons at 48 hr post-transfection for the axonal marker, neurofilament H (NF-H). Dendritic Sholl analysis was performed on thresholded images of the dendritic tree, which was identified by GFP fluorescence and an absence of NF-H immunoreactivity (**Figure 3.7A**). Sholl analysis revealed profound global changes in the dendritic tree, summarised as a significant reduction in the total number of dendritic intersections (30.8 ± 2.7, R320H vs. GFP, $p < 0.0001$; R320H vs. WT, $p < 0.0001$) and maximal dendritic length (51.4 ± 4.7 µm, R320H vs. GFP, $p < 0.0005$; R320H vs. WT, $p = 0.0008$) for neurons expressing $K_V3.1b^{R320H}$ ($n = 6$, **Figure 3.7B, C**). I did not observe any significant changes for $K_V3.1b^{WT}$ in maximal dendritic length (103.8 ± 10.7 µm, GFP vs. WT, $p = 0.960$) or in the total number of dendritic intersections (115.5 ± 12.4, GFP vs. WT, p = 0.274) compared to GFP (106.9 ± 7.3 µm and 137.5 ± 8.5 respectively) confirming that overexpression of the WT channel does not increase dendritic arborisation or outgrowth (GFP & WT n = 5, **Figure 3.7B, C**). Thus, it appears that the expression of mutant $K_V3.1b$ channels in young neurons in culture adversely affects dendritic development.

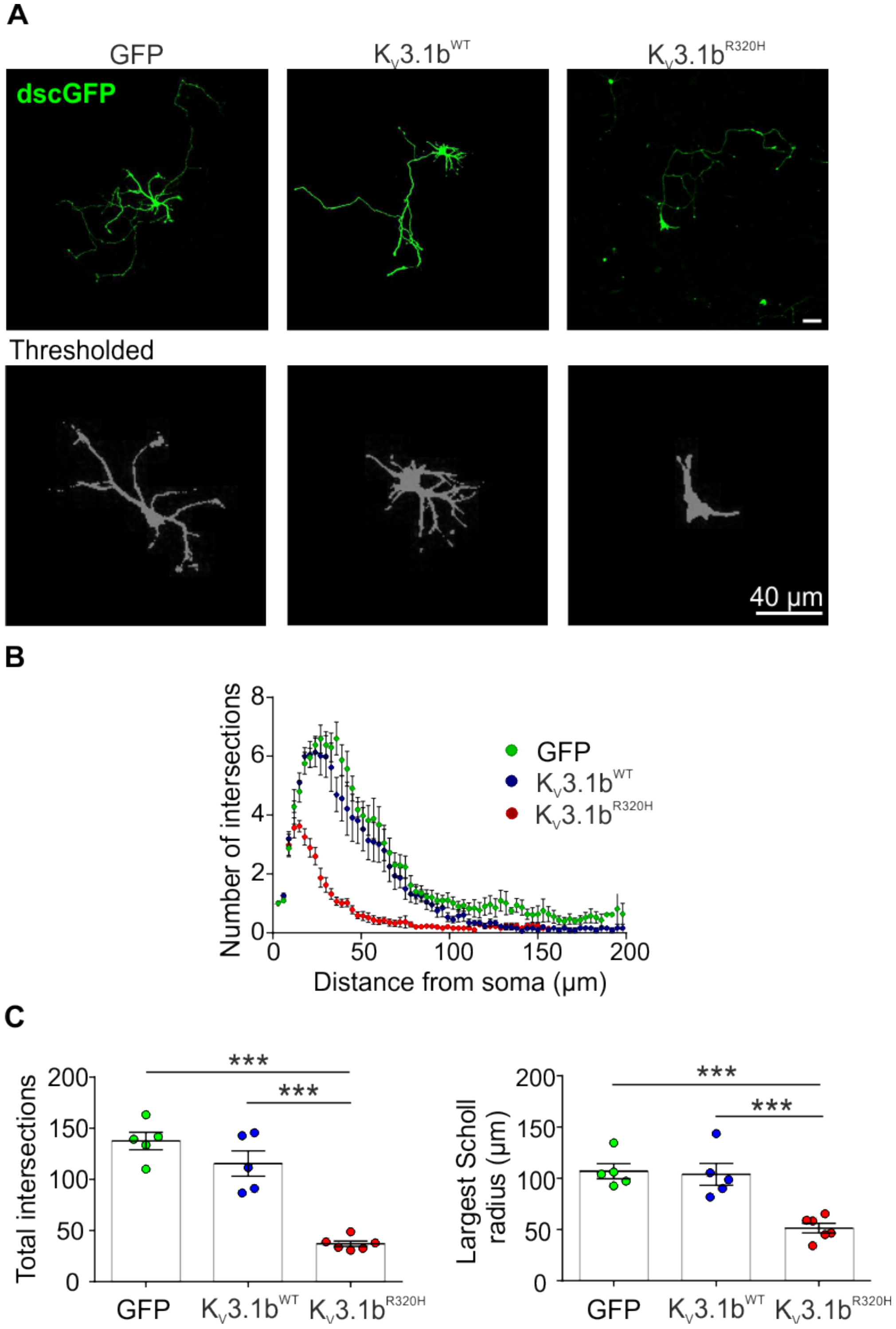

Figure 3.7. The developmental expression of $K_V3.1b^{R320H}$ induces a reduction in dendritic length. A) Representative immunofluorescent images of cortical interneurons at 6 DIV, 48 hr

post-transfection with mDlx-GFP, mDlx-K$_V$3.1b^{WT} or mDlx-K$_V$3.1b^{R320H} plasmids. Scale bar of the top panel is 50 µm. The dendrites were identified by the absence of NF-H reactivity (not shown). Pixels pertaining to GFP fluorescence of the axon were deleted. The subsequent immunofluorescent image of the dendritic tree was thresholded to form a binary image for Sholl analysis. **B)** Dendritic Sholl analysis reveals a profound reduction in the size and complexity of the dendritic tree for neurons expressing K$_V$3.1b^{R320H}. **C)** K$_V$3.1b^{R320H} significantly reduces the total number of dendritic intersections and maximal dendritic length, as indicated by the largest Sholl radius used in the analysis (Dendritic length: R320H vs. GFP, ***$p < 0.0005$; R320H vs. WT, ***$p = 0.0008$; WT vs. GFP, $p = 0.960$; Total intersections: R320H vs. GFP, ***$p < 0.0001$; R320H vs. WT, ***$p < 0.0001$; WT vs. GFP, $p = 0.274$: One-way ANOVA with Bonferroni's multiple comparisons test). Data are represented as means ± s.e.m. Note that each data point, 'n', represents the average of 7 neurons per coverslip across two independent neuronal preparations.

3.4.3.2 The developmental expression of K$_V$3.1b^{R320H} channels results in a reduction in axonal length

The profoundly severe and rapid alterations in dendritic morphology induced by K$_V$3.1b^{R320H} channels led us to ask whether this mutation also induces pathological changes in the axon. Using the axonal marker NF-H, I performed axonal tracings of neurons 48 hr post-transfection in order to quantify axonal length across the different conditions (**Figure 3.8A**). I found total axonal length to be significantly reduced for neurons overexpressing K$_V$3.1b^{R320H} (875.8 ± 69.6 pixel units, $n = 6$) compared to WT (1407 ± 120.7 pixel units, $n = 5$, R320H vs. WT, $p = 0.006$) and GFP controls (1436 ± 117.3 pixel units, $n = 5$, R320H vs. GFP, $p = 0.004$, **Figure 3.8B**). Again, there was no significant difference in axonal length for neurons overexpressing Kv3.1b^{WT} or GFP only, demonstrating that overexpression of the WT channel does not promote axonal growth (WT vs. GFP, $p = 0.98$, **Figure 3.8B**).

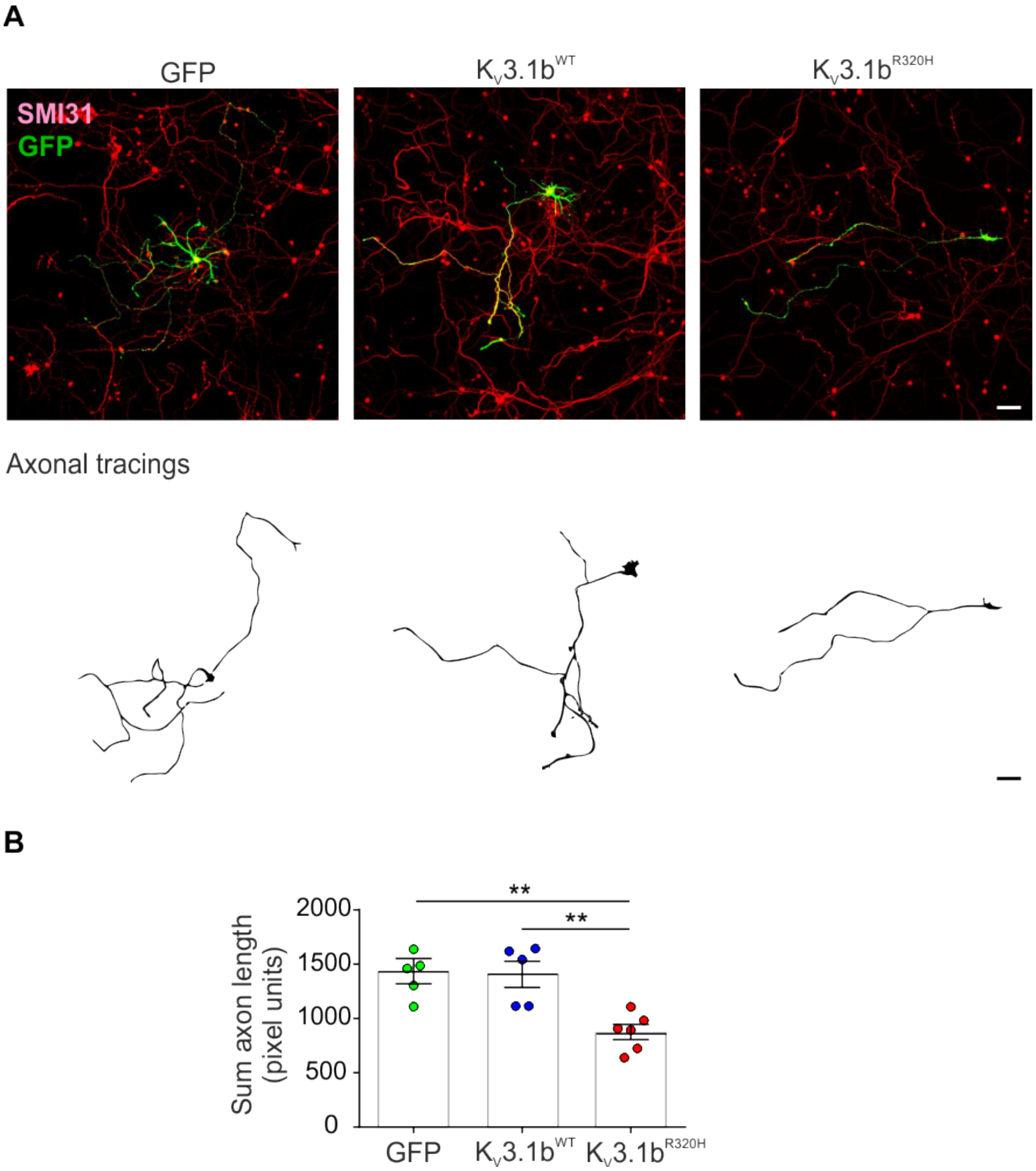

Figure 3.8. $K_V3.1b^{R320H}$ overexpression results in a reduction in axonal length. A) Representative immunofluorescence images of cortical interneurons at 6 DIV immunolabelled with the axonal marker, NF-H, 48 hr after transfection with mDlx-GFP, mDlx-$K_V3.1b^{WT}$ or mDlx-$K_V3.1b^{R320H}$ plasmids. Bottom panel: tracings of axonal arbours delimited by NF-H immunolabelling. **B)** $K_V3.1b^{R320H}$ results in a significant reduction in total axonal length compared to WT and GFP controls (GFP vs. R320H: ** $p = 0.004$; WT vs. R320H: ** $p = 0.006$; GFP vs. WT: $p = 0.98$, One-way ANOVA followed by Bonferroni's multiple comparisons test). Data are shown as means ± s.e.m. Each data point, 'n', represents the average axonal length of 7 GFP^+ neurons per coverslip, across two independent neuronal preparations. Scale bar is 50 μm.

3.5 Investigation of pathological gating pore currents in MEAK

3.5.1 The R320H mutation may introduce a proton pore into the VSD of $K_V3.1$

The detrimental effects that I observed for mutant $K_V3.1b$ channels on neuronal morphology and survival suggested that the R320H mutation represents a toxic gain-of-function. In particular, the specific location and nature of the mutation led us to wonder whether this mutation renders the VSD of $K_V3.1$ leaky to protons. Mutation of gating charge-carrying arginines have been previously shown to cause human disease via a non-canonical mechanism involving the introduction of pathological cation leaks through the VSD of the channel (gating pore) instead of the main pore (α pore). These leak currents through the VSD of a channel are termed 'gating pore currents' because they only occur upon channel gating. Such a phenomenon has been described for hypokalemic periodic paralysis where, for example, mutation of the first voltage-sensing arginine to a histidine in $Na_V1.4$ generates a proton-selective gating pore current that is activated by hyperpolarisation (Sokolov et al., 2007). The PME mutation, R320H, changes the fourth voltage-sensing arginine in the S4 domain of $K_V3.1$ to a histidine. In the Shaker potassium channel, the analogous mutation of the fourth voltage-sensing arginine (R371H) results in the formation of a proton pore in the VSD of the channel upon membrane depolarisation, which results in the generation of a H^+ current in the presence of a pH gradient (Starace & Bezanilla, 2001). I therefore wished to explore the hypothesis that gain-of-function changes unique to the VSD of $K_V3.1$ result in pathological H^+ currents that contribute to disease pathogenesis in patients with PME.

3.5.2 The W392F mutation effectively abolishes α-pore currents in $K_V3.1b$

In order to detect very small gating pore currents in $K_V3.1b^{R320H}$ I engineered a W392F mutation into WT and mutant $K_V3.1b$ channels with the purpose of blocking K^+ currents through the α-pore of the channel. The analogous mutation in Shaker (W434F) has been shown to completely abolish α-pore currents without significantly altering the channel's gating properties (Perozo et al., 1993; Yang et al., 1997). The W434 residue in the pore region of Shaker is highly conserved across potassium channels and so I were able to identify the analogous residue in $K_V3.1b$ using sequence alignment (**Figure 3.9**) (Yang et al., 1997). The α-pore mutants $Kv3.1b^{W392F.WT}$ and $Kv3.1b^{W392F.R320H}$ were subsequently generated. I found that the W392F mutation indeed abolished K^+ currents through the α-pore of the channel (**Figure 3.10**).

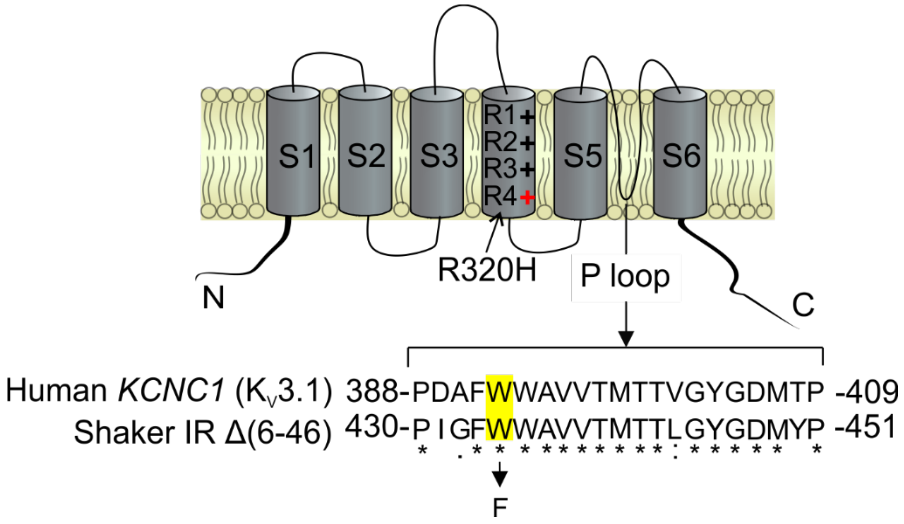

Figure 3.9. Engineering K$_V$3.1b α-pore mutants for gating pore measurements. Sequence alignment of the pore loop region of human K$_V$3.1b and Shaker was used to identify tryptophan 392 (W392) in K$_V$3.1b (highlighted) as the residue analogous to W434 in Shaker. In Shaker, substitution of W434 with phenylalanine (W434F) has been shown to completely abolish currents through the main ion-conducting pore (α-pore) of the channel. N: N-terminus; C: C-terminus; P loop: pore loop. *: conserved residues.

3.5.3 pH-dependent gating pore currents are not detected for K$_V$3.1b^{R320H} α-pore mutants

In order to detect gating pore currents for K$_V$3.1b α-pore mutants, I performed TEVC recordings of oocytes injected with cRNA for K$_V$3.1b$^{W392F.WT}$, K$_V$3.1b$^{W392F.R320H}$, Shaker$^{W434F.WT}$ or Shaker$^{W434F.R371H}$ α-pore mutants. I included Shaker$^{W434F.R371H}$ as a positive control in these experiments because significant H$^+$-carried gating pore currents have been observed for this channel when the fourth voltage-sensing arginine, analogous to R320 in K$_V$3.1, is mutated to a histidine residue (R371H).

Proton-carried gating pore currents show voltage and pH-dependence due to the fact that an H$^+$ permeable gating pore is formed only upon transition of the S4 voltage-sensor during membrane depolarisation. Oocytes were therefore injected with 200 ms depolarising steps from -100 mV to +60 mV in the presence of NaMeS external solutions at pH 7.4 or pH 5.5. For Shaker$^{W434F.R371H}$, we observed larger inward currents at pH 5.5 compared to pH 7.4, characteristic of H$^+$-carried gating pore currents, which could be represented as a significant increase in the area under the curve (n = 5, p = 0.0003, **Figure 3.10A-C,** experiments performed by MSc student, J.Heneine). Shaker$^{W434F.R371H}$ currents exhibited a bell-shaped component between the voltages of -60 mV to -20 mV, which corresponds to H$^+$ transport by histidine 371 (**Figure 3.10A &B**) (Starace &

Bezanilla, 2001). In this voltage range, proton transport occurs because the S4 voltage-sensor undergoes repeated transitions (corresponding to channel opening and closing) which enables 371H to transport protons across the cell membrane, thus generating an inward current in the presence of a pH gradient. Between the depolarised potentials of -20 mV to +50 mV, however, proton conduction occurs instead (**Figure 3.10A, B**) (Starace & Bezanilla, 2001). Proton conduction occurs in this voltage range because Shaker channels have a high open probability and so the S4 voltage-sensor remains in its up-state, driving 371H into a position where it can form a proton pore. Thus, in the voltage-range of -20 to +50 mV, a linear relationship between the magnitude of the H^+ current and the test voltage can be observed (**Figure 3.10A, B**).

Gating pore currents were not, however, detectable for oocytes expressing $\text{Shaker}^{\text{W434F.WT}}$ (n = 5), $\text{K}_\text{V}\text{3.1b}^{\text{W392F.WT}}$ (n = 5) or $\text{K}_\text{V}\text{3.1b}^{\text{W392F.R320H}}$ (n = 7) (**Figure 3.10A, B**). Instead, currents recorded for $\text{K}_\text{V}\text{3.1b}^{\text{W392F.R320H}}$ were generally well fit by a linear regression function, confirming that these currents do not exhibit voltage-dependency and instead represent linear leak components (**Figure 3.10A & B**). It therefore appears that the R320H mutation in K_V3.1b does not introduce a proton pore into the VSD upon channel activation.

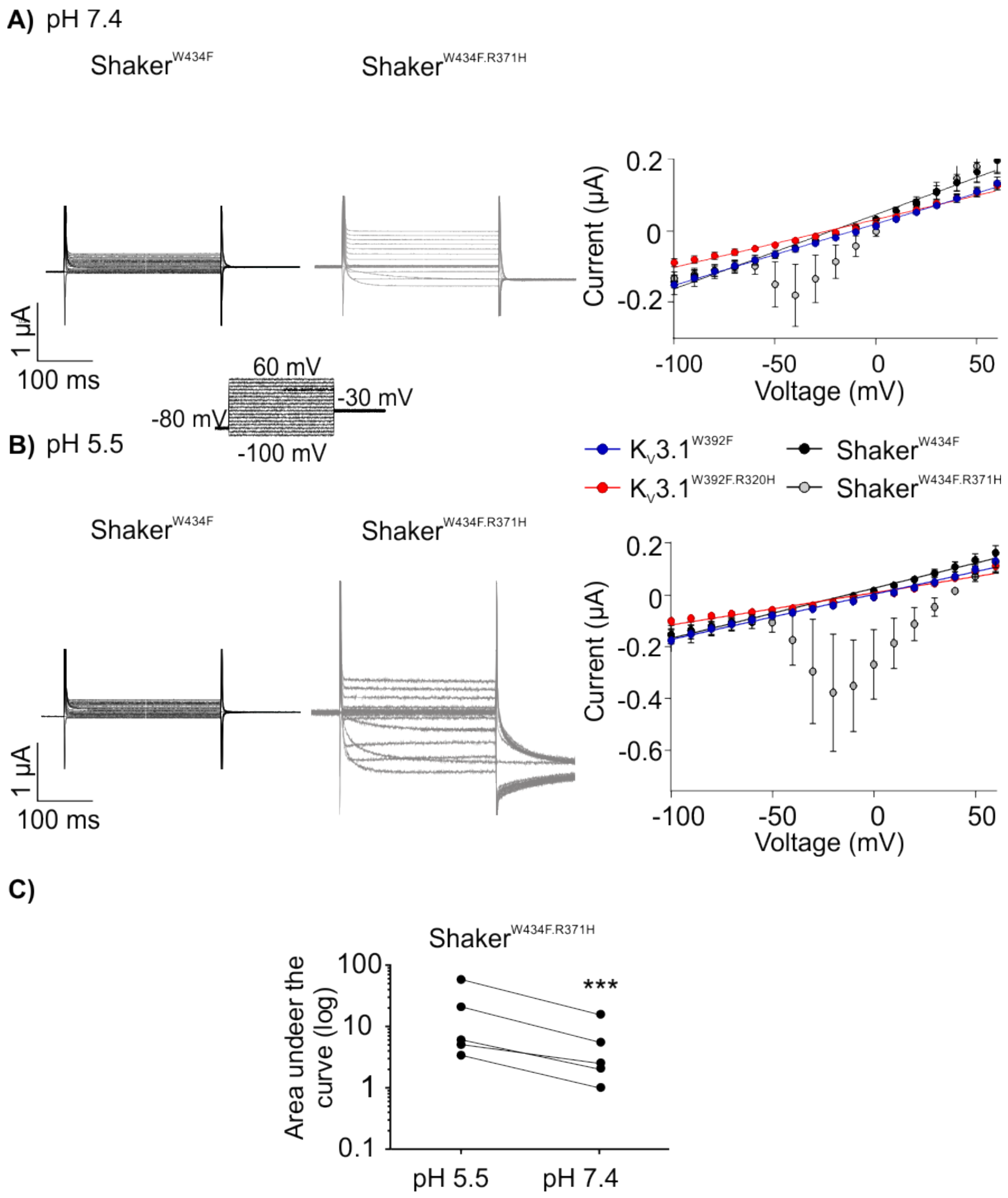

Figure 3.10. H$^+$-carried gating pore currents are not detectable for K$_V$3.1b^{R320H}. A-B) Left panel: representative TEVC recordings of oocytes expressing Shaker$^{W434F.WT}$ or Shaker$^{W434F.R371H}$ channels at pH 7.4 (A) and 5.5 (B). Currents were recorded from the same cell at different pHs. Right panel: current amplitudes measured at pH 7.4 (A) or pH 5.5 (B) were plotted against voltage for oocytes expressing K$_V$3.1b$^{W392F.WT}$, K$_V$3.1b$^{W392F.R320H}$, Shaker$^{W434F.WT}$ and Shaker$^{W434F.R371H}$ channels. Gating pore currents are clearly observable for Shaker channels carrying the R371H mutation. Gating pore currents for Shaker$^{W434F.R371H}$ show two components: a bell-shaped component that represents H$^+$ transport and a linear component that represents H$^+$ conductance. **C)** Gating pore currents measured for Shaker$^{W434F.R371H}$ channels are pH dependent. Scatter plot shows the area under the curve using a logarithmic scale at pH 5.5 compared to pH 7.4. The area

under the curve is significantly larger at pH 5.5 compared to pH 7.4, indicating that currents are carried by H^+ (***p=0.0003, Paired Student's *t*-test). No gating pore currents could be detected for $K_V3.1b^{W392F.R320H}$. Currents for oocytes expressing $K_V3.1b^{W392F.WT}$, $Kv3.1b^{W392F.R320H}$ and $Shaker^{W434F.WT}$ were fit using a linear regression function. Data are shown as means ± s.e.m.

3.6 Functional characterisation of interneurons expressing $K_V3.1b^{R320H}$ channels

Previously I had expressed mutant $K_V3.1b$ channels in young neurons in culture using transfection and revealed dramatic effects of this channel on neuronal morphology and viability. The rapid onset of cell death that occurred within 72 hr of channel expression, however, was prohibitive to characterising the effects of the channel on neuronal firing. As a result, I next decided to express mutant channels in cortical interneurons in culture using lentiviral-based gene delivery, which produces lower levels of transgene expression than transfection. I predicted that expression of the channel at lower levels would be less detrimental to neuronal survival, such that I could perform electrical recordings of neurons at an age when they are electrically mature.

3.6.1 $K_V3.1^{R320H}$ channels reduce interneuronal excitability

In order to investigate the firing properties of neurons expressing WT or mutant $K_V3.1b$ channels, I synthesised lentiviruses using vectors that were identical to those used in transfection experiments (**Figure 3.3**). Neurons were transduced at 2 DIV in order to investigate the developmental effects of this mutation that had been suggested by previous experiments using transfection (**Section 3.4**). Loss of $K_V3.1$ channel function is expected to contribute towards hyperexcitability phenotypes due to the 'inhibition of an inhibitor', as $K_V3.1$ channel expression in the cortex is largely restricted to PV^+ interneurons. Thus, I carried out current-clamp recordings at 14-16 DIV in order to assess the excitability of interneurons expressing $K_V3.1b$ channels (**Figure 3.11A**). I found no significant differences in the input-output curves for neurons expressing $K_V3.1b^{WT}$ channels or GFP only (**Figure 3.11B**). However, I found a significant difference in the input-output curves for $K_V3.1b^{R320H}$ vs. GFP (Interaction between genotype and current, p = 0.0164) and significant differences in firing frequency for current injection of 140-200 pA, indicating that this mutation renders neurons less excitable (**Figure 3.11B**).

I also observed a trend towards a reduction in the maximal firing frequency with current injection of 300 pA for neurons expressing $K_V3.1b^{R320H}$ (8.5 ± 3.7 Hz, n = 6) compared to GFP controls (25.4 ± 5.0 Hz, n = 12; p = 0.075), however this trend was not significant (**Figure 3.11A & C**). The current threshold for 500 ms depolarising stimuli was not significantly altered for neurons expressing $K_V3.1b^{R320H}$ channels (181.7 ± 41.5 pA) compared to GFP controls (GFP: 137.5 ± 20.3 pA; R320H vs. GFP: p = 0.505). There was, however, a significant increase in the current threshold for $K_V3.1b^{R320H}$ when defined using 5 ms depolarising steps (R320H: 1063 ± 116.4 pA; GFP: 653.7 ± 108.1 pA; R320H vs. GFP, p = 0.04, **Figure 3.11D**). There were no significant differences in current threshold for neurons expressing $K_V3.1b^{WT}$ channels with 500 ms depolarising steps (135 ± 20.6 pA, WT vs. GFP, p > 0.99) or 5 ms depolarising steps (487.1 ± 51.4 pA; WT vs. GFP: p = 0.46, **Figure 3.11C, D**).

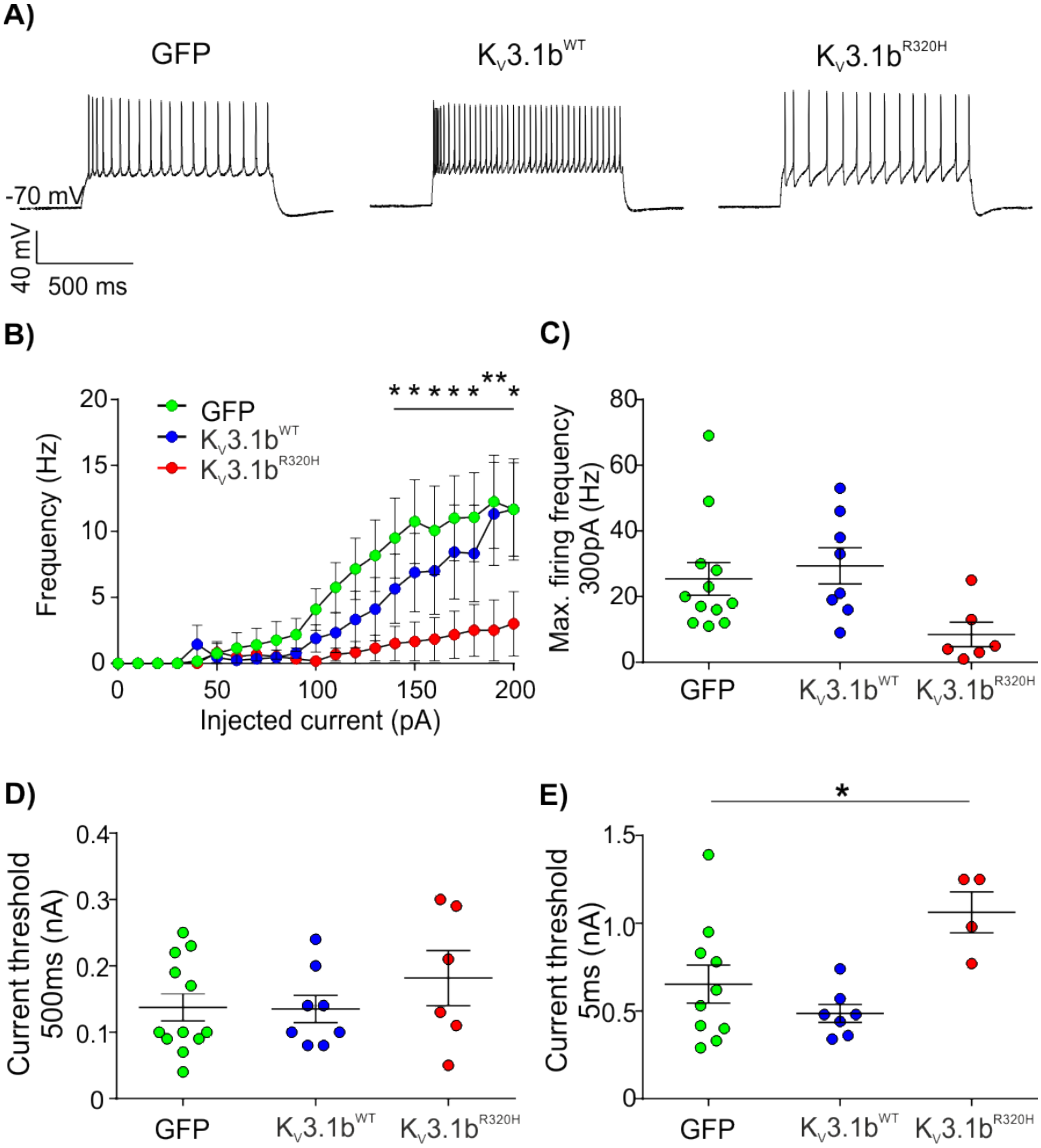

Figure 3.11. $K_V3.1b^{R320H}$ reduces interneuronal excitability. A) Representative current-clamp traces of interneuronal firing with 1 s, 300 pA current injection for neurons expressing GFP only, $K_V3.1b^{WT}$ or $K_V3.1b^{R320H}$ channels. **B)** The input-output relationship of interneurons expressing

K$_V$3.1^{WT}, K$_V$3.1^{R320H} or GFP only. Significant differences in firing frequency are observed with 140-200 pA current injection for K$_V$3.1b^{R320H} (GFP vs. R320H: 140 pA, *p = 0.030; 150 pA, *p = 0.011; 160 pA, *p = 0.024; 170pA, *p = 0.014; 180 pA, *p = 0.018; 190 pA, **p = 0.0061; 200 pA, *p = 0.017; Repeated measures Two-way ANOVA followed by Bonferroni's multiple comparisons test). There were no significant differences in the two curves between K$_V$3.1^{WT} and GFP. **B)** The current required to elicit the first action potential during 500 ms depolarising steps. **C)** The maximum firing frequency following injection of depolarising current steps up to a maximum current injection of 300 pA. **D)** The current threshold as determined using 5 ms current injection. Neurons expressing K$_V$3.1^{R320H} require significantly more current to elicit an AP compared to GFP control neurons (One-way ANOVA followed by Bonferroni's multiple comparisons test: R320H vs. GFP: *p = 0.04; WT vs. GFP: p = 0.46). All experiments were carried out at 32°C. Data are from three independent neuronal preparations and are shown as means ± s.e.m.

3.6.2 K$_V$3.1^{R320H} cannot support high frequency firing at high stimulation frequencies

K$_V$3.1 channels are involved in the rapid repolarisation of the AP and are important determinants of high frequency firing. Indeed, the ectopic expression of WT K$_V$3.1b channels in slow-spiking neurons *in vitro* has been shown to increase firing rates (Gu et al., 2012; 2018). I observed that mutant K$_V$3.1b channels decreased the excitability of cortical interneurons in culture (**Figure 3.11**) and resulted in an increased current threshold for AP initiation. I did not, however, observe a significant increase in the firing frequency of neurons expressing WT K$_V$3.1b channels upon increasing depolarising stimuli, as has been previously reported in the literature, suggesting that K$_V$3.1 channels are not the most important determinants of high frequency firing in cortical interneurons at 14 DIV (Gu et al., 2012). I therefore next investigated the effects of WT or mutant K$_V$3.1 channel expression on high frequency firing by stimulating neurons with 5 ms supra-threshold current pulses. In this protocol, the success of AP firing at high frequencies is highly dependent on the rapid repolarisation of the AP, i.e. K$_V$3 channels. Furthermore, by normalising for the current threshold, I am able to better assess the influence of the functional properties of mutant K$_V$3.1 channels on neuronal firing. I found that neurons overexpressing K$_V$3.1^{WT} had significantly higher AP success rates at 100 Hz (93.9 ± 4.4%, n = 9) compared to GFP control neurons (74.9 ± 8.5%, p = 0.038, n = 11, **Figure 3.12A**). Overexpression of K$_V$3.1b^{R320H}, on the other hand, had no effect on spike fidelity at 100 Hz (72.9 ± 8.1%, n = 7; p > 0.999). Thus, it appears that the K$^+$ currents generated by K$_V$3.1b^{R320H}, if indeed it is able to reach the cell surface membrane, are not sufficient to support high frequency firing.

Interestingly, I did not observe a dominant negative effect of mutant K$_V$3.1b channels on high frequency firing, as might have been predicted from biophysical studies that observed a dominant negative suppression of WT channel function (**Section 3.3.1**) (Munch et al., 2018; Muona et al., 2014; Oliver et al., 2017). In order to test whether this was due to cortical interneurons at 14 DIV lacking endogenous K$_V$3.1b channels, I immunolabelled neurons transduced with mDlx-GFP control lentiviruses for K$_V$3.1b. I found that interneurons, as identified by GFP fluorescence, were positive for K$_V$3.1b channel expression and thus appear to endogenously express K$_V$3.1b channels at this stage in culture (**Figure 3.12B**). As a positive control, I also immunolabelled interneurons overexpressing K$_V$3.1b^{WT}. I observed increased fluorescence signal intensity for the overexpression of K$_V$3.1b compared to neurons expressing GFP only, confirming that the K$_V$3.1b antibody is able to recognise the K$_V$3.1b antigen (**Figure 3.12B**). The reason why I do not observe a dominant negative effect of mutant K$_V$3.1b channel expression on high frequency firing, is therefore unlikely to be due to a lack of endogenous K$_V$3 channels. However, immunolabelling cultures prepared from K$_V$3.1 knockout mice for K$_V$3.1b represents an important negative control to confirm the specificity of the K$_V$3.1b antibody.

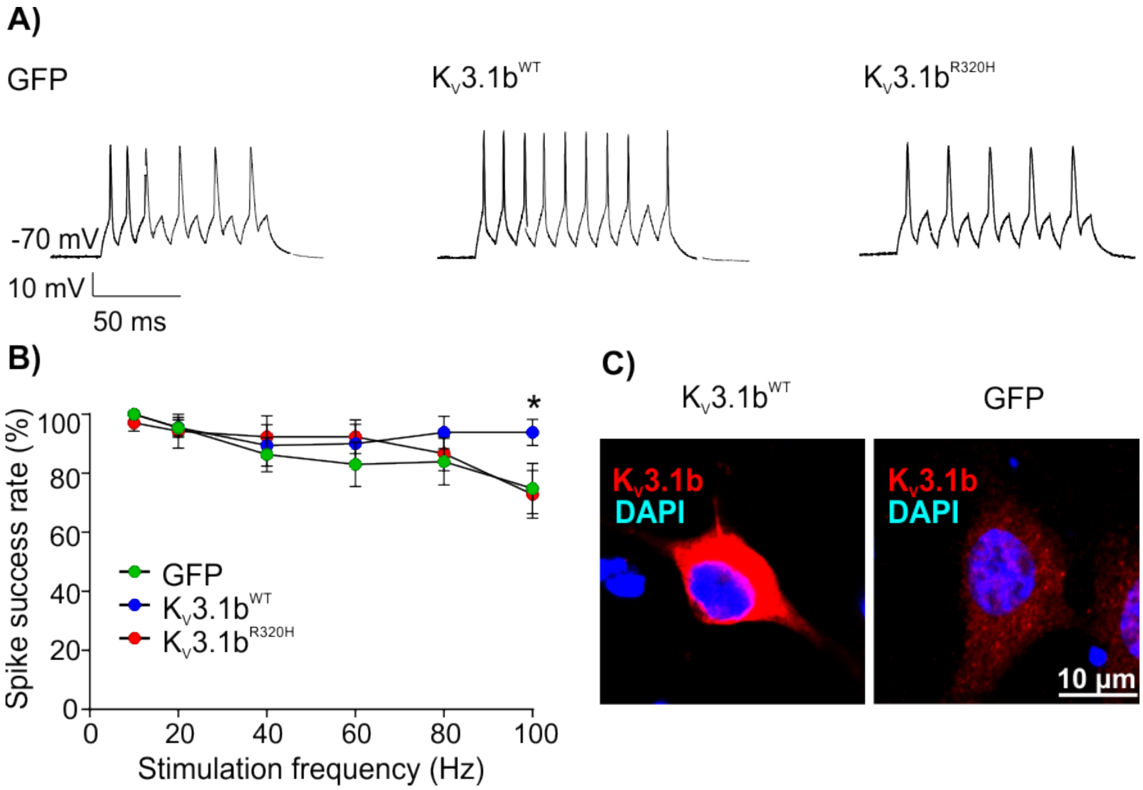

Figure 3.12. K$_V$3.1b^{R320H} cannot support high frequency firing of interneurons. A) Representative traces of interneuronal firing of cultured cortical neurons expressing GFP only, K$_V$3.1b^{WT} or K$_V$3.1b^{R320H} following suprathreshold current injection for 5 ms at a frequency of 100

Hz. **B)** Overexpression of $K_V3.1b^{WT}$ in cortical interneurons in culture increases spike fidelity at high stimulation frequencies, whereas overexpression of $K_V3.1b^{R320H}$ has no effect. A significant difference in spike success rate is observed for $K_V3.1b^{WT}$ compared to GFP control neurons at 100 Hz (*p = 0.038). No difference in spike success rate at 100 Hz for $K_V3.1b^{R320H}$ is observed compared to GFP controls (p > 0.999). Two-way ANOVA with Repeated Measures followed by Bonferroni's multiple comparison's test. **C)** Representative images of cultured cortical interneurons at 14 DIV immunolabelled for $K_V3.1b$. Left panel: strong immunofluorescence is observed with lentiviral-based overexpression of $K_V3.1b^{WT}$, confirming that the $K_V3.1b$ antibody (Alomone Labs) is able to detect its cognate antigen. Right panel: endogenous $K_V3.1b$ channel expression is observed in interneurons at 14 DIV transduced with mDlx-GFP lentivirus. In both cases, interneurons were identified by GFP fluorescence (channel not shown). Recordings were carried out at 32°C. Data are from three independent neuronal preparations and are shown as means ± s.e.m.

3.6.3 Expression of $K_V3.1b^{R320H}$ channels has no effect on the action potential waveform

$K_V3.1b$ channels support high frequency firing by facilitating the generation of narrow APs with a deep, but limited, AHP (Rudy & McBain, 2001). I wished to confirm that the increase in high frequency firing that I observed upon expression of $K_V3.1b^{WT}$ channels corresponded with facilitatory changes in the AP waveform (and that expression of $K_V3.1^{R320H}$ had no effect on the AP waveform). To do this I analysed the properties of the first AP fired during iterative rounds of 500 ms depolarizing steps (**Figure 3.13A**). As was expected, overexpression of $K_V3.1b^{WT}$ was found to result in a significantly faster rate of AP repolarization (-101.90 ± 17.19 V s^{-1}, n = 8) with respect to control neurons (-54.42 ± 5.49 V s^{-1}, n = 12; p = 0.005, **Figure 3.13B**) as well as a significantly smaller AP half-width (WT: 0.70 ± 0.08 ms; GFP: 1.31 ± 0.11 ms; p = 0.004, **Figure 3.13C**). Surprisingly, there were no significant differences in AHP amplitude for $K_V3.1b^{WT}$ expression (WT: -14.51 ± 2.18 mV; GFP: -11.6 ± 2.02 mV; p = 0.566, **Figure 3.13D**). Overexpression of $K_V3.1b^{R320H}$, on the other hand, had no effect on the rate of AP repolarization (-51.37 ± 6.80 V s^{-1}, p = 0.226, n = 6), half-width (1.62 ± 0.22 ms, p > 0.99) or AHP (-13.28 ± 3.2 mV, p = 0.847) compared to GFP control neurons, findings in line with the inability of the mutant channel to support neuronal firing at high stimulation frequencies compared to overexpression of the WT channel (**Figure 3.12**). Overexpression of $K_V3.1b^{WT}$ and $K_V3.1b^{R320H}$ channels had no effect on passive properties or the AP voltage threshold, rising slope or amplitude (**Table 3.1**).

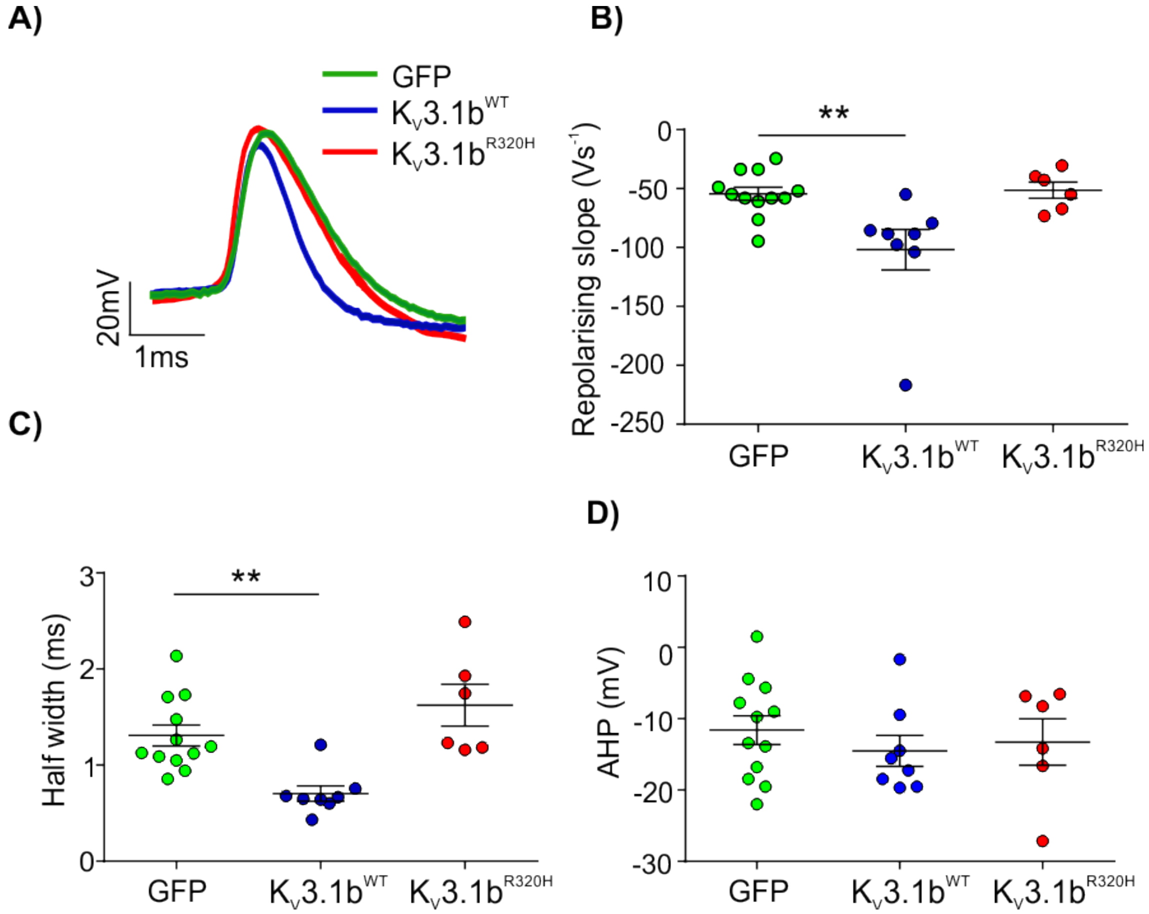

Figure 3.13. Kv3.1b^{R320H} does not alter the properties of the single AP. A) Representative AP waveforms of interneurons at 14-16 DIV expressing GFP, Kv3.1b^{WT} or Kv3.1b^{R320H}. APs were aligned by superimposing their rising slopes. **B-D)** Comparisons of the effects of Kv3.1b expression on single AP properties. **B-C)** Overexpression of Kv3.1b^{WT} results in a significant reduction in AP half-width (**p = 0.004) and the rate of AP repolarisation (**p = 0.005) when compared to GFP control neurons. Kv3.1b^{R320H} has no effect on the AP half-width ($p > 0.99$) and rate of repolarisation (p = 0.226) with respect to GFP. **D)** Neither expression of Kv3.1b^{WT} (p = 0.566) or Kv3.1b^{R320H} (p = 0.847) has a significant effect on the amplitude of the AHP compared to GFP neurons. All comparisons performed using One-way ANOVA with Bonferroni's multiple comparisons test. Data are from three independent neuronal preparations and are shown as means ± s.e.m.

Table 3.1. Active and passive properties of neurons expressing $K_V3.1b$ channels

Properties	**GFP (n = 12)**	**WT (n = 8)**	**R320H (n = 6)**
Resting membrane potential (mV)	-60.2 ± 2.1	-54.5 ± 1.6	-58.0 ± 5.7
Input Resistance (MΩ)	301.0 ± 53.3	241.1 ± 29.5	329.3 ± 118.5
Capacitance (pF)	135.2 ± 22.4	101.7 ± 18.4	111.3 ± 15.1
Threshold (mV)	-38.7 ± 2.3	-39.8 ± 1.5	-32.7 ± 5.1
AP Peak (mV)	53.8 ± 4.4	55.3 ± 3.7	65.6 ± 7.5
Max. Rising slope (V s^{-1})	151.5 ± 18.0	194.5 ± 17.4	191.2 ± 44.6
AP half-width (ms)	1.3 ± 0.1	0.7 ± 0.1**	1.6 ± 0.2
Max. repolarizing slope (V s^{-1})	-54.4 ± 5.5	-101.9 ± 17.2**	-51.4 ± 6.8
AHP (mV)	-11.6 ± 2.0	-14.5 ± 2.2	-13.3 ± 3.2
Current threshold (pA) (5ms stimulus)	653.7 ± 108.1 (n = 10)	487.1 ± 51.4 (n = 7)	1063 ± 116.4* (n = 4)

All data are presented as means ± s.e.m. $*p < 0.01$; $**p < 0.001$. Comparisons made vs. GFP using One-Way ANOVA followed by Bonferroni's multiple comparisons test.

3.7 Characterising the effects of $K_V3.1b^{R320H}$ channels in parvalbumin-positive interneurons in culture

3.7.1 An optogenetic approach for studying effects of $K_V3.1b^{R320H}$ on PV interneuron physiology

Despite a dominant negative effect of $K_V3.1b^{R320H}$ mutant channels on WT $K_V3.1b$ channel function having been implied by biophysical studies, I did not observe a dominant negative effect of $K_V3.1b^{R320H}$ channel expression on high frequency firing. This raised the question of the extent to which the interneurons that I was recording from at 14-16 DIV were limited in firing rate by factors other than the rate of action potential repolarization, which is thought to be the mechanism that allows neurons expressing Kv3 channels to sustain high frequency firing. Indeed, the overexpression of WT $K_V3.1b$ channels did not increase rates of interneuronal firing upon increasing depolarisation with respect to GFP control neurons. This suggested that the neurons I was recording from did not express a full complement of voltage-gated ion channels that would facilitate high frequency firing. For example, if the firing rate was limited by the size of the sodium channel population, faster repolarisation may not be sufficient to support recovery of enough voltage-gated sodium channels to allow for the generation of more action potentials.

In vivo, $K_V3.1b$ is highly expressed in fast-spiking PV^+ interneurons. The fast-firing phenotypes of PV^+ interneurons are determined by a ‘supercritical’ density of sodium channels in the axon as well as the combinatorial expression of other selected voltage-gated ion channels that contribute towards high frequency firing, especially $K_V3.1b$ (Hu et al., 2014; Saunders et al., 2018; Toledo-Rodriguez et al., 2004). Therefore, I hypothesised that I might reveal potential dominant negative effects of $K_V3.1b^{R320H}$ channels on high frequency firing by expressing these channels in PV^+ interneurons. Furthermore, $K_V3.1b$ has also been shown to be important for action potential repolarization at presynaptic terminals and the regulation of neurotransmitter release (Goldberg, 2005). Again, it would be pertinent to study the effects of mutant $K_V3.1b$ channels on synaptic transmission in PV^+ interneurons because PV synapses are highly specialized for high frequency, high fidelity neurotransmission (Hu et al., 2014).

3.7.1.1 Isolating the presynaptic effects of mutant $K_V3.1b$ channels in genetically defined cell types using optogenetics

Synaptic transmission can be studied using traditional electrophysiological methods, such as extracellular stimulation. However, extracellular stimulation non-specifically depolarises axons/terminals arising from different neuronal subtypes. An alternative method to study synaptic transmission is between predefined neuronal pairs using paired-patch recordings. In this recording configuration, the presynaptic cell is stimulated via current injection into the soma whilst post-synaptic responses are simultaneously recorded using whole-cell voltage-clamp. However, paired recordings are labour intensive and relatively low throughput.

To address the effects of $K_V3.1b^{R320H}$ channels on AP repolarisation in fast-spiking neurons and to isolate the effects of mutant $K_V3.1b$ channels on presynaptic function, I instead designed an optogenetic approach to allow for the selective stimulation of PV^+ interneurons that are transgenically overexpressing mutant $K_V3.1b$ channels (**Figure 3.14**). Optogenetics facilitates the non-invasive stimulation of genetically defined neurons and only requires electrical recording from a post-synaptic neuron. For this reason, optogenetics has been used with great success to interrogate neuronal connections both *in vitro* and *in vivo*. In this subchapter, I have used an optogenetic approach to complement and replicate some of our previous whole-cell electrophysiology data for $K_V3.1b^{R320H}$.

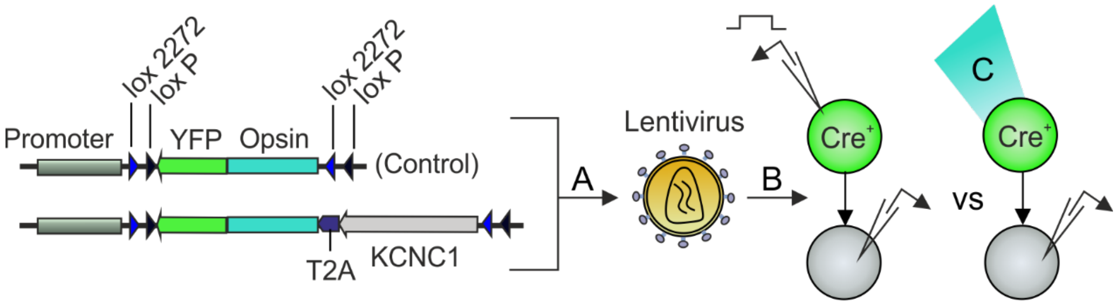

Figure 3.14. An optogenetic strategy for the isolation of the presynaptic effects of $K_V3.1b$ channels. A) A Cre-dependent expression cassette comprised of WT or mutant *KCNC1* transgenes and an opsin fused to fluorescent reporter is packaged into a lentivirus. **B)** Lentiviral infection of cortical neuronal cultures derived from PV^{CRE}/SST^{CRE} -driver mouse lines. **C)** Optical stimulation of transduced neurons (YFP^+) allows for the selective activation of genetically defined cell-types co-expressing (mutant) $K_V3.1b$ channels. Simultaneous electrophysiological recording from monosynaptically connected, non-transduced neurons allows for the pre-synaptic effect of the mutation to be isolated.

3.7.2 The Cre-lox genetic system can be used to effectively target opsin expression to PV^+ interneurons

Previously in this chapter I successfully targeted the expression of mutant $K_V3.1b$ channels to interneurons using the mDlx promoter element (**Section 3.4**). However, targeting of specific interneuronal sub-types, such as PV^+ interneurons, via short promoter sequences, remains ineffective (Callaway *et al.,* 2009; Mantoan Ritter *et al.,* 2016). Instead, I decided to exploit the **fl**ip-**ex**cision (FLEx) genetic switch system to achieve cell-type specific expression of opsin and *KCNC1* transgenes (Atasoy *et al.,* 2008; Schnütgen *et al.*, 2003). This system allows gene expression to be turned 'on' or 'off' in genetically defined neuronal cell types expressing Cre recombinase from cell-type specific promoters, following a DNA inversion event. The FLEx switch system has advantages over simple Lox-stop systems in that the coding sequence of the transgene is present in the inverse orientation, preventing 'leaky' expression of 'flexed' transgenes in Cre-negative cells.

I chose to use the opsin, ‘ChIEF’, a chimera of ChR1 and ChR2, in these experiments because ChIEF has been shown to be superior to ChR2 in its ability to drive high frequency spiking of both excitatory and inhibitory neurons and has also been used successfully in experiments aimed at investigating synaptic transmission and plasticity (Lin et al., 2009; Ben-Simon et al., 2015; Mattis et al., 2012). ChIEF has also been shown to be highly expressed by neurons in culture (Mattis et al., 2012). This is important because high levels of opsin expression is critically required in optogenetic experiments because light-evoked spiking is a function of the size and kinetics of the photocurrent (Packer et al., 2013).

The FLEx switch system also has the advantage of allowing highly specific transgene expression to be driven indirectly by strong, constitutive promoter sequences. I chose to use the mouse phosphoglycerate kinase (PGK) promoter in the first instance because it is a strong, ubiquitous promoter that could be expected to drive opsin expression to levels that would support high frequency firing (Li et al., 2010; Qin et al., 2010). However, I observed neuronal toxicity as a result of high levels of ChIEF expression, a ‘side-effect’ that has been previously documented for ChIEF due to its particularly efficient trafficking to the membrane (**Figure 3.15A**) (Mattis et al., 2011). I therefore chose to instead use the weaker human Synapsin (hSyn) promoter for our optogenetic experiments. I confirmed the specificity of our Cre-responsive targeting cassette by infecting cortical neuronal cultures derived from PV^{Cre}-tdTomato mice with lentiviruses synthesised using the Flex-ChiEFmCitrine control construct. These mice express Cre recombinase under the control of the PV promoter as well as having a lox-stop allele which results in the expression of the tdTomato reporter protein only in cells expressing Cre recombinase. I observed co-localisation of tdTomato and mCitrine fluorescence and therefore confirmed opsin expression to be specific to PV cells, although these cells were rare in cultures (**Figure 3.15B**).

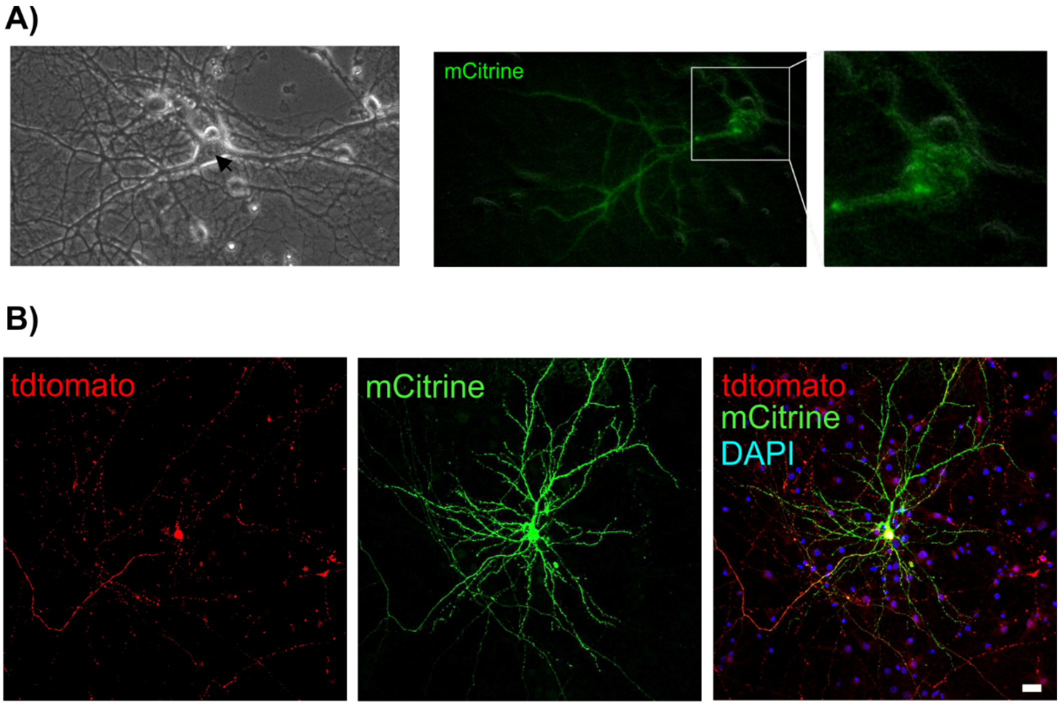

Figure 3.15. ChiEFmCitrine expression is specific to PV⁺ interneurons. A) Expression of ChIEF using the PGK promoter results in neuronal toxicity. Differential interference contrast image of a PV⁺ interneuron expressing ChIEF under the control of the PGK promoter. Note the prominent nucleus, as indicated by the arrow, as a sign of poor neuronal health. Right panel: fluorescent image of the same neuron suggestive of aggregation of opsin (tagged with mCitrine). **B)** ChIEF is effectively targeted to PV⁺ interneurons using the Cre-lox genetic system. Cortical neuronal cultures were prepared from PV^{Cre}:tdTomato mice and transduced with Flex-ChIEFmCitrine lentivirus at DIV 1. An immunocytochemical investigation of mCitrine and tdTomato fluorescence was performed at 21 DIV. The signal from mCitrine was amplified using an antibody against GFP. Scale bar is 20 µm.

3.7.3 ChIEF, is able to drive high frequency firing of PV⁺ interneurons

3.7.3.1 ChIEF can drive firing of PV⁺ interneurons up to 100 Hz

I next wanted to investigate whether our optogenetic vectors were able to drive the expression of ChIEF to high enough levels to direct the high frequency firing of PV⁺ interneurons. I performed whole-cell current clamp recordings of PV⁺ interneurons in cortical cultures prepared from PV^{Cre} mice that had been transduced with the control lentivirus, pCCL-FLEx-ChIEF (mCitrine-positive), and found that ChIEF driven by the hSyn promoter was able to direct high frequency firing of PV⁺ interneurons of up to 100 Hz when stimulated with 1 ms pulses of light of 470 nm (**Figure 3.16**).

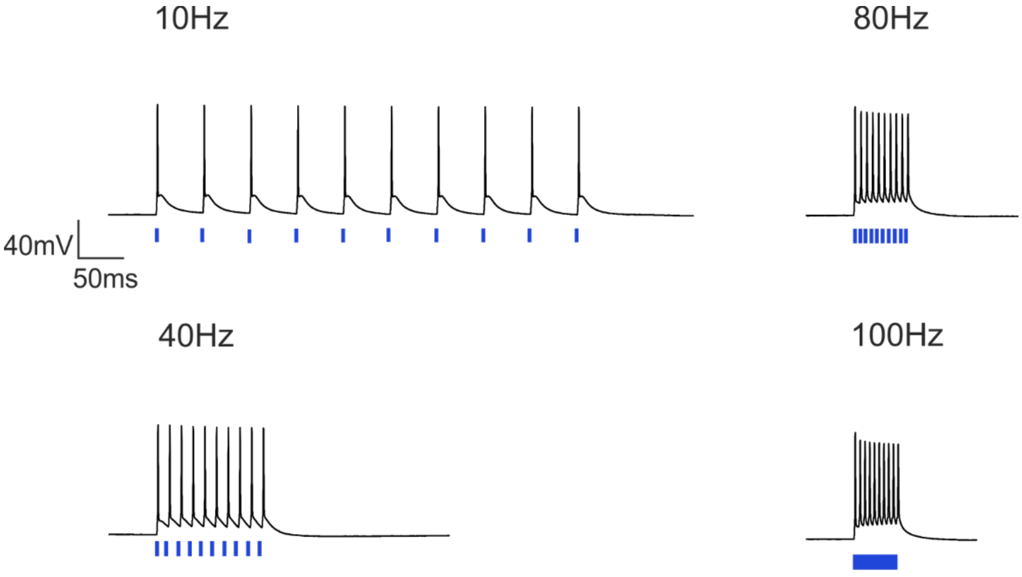

Figure 3.16. High frequency optogenetic stimulation of a PV$^+$ interneuron. Representative whole-cell current-clamp recordings of action potentials elicited by 10X 1 ms light pulses at 470 nm, at 10-100 Hz for a PV$^+$ interneuron expressing ChIEF, at 21 DIV.

3.7.3.2 High fidelity optical stimulation of PV-principle cell synaptic pairs

I next wished to demonstrate that synaptic responses could be evoked by optical stimulation of transduced neurons. I traced fluorescent axons to post-synaptic cells in order to identify synaptically connected neuronal pairs. Using whole-cell voltage-clamp of a non-transduced (not fluorescent) post-synaptic neuron, I demonstrated that robust inhibitory post-synaptic currents (IPSCs) could be recorded following optical stimulation of PV$^+$ interneurons transduced with pCCL-FLEx-ChIEF lentivirus (mCitrine$^+$) with 1 ms pulses of light (**Figure 3.17A**). It is clear, however, when one considers the magnitude of post-synaptic currents elicited by optical stimulation (**Figure 3.17A & B**), that the wide-field (40X objective) illumination of the culture results in the recruitment of multiple transduced interneurons, such that the post-synaptic currents recorded must correspond to population IPSCs rather than unitary IPSCs.

I next used different presynaptic stimulation paradigms to explore optically evoked short-term plasticity (STP) at PV$^+$ synapses. I found that postsynaptic responses depressed, but then remained stable, throughout trains of stimuli at 10, 20 and 40 Hz and that synaptic depression was most pronounced at higher frequencies (**Figure 3.17A**). This phenomenon may be attributed to rapid depletion of the readily releasable pool during high frequency stimulation. I also investigated STP at these synapses using paired-pulse stimulation, a widely used method of investigating initial release probability (pr) (Zucker & Regehr, 2002). PV cell synapses are known to have a high initial release probability and are therefore typically depressing. Indeed, I observed a greater depression of post-synaptic responses during shorter inter-stimulus intervals compared to longer-interstimulus intervals (**Figure 3.17B**).

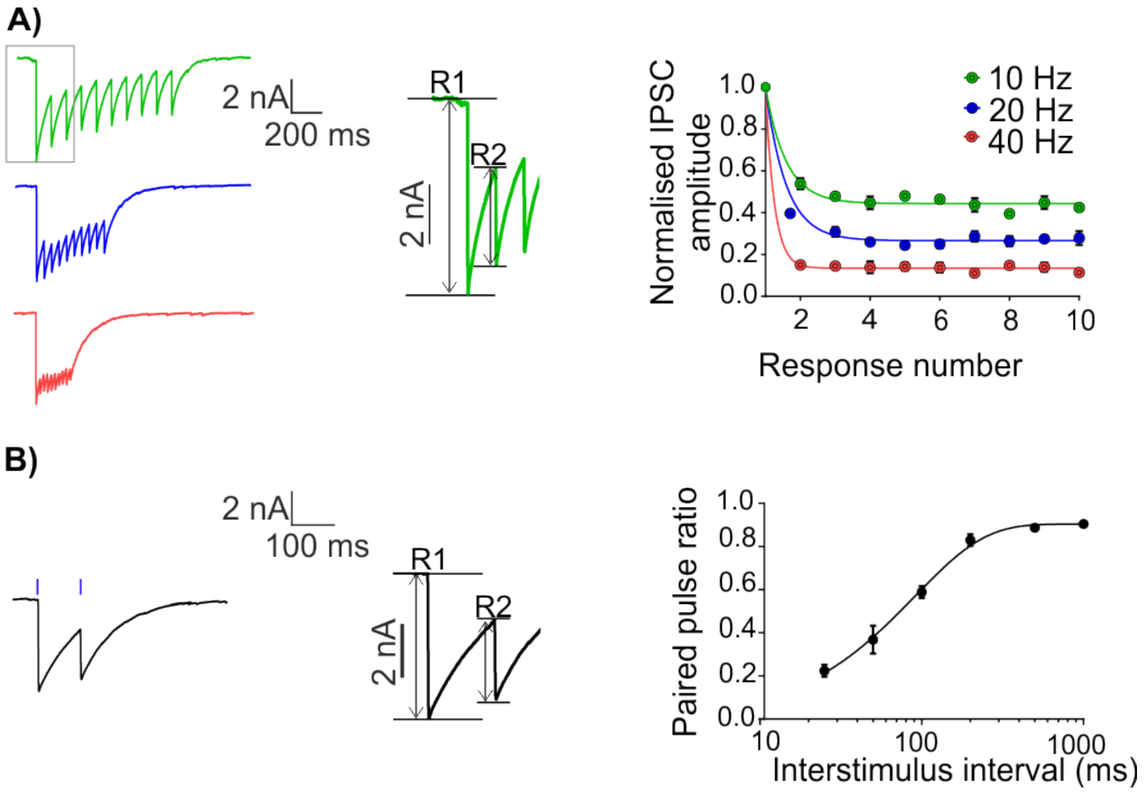

Figure 3.17. Post-synaptic responses of an excitatory neuron following optical stimulation of PV$^+$ interneurons. A) Depression of optically evoked post-synaptic responses resulting from the optical stimulation of transduced PV$^+$ interneurons at different frequencies. Inset: the method used to measure the amplitude of each response during trains of stimulation. The amplitude of each response in the train is normalised to the amplitude of the first response (R1) that is measured from the baseline current. R2: response 2. **B)** Paired-pulse depression of optically stimulated PV$^+$ synapses. Inset: the method used to measure the amplitude of post-synaptic responses during paired-pulse protocols. The amplitude of R2 was normalised to that of R1 to obtain the paired-pulse ratio. Neurons in A & B were stimulated with 1 ms pulses of light at 470 nm. Data was fit with a single-phase association curve. Data are represented as means ± s.e.m. Error bars correspond to the error of three trials recorded from the same post-synaptic cell.

3.7.4 Optically evoked synaptic responses can be recorded at SST-principle cell synapses

I chose to perform further preliminary characterisation of the optogenetic approach using cultures derived from SST^{Cre} mice, for which many more fluorescent neurons could be detected in cultures following transduction with control lentiviruses (FLEx-ChIEF). The

IPSCs previously recorded at PV$^+$-principle cell synapses (**Figure 3.17**) were very large - on the order of 7 nA – in part because they were recorded using a KCl based internal solution, used in anticipation of very small IPSC amplitudes when holding the cell at -70mV, close to the Cl$^-$ reversal potential. In order to prevent series resistance errors in the recording of optically evoked IPSCs, I therefore switched to a potassium gluconate based recording solution. Using this internal solution, I recorded currents on the order of ~100 pA at SST$^+$-principle cell synapses, when holding the cell at -60 mV (**Figure 3.18**). I found SST synapses also depressed during trains of high frequency stimulation (n = 4, **Figure 3.18A, B**) and paired-pulse protocols (n = 4, **Figure 3.18C**), where 'n' corresponds to a single post-synaptic neuron. Importantly, I demonstrated high fidelity optical stimulation of presynaptic SST$^+$ interneurons at frequencies up to 60 Hz, which was documented by robust, discrete post-synaptic responses.

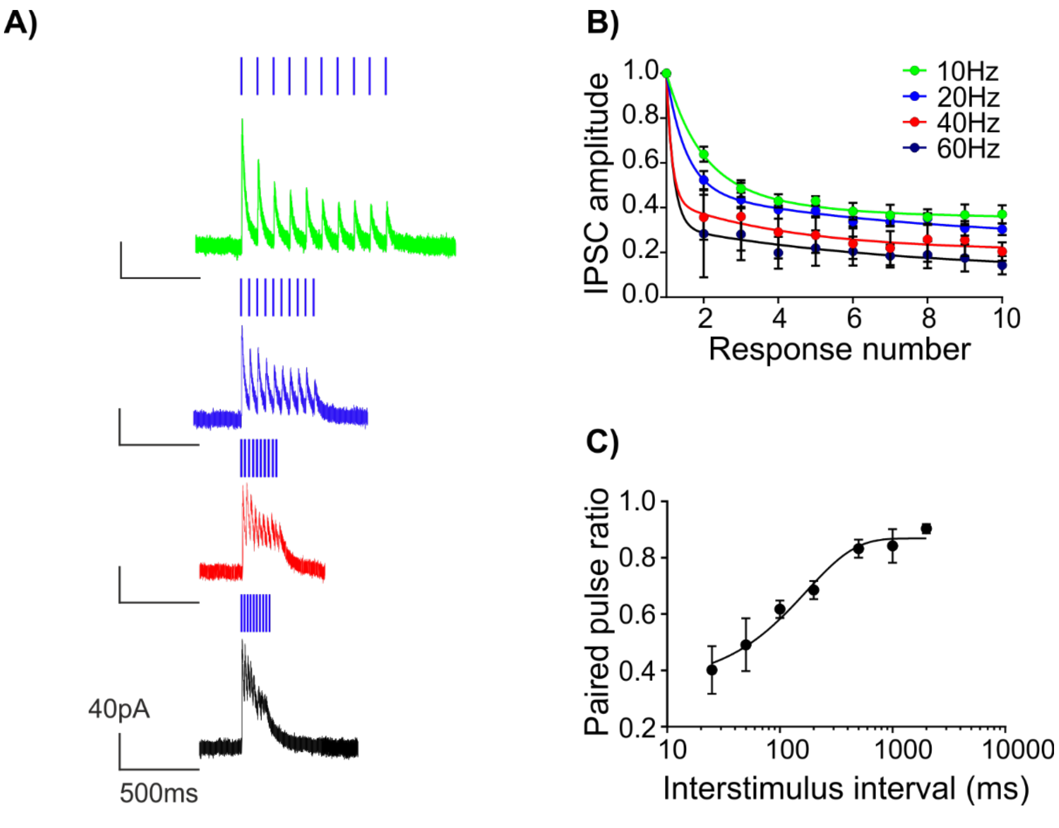

Figure 3.18. Post-synaptic responses of individual excitatory neurons following the optical stimulation of SST$^+$ interneurons. A) Representative whole-cell voltage-clamp recordings of IPSCs evoked by the wide-field optical stimulation of SST neurons at different frequencies. **B)** Post-synaptic responses to optical stimulation depress with increasing frequency of stimulation. SST neurons were stimulated with 10X 1 ms pulses of light at 470 nm. **C)** SST synapses exhibit short-term synaptic depression when post-synaptic responses are recorded from excitatory neurons. The paired-pulse ratio was calculated at different interstimulus intervals and plotted on a semi-logarithmic scale. Data was fit by a single-phase association curve. Post-synaptic

recordings were obtained from 4 excitatory neurons, across 3 coverslips from one neuronal preparation. Data are shown as means ± s.e.m.

3.7.5 Increasing the representation of PV^+ interneurons in cortical neuronal cultures

The Cre-dependent expression of ChiEF, and therefore the labelling of PV cells with mCitrine, is dependent upon the activity of the endogenous PV promoter. *In vivo,* cortical interneurons begin to express parvalbumin during the second postnatal week, with expression doubling between 14-21 postnatal days (Mukhopadhyay et al., 2009). *In vitro*, the PV promoter follows a temporal pattern of activation resembling that which occurs *in vivo*. However, despite waiting 21 DIV to perform our optogenetic experiments, I consistently, found PV cells to be rare in cultures derived from PV^{Cre} mice. In cortical cultures derived from SST^{Cre} mice, on the other hand, I was able to detect many fluorescent neurons at 21 DIV (and as early as 14 DIV) when controlling for differing rates of lentiviral transduction. The higher proportion of SST^+ interneurons in cortical cultures compared to PV^+ interneurons does not reflect the situation *in vivo,* where PV interneurons account for ~40% of all GABAergic interneurons and SST cells for ~30% (Rudy, Fishell, Lee, & Hjerling-Leffler, 2011).

I was concerned about our ability to generate enough data with so few PV neurons present in culture and so I sought a way to increase the representation of PV cells *in vitro*. The fate specification of interneuron precursors into SST or PV cells is thought to be due to the differential expression of genes within the medial ganglionic eminence (MGE), but also due to developmental cues received following the tangential migration of these precursors to the cortex (Mukhopadhyay et al., 2009). Previously, it has been shown that bone morphogenic protein 4 (BMP4) can promote the differentiation of a subset of interneuron precursors into PV cells, with a concomitant reduction in the number of SST cells, *in vivo* and *in vitro* (**Figure 3.19A**) (Mukhopadhyay et al., 2009). I thus treated cortical neuronal cultures from PV^{Cre}:tdTomato mice of different developmental ages (p0-p2) with 20 ng mL^{-1} of BMP4 for 4 DIV and assayed the number of $tdTomato^+$ neurons at 21 DIV. I found that BMP4 dramatically increased the number of PV cells in cultures prepared from p1 and p2 mice, and to a lesser extent in cultures derived from p0 mice (**Figure 3.19B**). I therefore found that I could increase the number of PV cells in culture in future experiments by using cortices from p1-2 neonates and supplementation of cultures with BMP4.

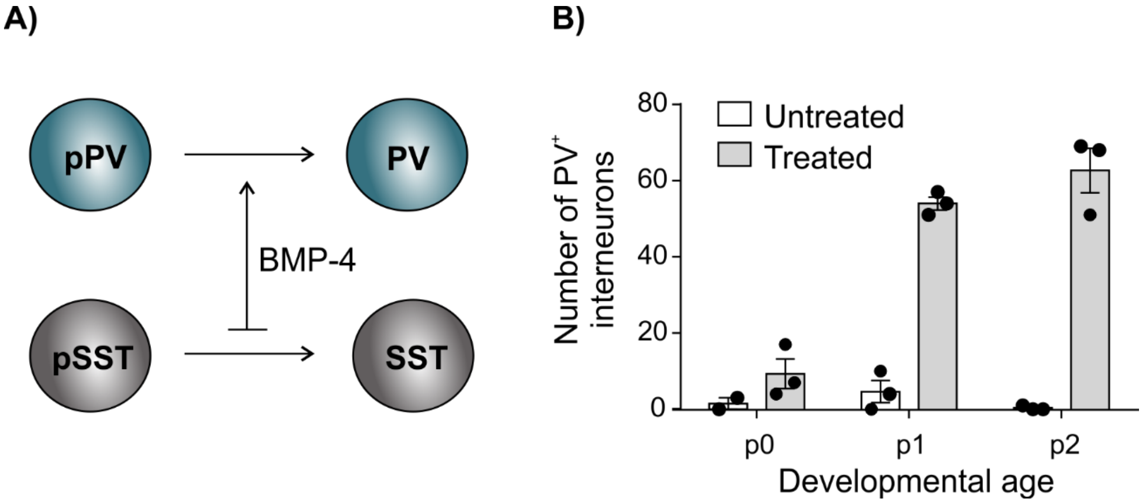

Figure 3.19. BMP-4 promotes the differentiation of PV+ interneurons. A) *In vivo* and *in vitro*, BMP-4 promotes the differentiation of PV progenitors (pPV) into PV$^+$ interneurons and inhibits the differentiation of SST progenitors (pSST) into SST$^+$ interneurons. **B)** BMP-4 increases the number of PV$^+$ interneurons in cortical neuronal culture. Primary cortical neuronal cultures were prepared from PV^{Cre}:tdTomato mice at different developmental ages (p0-p2) and seeded at a density of 120,000 cells/ coverslip. Cultures were treated with 20 ng mL^{-1} BMP-4 one hour after plating for 4 DIV. Neurons were fixed and imaged at 21 DIV and PV$^+$ interneurons were identified by native tdTomato fluorescence. Each data point, ‘n’, is the average number of cells from 3 coverslips that were treated separately, from one neuronal preparation. Data are presented as means ± s.e.m.

3.7.6 Co-expression of $K_V3.1$ and ChIEF results in sub-threshold optical responses

Having demonstrated that I could effectively stimulate PV$^+$ or SST$^+$ interneurons and record optically evoked IPSCs via the lentiviral delivery of the optogenetic actuator, ChIEF, I next wished to use this method to investigate the effects of $K_V3.1^{R320H}$ mutant channels on presynaptic function. I generated bicistronic lentiviral vectors for the co-expression of $K_V3.1$b channels and ChiEF and tested their functionality in primary cortical neuronal cultures using a Multiplicity of Infection (MOI, or number of viral particles per cell) of 1-10. However, I was unable to find fluorescent, transduced neurons in SST^{CRE} or PV^{CRE} cultures for lentiviruses expressing either $K_V3.1$ channel variant.

I therefore decided to outsource the production of these viruses, in case of issues with lentiviral synthesis in-house. I tested the efficacy of these viruses in cortical cultures derived from CAMKII^{CRE} mice because these mice drive opsin expression in excitatory neurons, which represent ~80% of all cells in culture, thus allowing for better estimates of lentiviral functionality. However, even with the commercially synthesised lentiviruses, it was extremely difficult to detect fluorescent neurons, live in our electrophysiology set-up. Furthermore, when I performed an immunocytochemical assay for mCitrine at 21

DIV, in order to amplify any low-level signal, I observed very low rates of viral transduction for lentiviruses expressing $K_V3.1$ channels (**Figure 3.20A**). The rates of lentiviral transduction varied considerably for the different lentiviral vectors. The FLEx-ChIEF control virus had a high rate of neuronal transduction, as evidenced by a high number of fluorescent neurons and the presence of many fluorescent processes, visible at 20X magnification, derived from fluorescent neurons outside of the field of view (**Figure 3.20B**). Comparatively, I saw far fewer fluorescent neurons for FLEx-$K_V3.1^{WT}$ lentiviruses (**Figure 3.20B**), and far fewer still for FLEx-$K_V3.1^{R320H}$ viruses, where fluorescent neurons could not be detected at a 20X magnification. The levels of mCitrine expression (and therefore ChiEF) were also much lower for lentiviruses co-expressing $K_V3.1$ channels. As a result, I was only ever able to generate small (~5 mV) sub-threshold optical depolarisations for lentiviruses expressing FLEx-$K_V3.1^{WT}$ (**Figure 3.20C**). I was unable to observe even small optical depolarisations in neurons transduced with FLEx-$K_V3.1^{R320H}$.

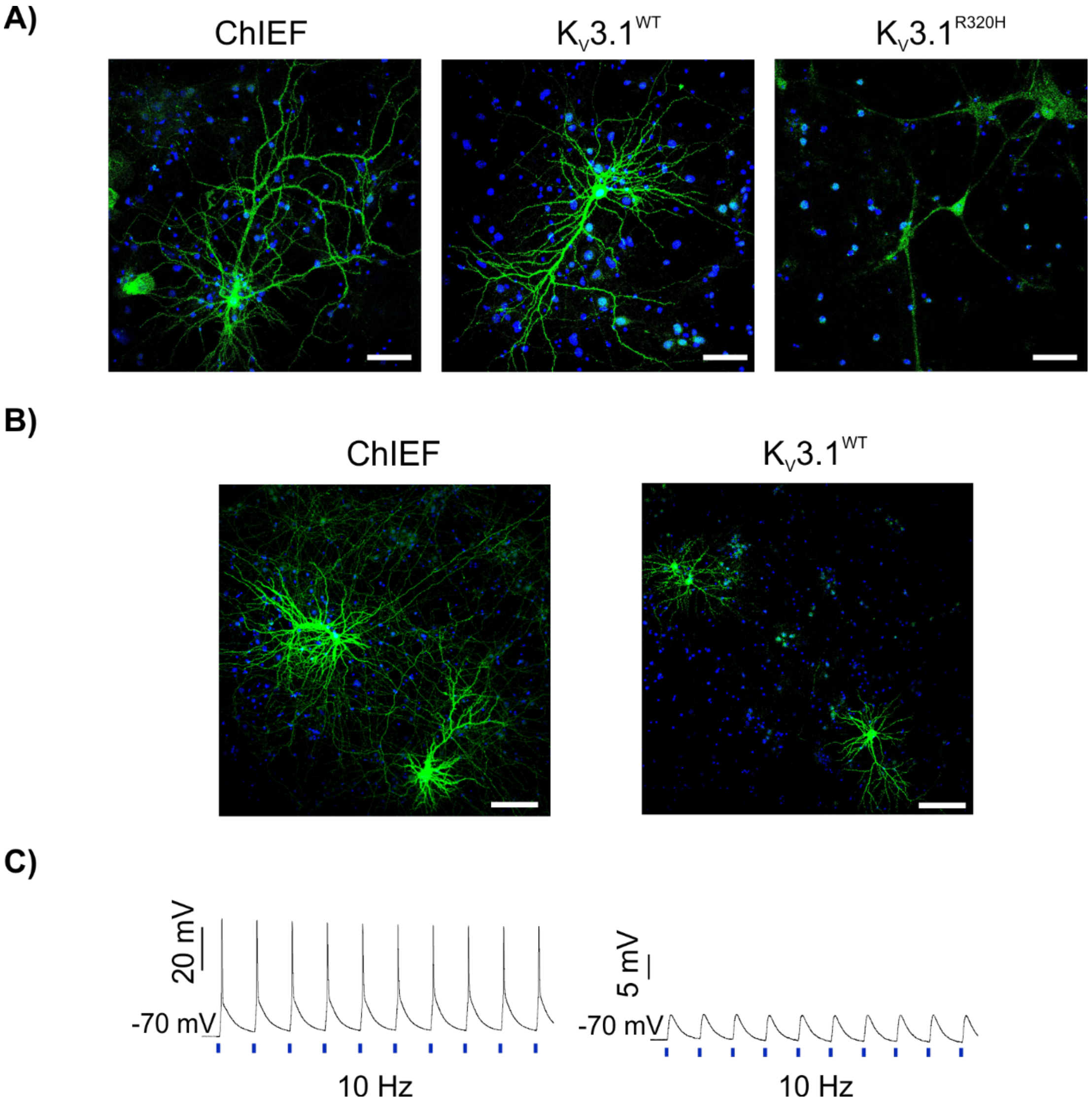

Figure 3.20. Immunofluorescent characterisation of optogenetic viral vectors in CAMKII^{CRE} neurons. A) Representative fluorescent images of neurons transduced with FLEx-ChIEF lentivirus (Control), FLEx-CHIEF-T2A-Kv3.1b^{WT} (WT) or FLEx-ChIEF-T2A-Kv3.1b^{R320H} (R320H) lentiviruses. Cortical neuronal cultures were prepared from p0 CAMKII^{Cre} mice and transduced with lentiviruses at DIV 1. mCitrine fluorescence was amplified using an antibody against GFP and analysed at DIV 21. Fluorescent neurons were difficult to find and visibly shrunken for cultures transduced with ChIEF-T2A-Kv3.1b^{R320H}. Scale bar is 50 µm. **B)** Representative images of transduced neurons at X20 magnification. The transduction efficiency of FLEx-ChIEF is much higher than for FLEx-ChIEF-T2A-Kv3.1b^{WT}, as evidenced by the large number of fluorescent processes derived from transduced neurons outside of the field of view. Neurons transduced with FLEx-ChIEF-T2A-Kv3.1b^{R320H} could not be detected at a 20X magnification. Scale bar is 100 µm. **C)** Co-expression of Kv3.1b with ChIEF results in reduced photoresponses. Representative current-clamp traces following the optical stimulation of lentivirally transduced neurons. When ChIEF is expressed in isolation, optical stimulation of transduced neurons results in optogenetic action potentials. Co-expression with Kv3.1b, however, results in sub-threshold depolarisations.

3.7.7 $K_V3.1^{R320H}$ cannot support PV^+ interneuronal firing at high stimulation frequencies

One of my original aims was to develop a method whereby I could selectively stimulate PV^+ or SST^+ interneurons expressing $K_V3.1b$ channels *in vitro* in order to investigate the effect of $K_V3.1b^{R320H}$ channels on presynaptic function. However, the low levels of CHIEF-mCitrine expression for lentiviruses co-expressing $K_V3.1b$ channels meant that I was unable to detect or stimulate these neurons, which also precluded the recording neuronal pairs. I instead focused on addressing our second aim, which was to try to replicate our previous findings for the effects of $K_V3.1b^{R320H}$ expression on high frequency firing in PV^+ interneurons.

3.7.7.1 High degree of mCitrine fluorescence co-localisation with PV^+ interneurons in cortical cultures treated with BMP-4

As I was unable to detect live mCitrine fluorescence for lentiviral vectors co-expressing $K_V3.1$ channels, I decided to use cortical cultures derived from PV^{Cre}:tdTomato reporter mice in order to detect PV interneurons *in vitro*. Ai9 (tdTomato) reporter mice carry a loxP-STOP cassette that results in the selective expression of tdTomato in PV^+ interneurons when these mice are crossed with PV^{Cre} driver lines. However, I still anticipated problems associated with the apparently low transduction efficiency of lentiviruses co-expressing $K_V3.1$ channels, as was previously observed for $CAMKII^{Cre}$ cultures (**Figure 3.20**). I had previously observed that incubation of cortical cultures with BMP4 for the first 4 DIV after plating increased the proportion PV^+ neurons at 21 DIV and wondered whether the indirect stimulation of the parvalbumin promoter via BMP4 signalling may also result in the upregulation of Cre recombinase and enhanced expression of lentivirally delivered, Cre-responsive transgenes. In order to test this hypothesis, I transduced cortical cultures derived from p1-2 PV^{CRE} mice with FLEx-ChIEF-$K_V3.1b^{R320H}$ at DIV 1 and treated them with BMP4 until DIV 4. At DIV 21, I performed an immunocytochemical assay for mCitrine and PV and remarkably found mCitrine fluorescence to highly co-localise with PV (**Figure 3.21**). The use of cortical cultures derived from PV^{Cre}:tdTomato mice and treated with BMP4, thus represented a viable strategy with which to identify neurons transgenically expressing $K_V3.1b$ channels.

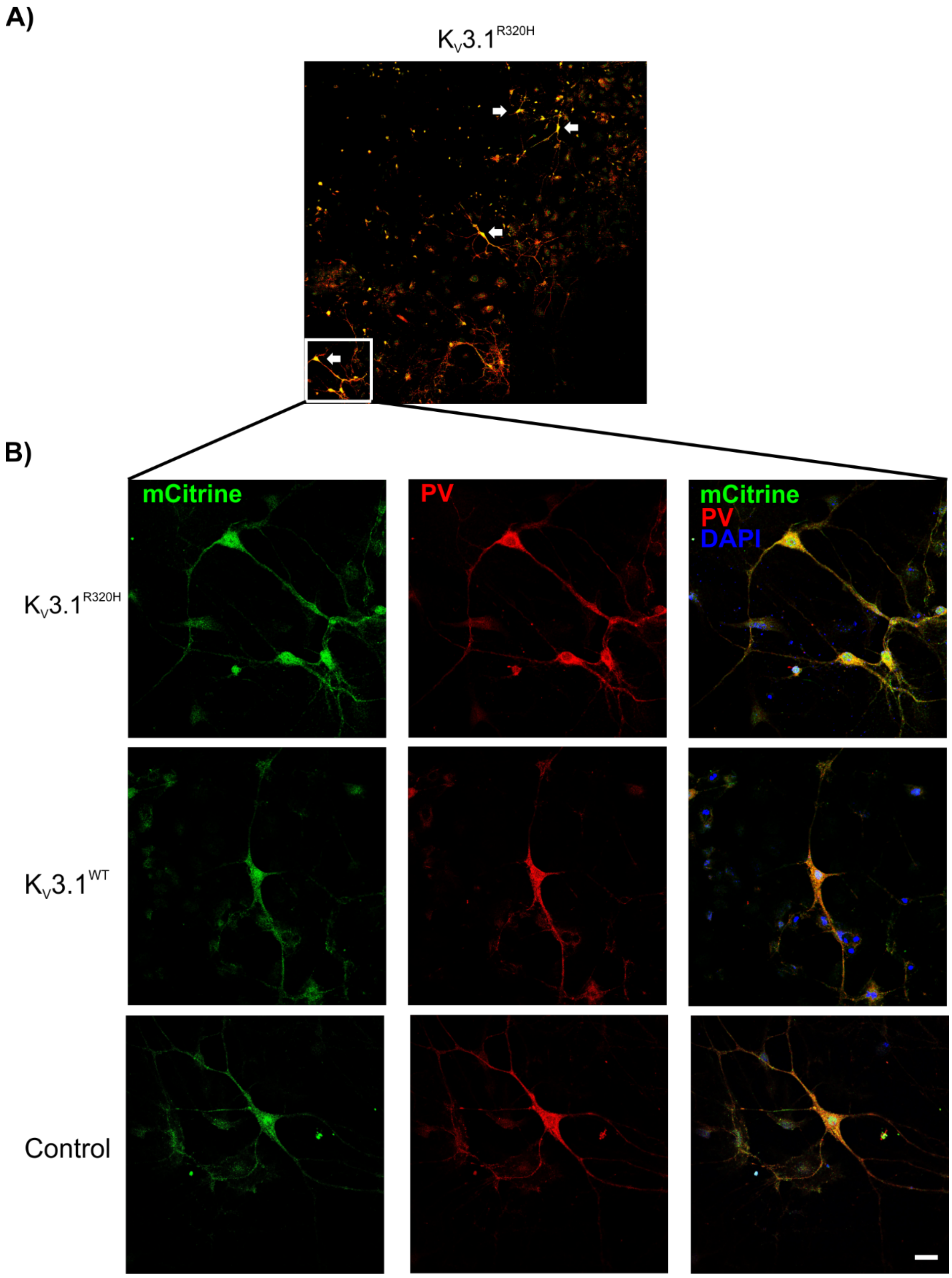

Figure 3.21. BMP4 increases the co-localisation of mCitrine and PV expression. A) Representative 20X immunofluorescent image of cortical neuronal cultures derived from PV^{Cre} mice transduced with FLEx-ChIEF-K$_V$3.1b^{R320H} lentivirus and immunolabelled for PV and mCitrine at 21 DIV. White arrows indicate neurons co-expressing mCitrine and tdTomato (yellow). **B)** Representative immunofluorescent images for the co-localisation of PV and mCitrine in cortical cultures transduced with FLEx-ChIEF-K$_V$3.1b^{R320H} (Top panel is a 40X magnified image of the boxed region in A); FLEx-ChIEF-K$_V$3.1b^{WT} and FLEx-ChIEF control lentiviruses. The fluorescent

signal derived from mCitrine was amplified using an antibody raised against EGFP (which shares the same epitope). Note the improved appearance of neurons infected with FLEx-ChIEF-K$_V$3.1b^{R320H} viruses, likely due to the reduced expression level of this protein. Scale bar is 20 µm.

3.7.7.2 Overexpression of K$_V$3.1^{WT}, but not K$_V$3.1^{R320H}, significantly increases high frequency firing in PV$^+$ interneurons.

Previously in this chapter (**Section 3.6**) I showed that overexpression of K$_V$3.1b^{WT} increased the spiking fidelity of interneurons targeted using the mDlx promoter element when stimulated at high frequencies, while K$_V$3.1b^{R320H} channels had no effect compared to GFP controls. Here I performed whole-cell current-clamp recordings of PV$^+$ interneurons (tdTomato$^+$) transduced with FLEx-ChIEF, FLEx-K$_V$3.1b^{WT} or FLEx-K$_V$3.1b^{R320H} lentiviruses at 21 DIV and found the same results, observing again that overexpression of K$_V$3.1b^{WT} significantly increased the spike success rate at 80 and 100 Hz (80 Hz: 96.6 ± 2.8%; 100 Hz: 80.6 ± 8.9%, n = 7) whereas K$_V$3.1b^{R320H} had no effect on high frequency firing compared to ChIEF controls (R320H: 80 Hz: 63.7 ± 7.7% and 100 Hz: 48.9 ± 5.7%, n = 7; ChIEF: 80 Hz: 60.8 ± 7.6% and 100 Hz: 44 ± 4.9%, n = 9, $p < 0.0001$, **Figure 3.22B & C**).

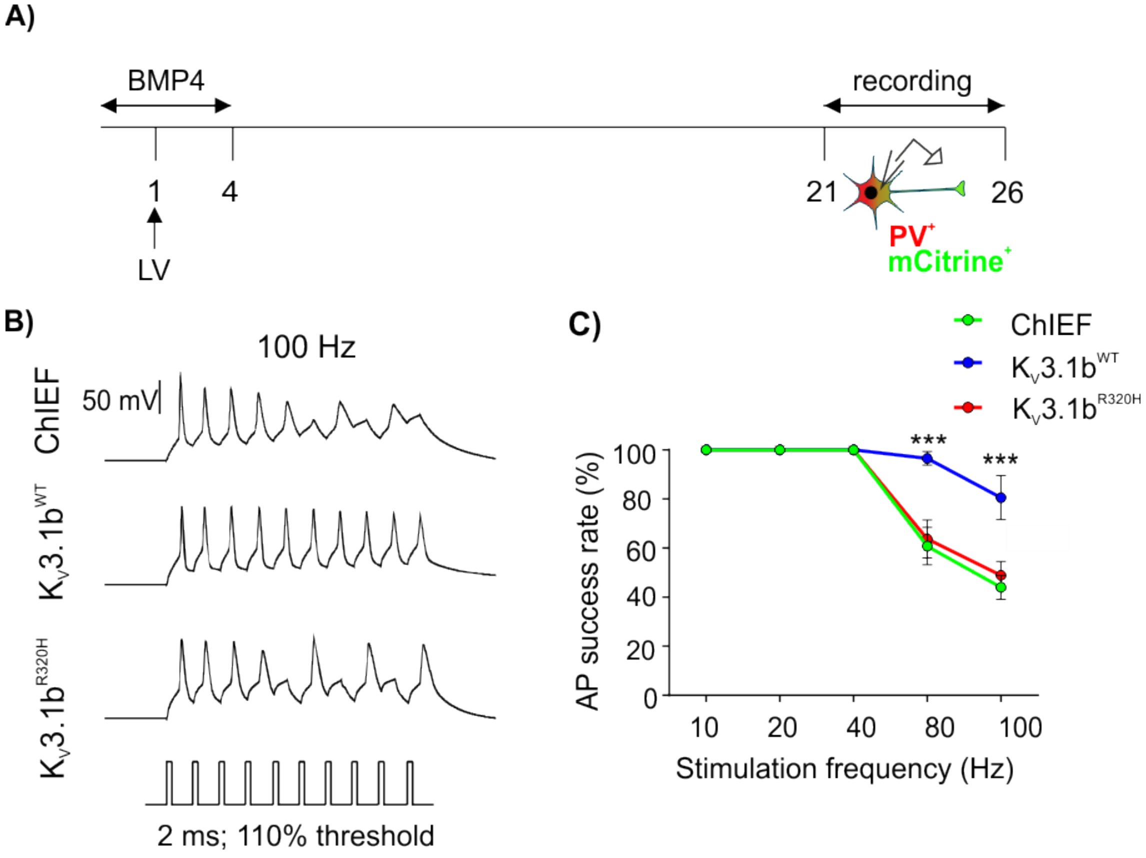

Figure 3.22. Overexpression of $K_V3.1^{R320H}$ does not support high frequency firing in PV^+ interneurons. A) Schematic of experimental workflow. Cortical cultures from PV^{Cre}:tdTomato mice were transduced with lentivirus (LV) at DIV 1 and maintained in BMP-4 containing media until 4 DIV. Neuronal cultures were maintained under standard conditions and electrophysiological recordings were carried out of $tdTomato^+$ and $mCitrine^+$ cells at 21-26 DIV**. B)** Representative recordings of APs induced by short-pulse current injections (2ms, at 110% of current threshold) at a frequency of 100 Hz, from neurons expressing ChiEF only (control), $K_V3.1b^{WT}$ or $K_V3.1b^{R320H}$. **C)** Significantly higher spike success rates are observed at 80 and 100 Hz only with the overexpression of $K_V3.1^{WT}$ compared to the overexpression of $K_V3.1b^{R320H}$ and control neurons (ChIEF). Two-way ANOVA followed by Bonferroni's multiple comparison test (80 Hz: R320H vs WT, ***$p < 0.0001$; ChiEF vs WT, ***$p < 0.0001$; ChiEF vs R320H, $p = 0.87$; 100 Hz: R320H vs WT ***$p < 0.0001$; ChiEF vs WT ***$p < 0.0001$; ChiEF vs R320H $p = 0.69$). Data are shown as mean ± s.e.m and are from 2 independent neuronal preparations.

3.7.7.3 Overexpression of $K_V3.1^{WT}$, but not $K_V3.1^{R320H}$ significantly alters single action potential properties.

Previously, I found that the inability of $K_V3.1b^{R320H}$ channels to support high frequency firing of interneurons during high frequency stimulation was reflected in the single AP properties of expressing neurons, whereby overexpression of $K_V3.1^{WT}$ resulted in a faster rate of action potential repolarisation and a narrower AP half-width, whereas $K_V3.1b^{R320H}$ expression had no effect on the AP waveform. Here, I observed the same results, finding that overexpression of $K_V3.1b^{R320H}$ in PV^+ interneurons had no effect on the rate of AP repolarization (R320H: -56.5 ± 3.6 V s^{-1}, n = 5; ChIEF: -38.7 ± 4.7 V s^{-1}; n = 8), half-width (R320H: 1.34 ± 0.13 ms, n = 5; ChIEF: 1.26 ± 0.27 ms, n = 8) or AHP (R320H: 10.2 ± 1.6 mV, n = 5; ChIEF: 9 ± 0.9 mV, n = 8, **Figure 3.23B**). Overexpression of $K_V3.1b^{WT}$, however, was found to result in a significantly faster rate of AP repolarization (-75.9 ± 13.5 V s^{-1}, n = 6, ChIEF vs. WT: $p = 0.009$), greater amplitude of AHP (13.7 ± 1.8 mV, ChIEF vs. WT: $p = 0.040$) and reduced AP half-width (0.75 ± 0.17 ms, ChIEF vs. WT: $p = 0.015$) (**Figure 3.23B**). Again, overexpression of $K_V3.1^{WT}$ and $K_V3.1^{R320H}$ channels had no effect on AP threshold, rising slope or peak amplitude (**Table 3.2**).

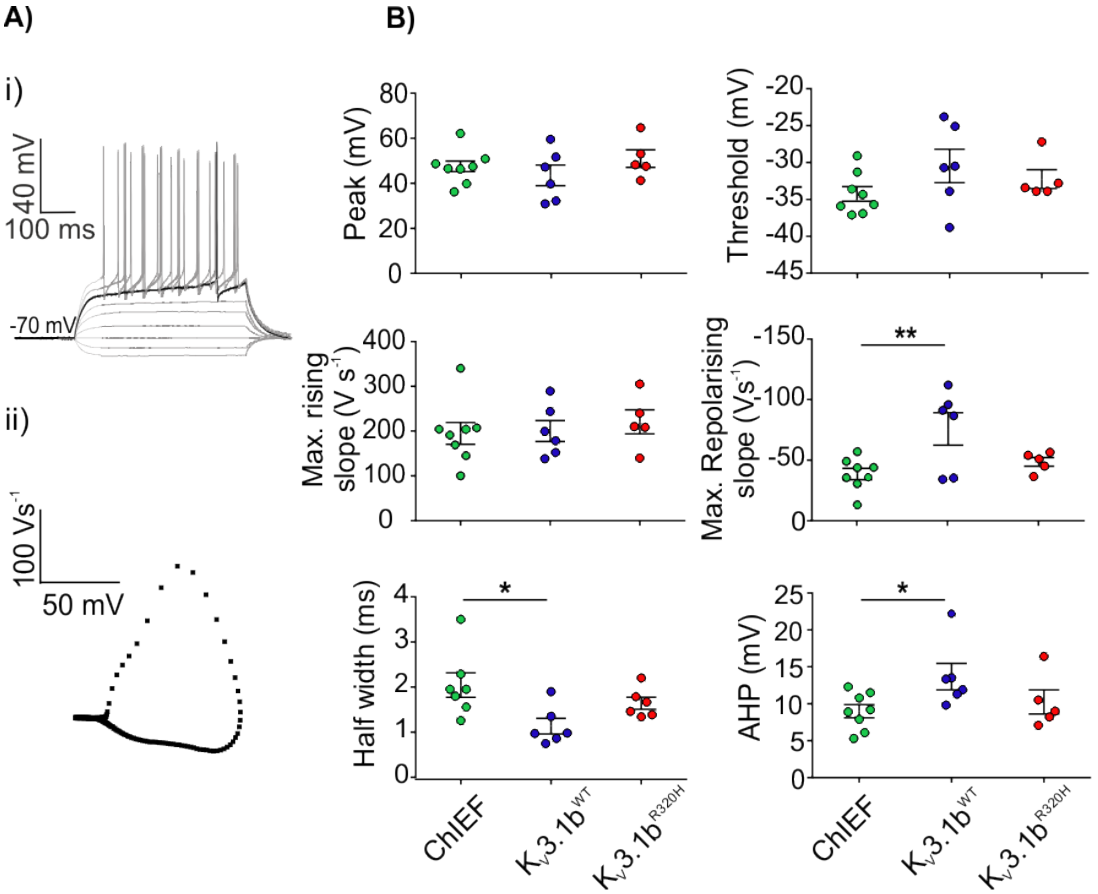

Figure 3.23. K$_{V}$3.1b^{R320H} does not alter the properties of the single AP in PV^{+} interneurons. A) (i) Neurons at 21-26 DIV were subjected to iterative rounds of depolarising steps (Δ20 mV) and the properties of the first elicited AP were analysed. **(ii)** AP parameters were extracted using a phase-plane plot. **B)** Comparisons of the effects of K$_{V}$3.1b expression on single AP properties in PV^{+} cells. Overexpression of K$_{V}$3.1b^{WT} results in a significant reduction in the rate of AP repolarisation (**p = 0.009), the AP half-width (*p = 0.015) and the amplitude of the AHP (*p = 0.040) when compared to GFP control neurons. K$_{V}$3.1b^{R320H} channels have no effect on the rate of AP repolarisation; the AP half-width (p > 0.99) or the amplitude of the AHP with respect to GFP control neurons, findings in line with a loss-of-function. All comparisons were made vs. GFP control neurons and performed using One-way ANOVA followed by Bonferroni's multiple comparisons test. Data are from two independent neuronal preparations and are shown as means ± s.e.m.

Table 3.2. Active properties of PV$^+$ interneurons overexpressing K_V3.1b channels

Properties	**CHIEF (n = 8)**	**K_V3.1b^{WT} (n = 6)**	**K_V3.1b^{R320H} (n = 5)**
Threshold (mV)	-34.3 ± 1.0	-30.47 ± 2.3	- 32.2 ± 1.3
AP Peak (mV)	47.5 ± 2.4	43.6 ± 4.6	51 ± 3.9
Max. Rising slope (V s^{-1})	195.1 ± 24.5	200.2 ± 23.4	220.6 ± 26.7
AP half-width (ms)	2.0 ± 0.3	1.1 ± 0.2 *	1.6 ± 0.1
Max, repolarizing slope (V s^{-1})	-57.1 ± 4.7	-112.0 ± 13.5 **	-56.5 ± 3.6
AHP (mV)	9.0 ± 0.9	13.7 ± 1.8 *	10.2 ± 1.6
Current threshold (pA)			

All data are presented as means ± s.e.m. * $p<0.01$ between K_V3.1b^{WT} and CHIEF control neurons; ** $p<0.001$ between K_V3.1b^{WT} and ChIEF control neurons.
Comparisons made using One-Way ANOVA with p value followed by Bonferroni's multiple comparisons test.

3.8 Discussion

3.8.1 The R320H mutation in K_V3.1b does not generate detectable gating pore currents

Arginine to histidine (R>H) transitions within the VSD of voltage-gated ion channels are one of the most common types of mutation of the channelopathies. It has been suggested that mutation of these highly conserved voltage-sensing arginine residues can result in the introduction of pathological gating pore currents through the VSD of the channel that contribute towards disease phenotypes, however, this has yet to be demonstrated in the context of neurological disease (Cannon, 2010; Catterall, 2010; Sokolov et al., 2007). The dramatic and detrimental effects of mutant K_V3.1b channel expression on neuronal viability suggested that the R320H mutation in the S4 segment of the channel might confer a toxic gain-of function, potentially represented by the creation of a proton pore (gating pore) in the VSD of the channel. However, I was unable to detect pH-dependent gating pore currents for K_V3.1b^{R320H} channels containing the W374F α pore-blocking mutation. Whilst it is possible that I were unable to detect these currents because gating pore currents are very small in amplitude, I was able to unambiguously detect gating pore currents conducted by Shaker^{R371H} channels, validating the sensitivity of our experimental approach (Struyk & Cannon, 2007).

Our results are perhaps not surprising in light of a previous study that showed that the analogous R>H mutation in K_V3.3 (causative for SCA13) does not introduce gating pore currents (Minassian et al., 2012). In evolutionary terms, K_V3.1 is more closely related to

$K_V3.3$ than it is to Shaker and taken together our findings suggest that proton transport or conduction are not a feature of arginine-histidine mutations within K_V3 channel VSDs (Minassian et al., 2012). Nevertheless, our study is limited in that I have not confirmed cell surface expression of our Kv3.1b α-pore mutants, which would be required to be able to detect gating pore currents. Indeed, Shaker channels are much more tolerant to mutation (such as the W434F α-pore mutation) than mammalian ion channels (Starace et al., 1997). In the future, cell surface membrane expression of α-pore mutants could be confirmed by recording of gating currents, however these currents are extremely small in amplitude and can only be detected using the cut-open oocyte recording configuration (Stefani & Bezanilla, 1998). Overall, I excluded pathogenic currents through the VSD of $K_V3.1b^{R320H}$ as the underlying disease mechanism in MEAK.

3.8.2 Early overexpression of $K_V3.1b^{R320H}$ results in neuronal loss

I have observed dramatic and unexpected effects on neuronal morphology and viability caused by $K_V3.1^{R320H}$ overexpression. One of our most striking findings was that the expression of $K_V3.1^{R320H}$ resulted in a dramatic reduction in dendritic length, a mere 48 hr post-transfection, as well as a reduction in axonal length. I also observed cell loss at 72 hr post-transfection. The mechanisms underlying these phenomena are unclear. In particular, cell death and neurite degeneration are intricately entwined cellular events, such that it can be difficult to say whether the reduction in dendritic length precedes neuron loss or whether the activation of cell death pathways triggers neurite retraction and degeneration. It is important to consider the time course/ order of these events because ultimately, they can provide clues as to the mechanism by which the mutant channel induces these changes. For example, neuronal death triggered at the soma, could result from activation of the unfolded protein response (UPR) in reaction to endoplasmic reticulum (ER) stress, potentially caused by misfolded, sequestered channel protein. Alternatively, changes in neurite length that precede (i.e. are independent of) cell death could indicate an entirely different disease mechanism, whereby pathogenicity is mediated by alterations in dendritic excitability, potentially relating to dysregulated calcium signalling.

Cell death can be monitored by performing assays that detect biochemical changes that occur as part of heavily stereotyped programmed cell death pathways. I labelled for the master executioner of apoptosis, CC-3, and also investigated neuronal viability using a PI exclusion assay. Unfortunately, I did not obtain any readouts of cell death or comprised neuronal viability using these methods at these time-points. There are a number of possible reasons as to why I have failed to obtain positive results for these markers of cell death. Firstly, it is possible that I have not chosen the right time point at which to detect CC-3 immunolabelling. CC-3 has a half-life of only 8 hours and so immunoreactivity could be missed by assaying cells too early or late post-transfection (Walsh et al., 2011). Likewise, cellular permeability to PI is an indicator of late-stage apoptosis, thus it is likely that neurons are still viable at 24 hr post-transfection and retain the integrity of their membrane. Neuronal viability should continue to be investigated using the PI exclusion assay at later time-points, such as 48 hr post-transfection.

Future experiments could employ alternative assays of apoptosis in order to investigate cell death in neurons expressing $K_V3.1b^{R320H}$ channels. For example, the Terminal deoxynucleotidyl transferase dUTP nick end labelling (TUNEL) assay is a convenient and widely adopted method for detecting chromosomal DNA cleavage that occurs during apoptosis (Gavrieli et al., 1992). In the TUNEL assay, free 3’-OH termini of DNA, which are generated by DNA cleavage, are labelled with a fluorophore, thus allowing for the identification and rapid quantification of apoptotic cells on the basis of nuclear fluorescence. Performing a TUNEL assay at 48 hr and 72 hr may represent the logical ‘next step’ in the quantification of apoptotic cell death in neurons expressing $K_V3.1b^{R320H}$, given the significant changes in nuclear morphology and DAPI staining that was observed for these neurons 48 hr post-transfection. Likewise, apoptotic cells could be detected in an AnnexinV-based assay, which detects the presentation of phosphatidyl serine on the cell surface (Schutte et al., 1998). These methods are complementary, detecting late and early-stage apoptosis, respectively.

Alternatively, it is possible that neurons transfected with $K_V3.1b^{R320H}$ are dying via a caspase-independent apoptotic pathway (Tait & Green, 2008). The fact that CC-3 immunoreactivity is not observed at 36 hr implies that the chromatin condensation that I observe at 48 hr may be triggered by a mechanism independent of caspases. Indeed, caspase-independent apoptosis is characterised by chromatin condensation, without fragmentation of the nucleus and compaction of nucleus into a globular or crescent shape that is typical of caspase-dependent apoptosis (Broker et al., 2005). I also cannot rule out autophagy, where cells are destroyed via the autophagosomic-lyosomal pathway, as a mechanism of cell death (Yang et al., 2013). I did not test for markers of autophagy in our transfected neurons, however autophagy is normally indicated by vacuolation of the cytoplasm, which was not overtly apparent during our imaging experiments.

3.8.3 MEAK may represent a neurodevelopmental disorder

3.8.3.1 The developmental expression of $K_V3.1b^{R320H}$ channels in interneurons *in vitro* induces a reduction in dendritic length

Despite the pathway of neuronal death remaining unclear, a reduction in dendritic length occurs as an early event following the expression of mutant $K_V3.1b$ channels and as such, may be a cause, and not a consequence, of cell death. How mutant $K_V3.1b$ channels trigger changes in dendritic length is uncertain, however the endogenous expression of $K_V3.1b$ channels in dendrites *in vivo* and *in vitro* suggest that $K_V3.1b$ channels directly contribute towards the regulation of dendritic excitability (Gu et al., 2012; Ozaita et al., 2002).

One way in which $K_V3.1b$ channels may regulate dendritic excitability under physiological conditions is through the attenuation of back-propagating action potentials, as suggested by their expression in proximal dendrites (Ozaita et al., 2002). This is unlikely to be the mechanism involved here, however, because I expressed $K_V3.1b$ channels in electrically immature neurons (4-6 DIV) that mainly exhibit spontaneous activity (Andreae & Burrone, 2015; Redmond et al., 2002). The dendritic expression of $K_V3.1b$ channels at this age may instead play a role in the local regulation of spontaneous activity by limiting the time course of calcium-dependent membrane depolarisations, mediated by voltage-gated calcium channels and N-methyl-$_D$-aspartate receptors (NMDARs) (Konur & Ghosh, 2005). Interestingly, it has been shown in cortical neurons, both *in vivo* and *in vitro*, that periods of high spontaneous activity correspond with periods of rapid dendritic growth and that this process is partly calcium-dependent (Redmond et al., 2002). Indeed, it has been shown using computational modelling that enhanced calcium signalling promotes dendritic outgrowth and branching, whereas pathologically high dendritic calcium levels (such as those experienced during a seizure) can cause the collapse of spines and retraction of the dendrites (Dur-e-Ahmad et al., 2007; Segal, Korkotian, & Murphy, 2000). Thus, it is possible that the dramatic effects on dendritic morphology that I observed following mutant $K_V3.1b$ channel expression, resulted from dysregulated dendritic calcium signaling as a result of the loss of K_V3-mediated K^+ conductances.

3.8.3.2 Mutant $K_V3.1b$ channels result in axonal degeneration

In addition to a reduction in dendritic length, I also observed a reduction in axonal length upon the expression of $K_V3.1b^{R320H}$ channels in young cortical interneurons *in vitro*. It is possible that axonal degeneration is occurring as a consequence, and not a cause, of cell death. This is because axonal degeneration occurring in the context of global neuronal changes, such as what I observed, is a typical feature of apoptosis, whereas acute axonal degeneration has been shown to be able to occur in isolation without triggering cell death (Saxena & Caroni, 2007).

Alternatively, what I observed as axonal 'retraction' may instead represent impaired axonal outgrowth. Whilst K_V3.1b channels have not been shown to be involved in axon development, K_V3.4 channels have been shown to be present in the axonal growth cone and are important for the regulation of calcium influx during axonal pathfinding (Huang et al., 2017). K_V3.4 channels have been shown to be expressed in primary neuronal cultures and so it is possible that mutant K_V3.1b channels act dominantly negatively on Kv3.4 channels in the growth cone (Pannaccione et al., 2007). I would, however, have to perform longitudinal live imaging of the axons and dendrites of neurons transfected with Kv3.1b^{R320H} channels and controls in order to investigate the order of the evoked morphological changes in an attempt to establish whether the reduction I observed in axonal length is due to axonal degeneration or impaired outgrowth.

3.8.3.3 K_V3.1b channels may play a role in neuronal development and migration

The role of K_V3.1b channels in neuronal development has not been explicitly interrogated. However, neurodevelopmental roles for K_V3 family members is suggested by studies that have shown the expression of K_V3 channel family members to increase throughout development and into adulthood, which likely corresponds to the maturation of electrical circuits (Boda et al., 2012). A role for K_V3.1 channels in neuronal migration has also been suggested, following the observation that the greatest increases in K_V3.1 mRNA levels occurs between P4 and P15 during the migration of granule cells from the external germinal layer to the internal granule in the developing cerebellar cortex (Shibata et al., 1999). The migration of cerebellar granule cells is also calcium dependent, although the authors speculated only about the effects of K_V3.1-mediated changes in the action potential waveform on calcium influx and did not consider any potential changes in dendritic calcium (Komuro & Rakic, 1996). Interestingly, K_V3.1 channels have also been shown to be important for the differentiation and proliferation of neural precursor cells via the regulation of calcium influx (Yasuda et al., 2013).

3.8.3.4 Alterations in interneuronal input-output properties suggest that expression of $K_V3.1b^{R320H}$ channels during development induces alterations at the cellular level

I have observed a dramatic effect on the input-output properties of interneurons expressing $K_V3.1b^{R320H}$ channels at 14-16 DIV, with mutant neurons firing significantly fewer APs upon increasing current injection than controls. This effect was not due to alterations in the AP waveform and so it is possible that it could be due instead to changes in cell morphology. The morphological defects that I previously observed when mutant $K_V3.1b$ channels were expressed at high levels early in development align with this hypothesis. However, neurons transduced with $K_V3.1b^{R320H}$ viruses, although few, were viable and did not display changes in the resting membrane potential or other passive properties. It is possible that the cell death phenotypes I observed for transfected neurons result from an almost complete loss of dendritic inputs and survival cues, especially because young neurons in culture are particularly sensitive to apoptosis.

Theoretically, I should see alterations in capacitance measurements upon significant morphological changes in neurons expressing $K_V3.1b^{R320H}$ channels. However, neurites in culture are capable of spreading very far from the cell body and so an accurate measure of this parameter via a somatic patch pipette is not trivial. Future experiments will aim to perform dendritic Sholl analysis for neurons transduced with $K_V3.1b^{R320H}$ lentiviruses in order to assess what impact expressing the mutation at lower levels has the development of the dendritic tree.

3.8.4 A dominant negative effect of $K_V3.1b^{R320H}$ channels is not observed at the level of the single action potential

The dramatic morphological and electrophysiological effects observed upon $K_V3.1b^{R320H}$ expression are unlikely to result from a simple loss-of-channel function. Indeed, whilst $K_V3.1$ knock-out mice are relatively phenotypically normal, severe neurological phenotypes are observed for $K_V3.1/3.3$ double knock-out mice, which likely reflect functional redundancy within the K_V3 family (Espinosa et al., 2001; 2004). Furthermore, loss-of-function of $K_V3.1$ in humans results in intellectual disability and follows an autosomal recessive mode of inheritance whereas MEAK has a dominant mode of inheritance (Muona et al., 2014; Poirier et al., 2017).

Biophysical studies in HEK cells have previously indicated that $Kv3.1b^{R320H}$ exerts a dominant negative effect on WT channel function (Munch et al., 2018; Muona et al., 2014). Our preliminary results in oocytes support these findings, as we also observed a dominant negative effect of Kv3.1b^{R320H} on current amplitude when WT and mutant channels are expressed at a 1:1 ratio (although I need to increase this sample size). It is interesting, therefore, that I do not observe a dominant negative effect of $K_V3.1^{R320H}$ expression on the properties of the single action potential and also spike fidelity when neurons are stimulated at high frequencies. I have confirmed that cortical interneurons in culture endogenously express $K_V3.1b$ channels at 14 DIV however, it is possible that these neurons do not heavily rely upon these channels for AP repolarisation at this age in culture. Interestingly, unlike what has been previously reported, I did not see an increase in firing frequency upon increasing current injection with the overexpression of WT $K_V3.1b$ channels (Gu et al., 2012). This indicates that these neurons are not yet expressing sufficiently high levels of other voltage-gated ion channels that support high frequency firing, such as $Na_V1.1$ (Gu et al., 2018). Future experiments should aim to pharmacologically modulate $K_V3.1$ channels (or all K_V3 family members using low concentrations of TEA as specific $K_V3.1$ blockers are not well characterised) in order to assess the extent to which the cells I am recording from rely upon K_V3 channels for AP repolarisation and high frequency firing.

Alternatively, it is possible that mutant $K_V3.1b$ channels have a dominant negative effect on the trafficking of other K_V3 channel family members to the cell membrane. Potassium channel tetramerisation is known to occur within the K_V3 family and can influence the subcellular targeting of family members, depending on which channels are expressed in the target cell type (Jensen et al., 2011). If $K_V3.1b^{R320H}$ channels are aberrantly retained intracellularly, then it is possible that this also results in the intracellular sequestration of other K_V3 family members. Indeed, the analogous R>H mutation, affecting the 4th voltage-sensing arginine of the S4 domain in $K_V3.3$ (SCA13), has recently been shown to result in the retention of the channel in anterograde vesicles or trafficking endosomes and a loss of cell surface expression (Khare et al., 2018). Interestingly, this mutation also resulted in the intracellular retention of epidermal growth factor receptor (EGFR), which is involved in dendritic development (Khare et al., 2018). Thus, the R320H mutation in $K_V3.1$ may induce neurodevelopmental changes via excitability changes that indirectly involve the dominant suppression of K_V3 channel function or via an altogether unrelated mechanism, such as that which was observed for $K_V3.3^{R423H}$. Future studies should assess the ratio of surface expression to internal localisation of $K_V3.1b$ channels in order to ascertain whether $K_V3.1b^{R320H}$ channels are efficiently trafficked to the membrane.

3.8.5 $K_V3.1b^{R320H}$ is a partial loss-of-function

3.8.5.1 The R320H mutation in $K_V3.1b$ confers a partial loss-of-function

Previous studies in oocytes have shown the R320H mutation in $K_V3.1a$ to confer an almost complete loss-of-channel function, with the channel rendered insensitive to changes in transmembrane voltage (Muona et al., 2014). Here, however, I show that $K_V3.1b^{R320H}$ channels are still able to conduct appreciable K^+ currents - of around half the amplitude of those conducted by WT channels. An important control, however, that was not performed, would be to immunoblot for $K_V3.1b$ protein in order to confirm that the reduction in current amplitude for $K_V3.1b^{R320H}$ is not due to reduced channel expression compared to the WT. However, it should be noted that for the Kv3.1a isoform, the introduction of the p.R320H mutation did not result in a reduction in channel expression in oocytes (Muona et al., 2014).

Our results support previous studies in HEK cells that also found a partial loss of function on total current amplitude for $K_V3.1b^{R320H}$ channels (Munch et al., 2018). The discrepancies between our findings and Munch et al., and the findings of Muona et al., likely lie in the different $K_V3.1$ channel isoform used and not differences in trafficking between the amphibian and mammalian trafficking systems, as purported by Munch *et al* (Munch et al., 2018).

3.8.5.2 $K_V3.1b^{R320H}$ has no effect on spiking fidelity at high stimulation frequencies

High frequency neuronal firing has been shown to be heavily influenced by the expression of $K_V3.1b$ channels (Gu et al., 2012; 2018). Indeed, I have shown *in vitro* that the transgenic overexpression of WT $K_V3.1b$ channels can increase interneuronal spike fidelity at high stimulation frequencies. I was unable to reproduce this effect with the expression of $K_V3.1b^{R320H}$, findings in line with a loss-of-function effect of this mutation. However, there was no difference in spike fidelity between control neurons and neurons overexpressing $K_V3.1b^{R320H}$, suggesting that this channel is not having dominant negative effects on endogenous WT K_V3 channels. This finding is supported by the fact that I did not observe changes in single AP properties upon $K_V3.1b^{R320H}$ overexpression.

Despite not being able to optically stimulate transduced PV^+ interneurons in culture, I was still able to investigate their firing properties using electrical stimulation. Crucially, I managed to replicate some of our results of **Section 3.6**, finding again that $K_V3.1b^{R320H}$ channels cannot support high frequency firing at high stimulation frequencies. In PV^+

interneurons overexpressing $K_V3.1b^{R320H}$ *in vitro*, I found no alterations in AP properties that are sensitive to the expression of fast-delayed rectifier K^+ currents compared to the overexpression of WT channels. In this instance, I also observed a significant increase in the AHP in neurons expressing $K_V3.1b^{WT}$ that I previously did not see when recording from mDlx-targeted interneurons expressing the channel at ~14 DIV. This is likely because here I recorded from PV^+ interneurons at ~24 DIV, which likely display a different balance of ionic conductances that influence the AHP.

Interestingly, as previously found, I did not observe a dominant negative effect of $K_V3.1b^{R320H}$ on AP properties or high frequency firing in PV^+ cells. Unfortunately, due to limitations associated with the methods used in this chapter, I did not gain any further insights as to why this is the case. Originally, I aimed to express $K_V3.1b$ channels specifically in PV^+ interneurons because they are known to endogenously express these channels at high levels *in vivo*, such that I hoped that I might be able to reveal previously concealed dominant negative effects of $K_V3.1b^{R320H}$ expression on K_V3 conductances (Rudy et al., 1999). However, the PV^+ control neurons (ChiEF only) I recorded from at ~24 DIV appeared to be even less able to support fast-spiking than the interneurons recorded from at 14 DIV, hence the exaggerated divergence in spike success rates observed as early as 80 Hz for this experiment.

The regular spiking phenotypes of the PV cells in these experiments are likely due to BMP4 treatment, which I used to encourage the differentiation of interneuron precursors into PV cells – to try and increase PV cell representation in culture (Mukhopadhyay et al., 2009). Prior to this work, electrophysiological characterisation of BMP4 'converted' PV^+ interneurons had not been carried out and indeed, it appears to us that 'PV' cells of neuronal cultures treated with BMP4 display electrical behaviour that is more characteristic of their SST^+ predecessors. Unfortunately, this suggests that the cells are not expressing $K_V3.1$, or indeed other molecular determinants of high frequency firing at high levels, such that studying the effect of R320H in this cell type becomes less physiologically relevant. Future studies wishing to use BMP4 to promote PV cell numbers *in vitro* should perform a systematic comparison of the electrophysiological properties of PV cells from BMP-4 treated/ non-treated cortical cultures in order to determine whether slower firing properties are a general limitation of neuronal culture or an effect of BMP-4 conversion.

3.8.6 Investigation of the cell-type specific effects of mutant $K_V3.1b$ channels is hindered by transgene specific effects when combined with the Cre/lox system

A major challenge encountered in this chapter (**Section 3.7**) lay with the difficulties in being able to co-express $K_V3.1b$ with the opsin, ChiEF. I found that not only was expression of ChiEF weaker for lentiviruses co-expressing $K_V3.1b$ (which precluded optical stimulation) but also that many fewer transduced neurons could be detected compared to control conditions (ChiEF only). This could be a transgene specific issue for a number of reasons. Firstly, low transduction efficiencies were observed for both WT and mutant *KCNC1* transgenes, implying that there is something structurally specific about the *KCNC1* gene, regardless of the 959G>A point mutation, which reduces the efficiency of viral synthesis or gene expression. Secondly, I observed an increased co-localisation of PV and mCitrine expression following incubation with BMP-4, which would suggest that many neurons had in fact been effectively transduced with virus and that increased co-localisation was due to the increased stimulation of the PV promoter, increased Cre production and therefore more efficient transgene recombination. The difficulties finding fluorescent neurons for R320H may be a combination of steric problems regarding gene recombination as well as potential toxic effects of $K_V3.1b^{R320H}$ expression.

Interestingly, I consistently saw reduced transduction efficiencies for Cre-based viruses and also mDlx viruses, for mutant $K_V3.1b$ channels, suggesting that this mutation results in reduced expression levels or that cell loss still remains a significant component of the disease mechanism. Future experiments should try to address this issue using a combination of functional viral titering methods (i.e. use genomic integration and quantitative PCR using genomic DNA of infected HEK cells) and fluorescent assays in neuronal cultures.

3.9 Conclusions and future directions

Previous to this study, the neuronal effects of the R320H mutation in $K_V3.1$, causative for MEAK, had not been investigated. Here I obtain evidence to suggest that MEAK may represent a neurodevelopmental disorder. I find that the developmental expression of mutant $K_V3.1b$ channels at high levels in young cortical interneurons *in vitro*, results in global cellular degenerative changes and eventual cell loss, via an as of yet undetermined pathway of cell death. Neuronal death upon $K_V3.1b^{R320H}$ expression appears to be triggered by the almost complete loss of the dendritic arbour at a developmental stage where neurons are particularly dependent on survival cues and exquisitely vulnerable to apoptosis. When K_V3.1b channels are expressed at lower levels using lentiviral-mediated gene delivery, I find mutant K_V3.1b channels to profoundly alter the input-output properties of expressing neurons, which could result from developmental perturbation as I find the single AP properties to be unaltered. Thus, I prospectively reveal a previously undescribed role for K_V3.1b (and potentially other K_V3 channel family members) in dendritic development.

3.9.1 Future Directions

3.9.1.1 The role of K_V3.1 in neurodevelopment

Much research has focused on the role of K_V3.1 channels in AP repolarisation and as determinants of high frequency firing. K_V3 channels also contribute towards the regulation of the timing and duration of calcium transients, which has been best studied with respect to the role of K_V3.1b channels in regulating neurotransmitter release at presynaptic terminals (Goldberg, 2005). Given that much electrical signalling early in development depends upon calcium signalling, it follows, therefore, that K_V3 channels could also play an important role in neurodevelopment. Indeed, a role for K_V3.4 in regulating calcium influx during axon growth has recently been described (Huang et al., 2017).

In order to test the hypothesis that mutant Kv3.1b^{R320H} channels induce neurodevelopmental changes via the dysregulation of calcium signalling, it would be interesting to perform calcium imaging of neurons transfected or transduced with K_V3.1b^{R320H} channels. The morphological effects of lentivirus-mediated overexpression of K_V3.1b^{R320H}, which were suggested by electrophysiological recordings, should also be confirmed by immunocytochemistry. Following this, it would be interesting to see whether K_V3.1b^{R320H} channels alter neurodevelopment *in vivo* and whether they have an effect on the firing frequency of PV$^+$ interneurons, a cell type that highly expresses K_V3.1b channels.

3.9.1.2 Targeting K_V3.1b channel expression to relevant cell types

Given the challenges of expressing K_V3.1b in PV interneurons *in vitro*, the next step would be to express K_V3.1b in relevant cell types *in vivo*. Our *in vitro* data, however, suggests that a Cre/lox-based approach for cell type specific expression of K_V3.1b would be highly ineffective. Furthermore, I have also experienced difficulties in synthesising high titre viruses containing K_V3.1b^{R320H} and so viral methods are also likely precluded.

Instead, in utero electroporation could be used to deliver $K_V3.1b$ containing constructs to the developing brain. In utero electroporation has the advantage that it allows the effect of mutant $K_V3.1$ channels on neuronal development to be investigated and it does not require viral-based gene delivery. Furthermore, interneurons can be targeted by targeting neurons of the MGE at the correct embryonic age (De Marco Garcia & Fishell, 2014). As a continuation of our work *in vitro*, I could also express $K_V3.1$ channels in cerebellar granule cell cultures, a highly disease relevant cell type that expresses $K_V3.1$ channels at very high levels (Shibata et al., 1999).

Chapter 4

CRISPR/Cas9 based technologies to model MEAK

4.1 Introduction

4.1.1 Genomic knock-in to model MEAK

MEAK is caused by a recurrent point mutation affecting a single nucleic acid in the *KCNC1* gene (c.959 G>A), which results in the substitution of an arginine with a histidine at amino acid position 320 in the voltage-sensing, S4, domain of the channel. Patients with MEAK are heterozygous for the c.995 G>A mutation, which has an autosomal dominant mode of inheritance (Muona et al., 2014). Prior to this thesis, no mouse models were available for MEAK, and the neuronal effects of the mutant channel had not been investigated.

In **Chapter 3** of this thesis, I used an overexpression strategy to characterize the neuronal effects of $K_V3.1b^{R320H}$ *in vitro*, because $K_V3.1b^{R320H}$ had been previously shown to exert a dominant negative effect on WT channel function (Muona et al., 2014). I used two different methods to deliver the mutant transgene to neurons in culture: transfection at 4 DIV or lentiviral transduction at 1 DIV. With transfection, I observed a dramatic reduction in dendritic length and cell loss within 72 hr. I also observed clear alterations in morphology and firing phenotypes with lentiviral transduction, however the phenotype was less severe and significant cell death was not observed within experimental time-frame (14-16 DIV). The differences in phenotypic severity that I observed with these two different methods of transgene delivery are likely because they afford different levels of transgene expression; transfection is known to achieve higher levels of transgene expression than lentivirus-mediated delivery. Whilst transduction achieves far more disease-relevant levels of transgene expression than transfection, I still cannot rule out that the very severe neuronal effects of the mutant $K_V3.1b^{R320H}$ channel that I observe are not artefacts of overexpression.

The ideal strategy with which to model the dominant negative effects of $K_V3.1b^{R320H}$, both *in vitro* and *in vivo* in mice, would be to insert the mutant allele into the *Kcnc1* genomic locus (knock-in). A targeted knock-in has the advantage that the mutant transgene is placed under the control of the endogenous promoter and is therefore expressed at physiological levels. Targeted knock-ins are conventionally achieved using homologous recombination (HR) (**Figure 4.1**). However, HR is extremely inefficient, especially in post-mitotic cell-types, such as neurons, emphasising the need for an alternative technology.

4.1.2 CRISPR/Cas9 technologies for site-directed transgene integration

The efficiency of HR can be increased by engineering double-stranded DNA breaks (DSBs) into the target genomic locus (Rouet et al., 1994). The targeted generation of DSBs can be achieved using CRISPR/Cas9 system. CRISPR/Cas9 is a revolutionary technology that employs an endonuclease from *Streptococcus pyogenes*, Cas9, whose substrate specificity and endonucleatic activity can be programmed by single-guide RNA (sgRNA) molecules. sgRNAs guide Cas9 to the correct genomic locus by complementary base-pairing of a 20nt ‘protospacer’ element with the target DNA sequence. The introduction of DSBs by Cas9 then occurs 6 nucleotides immediately downstream of a ‘protospacer adjacent motif’ (PAM site), of consensus sequence, ‘-NGG’. Following DNA cleavage, the type of genome edit that subsequently occurs depends upon endogenous cellular DSB repair pathways.

Two major DSB repair pathways exist in mammalian cells: homology directed repair (HDR) and non-homologous end-joining (NHEJ). HDR is similar to HR, in that it relies on the provision of a donor template with regions of homology to the targeted genomic locus. As a result, HDR can generate highly precise genomic edits, to the level of a single base-pair change (**Figure 4.1B**). NHEJ, on the other hand, is an error-prone DNA repair mechanism that repairs DSBs via the random insertion or deletion of nucleotides, referred to as ‘indels’ (**Figure 4.1C**). The varying level of precision of these two DSB repair pathways have been exploited for different CRISPR/Cas9-based gene editing applications. For example, HDR has been rapidly incorporated into mouse model pipelines for the generation of gene knock-ins because of its superior efficiency to HR. In contrast, the error-prone nature of NHEJ has been used with great success in the generation of targeted gene knock-outs (**Figure 4.1C**).

Whilst HDR can efficiently generate gene knock-ins in mitotic cells, such as embryonic stem cells, HDR is extremely inefficient in terminally differentiated cell types, such as neurons. NHEJ, however, is generally more efficient than HDR and is active in both mitotic and post-mitotic cells, nonetheless, its error-prone nature has largely prohibited its application in the generation of precise gene knock-ins. Recently, however, it was shown that NHEJ retains some intrinsic precision in DSB repair and as such has been harnessed for the generation of gene knock-ins in post-mitotic cell types (Maresca et al., 2013; Suzuki et al., 2016).

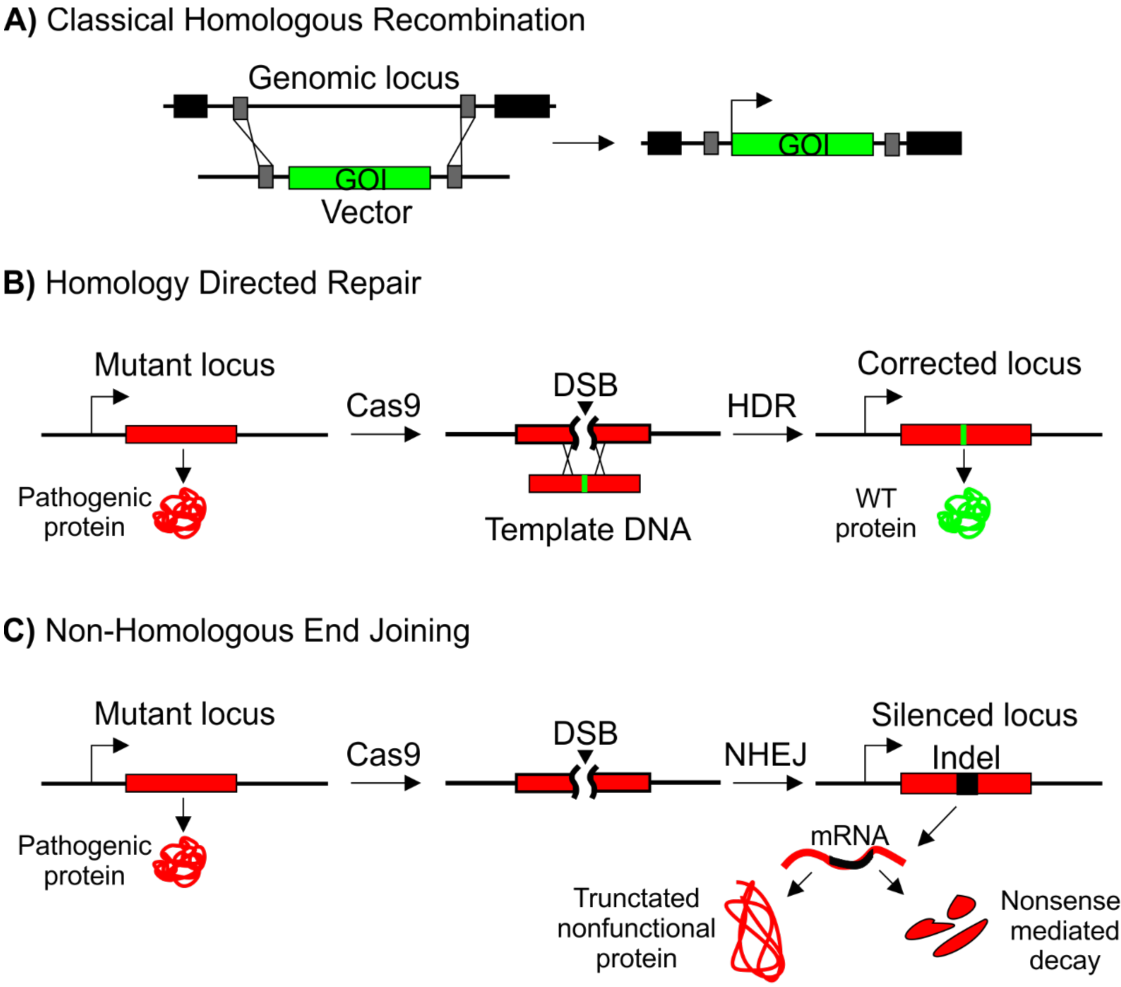

Figure 4.1. Types of genome editing events. A) Targeted gene knock-in via homologous recombination (HR). A gene of interest (GOI) is inserted into a target genomic locus by DNA recombination between regions of homology (grey boxes) in the donor vector and the target genomic locus. **B)** Targeted gene knock-in via HDR. The efficiency of HR can be increased by the targeted introduction of DSBs into the genomic locus using CRISPR/Cas9. Precise gene edits can be achieved using HDR, following the provision of a corrective gene template. **C)** Gene knock-out by NHEJ. CRISPR/Cas9 introduces DSBs into the mutant genomic locus, which are repaired by NHEJ. The error-prone nature of NHEJ results in the introduction of indels into the target locus, which knocks-out gene function due to the generation of a truncated, non-functional protein or nonsense mediated decay of the mRNA transcript.

4.1.2.1 Genomic knock-in in post-mitotic cells using CRISPR/Cas9

Genomic knock-in events in post-mitotic cells, such as neurons, *in vitro* and *in vivo*, can be achieved using a NHEJ-based CRISPR/Cas9 strategy, termed homology-independent targeted integration (HITI) (**Figure 4.2A**) (Suzuki et al., 2016). HITI has been used successfully in the adult mouse brain to correct gene mutations associated with the neurodegenerative condition, retinitis pigmentosa, with moderate efficiency (Suzuki et al., 2016). Genomic knock-in of the mutant *KCNC1* gene, using HITI, therefore represents one strategy by which the effects of $K_V3.1b^{R320H}$ could be modelled *in vitro*.

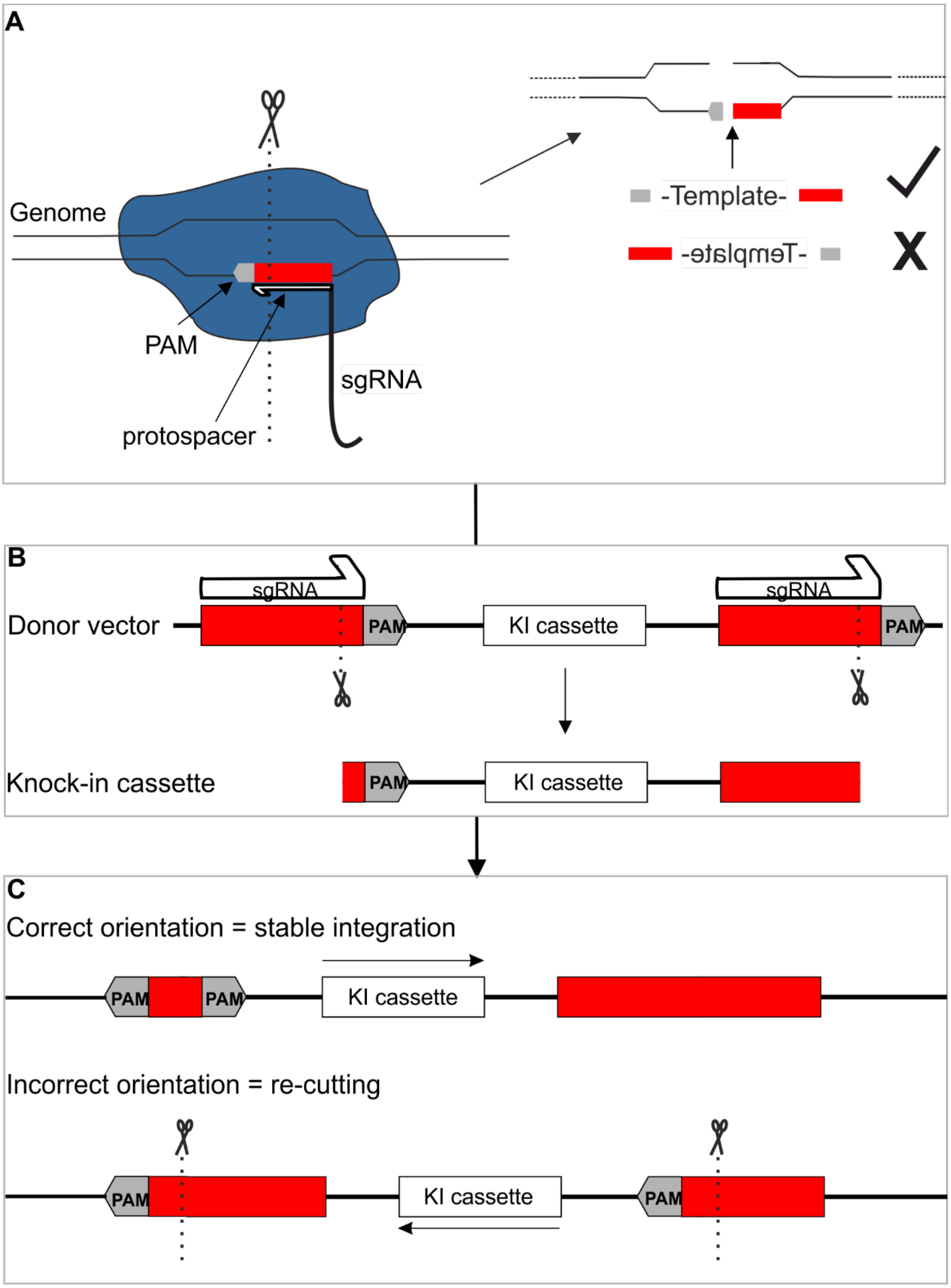

Figure 4.2. Homology-independent targeted integration (HITI). **A)** Schematic overview of HITI. sgRNA molecules direct the Cas9 endonuclease to the target genomic locus via complementary base-pairing of the 20 nucleotide sgRNA protospacer element of the sgRNA with its target sequence. Once recruited to the genome, Cas9 introduces DSBs 6 nucleotides immediately downstream of the PAM site. The HITI template is inserted at the site of the DSB via NHEJ. Stable transgene expression is only achieved when the template is inserted in the correct orientation (tick). **B)** The HITI template is released from the donor vector by sgRNA-guided Cas9 activity, using identical sgRNA target sequences and PAM sites found within the target genomic locus. **C)** Stable transgene integration is achieved only when the sgRNA-PAM configuration, required for Cas9 cleavage, is destroyed. This occurs when the transgene is inserted in the correct orientation. When the HITI template is inserted in the incorrect orientation, the sgRNA-PAM target site is regenerated, resulting in re-excision of the HITI template by Cas9.

HITI, like HDR-based methods, requires the delivery of three components: the Cas9, the sgRNAs and the DNA template for transgene integration. The HITI method uniquely, however, employs a specific vector configuration that simultaneously facilitates the release of a linear dsDNA knock-in cassette and ensures the correct orientation of transgene integration (**Figure 4.2B & C**). Recently, I successfully used HITI, in cortical neuronal culture, to knock-in a WT *KCNA1* exon into the *Kcna1* genomic locus, as part of a gene therapy strategy aimed at correcting disease-causing dominant negative mutations in $K_V1.1$ (**Figure 4.3**).

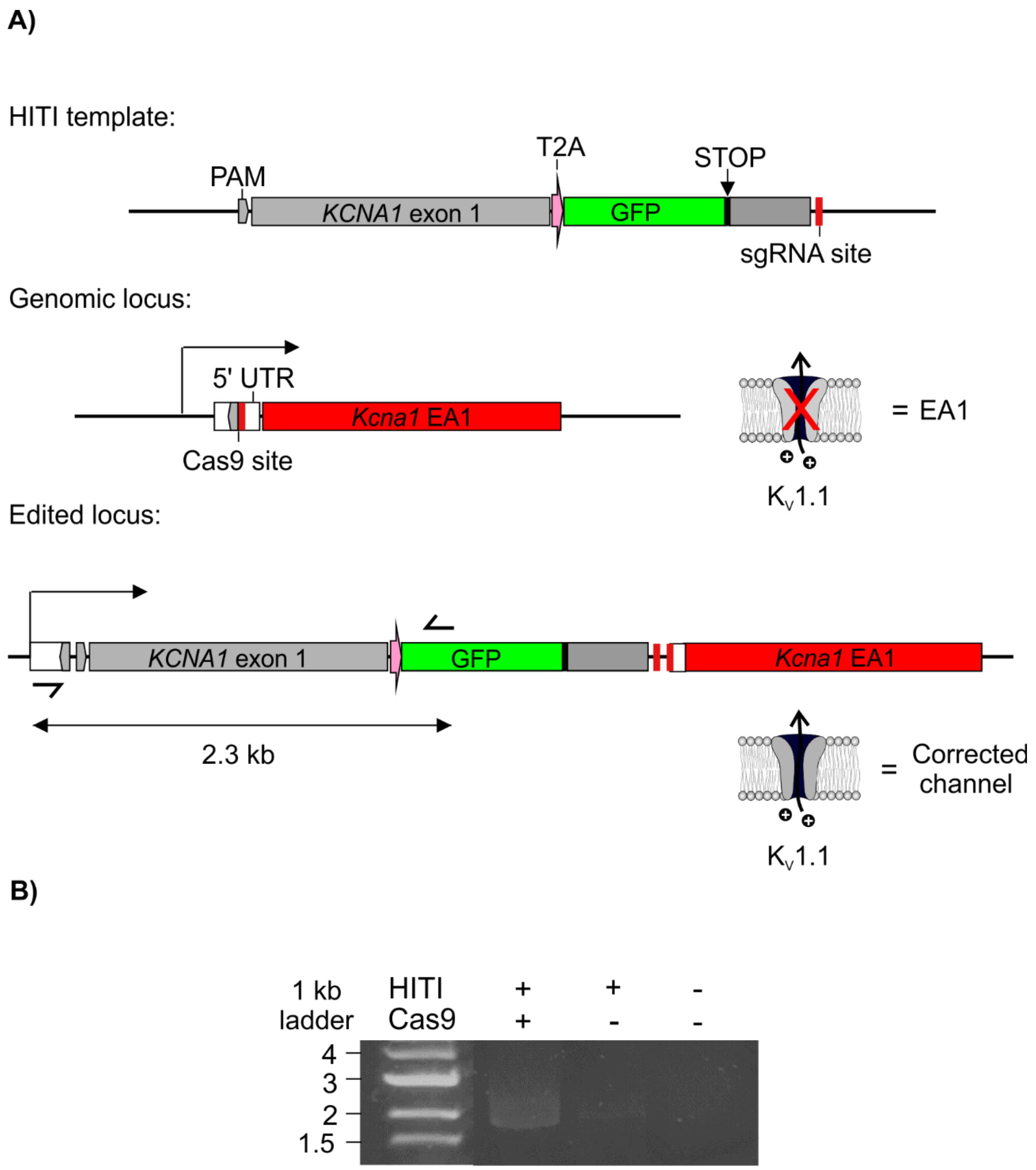

Figure 4.3. HITI to correct dominant negative mutations in *KCNA1* (Kv1.1). A) Dominant negative mutations in *KCNA1* can be causative for Episodic Ataxia Type 1 (EA1). Conveniently, Kv1.1 is encoded by a single exon, thus the mere insertion of the WT *KCNA1* gene (followed by a stop codon) into the *KCNA1* genomic locus (or in this case the murine *Kcna1* locus) can be corrective (because transcription of the mutant Kv1.1 exon is prevented). The *KCNA1*-HITI template includes GFP as a reporter of successful genomic knock-in. Knock-in of the HITI template can therefore be confirmed by genomic PCR using PCR primers that prime within GFP (which is not endogenously present in the genome under control conditions) and the 5' untranslated region (UTR) of (genomic) *Kcna1*. If HITI is successful, a PCR amplicon of 2.3 kb is expected. **B)** Genomic PCR reveals successful integration of the HITI template in neurons. Cortical neurons were transduced with AAV9-*KCNA1*-HITI and AAV9-Cas9 at 6 DIV. Genomic DNA was harvested at 14 DIV and PCR was performed using the forward and reverse primers

indicated in panel A. A single band at ~2 kb was observed in the HITI condition, which is indicative of successful template integration. Very faint or absent bands are observed in the AAV9-HITI only condition (HITI +/ Cas9 -) and non-transduced (HITI -/ Cas9 -) conditions. Genomic PCR was performed by T.Turner, a PhD rotation student under my supervision.

NHEJ-based HITI thus represents a suitable strategy with which to generate a CRISPR/Cas9-based *in vitro* model of MEAK. In this chapter, I will discuss the development of such an approach and present preliminary data pertaining to its eventual implementation. Here, I also describe the design of a conditional knock-in mouse model of MEAK that will be generated in collaboration with Harwell, Oxford, using HDR-based CRISPR/Cas9 technology.

4.2 The development of an *in vitro* CRISPR/Cas9 model of MEAK

4.2.1 Towards a CRISPR/Cas9-based knock-in model of MEAK

The c.959.G>A mutation, causative for MEAK, is harboured by exon 2 of the *KCNC1* gene, which is common to the two functional splice isoforms of $K_V3.1$: $K_V3.1a$ and $K_V3.1b$ (**Figure 4.4**). The c.959 G>A mutation could therefore be incorporated into *Kcnc1* transcripts (in murine neuronal cultures) via the genomic insertion of a transgene containing the mutant version of exon2 into the *Kcnc1* genomic locus. HITI for gene knock-in insurmountably adds a few nucleotides (~10 bp) 5’ and 3’ of the site of transgene integration. As a result, I chose to target our knock-in to intron 1, 200 bp upstream of the WT exon 2, in order to avoid disrupting protein coding sequences as well as any sequences involved in splice regulation, which tend to be found at intron-exon boundaries (**Figure 4.4**).

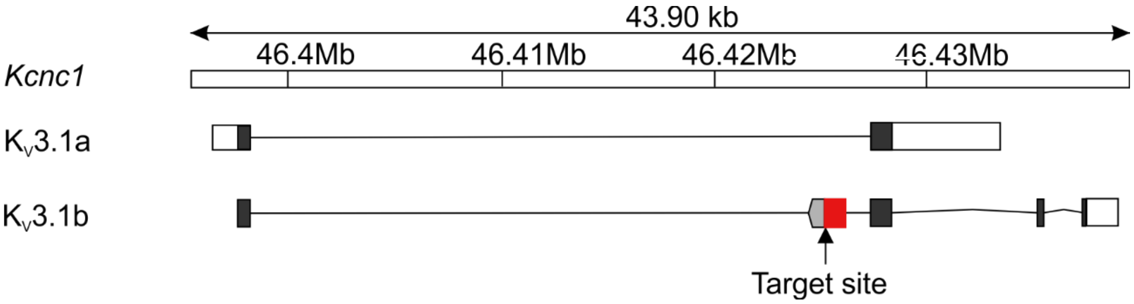

Figure 4.4. The exon-intron structure of the murine *Kcnc1* gene. The *Kcnc1* genomic locus is comprised of 4 exons and 3 introns. Alternative splicing of *Kcnc1* gene results in the generation of two splice isoforms: $K_V3.1a$ and $K_V3.1b$. $K_V3.1a$ is the shorter isoform and is comprised of exons 1 and 2 only. $K_V3.1b$ is comprised of all 4 exons. I chose to target intron1 of the *Kcnc1* gene for our HITI approach. Open rectangles: UTR; filled rectangles: exons; grey arrow: PAM site; red rectangle: sgRNA target sequence.

In order to express the $K_V3.1^{R320H}$ channel, I needed to exclude WT exon 2 from the *Kcnc1* transcript. This approach would require the inclusion of a stop codon after the inserted mutant exon, in order to terminate translation. However, this approach comes with the limitation that WT exons 3 and 4 would also be excluded from the transcript, resulting in the generation of $K_V3.1a$ only. As $K_V3.1b$ is the predominant isoform in the adult brain, I preferred to exclusively express $K_V3.1b$ instead of $K_V3.1a$, and designed our transgene so that it contained cDNA encoding exons 2 (carrying the c.959 G>A mutation) 3 and 4, followed by a stop codon (**Figure 4.5**) (Liu & Kaczmarek, 1998; Perney et al., 1992). A schematic of the HITI template, which will be used in future experiments for this application, can be found in **Figure 4.5**.

Genomic insertion of the HITI template requires that other molecular components also be delivered. First, a separate plasmid encoding Cas9 is required in order to generate DSBs in the targeted *Kcnc1* genomic locus (**Figure 4.5**). Secondly, the plasmid containing the HITI template also requires some additional features to make possible the targeting of the Cas9 to the *Kcnc1* gene locus (production of sgRNAs) as well as to provide a readout of successful transduction/ genomic knock-in (fluorescent reporter, **Figure 4.5**). The design and validation of sgRNA sequences will be discussed in **Section 4.2.2** and the development of a fluorescent reporter system will be discussed in **Section 4.2.3**.

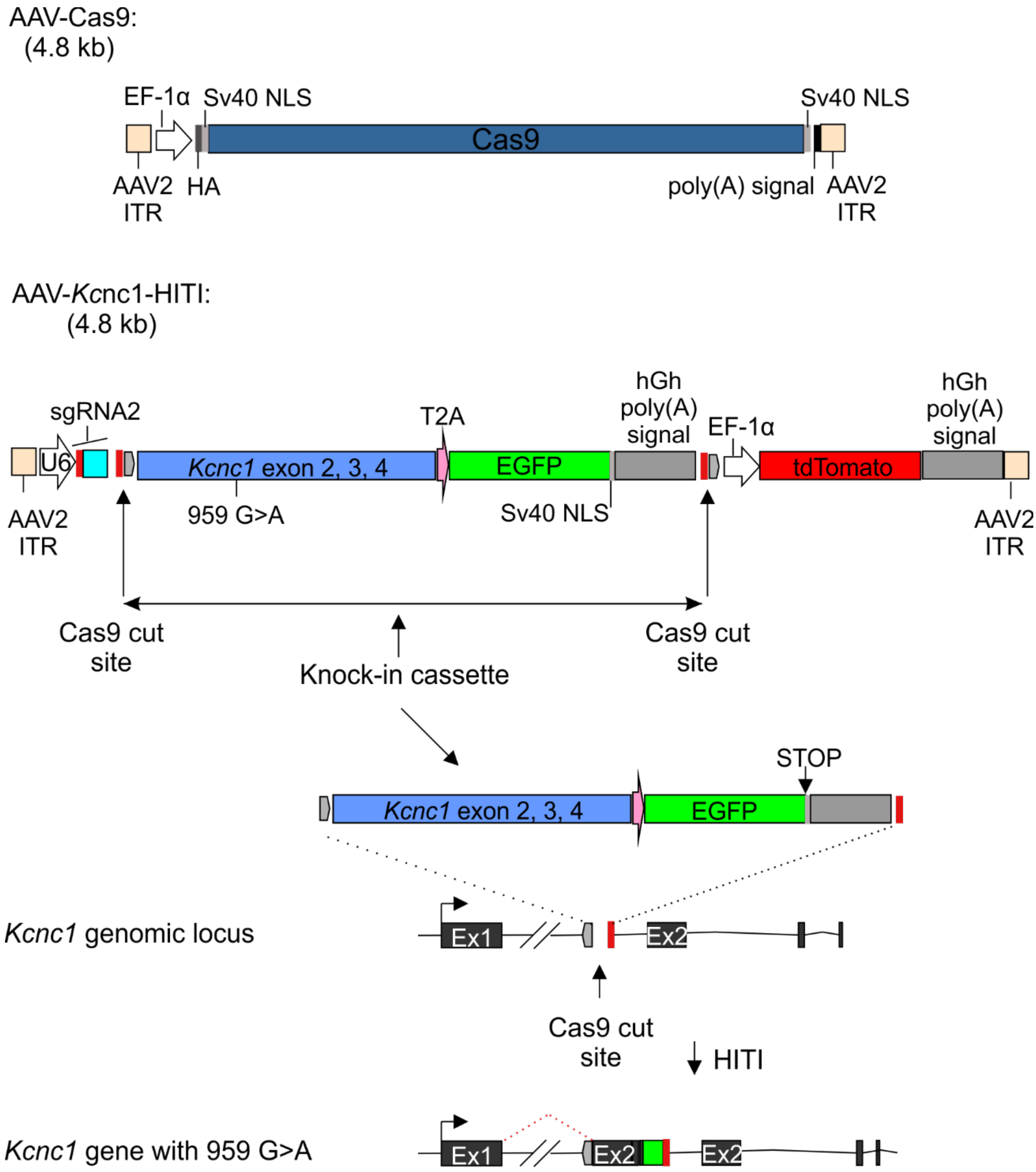

Figure 4.5. Schematic of *Kcnc1*-HITI vectors. The generation of a CRISPR/Cas9 knock-in model of MEAK in murine neuronal cultures would require the delivery of two vectors: AAV-Cas9 and AAV-*Kcnc1*-HITI. AAV-Cas9 delivers an HA-tagged, Cas9 protein that is required for the introduction of DSB into the genome. AAV-*Kcnc1*-HITI delivers: the sgRNA sequence under the control of the U6 promoter, required to target Cas9 to *Kcnc1* intron 1; the HITI template, consisting of cDNA for *Kcnc1* exon 2 carrying the 959G.A mutation as well as exons 3 and 4 and a tdTomato fluorescent reporter of transduction, driven by the EF-1α promoter. The HITI template also includes a GFP gene to act as a reporter of successful gene knock-in. The *Kcnc1* cDNA HITI template is flanked by Cas9 target sites that allow for the release of the template from the vector. This template is then integrated into *Kcnc1* intron1 via HITI. The inclusion of a splice acceptor site upstream of the inserted *Kcnc1* cDNA facilitates the incorporation of the mutant exon into the

mRNA transcript. The inclusion of a stop codon after the EGFP reporter gene prevents the incorporation of downstream WT *Kcnc1* exons into the mRNA transcript.

4.2.2 The *Kcnc1* genomic locus can be effectively targeted using sgRNAs

Targeting of Cas9 to the *Kcnc1* genomic locus first required the design and validation of sgRNAs. sgRNAs were designed to target ~200 bp upstream of *Kcnc1* WT exon 2, within the first intron, using an online CRISPR design tool (CRISPR.mit.edu, Zhang lab). I selected 3 of the most promising sgRNA sequences and interrogated their targeting specificity using an online tool. I found that none of the sgRNA candidates had off-target effects in protein coding genes (**Table 4.1**).

Table 4.1. Assessment of sgRNA targeting specificity

sgRNA	PAM	Probability off-target binding (%)	Number of off-target sites	Off-targets in ORFs
1	AGG	38.95	107	0
2	AGG	41.31	162	0
4	AGG	27.49	137	0

I next tested the efficiency of our selected sgRNA targeting sequences in P19 cells. A mouse cell line (P19) was used in these experiments to minimise the occurrence of sequence mismatches between sgRNAs and the target genomic locus because a mouse reference genome was used in the design of the sgRNAs. P19 cells were co-transfected with a plasmid encoding Cas9 and a plasmid containing the specific sgRNA sequence under the control of the U6 promoter. Co-transfected cells were isolated by incubation in selective media and genomic DNA of the surviving cells was harvested 48 hr post-transfection.

sgRNA efficiency was assessed using a T7 Endonuclease I (T7E1) mismatch cleavage assay. The T7E1 assay is a semi-quantitative approach designed to detect indels at sites of Cas9 cleavage that result from error-prone NHEJ DNA repair pathways. I performed a PCR of the genomic region encompassing the 3’ end of intron 1 and the 5’ end of exon 2 to act as a substrate for the assay. I subjected the PCR amplicon to repetitive rounds of denaturation and re-annealing in order to generate a pool of heteroduplexes where base-pair mismatches occur around sites of Cas9 cleavage. Mismatches result in regions of single-stranded DNA that form the substrate for T7E1 cleavage (Mashal et al., 1995).

I used gel electrophoresis to analyse the DNA fragments resulting from T7E1 endonucleatic cleavage. I found that sgRNAs 1, 2 and 4 were able to effectively edit the target genomic locus, as evidenced by the reduction in signal intensity of parental DNA band (883bp amplicon) as well as the appearance of additional bands corresponding to T7E1 DNA cleavage products in sgRNA conditions, with respect to the control (Cas9 only) condition (**Figure 4.6C,** experiment performed by J.Heneine, an MSc student under my supervision). In order to determine which sgRNA was the most efficient at editing the *Kcnc1* genomic locus, I calculated the indel frequency for each sgRNA. sgRNA2 was found to be the most efficient of all the candidate sequences, with an indel frequency of 36.6%. The lower editing efficiency of sgRNA1 was expected following the identification of a single nucleotide polymorphism in its targeting sequence following sequencing of the PCR amplicon obtained for the control condition (Cas9 only) (**Figure 4.6A**). Indeed, I decided not to include sgRNA3 in the T7E1 cleavage assay of **Figure 4.6C** because its genomic target sequence overlapped with that of sgRNA1 which also included the single nucleotide polymorphism. I therefore chose sgRNA2 as the gRNA for our HITI approach.

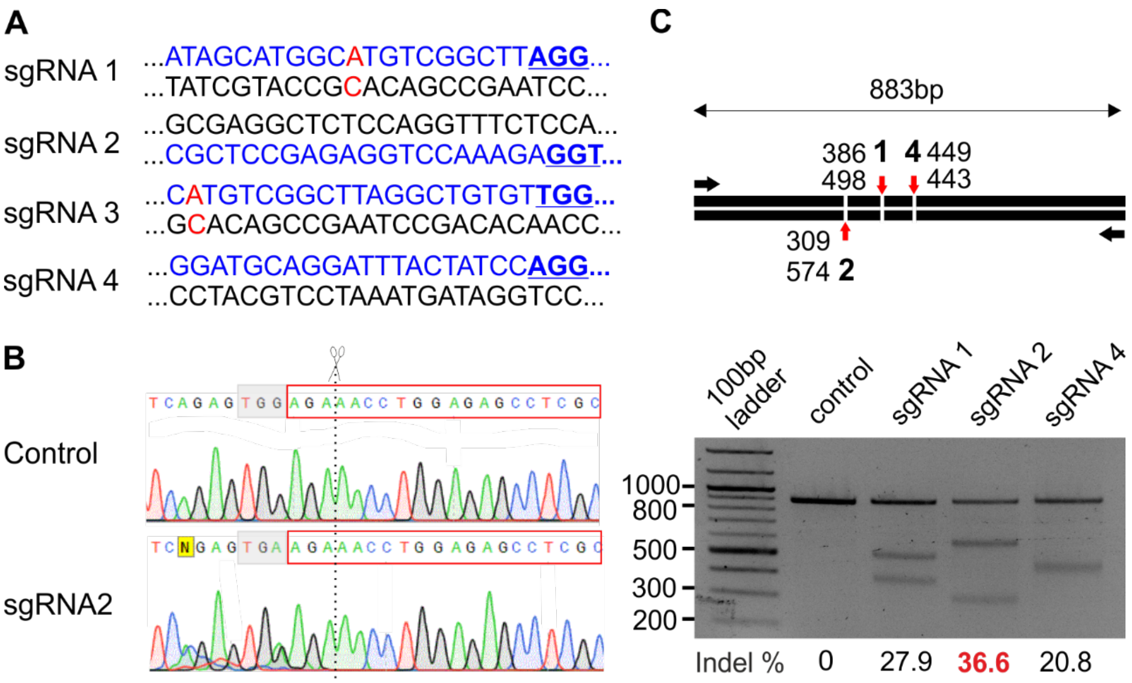

Figure 4.6. Effective targeting of the *Kcnc1* genomic locus by sgRNAs. A) Candidate sgRNA sequences and their genomic targets. Blue: sgRNA protospacer; underlined: PAM site; red: sgRNA-target mismatches resulting from the presence of single nucleotide polymorphisms (deviation from the Ensembl genome reference sequence). **B)** Confirmation of indels by DNA sequencing. Cas9-guided cutting by sgRNA2 results in a scrambled DNA sequence around the PAM site. Control: P19 cells transfected with Cas9 only; sgRNA2: P19 cells transfected with Cas9 and pKLV-sgRNA2; red box: 20 nucleotide target sequence; grey box: PAM site. **C)** T7E1 endonuclease assay to assess sgRNA targeting efficiencies. Upper panel: schematic of 883 bp

PCR amplicon following PCR of the *Kcnc1* intron 1-exon 2 boundary. Red arrows indicate sites of sgRNA-guided Cas9 cleavage with the expected size of T7E1 cleavage products. Bottom panel: 2% analytical agarose gel for the T7E1 endonuclease assay. Control lane: P19 cells transfected with Cas9 only; sgRNA1, 2 & 4: multiple bands are observed due to T7E1-mediated cleavage of single-stranded DNA mismatches - created by the presence of indels. Genomic PCR and T7E1 endonuclease assay performed by J.Heneine, an MSc student under my supervision.

4.2.3 Developing a live fluorescent reporter of gene knock-in events

The overall aim of our approach was to generate an *in vitro* CRISPR-Cas9-based model of MEAK using primary neuronal cultures. I was aware, however, that even if successful genomic knock-in of our HITI cassette was achieved, the utility of such an approach will depend largely on the ability to identify edited cells in culture. The only published study to attempt this, transfected primary neuronal cultures with HITI constructs and used GFP as a reporter for HITI-mediated genomic integration – via GFP knock-in downstream of the TubIII gene, to create a β-III tubulin-GFP fusion protein (Suzuki et al., 2016). However, this experiment served more as a proof-of-principle of the feasibility of the HITI method in neurons, rather than as a live reporter of gene knock-in. Indeed, the authors estimated the editing efficiency of HITI by immunolabelling for GFP, suggesting that a live fluorescence readout was not attainable. In transfected primary cortical cultures the editing efficiency was found to be ~56% of transfected cells and only 0.58% of the total cell population, emphasising the need for a reporter of transfection as well as of gene editing. I therefore sought to develop a live fluorescence reporter system of genomic knock-in.

4.2.3.1 The development of a PTG-based live fluorescent reporter system

Our original strategy was to express a fluorescent reporter gene (GFP) downstream of the inserted transgenic *Kcnc1* exons using a T2A-signal peptide sequence (**Figure 4.5**). However, preliminary findings from the lab (in association with the *KCNA1*-HITI project of **Figure 4.3**) has shown that this approach does not allow for the live detection of GFP, presumably because of low expression from weak endogenous promoters. I instead aimed to develop an alternative approach that exploits the multiplexing capabilities of the CRISPR/Cas9 system, whereby knock-out (as opposed to knock-in) of GFP is conditional upon successful template integration. In our proposed approach, GFP knock-out is achieved by NHEJ following the engineering of DSBs into the GFP gene by Cas9, guided by sgRNAs complementary to GFP.

Cas9 multiplexing in mammalian cells typically requires the expression of multiple sgRNAs from multiple Pol III promoters, such as the U6 promoter. Recently, however, it has been demonstrated that multiple sgRNAs can be produced from a single U6 promoter using a polycistronic-tRNA-gRNA (PTG) gene in human and mouse cells (Dong et al., 2017; Xie et al., 2015; Xu et al., 2017). A PTG gene has a tRNA precursor – gRNA architecture that is tandemly repeated (**Figure 4.7**) (Xie, Minkenberg, & Yang, 2015). The processing and release of sgRNAs from tRNA precursors is achieved using the cell's endogenous tRNA-processing system, using the ribonucleases, RNaseP and RNaseX. This tRNA processing system is thought to be highly conserved across all living species and has shown to be active in human cells *in vitro* and in murine cells *in vivo* (**Figure 4.7**) (Xie & Yang, 2015; Xu et al., 2017). A PTG gene, therefore, is one way in which sgRNAs targeted to the *Kcnc1* genomic locus and GFP could be simultaneously expressed.

As a proof-of-principle of a PTG-based GFP knock-out reporter strategy for HITI events, I designed a vector that contained a PTG gene driven by the U6 promoter, as well as two fluorescent reporters, tdTomato and EGFP, driven by the EF-1α promoter (**Figure 4.7**). The PTG gene contained two sgRNA sequences that had previously been shown to be effective in targeting EGFP (Hu et al., 2018). I decided to include two gRNA sequences targeting EGFP to increase the probability of gene knock-out resulting from NHEJ. The bicistronic expression of tdTomato and EGFP was achieved using a T2A signal peptide so that tdTomato and EGFP would be expressed at a 1:1 ratio. EGFP was sub-cloned downstream of tdTomato so as to prevent any frameshift mutations introduced in the EGFP gene interfering with the expression of tdTomato fluorescence.

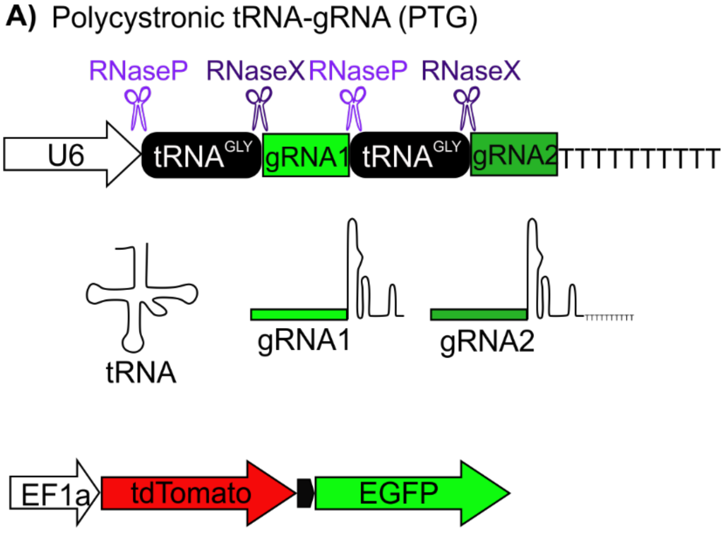

Figure 4.7. A PTG-based fluorescent reporter system. Our proposed live dual fluorescent reporter system is based upon GFP knock-out following the synthesis of sgRNAs, targeting Cas9 to GFP, from a PTG gene. PTG genes have a tRNA-gRNA tandemly repeated structure. sgRNAs can be precisely processed and released from PTG transcripts by the endogenous ribonuclease activities of RNaseP and RNaseX. Bottom panel: schematic of the dual fluorescent reporter construct (pCCL-PTG) that provides a readout of successful HITI events. Bicistronic expression of tdTomato and GFP, at a 1:1 ratio, is achieved using a T2A signal peptide sequence. tdTomato fluorescence in the absence of GFP fluorescence acts as a reporter of HITI-mediated knock-in events (when the PTG gene is inserted in the intron of the transcribed gene locus) or as a reporter of co-transduction (the presence of Cas9). Adapted from Xie, Minkenberg, & Yang, 2015.

In order to test whether this system is effective in nullifying the expression of GFP fluorescence, I co-transfected HEK cells with the PTG reporter construct (pCCL-PTG) (**Figure 4.7**) and a plasmid encoding FLAG-tagged Cas9 (experiment performed by T.Turner). As a control, HEK cells were transfected with pCCL-PTG only. HEK cells were fixed 72hr post-transfection and immunolabelled for the FLAG-tag marker (if co-transfected with Cas9). In HEK cells co-transfected with Cas9 plasmid, I found many cells expressing FLAG-tagged Cas9 protein, however the occurrence of both GFP fluorescence and tdTomato was rare (**Figure 4.8**). This is in contrast with HEK cells transfected with the PTG-reporter plasmid only, where many cells were observed to express both GFP and tdTomato (**Figure 4.8**). This unexpected result suggests that sgRNA-directed destruction of GFP was effective, but also interferes with the expression of tdTomato.

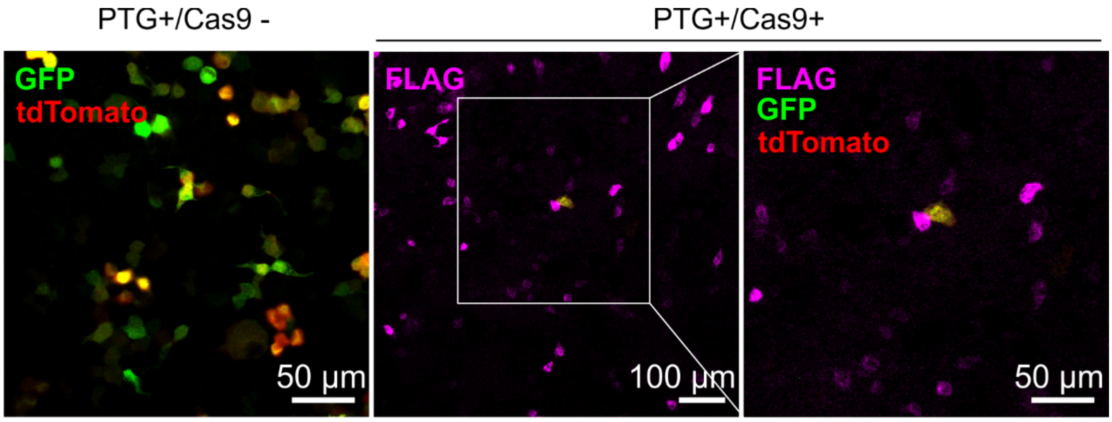

Figure 4.8. Cas9 ablates both GFP and tdTomato fluorescence when sgRNAs are targeted to GFP as part of a bicistronic reporter construct. P19 cells transfected with the PTG-reporter plasmid in the absence of Cas9 (PTG+/Cas9-) express both GFP and tdTomato fluorescence. P19 cells expressing either tdTomato or GFP fluorescence are rare when co-transfected with Cas9, as indicated by FLAG-tag immunolabelling. HEK cell transfection and confocal imaging performed by T.Turner, a PhD rotation student under my supervision.

4.2.3.2 A PTG-based approach as a reporter of successful genomic knock-in

I have shown in preliminary proof-of-principle experiments, that a PTG-based dual fluorescence reporter approach to label edited cells, holds potential, but needs refining. The implementation of such an approach as a genuine readout of template integration (not merely the presence of Cas9) is, however, majorly limited by the fact that the U6 promoter (and thus the production of GFP sgRNAs) is constitutively active. Recently, however, it has been demonstrated in rice plants that introns can be engineered to express PTG genes, thus circumventing the requirement for a U6 promoter (Ding et al., 2018).

I therefore envisage an approach whereby a PTG-gene, expressing gRNA against GFP, is inserted into the intron of the *Kcnc1* gene alongside cDNA encoding the 959>G.A mutation in the *Kcnc1* gene (**Figure 4.9**). I reasoned that the expression of the edited *Kcnc1* gene would allow for the production and release of sgRNAs directed against GFP, such that GFP knock-out becomes conditional upon successful integration of the HITI template. Neurons that express tdTomato fluorescence only, therefore, would represent cells expressing the K$_V$3.1b^{R320H} mutant channel. This approach needs experimental validation.

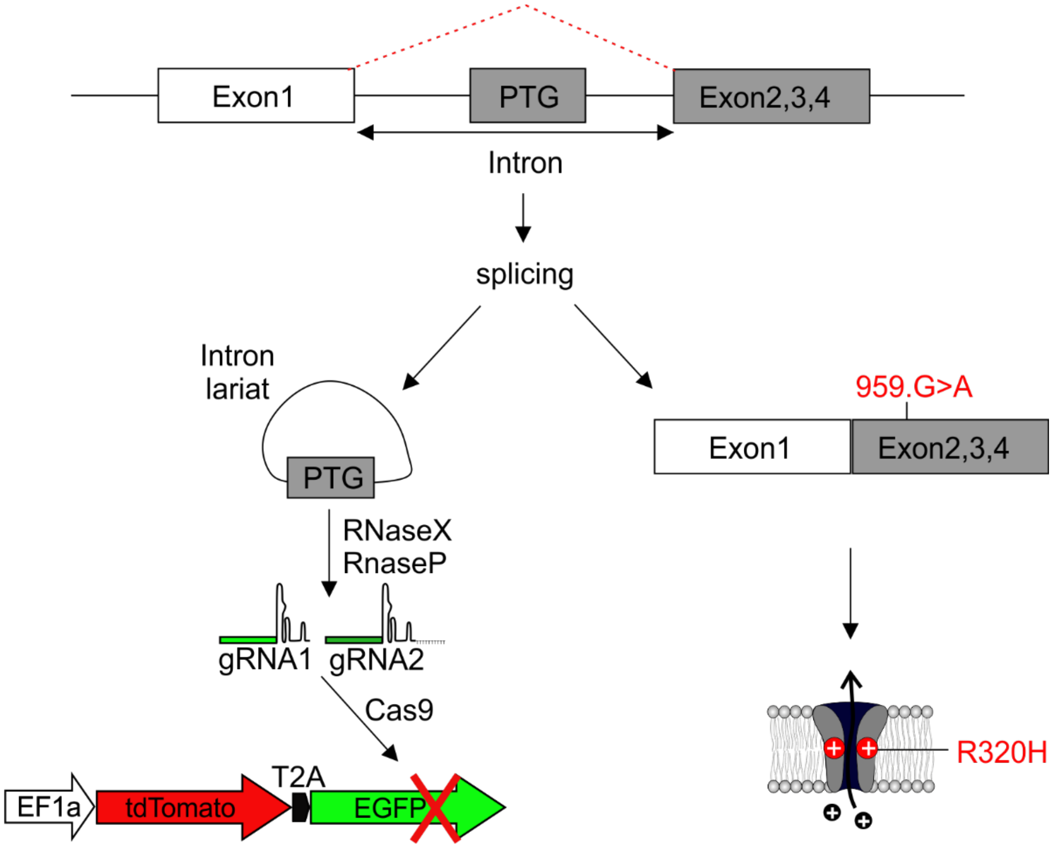

Figure 4.9. A PTG-based, live fluorescent reporter strategy for the visualization of gene edited neurons. A HITI template containing a PTG gene and transgenic exons 2-4 of the *Kcnc1* gene is knocked-in to intron1 of the *Kcnc1* genomic locus. Expression of the *Kcnc1* gene results in splicing of WT exon1 to mutant exons 2, 3 and 4 and the release of an intron lariat containing the PTG gene. The endogenous tRNA processing machinery, acts on the intron lariat to precisely release sgRNAs targeted to GFP. These sgRNAs direct the destruction of the GFP gene via NHEJ mechanisms following the introduction of Cas9-mediated DSBs. Thus, cells that are expressing the mutant $K_V3.1b^{R320H}$ channel can be identified by the presence of tdTomato, in the absence of GFP.

4.3 The development of a conditional knock-in mouse model of MEAK

Modelling the neuronal effects of genetic mutations *in vitro* can provide important early insights into disease mechanisms. However, even when the mutation is expressed at physiological levels, as might be achieved with CRISPR-based methods such as HITI, the developmental, circuit and behavioural effects can only be well understood and appropriately examined in *vivo*. Unfortunately, during this PhD I had no access to a mouse model of MEAK and were unable to model the effects of $K_V3.1^{R320H}$ expression *in vivo,* using stereotaxic viral injection, because of difficulties involved in obtaining high titre lentivirus, potentially due to HEK cell toxicity during viral production.

Instead, during this PhD project, I applied for a conditional knock-in mouse model of MEAK, which was awarded funding by the Genome Editing Mice for Medicine (GEMM) initiative, in association with the MRC Harwell Institute in Oxford. I proposed that the generation of this mouse model will facilitate multiple advances in neurological research. Firstly, it would allow for the assessment of the effects of $K_V3.1^{R320H}$ on neuronal survival when expressed at physiological relevant levels. Secondly, it would allow for us to more accurately assess whether the pathogenic effects of $K_V3.1^{R320H}$ is via a dominant negative mechanism, as neurons *in situ* are likely express a different complement of K_V3 channels (again more physiologically relevant) compared to neurons culture, especially depending on the cell type. Finally, the conditional nature of our proposed knock-in mouse promises to address important mechanistic questions relevant to a range of epileptic disorders, such as the circuit bases for the generation of seizures and myoclonus, by crossing the mouse to relevant Cre-driver lines. This mouse will be available to the wider scientific community via the European mouse mutant archive.

4.3.1 Achieving conditional genomic knock-in of the *Kcnc1* c.959.G>A mutation

In order generate a conditional knock-in model of MEAK, I designed an expression cassette that would be used as the template for site-directed integration following the guided generation of DSBs by CRISPR/Cas9 (**Figure 4.10**). The cassette consists of a flexed mutant allele (comprised of cDNA encoding exons 2, 3 and 4, with the c.959 G>A mutation) and a floxed WT allele (composed of WT exons 2, 3, 4). The mutant allele is present in the inverse orientation, such that the expression of the mutant *Kcnc1* transgene is conditional upon Cre-recombinase (**Figure 4.10A**). The WT allele is floxed (flanked by LoxP sites) and is knocked-out upon the expression of Cre (**Figure 4.10B**). The cassette will be knocked-in to intron 1 ~200bp upstream of the splice acceptor site of exon 2.

The combination of Flexed and floxed elements ultimately results in the incorporation of mutant exons containing the pathogenic mutation into transcripts of the *Kcnc1* gene, within the cell types in which K_V3.1 endogenously expressed. This configuration allows for the production of the K_V3.1b isoform only; the rational for choosing this isoform, over K_V3.1a, has been discussed previously in this chapter. The sequences used in the design of the knock-in cassette can be found in the Appendix of this chapter. Technical and logistical expertise for the generation of this knock-in (i.e. the design of sgRNA and embryonic stem cell work) will be provided by Harwell.

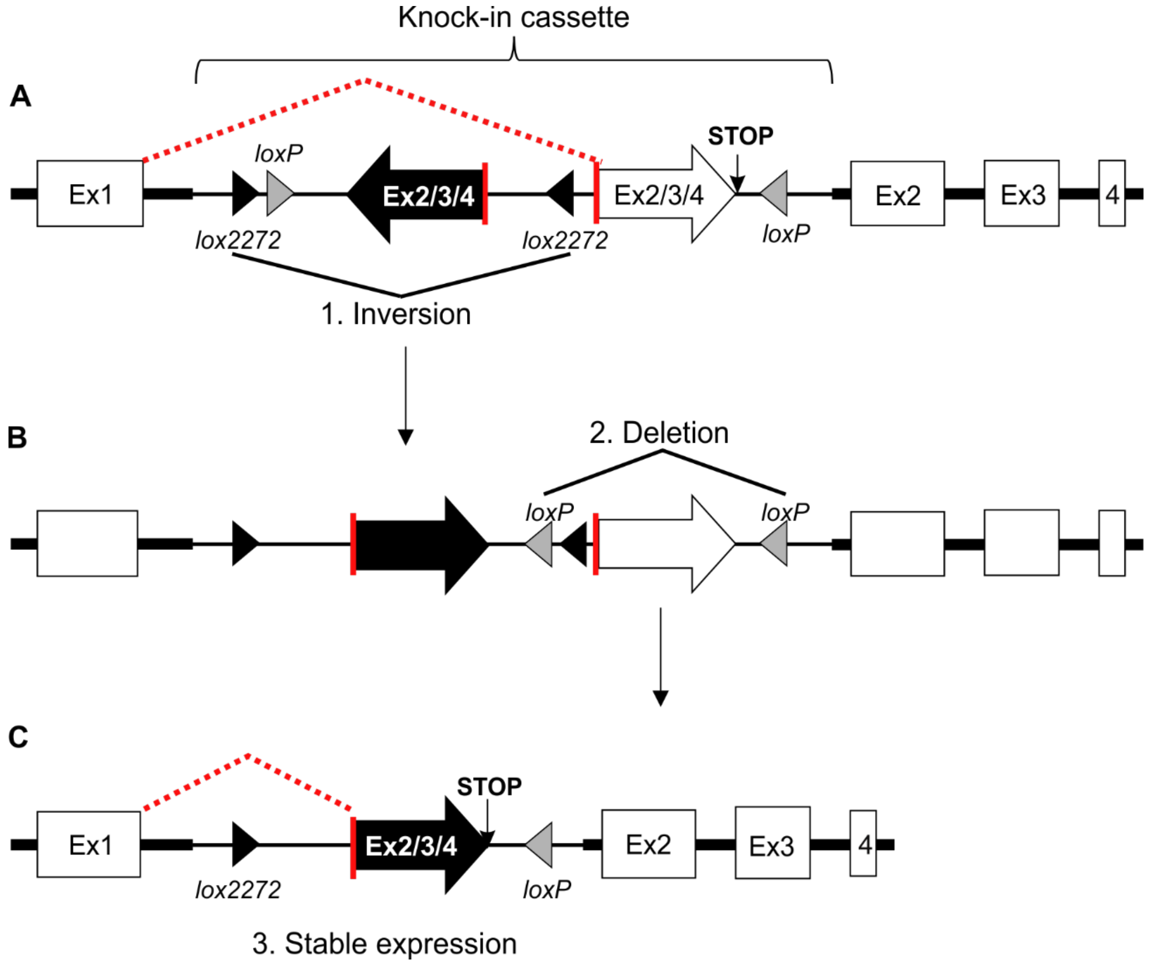

Figure 4.10. Genetic architecture of a conditional knock-in mouse model of MEAK. A) In the absence of Cre recombinase, WT exon 1 is spliced to a transgenic exon containing cDNA for WT exons 2, 3 and 4 (white arrow) located within intron 1 of the *Kcnc1* genomic locus. In the presence of Cre-recombinase, a DNA recombination event occurs between two inversely orientated lox2272 sites resulting in the inversion of the intervening genomic DNA sequence. **B)** Following recombination of lox2272 sites, transgenic exon 2, 3 and 4, which contains the c.959G>A PME-associated mutation (black arrow) is now found in the sense orientation and can be incorporated into a mRNA transcript by splicing (dashed red line) due to the correct orientation and availability of a splice acceptor (red line). A second DNA recombination event occurs between lox P sites in the same orientation resulting in the deletion of the intervening DNA sequence, which comprises the transgenic WT exon 2, 3, 4 (white arrow). **C)** In Cre-recombinase containing cells, WT exon1 is spliced to mutant exon 2, 3 & 4 to result in the expression of the mutant channel, $K_V3.1b^{R320H}$.

4.4 Discussion

Neurological disease models are experimental systems that aim to recreate some or all of the pathological processes observed in the human disease. By definition, a disease model will never perfectly appropriate all aspects of a disease and so experimental results should be interpreted with the specific limitations of the model in mind. In light of the severe phenotypes observed for $K_V3.1b^{R320H}$ overexpression I sought to develop an *in vitro* and *in vivo* model of MEAK based on genomic expression of the mutant channel. These models are based upon the use of CRISPR/Cas9 technology which facilitate efficient gene knock-ins via the engineering of precisely targeted DSBs. I propose that these models have high physiological relevance and will enhance our understanding of the disease mechanisms underlying MEAK.

4.4.1 The feasibility of an *in vitro* CRISPR/Cas9 model for MEAK

While, due to time limitations, I have not been able to implement our HITI approach in neuronal cultures, I have performed some essential early experiments to demonstrate the feasibility of the approach. Firstly, I have demonstrated that I are able to efficiently target the *Kcnc1* genomic locus using sgRNAs and have designed a vector for the delivery of knock-in cassette following sgRNA-mediated cutting by Cas9. In association with another project that aims to cure, rather than model, dominant negative mutations in neurological disease, I have also demonstrated successful HITI in primary cortical neurons.

I have also gone some way towards developing a live fluorescent reporter system of gene knock-in events based on the multiplexing capabilities of the CRISPR/Cas9 system. However, whilst early characterisation suggests that this approach is promising it has also revealed some limitations. Firstly, whilst sgRNAs against GFP can be processed from the PTG and are effective in nullifying the expression of GFP fluorescence, it appears that the destruction of the GFP gene also prevents the expression of tdTomato fluorescence. The bicistronic expression of these two fluorescent reporters is achieved using a T2A signal peptide sequence which means that GFP and tdTomato are encoded by a single gene transcript. The separate production of these two polypeptides is achieved at the post-translation level by ribosome skipping. I speculate that the disappearance of both fluorescent markers when Cas9 is expressed could be due to nonsense mediated decay of the mRNA transcript, resulting from nonsense mutations inserted into the GFP gene. Thus, in the future, this approach will require the production of the two reporter genes from two different promoters. If this strategy is shown to be effective it will then be necessary to show that this tRNA processing system is active in neurons in culture. Following this, I will need to show that processing of the PTG gene can still occur in the context of an intron.

If I am able to successfully perform HITI of mutant *Kcnc1* exons in primary neuronal cultures, I hope to use this approach in the future in order to see if I can replicate some of our early findings regarding the effects of $K_V3.1b^{R320H}$ neuronal survival and development. Once implemented, such an approach using CRISPR/Cas9-based gene knock-in in neuronal cultures might also be applied to the study of other dominant negative mutations.

C**.**G to T**.**A base pair transitions, such as that which occurs in $K_V3.1$, account for over half of known pathogenic point mutations found in humans (Krokan et al., 2002). In the future, such base pair transitions are likely to be corrected or modelled using base-pair editing, a type of genome editing technology that involves the irreversible conversion of one base-pair to another without the introduction of DSBs or donor DNA templates (Komor et al., 2016). Currently, base pair editors are in their infancy and are broadly limited in application due to highly restrictive targeting sequence requirements (Gaudelli et al., 2017). However, in the future, the advancement of such technologies will likely supersede HITI-based approaches for correcting/modelling diseases caused by point mutations at the genomic level.

4.4.2 A conditional mouse model of MEAK may provide deeper insights into PME disease mechanisms

Currently only a few mouse models of PME exist. These models are mainly gene knockouts, because most forms of PME are autosomal recessive. Examples include ULD, LBD and selected CLNs. Fly models are also available for selected PMEs such as NS-PME and PME and Ataxia caused by mutation in the *PRICKLE1* gene. These animal models have been useful for providing insights into the individual genetic pathologies, but attempts have not yet been made to develop a model that would help to identify disease mechanisms common across the syndrome.

No animal models for MEAK currently exist or are publicly available. Here, I have outlined the design of a conditional knock-in mouse model of MEAK that promises to lend insight not only into disease mechanisms specific to mutation of $K_V3.1$, but also into other types of PME, by allowing for the effects of the mutation to be studied in specific cell types and developmental ages. This mouse model promises to be an exciting step-forward for the field of PME research and may help us to more broadly understand the circuit mechanisms underlying ataxia and myoclonus.

4.5 Appendix

4.5.1 DNA sequences for the creation of a conditional knock-in mouse model

Below is the annotated DNA sequence of the knock-in cassette that will be used in the generation of a conditional knock-in mouse model of K_V3.1-based PME, or MEAK. Insertion of a knock-in cassette of 2854bp between 46427196–46428478 on chromosome 7.

ATAACTTCGTATAGGATACTTTATACGAAGTTATGCAGAATGGTAGCTGGATTGTAGCTGCT
ATTAGCAATATGAAACCTCTTA**ATAACTTCGTATAGCATACATTATACGAAGTTAT***AGATTC*
CTCTAGTAAGCTCCTGCCTTCCGAATTTGGCCGCCCAGCATCTCCCTGGGGTCCCAGGCT
CCACAACTCAAAGTTGGGCACAGGATCCTGGGTCGCCCGTGGAACTAAGGAAGCAGTCTG
ACTGGATCTGGAATCATTGCTACAGGGGGCGGAGGTGAAAGGTCAGATCGACATGCCTCT
*GAGAGGTTTCC*TAC*CTGCTCTGTTAATTTCTAAAATTTCTTCCTGGGCCAGCGGGCATGTG*
TCACTCTGAGTACTGTGGTGTGGAGAGTTTACGACAGATTTACAATAATTGGGAGATCCCA
GCTGTGGTGGCCGCGGAATATGCTTCTTTTTTTTCTTTGGTAGTTTCTGCTTAGCCATGGCT
AAAGAGTAGTACATCCCAAAATTGTTCACGATGACAGGCACCGGCATGGCAATGGTCAGCA
CACCAGCCAGAGCACACAAGGCTCCCACCAGCATTCCAGACCACGTCTGGGGATACATGT
CTCCATAGCCCAGTGTCGTCATGGTGACCACAGCCCACCAGAAGCCGATGGGGATGTTTT
TAAAGTGTGTGTGTTCGCTGGCGCTGGGGTCATTGGGCTGTGCCCCTATCCTCTCGGCGT
AGTAGATCATGGTGGCAAAGATGAGCACTCCCAGGGCCAGGAAGATGATAAGCAGCAGGA
ACTCGTTGGTGCTGGCACGGAGCGTGTGGCCCAGGACCCTCAGGCCCACGAAGTGGCGG
*GTCAGCTTGAAGATG**T**GCAGGATGCGCACGAAGCGGACGACGCGCAGGAAGCCCAGAAC*
GTCCTTGGCGGCTTTTGAGGACAGGCCGCTTAGGCCCACCTCCAGGTAGAAGGGGAGAAT
GGCCACAAAGTCAATGATATTGAGGGAGTTCTTGATGAATTCCACCTTGTTGGGGCAGAAG
ACGACACGCATGAGGAACTCGAAGGTGAACCAGACCACGCAGACGCCCTCGATGTAGGT
GAGGAAGGCCTCCGTCTCTGCTTCCCGGTAGTACCGCACTTGGGTGCCGTTTCGAACGTT
CTCGATTTCGGTCTTGTTCACGATGGGGTTGAAGCGCTCGTGAGTCTCCAGACAGAAGGTT
GTGATGGAGACCAGGATGAAGAAGAGGGAGGCAAAGGCCACATACTGTGGGTGAGAAAC
ATAGGGGGTCAGAGTAAAGGCTTCCCTTTCAGAGTGGAGAAACCTGGAGAGCCTCGCAGG
CCCAGGCCCAGTGGGCCACACCAGGGGCAGGTAATGCACAGAGCCCGTCCACTCCAACA
CAGCCTAAGCCGACATGCCATGCTATCCTCCTCAGAGCCTGGGGGTGGGGGGTAGGTGC
*TGCTGCT*ATAACTTCGTATAAAGTATCCTATACGAAGTTATAGCAGCAGCACCTACCCCCCA
CCCCCAGGCTCTGAGGAGGATAGCATGGCATGTCGGCTTAGGCTGTGTTGGAGTGGACG
GGCTCTGTGCATTACCTGCCCCTGGTGTGGCCCACTGGGCCTGGGCCTGCGAGGCTCTC
CAGGTTTCTCCACTCTGAAAGGGAAGCCTTTACTCTGACCCCCTATGTTTCTCACCCACAG
TATGTGGCCTTTGCCTCCCTCTTCTTCATCCTGGTCTCCATCACAACCTTCTGTCTGGAGAC
TCACGAGCGCTTCAACCCCATCGTGAACAAGACCGAAATCGAGAACGTTCGAAACGGCAC
CCAAGTGCGGTACTACCGGGAAGCAGAGACGGAGGCCTTCCTCACCTACATCGAGGGCG
TCTGCGTGGTCTGGTTCACCTTCGAGTTCCTCATGCGTGTCGTCTTCTGCCCCAACAAGGT
GGAATTCATCAAGAACTCCCTCAATATCATTGACTTTGTGGCCATTCTCCCCTTCTACCTGG
AGGTGGGCCTAAGCGGCCTGTCCTCAAAAGCCGCCAAGGACGTTCTGGGCTTCCTGCGC
GTCGTCCGCTTCGTGCGCATCCTGCGCATCTTCAAGCTGACCCGCCACTTCGTGGGCCTG
AGGGTCCTGGGCCACACGCTCCGTGCCAGCACCAACGAGTTCCTGCTGCTTATCATCTTC
CTGGCCCTGGGAGTGCTCATCTTTGCCACCATGATCTACTACGCCGAGAGGATAGGGGCA
CAGCCCAATGACCCCAGCGCCAGCGAACACACACACTTTAAAAACATCCCCATCGGCTTCT
GGTGGGCTGTGGTCACCATGACGACACTGGGCTATGGAGACATGTATCCCCAGACGTGGT
CTGGAATGCTGGTGGGAGCCTTGTGTGCTCTGGCTGGTGTGCTGACCATTGCCATGCCGG
TGCCTGTCATCGTGAACAATTTTGGGATGTACTACTCTTTAGCCATGGCTAAGCAGAAACTA
CCAAAGAAAAAAAAGAAGCATATTCCGCGGCCACCACAGCTGGGATCTCCCAATTATTGTA
AATCTGTCGTAAACTCTCCACACCACAGTACTCAGAGTGACACATGCCCGCTGGCCCAGG
AAGAAATTTTAGAAATTAACAGAGCAGGTAGGAAACCTCTCAGAGGCATGTCGATCTGACC

TTTCACCTCCGCCCCCTGTAGCAATGATTCCAGATCCAGTCAGACTGCTTCCTTAGTTCCA
CGGGCGACCCAGGATCCTGTGCCCAACTTTGAGTTGTGGAGCCTGGGACCCCAGGGAGA
TGCTGGGCGGCCAAATTCGGAAGGCAGGAGCTTACTAGAGGAATCT**ATAACTTCGTATAA
TGTATGCTATACGAAGTTAT**

4.5.1.1 Key:

Lox2272

loxP

Italicised: sequence found in the reverse complement

200bp 5’ intron 2

Exon 2

200bp 3’ intron 1

Branch-point

Polypyrimidine tract (Py10)

Acceptor-splice boundary

Donor-splice boundary

959 G>A in the reverse complement (T)

Chapter 5

Investigating the mechanisms of *GOSR2*-related PME (North Sea PME)

5.1 Introduction

North Sea PME (NS-PME) is caused by recessive, loss-of-function mutations in the gene encoding GOSR2. Patients homozygous for these mutations are severely ataxic, exhibit frequent and severe myoclonus and have infrequent epileptic seizures (Boissé Lomax et al., 2013). GOSR2 is an essential and ubiquitously expressed Qb-SNARE protein that is localized mainly to the cis Golgi and is required for ER-Golgi trafficking of secretory cargo, as well as cis-trans transport through the Golgi stack (Fusella et al., 2013; Kloepper et al., 2007; Volchuk et al., 2004). The substitution of a glycine for a tryptophan at amino acid position 144 (G144W), within the SNARE domain of GOSR2, is the major causative mutation for NS-PME (Corbett et al., 2011). Only one patient has been described with a different mutation in GOSR2 – the deletion of a lysine residue at position 164 (ΔK164) – which is also located within the SNARE domain of the protein (Praschberger et al., 2015). This patient is, however, compound heterozygous also for the G144W mutation (Praschberger et al., 2015).

In vitro liposome-fusion assays have shown that G144W and ΔK164 mutations in GOSR2 confer a partial loss of SNARE function (Praschberger et al., 2017; Völker et al., 2017). When the equivalent mutations were engineered into Bos1, the yeast orthologue of GOSR2, ΔK164 was shown to more severely reduce rates of membrane fusion than G144W (Praschberger et al., 2017). Reduced SNARE functionality seems to be the main cause of cellular dysfunction in PME as GOSR2 mutants have been shown to exit the ER and retain their ability to localize to the cis Golgi (Praschberger et al., 2017). Cellular dysfunction therefore most likely results from the downstream effects of an ER-Golgi trafficking bottleneck within the secretory pathway.

GOSR2 is expressed in all cells, yet PME-associated mutations in GOSR2 result in a remarkably restricted neurological disorder. Golgi trafficking assays in skin fibroblasts derived from a G144W GOSR2-PME patient did not reveal any alterations in trafficking kinetics, indicating that disease phenotypes are only precipitated under conditions of high secretory pathway demand (Praschberger et al., 2017). Neurons, on the other hand, may be more vulnerable to the effects of GOSR2 mutations because they are highly polarized cells that place significant demands on the secretory pathway. Indeed, previous unrelated studies have shown that blockade of ER-Golgi transport in neurons results in severely impaired dendritic growth that likely results from a shortage of ER-derived lipids and proteins required for plasmalemma expansion (Horton et al., 2005).

The effects of GOSR2 mutants have been studied *in vivo* using Drosophila. In Drosophila, the restricted expression of GOSR2 mutants to the CNS was shown to recapitulate all the behavioural phenotypes achieved by global expression of Membrin mutants, confirming that GOSR2 mutants disproportionately impair the functioning of the nervous system (Praschberger et al., 2017). Indeed, overexpression of Membrin mutants in sensory neurons of the fly larval body wall (ddaC) was found to result in a profound reduction in total dendritic length and arborisation (Praschberger et al., 2017). Mutations in GOSR2 have also been shown to alter neurotransmission. At the fly neuromuscular junction, morphological abnormalities and impaired neurotransmission at high stimulation frequencies have been observed (Praschberger et al., 2017). At the level of the whole organism, flies overexpressing Membrin mutants have a reduced electroconvulsive seizure threshold and impaired locomotion (Praschberger et al., 2017).

5.2 Aims and Objectives

In this chapter I aimed to characterise the effects of GOSR2 mutations in mammalian neurons.

1. I first aimed to develop an *in vitro* overexpression model of GOSR2-based PME. I chose cortical neuronal cultures as a model system because they are amenable to genetic manipulation, are an appropriate model with which to study neurite outgrowth and enable efficient electrophysiological recording.
2. My second aim was to characterise the effects of GOSR2 mutants on synaptic function. My first objective was to record mEPSCs in neuronal cultures overexpressing *GOSR2* transgenes. My second objective was to complement these recordings with immunocytochemical investigation of pre- and post-synaptic markers and western blotting for presynaptic proteins of interest.
3. My third aim was to characterise the effects of GOSR2 mutants on dendritic outgrowth and maintenance. Here, my main objective was to express *GOSR2* transgenes in cerebellar Purkinje cells *in vivo*, a highly relevant cell-type in the pathogenesis of ataxia.

5.3 An overexpression model of NS-PME

5.3.1 Overexpression of Membrin mutants phenocopies GOSR2 loss-of-function in a fly model of PME

The behavioural and neurophysiological effects of GOSR2 mutations have been previously studied using the model organism, *Drosophila melanogaster*. Base pair changes equivalent to the human G144W and K164Del mutations GOSR2 gene, were engineered into Membrin, the fly orthologue of GOSR2, and denoted Mem-G147W and Mem-ΔK166. Membrin mutants were then expressed on a Membrin null-background via targeted knock-in of Membrin transgenes into a safe-harbour in the fly genome, using HR (Praschberger et al., 2017).

Modelling the effects of Membrin/GOSR2 mutants in mammalian neurons poses more of a challenge than it does in flies. Genomic modification in flies is cheap, relatively rapid and well established. While genome editing in mammals has advanced considerably in the last decade, the generation of a mouse model is still time consuming and expensive, and thus was prohibitive for this project. The generation of a mouse model can be circumvented, however, via the exogenous delivery of mutant transgenes using viral vectors *in vivo* (stereotaxic injection), *ex vivo* (infection of organotypic slice) or *in vitro* (transduction of neuronal cultures).

In lieu of the viral delivery of GOSR2 mutants to mammalian neurons as the logical next step in modelling NS-PME, Jepson and Praschberger generated an additional fly model in which Membrin mutants were overexpressed on a WT background (instead of a null background) in order to investigate whether the simple overexpression of Membrin mutants could recapitulate the PME phenotypes described for the fly model above (Praschberger et al., 2017). They found that overexpression of both mutants resulted in a reduction in the total length and arborisation of the dendritic tree of ddaC neurons, thus reproducing the results seen when Membrin mutants were overexpressed on a null background, albeit with a weaker effect – as expected (**Figure 5.1**, unpublished data courtesy of Dr Praschberger). Overexpression of Mem-G147W and Mem-ΔK164 mutants on a WT background is therefore able to phenocopy the effects of Membrin loss-of-function and argues for the use of an overexpression approach in mammalian neurons.

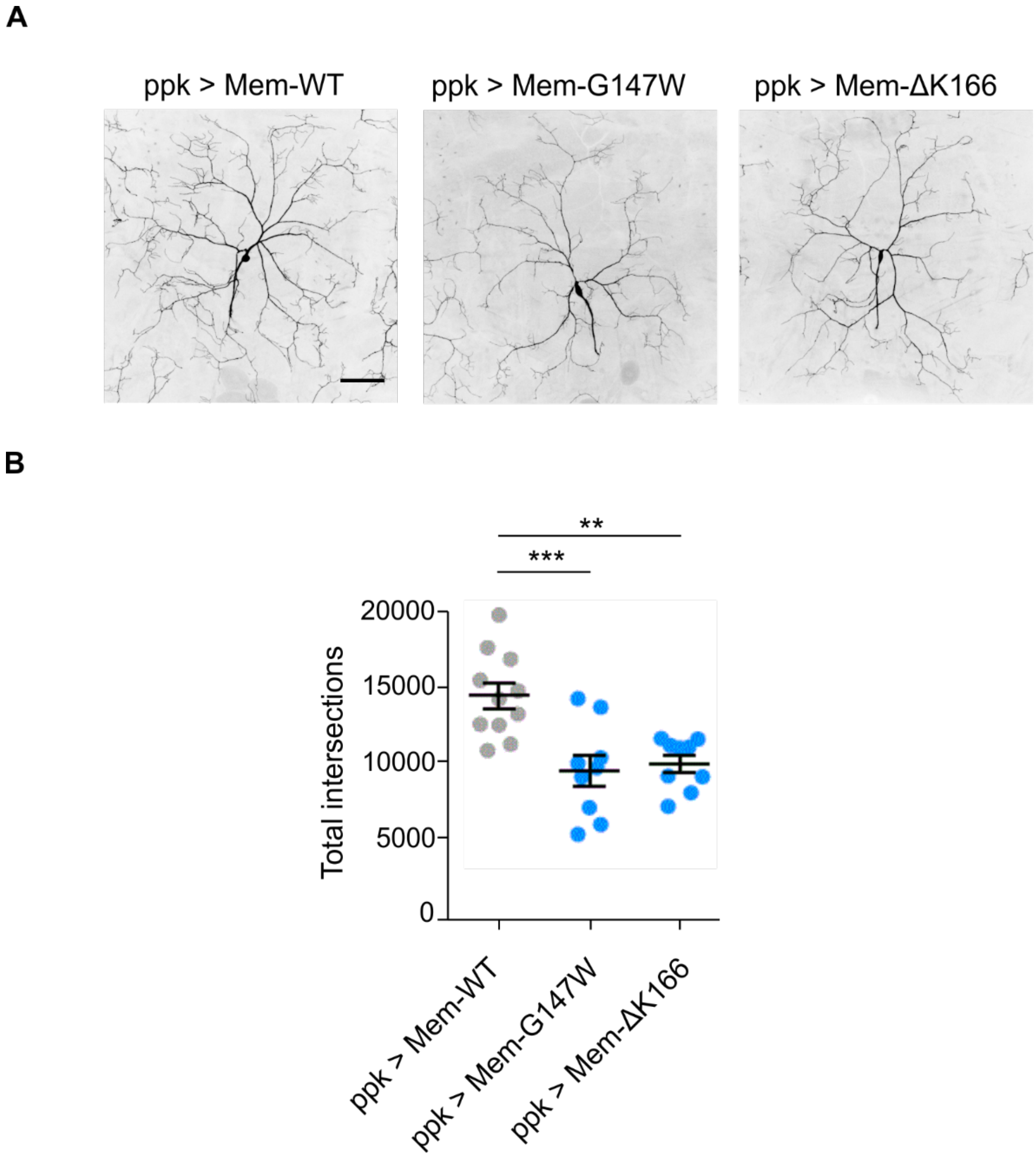

Figure 5.1. Overexpression of Membrin mutants phenocopies Membrin loss-of-function. A) Epifluorescence images of ddaC sensory neurons from flies overexpressing WT and Membrin mutants (G147W and ΔK166). Scale bar is 100 µm. **B)** Summary data of Sholl analysis of ddaC dendritic arbors from flies overexpressing Membrin transgenes. A significant reduction in dendritic arborisation is observed for neurons overexpressing Membrin mutants (WT vs. G147W, ***$p < 0.0005$; WT vs. ΔK166, **$p < 0.05$, One-way ANOVA with Dunnett's post-hoc test). Data are shown as means ± s.e.m. Unpublished data from Dr Praschberger.

5.3.2 An overexpression model of *GOSR2*-based PME in mammalian neurons

The G144W and ΔK164 mutations in GOSR2 both confer a partial loss-of-function and have to be present in the homozygous (or compound heterozygous) condition in order to precipitate disease phenotypes. As a loss-of-function mutation, GOSR2 mutants might be modelled using gene knockout or gene knock-down (RNA interference). However, GOSR2 is an essential protein and homozygous knockout is lethal (Praschberger et al., 2017; Meehan et al., 2017). Furthermore, GOSR2 mutants have been found to confer reduced rates of ER-Golgi trafficking that may not be appropriately modelled by a reduction in protein levels (Praschberger et al., 2017; Völker et al., 2017). The ideal strategy would be to combine RNA interference against the endogenous WT protein with the overexpression of GOSR2 mutants, however this approach is technically challenging. Instead, the fact that overexpression of Membrin mutants on a WT background can phenocopy GOSR2 loss-of-function in flies, argues for the use of a similar approach in WT mammalian neurons. In this scenario, mutant phenotypes are attained by out-competition of the WT protein, resulting in the formation of cis Golgi SNARE complexes that predominantly contain mutated GOSR2. I therefore chose to use an overexpression model of NS-PME in mammalian neuronal cultures derived from WT mice.

In recognition of the fact that GOSR2 is expressed in all cell types, I chose to use the ubiquitous PGK promoter to drive strong, constitutive expression of GOSR2 transgenes. WT or mutant (G144W or ΔK164) GOSR2 transgenes, containing an N-terminal FLAG epitope tag, were subcloned downstream of dscGFP and a T2A signal peptide sequence into a third-generation lentiviral vector (**Figure 5.2A**). A construct expressing GFP only was also generated in order to control for any potential mutant phenotypes caused by overexpression of the WT protein (**Figure 5.2A**). A total of four lentiviral vectors were generated, which will subsequently be referred to as: GFP, GOSR2-WT, GOSR2-G144W and GOSR2- ΔK164 (**Figure 5.2A**), note that all 'GOSR2' constructs also contain GFP.

In order to confirm expression and the correct localization of GOSR2 transgenes, I performed an immunofluorescence assay for FLAG-tagged GOSR2, in order to discriminate transgenically expressed GOSR2 from the endogenous protein, and the cis Golgi marker, GM130. Primary cortical neuronal cultures, at 4 DIV, were transfected with GOSR2-WT lentiviral DNA and fixed at 6 DIV to allow 48 hrs for transgene expression. FLAG-tag immunofluorescence was found to co-localise with GM130, confirming the functionality of the transfected constructs and the correct localization of GOSR2 transgenes to the cis Golgi (**Figure 5.2B**).

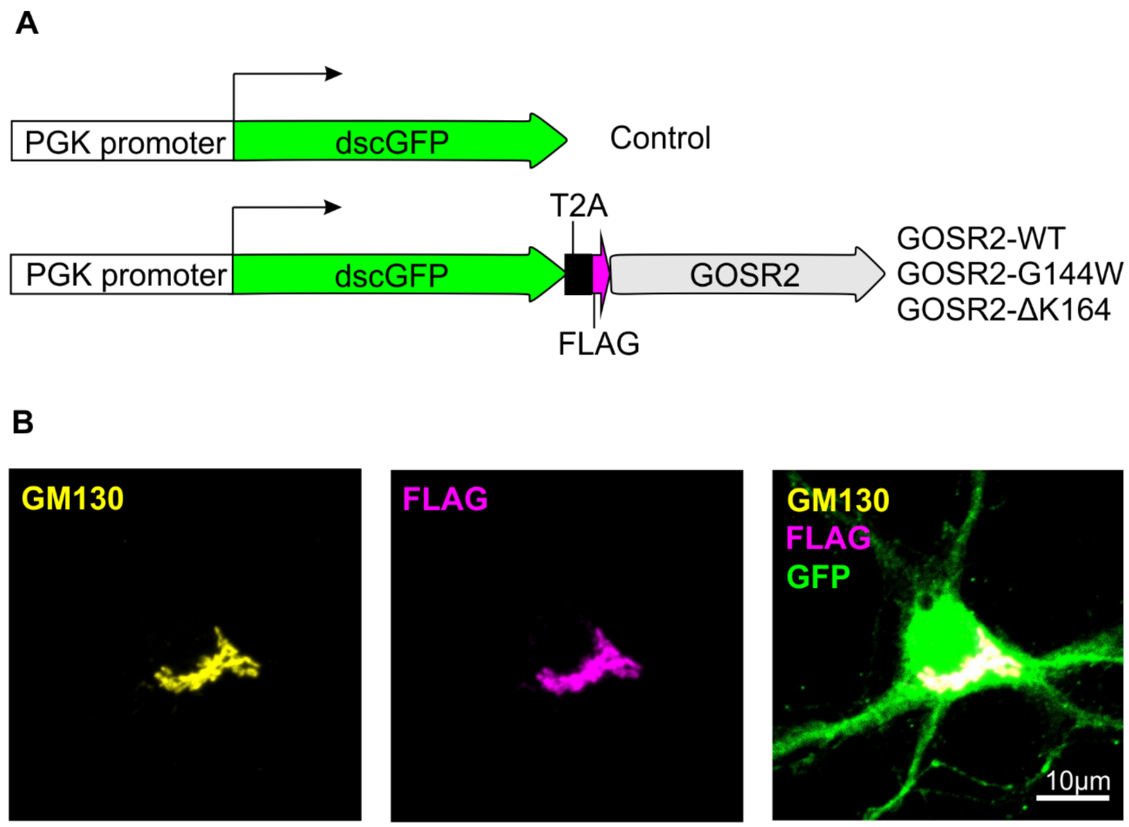

Figure 5.2. An overexpression model of NS-PME in cortical mammalian neurons. A) DNA expression constructs for the GFP-only control and *GOSR2* WT and mutant transgenes (*GOSR2*-G144W and GOSR2-ΔK164). **B)** *GOSR2* transgenes are efficiently expressed and localise to the cis Golgi**.** FLAG-tagged GOSR2 was confirmed to co-localise with the cis Golgi marker, GM130, in GFP^{+} neurons.

5.3.3 The G144W mutation reduces GOSR2 expression levels

I next wished to determine the degree to which WT and mutant *GOSR2* transgenes were overexpressed with respect to endogenous GOSR2 protein levels. Murine cortical neuronal cultures were transduced with GFP, GOSR2-WT or GOSR2-G144W lentiviruses at a multiplicity of infection (MOI) of 10 - to ensure a high rate of transduction (not experimentally quantified independently of virus infection on HEK cells) - and harvested at 16-17 DIV for the preparation of protein lysates. Quantitative immunoblotting for GOSR2 revealed that the exogenous lentiviral delivery of GOSR2-WT transgenes, driven by the PGK promoter, resulted in 259.9 ± 162.7-fold greater levels of expression with respect to the endogenous WT protein, quantified using GFP expressing neuronal lysates (GOSR2-WT: n = 3, GFP: n = 3, **Figure 5.3A & B**). Interestingly, the G144W mutation was found to result in significant reduction in GOSR2 protein levels (p = 0.046, 3.7 ± 1.0-fold reduction) compared to GOSR2-WT (**Figure 5.3B**). Despite this, GOSR2-G144W was still expressed at a level that was 100.7 ± 79.9-fold greater than the endogenous protein and would therefore still be expected to outcompete WT GOSR2 from SNARE complexes (G144W: n = 3, **Figure 5.3B**). Overexpression of GOSR2 transgenes thus remains a valid strategy with which to model the neuronal effects of GOSR2 mutations. However, it remains to be stated that an additional important control would be to confirm that GOSR2-G144W exerts a dominant negative effect on WT SNARE function, for example in a liposome-fusion assay.

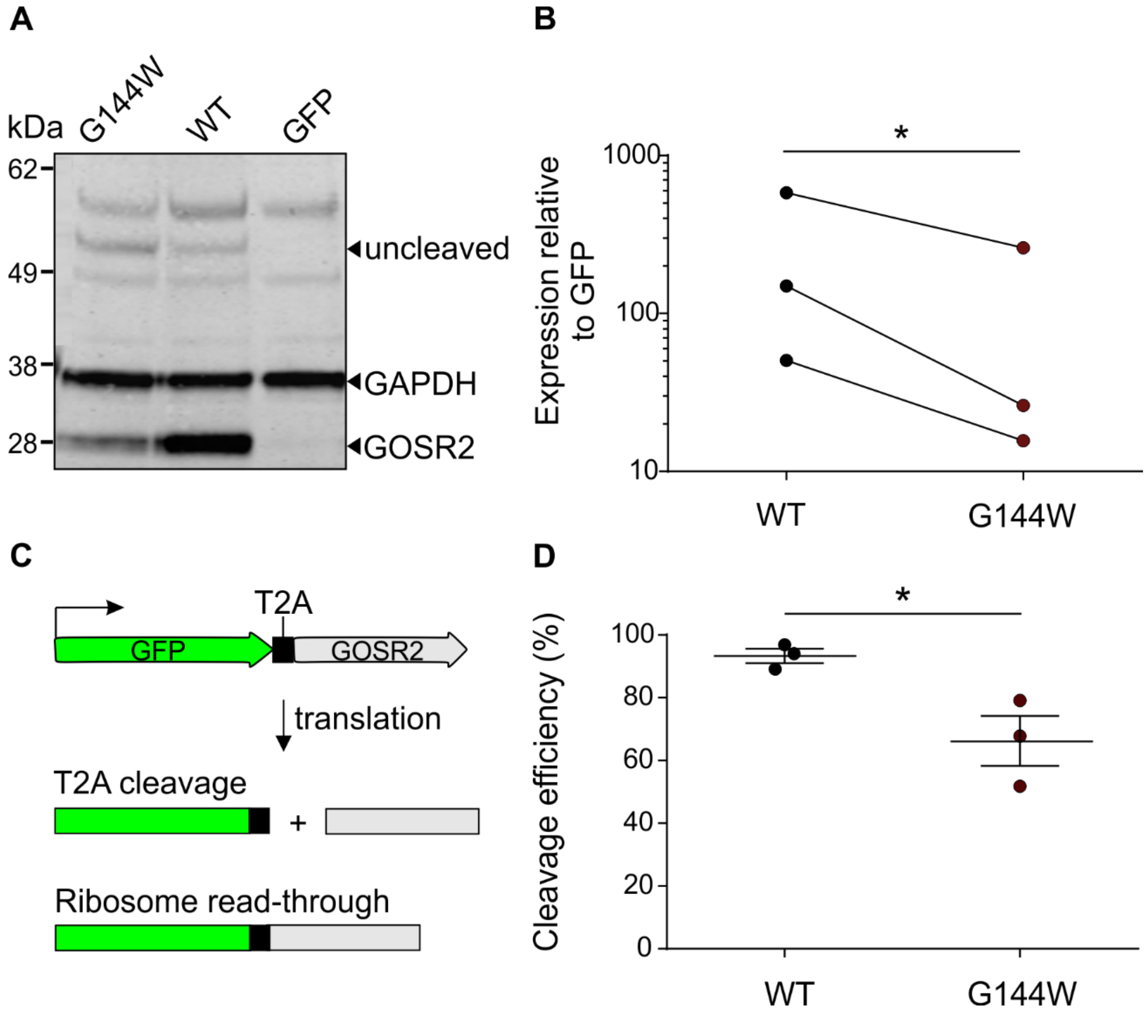

Figure 5.3. The G144W mutation results in a reduction of GOSR2 protein levels. A) Representative quantitative immunoblot for GOSR2 protein levels in 16-17 DIV cortical neuronal cultures. Protein lysates were prepared from neuronal cultures transduced with GFP, GOSR2-WT or GOSR2-G144W lentiviruses and blotted with antibodies against GOSR2 and glyceraldehyde 3-phosphate dehydrogenase (GAPDH). **Arrow:** GFP-GOSR2 fusion protein at ~ 51 kDa. Note the absence of this band in the GFP control. **B)** GOSR2 protein levels, achieved by transgenic overexpression. Scatter plot shows GOSR2 protein level relative to endogenous GOSR2 protein (GFP control) for each blot using a logarithmic scale. In each instance, GOSR2 protein levels were first normalised to a GAPDH loading control. The G144W mutation in GOSR2 results in a significant reduction in transgenic GOSR2 protein levels (*p = 0.046, Ratio Paired *t*-test). **C)** Schematic of GFP and GOSR2 bicistronic expression construct. GFP is linked to GOSR2 via a T2A signal peptide. In the majority of cases, T2A-mediated cleavage occurs during

translation, resulting in the production of two separate polypeptides. Occasionally, however, ribosome read-through occurs, resulting the production of a fusion protein. **D)** T2A-mediated cleavage efficiency was found to be significantly reduced for GOSR2-G144W compared to GOSR2 WT (*p = 0.03, Unpaired Student's *t*-test). The efficiency of T2A-mediated cleavage was calculated by measuring the ratio of cleaved/ (uncleaved + cleaved) protein (uncleaved/ GFP-GOSR2 fusion: ~ 51 kDa and cleaved: ~ 24 kDa). Data are from three independent neuronal preparations and are shown as mean ± s.e.m.

5.3.4 Reduction in T2A-mediated cleavage efficiency for GOSR2-G144W

In order to allow for the identification of neurons expressing GOSR2 transgenes, I co-expressed GFP and GOSR2 from a single promoter using the T2A self-cleaving peptide (**Figure 5.2A & 3C**). 2A peptides are short viral oligopeptide sequences that facilitate the cleavage of polypeptides during translation and are thus often employed as part of bicistronic expression vectors. The mechanism of 2A-mediated cleavage is 'ribosome-skipping', where the ribosome fails to form a peptidyl bond between the terminal glycine and proline of the 2A sequence, resulting in the production of two separate polypeptides (**Figure 5.3C**) (Liu et al., 2017). The T2A peptide was specifically chosen because it is recognized as having one of the highest cleavage efficiencies of all the 2A peptides (Liu et al., 2017). Despite this, it is increasingly recognized that T2A-mediated cleavage is not maximally efficient and that ribosome read-through can often occur, resulting in the formation of a fusion protein (**Figure 5.3C**). Indeed, in our immunofluorescent analysis of GOSR2 transgene localization, I observed that regions of higher GFP signal intensity in the soma that appeared to co-localise with the Golgi marker, GM130, which possibly corresponded to GFP fusion protein (**Figure 5.4**).

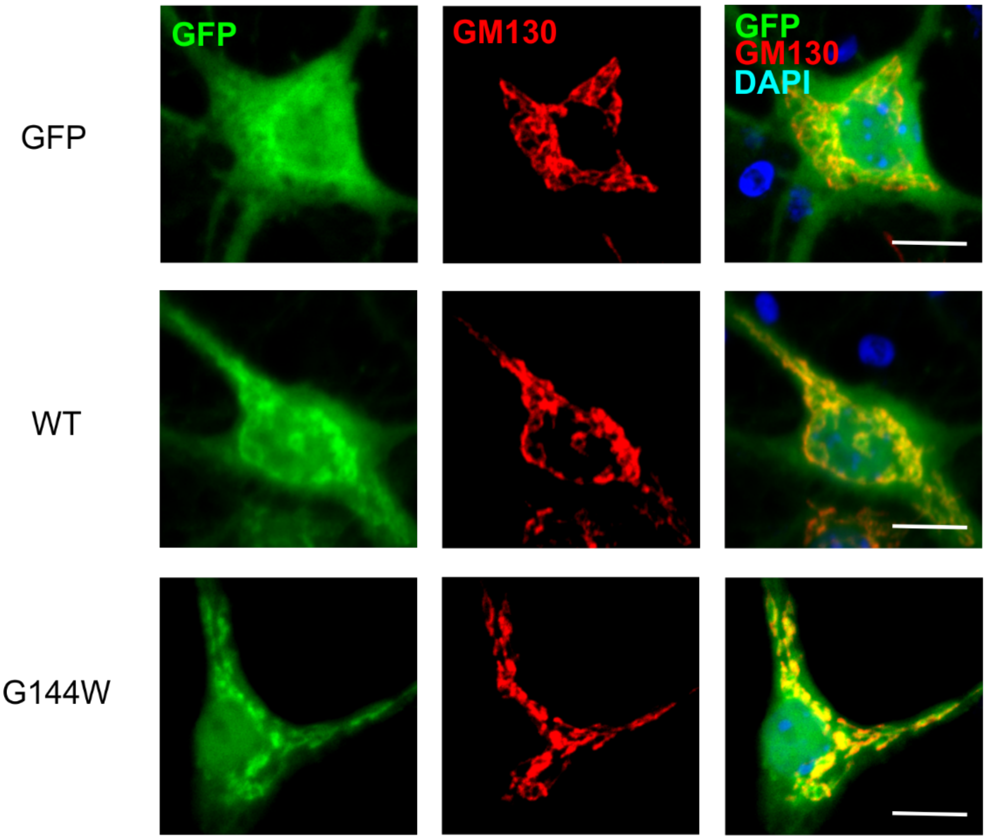

Figure 5.4. Golgi localised GFP signal caused by the production of GFP-GOSR2 fusion proteins. Immunofluorescent assay for GM130 and GFP in 14 DIV cortical neurons transduced with GFP, GOSR2-WT or GOSR2-G144W lentiviruses. The bicistronic overexpression of GOSR2 transgenes via inefficient T2A-mediated cleavage results in the formation of GFP-GOSR2 fusion protein that is localized to the Golgi, as indicated by co-labelling for the cis Golgi marker, GM130. Scale bar is 10 µm.

In order to test whether the increased GFP signal in the Golgi for GOSR2 expressing neurons was due to trafficking defects of GOSR2 overexpression (and therefore GFP accumulation in the Golgi) or a preponderance of GOSR2-GFP fusion protein, I performed western blot analysis of T2A-mediated cleavage (**Figure 5.3**). For both GOSR2-WT and GOSR2-G144W, I observed a single band migrating between 50-60 kDa that corresponded to a GFP-GOSR2 fusion protein (~51 kDa) and that was absent from the GFP control (**Figure 5.3A**, arrow). Interestingly, when I calculated the ratio of cleaved GOSR2 (~25 kDa) to un-cleaved GOSR2 (~51 kDa), for GOSR2-WT and GOSR2-G144W, I found that the cleavage efficiency for GOSR2-G144W was significantly less than that for GOSR2-WT (WT: 93.3 ± 2.3%, n = 3 vs. G144W: 66.2 ± 7.9%, n = 3, *p: 0.03, **Figure 5.3D**). The increased GFP signal localised to the Golgi that occurs with the overexpression of GOSR2 transgenes therefore appears to correspond to a reduced efficiency of T2A-cleavage (GFP-GOSR2 fusion protein) and not trafficking defects conferred by GOSR2 overexpression.

5.4 GOSR2-G144W causes a reduction mEPSCs

5.4.1 Overexpression of GOSR2-G144W results in a reduction in the frequency of mEPSCs

Previous work in Drosophila has found PME-associated mutations in GOSR2 to result in a profound reduction in dendritic length in sensory neurons of the fly larval wall as well as structural and functional synaptic abnormalities at the NMJ. The effects of GOSR2 mutants have not, however, been characterised at mammalian central synapses. Insights into developmental or disease-modifying effects on neurotransmitter release may be gained by recording miniature post-synaptic currents, or ‘minis’. Minis result from the spontaneous fusion of a single synaptic vesicle (SV) with the presynaptic membrane and the release of a ‘quanta’ of neurotransmitter into the synaptic cleft. Analysis of the frequency and amplitude of miniature events can provide important insights into the release probability of a large population of presynaptic terminals as well as postsynaptic changes in neurotransmitter receptors. To this end, I performed *in vitro* whole-cell voltage clamp recordings of mEPSCs from transduced cortical neurons overexpressing GFP, *GOSR2*-WT and *GOSR2*-G144W or *GOSR2*-ΔK164 transgenes.

In recognition of the possibility that GOSR2 mutants might negatively impact neurite outgrowth, and that GOSR2-based PME may represent a neurodevelopmental disorder, murine cortical neuronal cultures were transduced with lentivirus at DIV 1, when the initial phase of neurite outgrowth begins. Cultures were transduced using a MOI5, a functional titer calculated using GFP expression, resulting in a neuronal transduction efficiency of >90% for all viruses. Electrophysiological recordings of transduced neurons were performed between 14-17 DIV, when neurons show mature synaptic functionality (**Figure 5.5A**) and incorporate AMPA receptor (AMPAR)-mediated currents (Renger et al., 2001). Spontaneous AMPAR-mediated mEPSCs were isolated by the bath application of 1 µM TTX (**Figure 5.5B**) PTX and CNQX, in order to block action potential firing, $GABA_A$-receptor mediated inhibitory neurotransmission and NMDAR-mediated responses, respectively. Example current traces are shown in **Figure 5.6**.

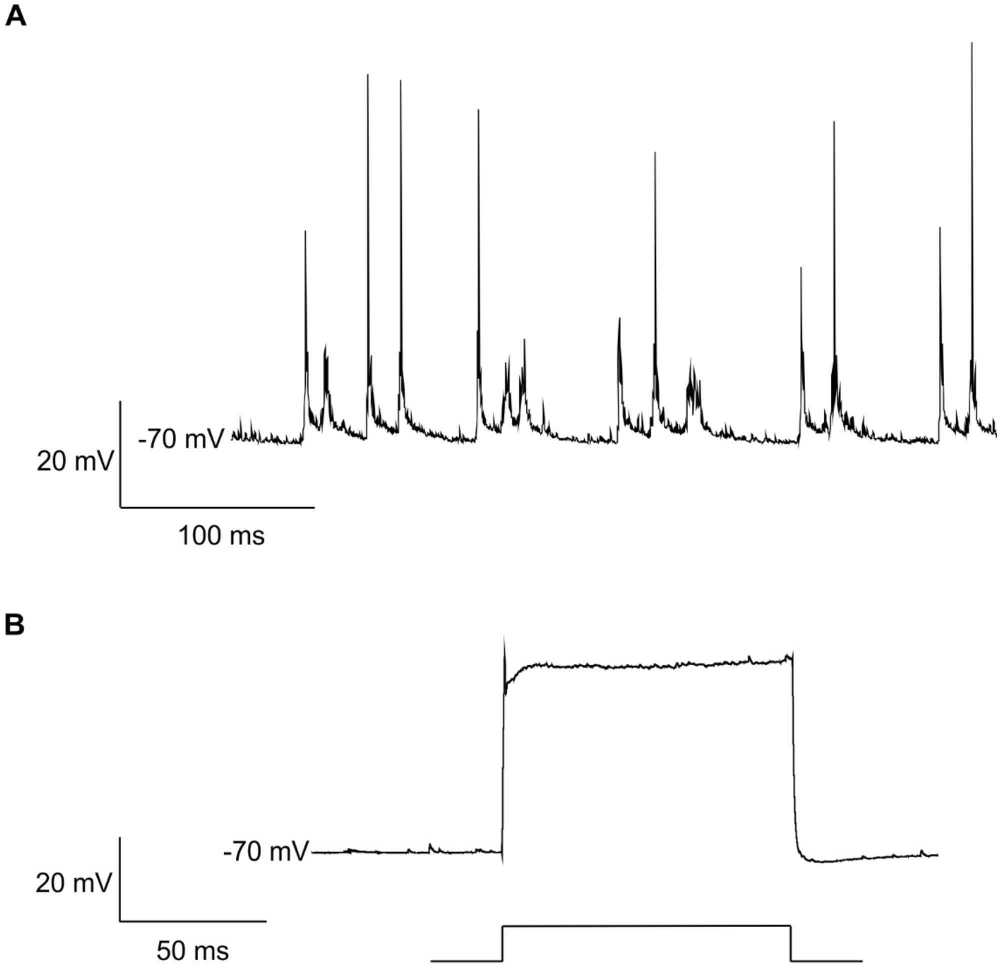

Figure 5.5. Pharmacological blockade of spontaneous activity in cortical neuronal cultures with TTX. A) High levels of spontaneous activity in high density cortical neuronal cultures at 14 DIV recorded at -70 mV at room temperature. **B)** Inhibition of action potential initiation with TTX. Representative trace from a cortical neuron held at -70 mV and injected with a suprathreshold current step of 150 pA in the presence of TTX.

I found a significant reduction in mEPSC frequency for neurons expressing GOSR2-G144W (2.8 ± 0.5 Hz, n = 17) compared to GOSR2-WT (5.7 ± 1.1 Hz, n = 14, G144W vs. WT: p = 0.019, **Figure 5.6C**). Importantly, no significant differences in mEPSC frequency were found for GFP (5.6 ± 1.4 Hz, n = 5) vs. GOSR2-WT, indicating that overexpression of GOSR2 does not elicit gain-of-function or loss-of-function phenotypes (GFP vs. WT: p > 0.99, **Figure 5.6C**). Interestingly, no significant differences in mEPSC frequency were found for the deletion mutant, GOSR2-ΔK164 (4.1 ± 0.4 Hz, n = 13) compared to WT (ΔK164 vs. WT: p = 0.48, **Figure 5.6C**). Note, that the frequency of mEPSCs was high across all conditions because neurons were plated at a high density and exhibited high levels of spontaneous activity (**Figure 5.6A**). No significant differences in mEPSC amplitude were observed for neurons overexpressing any of the GOSR2 mutants, or for GFP control neurons, compared to GOSR2-WT (GFP: -28.9 pA ± 3.9 pA, n = 5; WT: -27.2 ± 2.3 pA, n = 14; G144W: -22.9 ± 2.2 pA, n = 17 and K164Del: -26.2 ± 4.5 pA, n = 13, **Figure 5.6D**).

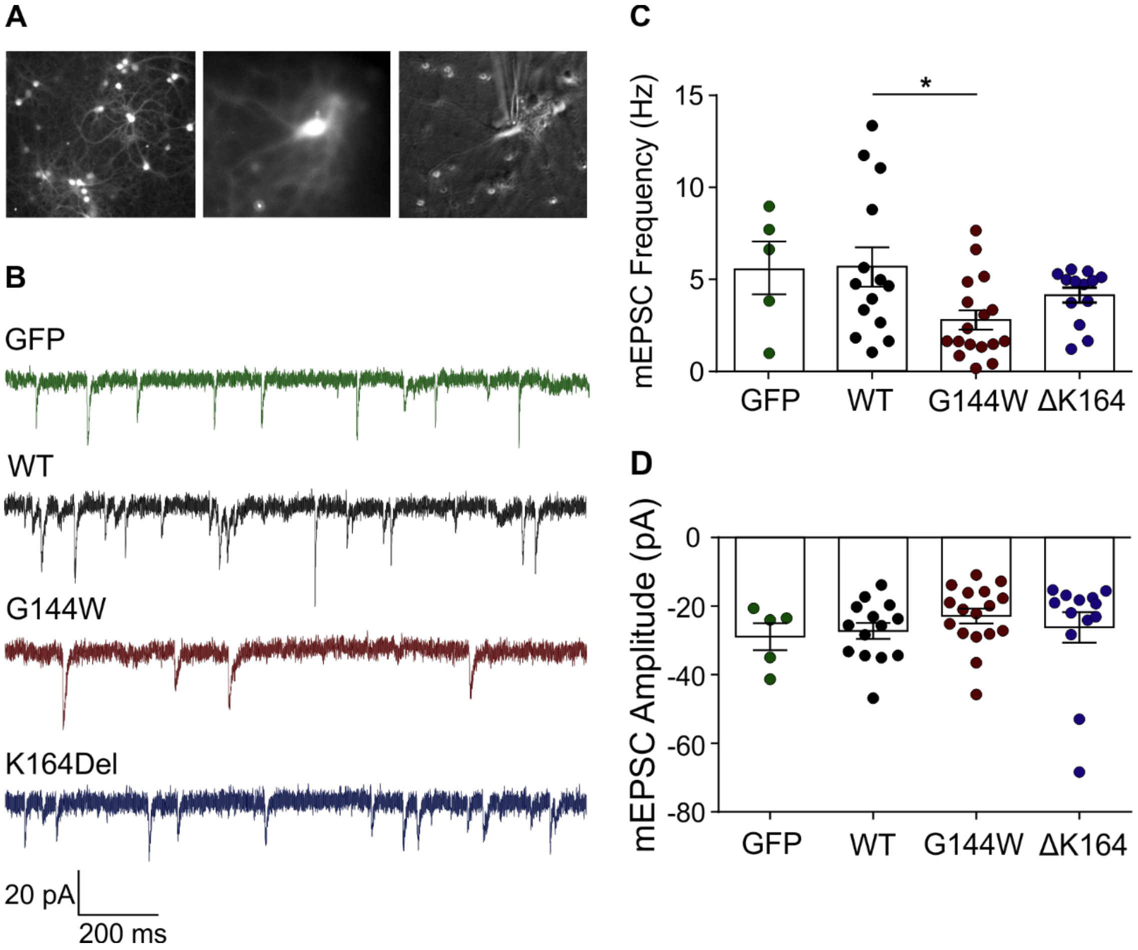

Figure 5.6. GOSR2-G144W results in a reduction in mEPSC frequency. A) Epifluorescence images of a cortical neuronal culture transduced with lentivirus expressing GFP. Whole cell voltage-clamp recordings were obtained from GFP$^+$ neurons. **B)** Representative traces of AMPAR-mediated mEPSCs recorded at -70 mV from cortical neuronal cultures at 14-16 DIV, which had been transduced with GFP, GOSR2-WT, GOSR2-G144W or GOSR2-ΔK164 lentiviruses. **C)** The G144W, but not the ΔK164, mutation in GOSR2 resulted in a significant reduction in mEPSC frequency (WT vs. G144W: *p = 0.019; WT vs. ΔK164: p = 0.48; WT vs. GFP: p > 0.99, One-way ANOVA with Bonferroni's multiple comparisons test). **D)** Overexpression of GOSR2-G144W or GOSR2-ΔK164 has no significant effect on mEPSC amplitude (WT vs. G144W: p = 0.86; WT vs. K164Del: p = 0.99; WT vs. GFP: p = 0.99, One-way ANOVA followed by Bonferroni's multiple comparisons test). Data are obtained from three independent neuronal preparations and 'n' represents a single recorded neuron. Data are shown as means ± s.e.m.

5.4.2 mEPSC reduction with GOSR2-G144W overexpression is not due to a reduction in the number of excitatory synapses

The striking reduction in mEPSC frequency caused by GOSR2-G144W could result either from 1) a presynaptic deficit, such as a reduction in release probability or 2) a reduction in the number of excitatory synapses. I investigated whether the reduction in mEPSC frequency was due to the latter by performing immunocytochemical analysis for the excitatory synaptic markers, VGLUT1 and HOMER1. I chose VGLUT1 as a marker of excitatory presynaptic boutons because it is localized to glutamatergic synaptic vesicles and has a low incidence of ectopic expression (Fremeau et al., 2004). HOMER1 was chosen as a post-synaptic marker because it is a major component of the post-synaptic density and functions in the anchoring of metabotropic glutamate receptors. The spatial overlap (colocalisation) of these two markers represented a structurally completed synapse.

In order to determine the number of excitatory synapses for each condition I counted the number of colocalised VGLUT1 and HOMER1 puncta along a linear portion of GFP$^+$ dendrite (**Figure 5.7A**). I found no significant differences in the number of excitatory synapses per unit length of dendrite for GOSR2-G144W (0.45 ± 0.04 synapses µm^{-1}, n = 8) compared to GOSR2-WT (0.49 ± 0.03 synapses µm^{-1}, n = 9; G144W vs. WT: p = 0.84, **Figure 5.7B**). As expected, given the results of mEPSC frequency analysis (**Section 5.3.1**), significant differences in the number of excitatory synapses between GOSR2-WT and GOSR2-ΔK164 (0.45 ± 0.04 synapses µm^{-1}, n = 8) and GOSR2-WT and GFP (0.52 ± 0.04 synapses µm^{-1}, n = 6) were not detected (ΔK164 vs. WT: p = 0.81; GFP vs. WT: p = 0.86, **Figure 5.7B**).

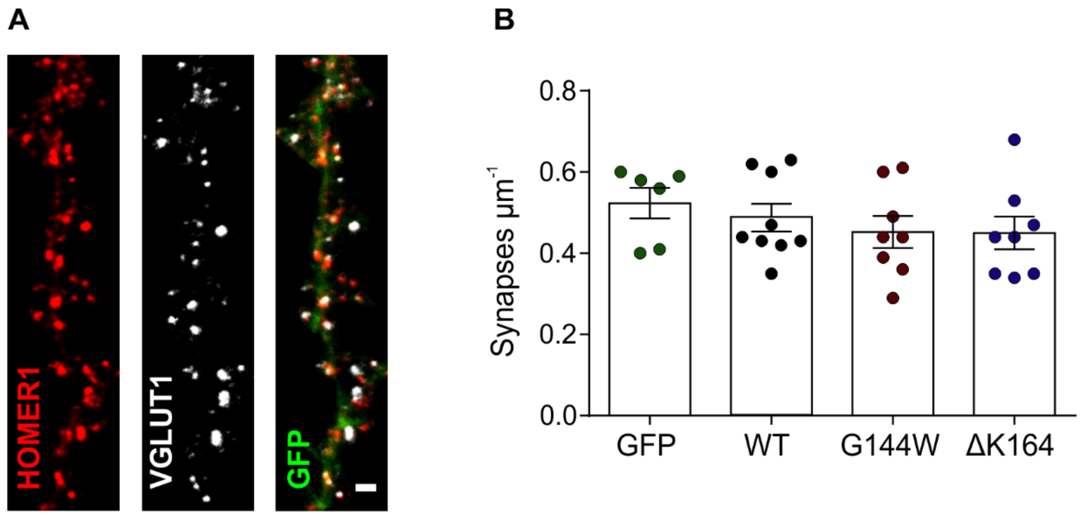

Figure 5.7. GOSR2-G144W has no effect on excitatory synapse number. A) Representative images of HOMER1 and VGLUT1 immunolabelling along a GFP$^+$ dendrite for a predefined region of interest. Scale bar is 2 µm. **B)** Excitatory synapse number is unaffected by the overexpression of GOSR2 transgenes (G144W vs. WT: $p = 0.84$; ΔK164 vs. WT: $p = 0.81$; GFP vs. WT: $p = 0.86$, One-way ANOVA followed by Bonferroni's multiple comparisons test). Analysis of synapse number per unit of dendrite length was performed in cortical neuronal cultures at 14 DIV. VGLUT1 and HOMER1 puncta along a pre-determined length of dendrite were counted and the number of colocalised puncta found by multiplying the number of Homer1 puncta by the overlap coefficient for HOMER1 and VGLUT1. Data are from four independent neuronal preparations and 'n' is the average number of synapses per unit length for 5 dendrites per coverslip. Data are shown as means ± s.e.m.

5.5 GOSR2-G144W may result in a reduction of SNAP-25 protein that is incorporated into SNAP-25 associated complexes

The reduction in mEPSC frequency observed in neuronal cultures overexpressing GOSR2-G144W is not caused by a reduction in excitatory synapse number, which may imply a presynaptic deficit. Presynaptic deficits have previously been detected for GOSR2 mutants in a fly model of PME (Praschberger et al., 2017). GOSR2 loss-of-function was anticipated to broadly alter trafficking of synaptic cargoes to the presynapse, resulting in unpredictable changes in the steady-state levels of a number of synaptic proteins. Interestingly, however, a specific reduction in the steady-state levels of CSPα, a synaptic vesicle protein, was detected in a proteomics screen of Membrin-G147W flies (Praschberger et al., 2017).

CSPα acts as a chaperone for a number of presynaptic proteins, including synaptosomal nerve-associated protein 25 (SNAP-25), a major SNARE protein required for synaptic vesicle exocytosis (Sharma et al., 2012). CSPα promotes the incorporation of SNAP-25 into SNARE complexes and prevents its ubiquitination and degradation (Sharma et al., 2011). I therefore hypothesised that impaired trafficking of CSPα to the presynapse might alter the incorporation of SNAP-25 into functional SNARE complexes, which might account for the reduction in mEPSC frequency observed in GOSR2-G144W overexpressing cultures.

5.5.1 Neuronal overexpression of GOSR2-G144W does not reduce SNAP-25 protein levels

Given that CSPα post-translationally regulates SNAP-25 levels, I performed a quantitative immunoblot for SNAP-25 in neuronal cultures expressing GOSR2 transgenes. Protein lysates were prepared from murine cortical neuronal cultures, transduced with GFP, GOSR2-WT or GOSR2–G144W lentiviruses, at 16-17 DIV. In all neuronal lysates, I observed a strong immunoreactive band migrating at ~26 kDa that corresponded to monomeric SNAP-25 (**Figure 5.8A**). I also observed fainter additional bands, the largest of which migrating at ~62 kDa, which likely correspond to SNAP-25 in higher-order complexes, which may correspond to SNARE complexes (**Figure 5.8A,** arrow). I did not observe any significant differences in the level of monomeric SNAP-25 protein, relative to GFP control lysates, in cultures overexpressing GOSR2-G144W compared to GOSR2-WT, suggesting that degradation of SNAP-25 is not upregulated in neuronal cultures overexpressing GOSR2-G144W (WT: 1.03 ± 0.18, n = 3; G144W: 0.95 ± 0.18, n = 3, WT vs. G144W: p = 0.75, **Figure 5.8B**).

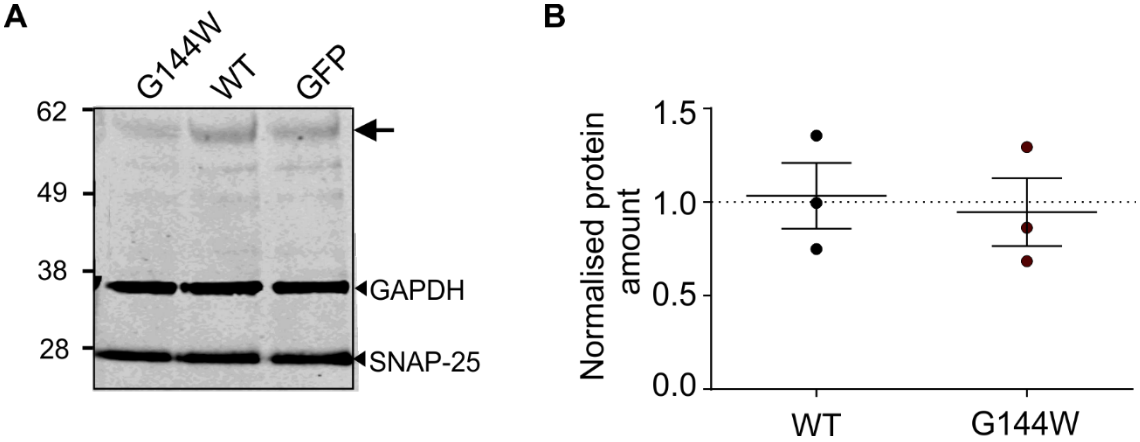

Figure 5.8. Monomeric SNAP-25 levels are unaltered in neurons overexpressing GOSR2-G144W. A) Representative quantitative immunoblot for SNAP-25, performed using protein lysates prepared from cortical neuronal cultures at 16-17 DIV, transduced with GFP, GOSR2-WT or -G144W lentiviruses. A strong immunoreactive band corresponding to SNAP-25 can be observed at ~26 kDa. Lysates were also blotted for GAPDH as a control for protein loading. **Arrow**: uppermost band immunoreactive for SNAP-25 that may correspond to SNAP-25 associated complexes, such as SNARE complexes. **B)** Quantification of monomeric SNAP-25 levels in neurons overexpressing GFP, GOSR2-WT or GOSR2-G144W transgenes. In all conditions, SNAP-25 signal was first normalized to GAPDH and then to SNAP-25 signal measured in lysates from GFP control neurons. There was no significant difference in the relative level of monomeric SNAP-25 protein for GOSR2-G144W compared to GOSR2-WT (p = 0.75, Student's Unpaired *t*-test). Data are from three independent neuronal preparations and are shown as means ± s.e.m.

5.5.2 Neuronal overexpression of GOSR2-G144W may decrease the amount of SNAP-25 that is incorporated into higher order complexes

CSPα protects SNAP-25 from ubiquitination - and therefore degradation - but also acts as a chaperone for the incorporation of SNAP-25 into SNARE complexes with synaptobrevin and syntaxin-1. Higher-order bands, of ~62 kDa, observed when immunoblotting for SNAP-25 (**Figure 5.8A,** arrow), are suggestive of SNAP-25 within SNARE complexes. I calculated the signal ratio of the highest migrating band at ~62 kDa (termed upper band) to that of monomeric SNAP-25, and found a trend towards a reduction in the ratio of upper/lower bands for GOSR2-G144W (0.81 ± 0.14, n = 3) compared GOSR2-WT controls (WT: 1.05 ± 0.09, n = 3, **Figure 5.11**) following normalisation to SNAP-25 levels for GFP transduced control neurons, however this was not significant. This result suggests that whilst the overall levels of monomeric SNAP-25 are not altered (or the sensitivity is not sufficient to detect changes), a reduced proportion of SNAP-25 is incorporated into higher order complexes. These higher order complexes may represent quaternary SNARE complexes, the reduction of which, may contribute towards functional deficits at GOSR2-G144W synapses. However, I cannot rule out a postsynaptic effect of GOSR2 mutation on mEPSC frequency, such as a reduction in the proportion of functional synapses expressing AMPARs.

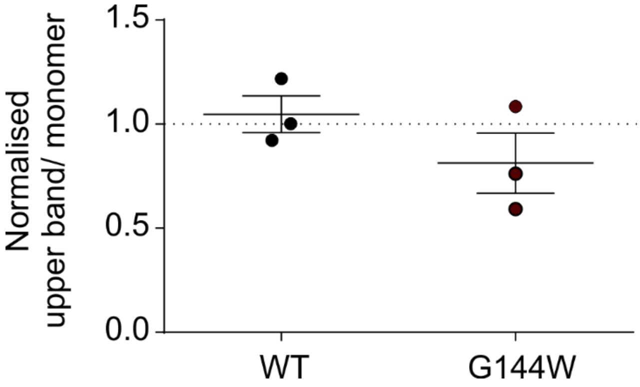

Figure 5.9. Incorporation of SNAP-25 into higher molecular weight complexes shows a trend of reduction in neurons overexpressing GOSR2-G144W. The ratio of the upper SNAP-25 immunoreactive band (~ 62 kDa) to monomeric SNAP-25 (~26 kDa) was investigated using quantitative immunoblotting, using protein lysates prepared from 16-17 DIV cortical neuronal cultures expressing GFP, GOSR2-WT or GOSR2–G144W. The ratio of upper-lower SNAP-25 bands for each blot was normalized to the ratio calculated for GFP control neurons. There was a non-significant trend towards a reduction in the ratio of upper:lower SNAP-25 bands (p = 0.24, Unpaired Student's *t*-test). Data are from three independent neuronal preparations and are shown as mean ± s.e.m.

5.6 Targeting *GOSR2* transgene expression to Purkinje cells

GOSR2 is ubiquitously expressed and yet elicits a unique PME phenotype when mutated. This would suggest that selected subsets of neurons are uniquely vulnerable to trafficking deficits within the secretory pathway caused by GOSR2 mutation. Investigations using a fly model of PME, discussed in **Section 5.3.1**, found that dendritic arborisation and outgrowth of ddaC sensory neurons was significantly impaired in Mem-G147W flies, implicating dendrite outgrowth and maintenance in PME disease pathology. It follows, therefore, that neurons with larger and more complex dendritic trees might be more severely affected by mutations in GOSR2.

Ataxia is a major disease feature of NS-PME and is the major presenting symptom between 2-3 years of age. Ataxia is a movement disorder caused by cerebellar dysfunction, towards which Purkinje cell dysfunction or degeneration contributes significantly (Hoxha et al., 2018). Purkinje cells have highly elaborate dendritic trees and as such would be expected to place significant biosynthetic demands on the secretory pathway, within which the GA is central. Indeed, deletion of the structural Golgi protein, GM130, in mice was recently shown to result in secretory deficits, dendritic atrophy, Purkinje cell loss and severe ataxic phenotypes (Chunyi Liu et al., 2017). Furthermore, GOSR2 double knock-out mice are characterised by disordered movements early in life (they die shortly after birth) (Meehan et al., 2017). I hypothesise, therefore, that Purkinje cells are uniquely vulnerable in NS-PME and that their dysfunction contributes significantly towards disease phenotypes.

In order to investigate the effects of GOSR2-G144W on Purkinje cell morphology *in vivo*, I cloned GOSR2-WT, -G144W and GFP transgenes into an AAV2 transfer vector under the control of the human PCP2, or Ple155, promoter (**Figure 5.12A**) (De Leeuw et al., 2016). The minimal PCP2/Ple155 promoter was chosen because of its ability to target gene expression specifically to Purkinje cells and its proven AAV compatibility (De Leeuw et al., 2016). Pseudotyped AAV9 viral particles (containing AAV9 capsid proteins) were produced from these AAV2 transfer vectors (AAV2/9) and subsequently injected into the lateral ventricles of WT postnatal day 0 (P0) mice, in order to achieve whole brain transduction (Chan et al., 2017). Brains were harvested after 3 weeks and analysed for GFP expression. Unfortunately, I was unable to detect native GFP expression in Purkinje cells of the cerebellum. As a result of not being able to detect GFP signal, I decided to perform an immunohistochemical analysis for GFP, in order to amplify any signal present at a low level. However, even after GFP immunolabelling, I was only able to detect sparse and weak labelling of Purkinje cells, which precluded any further analysis due a low signal to noise ratio (**Figure 5.12B**).

A

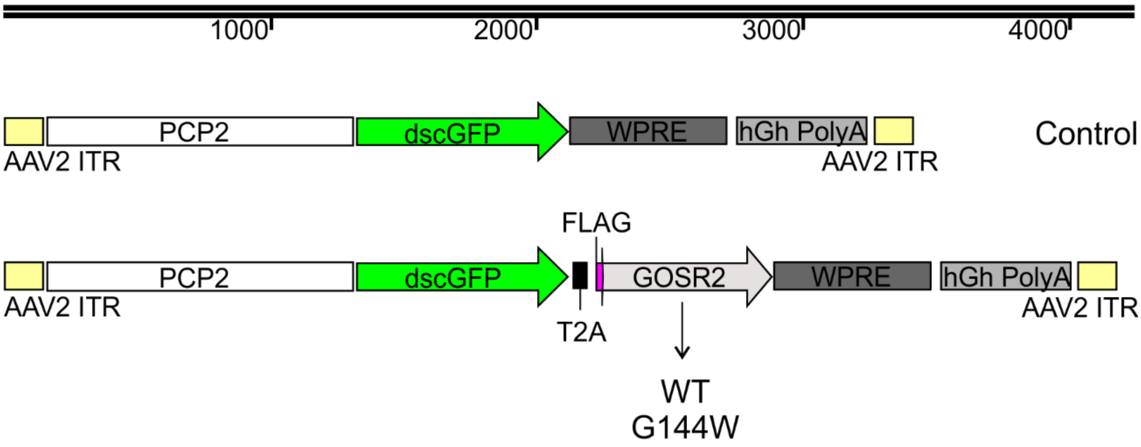

B

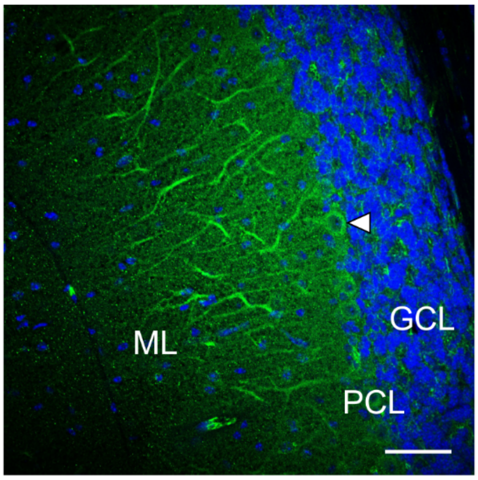

Figure 5.10. Targeting Purkinje cells with the PCP2 promoter. A) AAV2 DNA constructs used in the synthesis of AAV9 pseudotyped viral particles. **B)** Confocal immunofluorescence image of Purkinje cells transduced with AAV9-GFP. AAV9-GFP virus was injected into the cerebellum of a 2-month-old WT mouse and the brain harvested 4 weeks later. GCL: granule cell layer; PCL: Purkinje cell layer, ML: molecular layer. White arrow: somatic GFP fluorescence of a Purkinje cell. Scale bar is 50 µm.

After observing extremely low transduction efficiencies of Purkinje cells following P0 injection of AAV9-GFP into the lateral ventricles, I wondered whether the transduction efficiency of Purkinje cells could be increased by directly injecting AAV9-GFP into the cerebellum of an adult mouse. I performed stereotaxic injection of the cerebellum of a 2-month-old adult mouse with 2 µL of AAV9 and harvested the brain after 4 weeks.

Unfortunately, yet again, I was unable to detect GFP fluorescence in the Purkinje cells of the adult brain, with or without immunohistochemical amplification of the GFP signal.

5.7 Discussion

Mutations in GOSR2 give rise to a remarkably restricted neurological disorder, NS-PME, despite GOSR2 being an essential and ubiquitously expressed SNARE protein required for ER-Golgi transport. In this chapter, I present data that investigates, for the first time, the impact of mutations in GOSR2 on the physiology of mammalian neurons. Previously, it has been shown in neurons of the fly that reduced rates of vesicular transport and fusion in the early secretory pathway impact upon neurotransmitter release at presynaptic active zones as well as trafficking of biosynthetic materials necessary for building dendritic trees. Here I extend these findings and demonstrate that the pervasive G144W mutation in GOSR2, causative for NS-PME, partially impairs spontaneous neurotransmitter release at central mammalian synapses, potentially via a presynaptic mechanism.

5.7.1 Neuronal overexpression of GOSR2 mutants is a valid model of NS-PME

PME-associated mutations in GOSR2 are loss-of-function, however, I chose to model NS-PME using an overexpression strategy in WT neurons. I have demonstrated the validity of this model by showing that the recombinant expression of GOSR2-G144W can exceed levels >100X that of the endogenous WT protein; levels that likely to facilitate the out-competition of WT GOSR2 from cis Golgi SNARE complexes by GOSR2 mutants. Indeed, the fact that I observe alterations in spontaneous neurotransmission as a result of GOSR2-G144W overexpression, indirectly supports our hypothesis that overexpression of GOSR2 mutants induces functional deficits in the early secretory pathway and demonstrates the utility of this model for future experiments. Furthermore, I do not observe ‘disease’ phenotypes for the overexpression of WT GOSR2, suggesting that the effects I observe in the presence of GOSR2-G144W mutants specifically result from a loss of SNARE function and are not artefacts of GOSR2 overexpression.

5.7.2 The ΔK164 mutation in GOSR2 does not induce a neuronal phenotype

I did not observe any synaptic phenotypes with the overexpression of GOSR2-ΔK164 and as such chose to discontinue studying this mutant, particularly because only one patient with this mutation has been described (who also carries the G144W mutation). It is unclear why overexpression of this mutant had no effect compared to G144W. One possible reason is that ΔK164 is mislocalised from the Golgi and therefore cannot outcompete WT GOSR2, nevertheless, this mutant was found to correctly localize to the cis Golgi when overexpressed in human control fibroblasts (Praschberger et al., 2017). A more likely explanation is that overexpression is not a suitable model to study the effects of the ΔK164 mutant. For example, the ΔK164 mutant may be rapidly degraded or have a milder effect on SNARE function, deficits that might be rescued by endogenous WT GOSR2. Indeed, previous biochemical studies have shown SNARE function to be more severely impaired by G144W than by ΔK164 (Völker et al., 2017). Our findings, as well as those of Völker, might explain the milder disease phenotype experienced by the one patient compound heterozygous for the ΔK164 mutation, however one cannot discount the potential role of modifier genes.

5.7.3 Further evidence of G144W as a loss-of-function mutation

Mutations in GOSR2 display an autosomal recessive mode of inheritance (Corbett et al., 2011). Both the G144W and the ΔK164 mutations occur within the SNARE domain of the protein and confer a partial loss-of-function, resulting in reduced rates of membrane fusion. The G144W mutation in GOSR2 may also confer a loss-of-function by resulting in reduced expression levels of the protein. Reduced levels of GOSR2 protein have previously been found in PME-G144W patient fibroblasts (Praschberger et al., 2017). However, fibroblasts were obtained from only one patient and GOSR2 expression levels were found to be highly variable in control fibroblasts (Praschberger et al., 2017). My results lend support to the findings of Praschberger et al, because I found a consistent reduction in the recombinant expression levels of GOSR2-G144W with respect to GOSR2-WT when I overexpressed these proteins in murine cortical neurons using lentiviral-based transgene delivery.

The reduction in endogenous GOSR2 protein levels in PME patient fibroblasts, reported by Praschberger et al., is likely caused by a reduction in protein stability. This is also likely true of my findings, however, the reduction in protein levels that I observe could also be due to a reduced rate of lentiviral transduction or a T2A-related mechanism. The reduction in GOSR2-G144W that I observe is unlikely to be due to variation in viral transduction efficiency because I attempted to control for this using a high MOI that was based upon the calculation of functional (fluorescent-based) lentiviral titres, which was double the amount of virus that had been experimentally verified to result in the transduction of >90% of neurons in culture. However, I cannot rule out the contribution of a T2A-related mechanism in the reduction of GOSR2-G144W levels - in light of the significantly reduced T2A-mediated cleavage efficiencies that I observed for the recombinant expression of GOSR2-G144W compared to GOSR2-WT. Imperfect T2A-mediated cleavage results in the production of uncleaved protein (GFP-GOSR2 fusion) and is caused by ribosome read-through instead of ribosome skipping. It appears that ribosome read-through is increased for expression cassettes containing GOSR2-G144W, likely due steric interference related to GOSR2 mRNA secondary structure. If this is the case, then it follows that an increased rate of ribosome drop-off (the premature termination of translation) might also occur. In my expression cassette, GFP is upstream of the T2A signal peptide, thus ribosome drop-off would result in the synthesis of GFP only and may contribute towards the reduced expression of GOSR2-G144W.

5.7.4 GOSR2-G144W results in a reduction in the frequency of spontaneous neurotransmitter release, potentially via a presynaptic mechanism

For the first time, I have demonstrated a reduction in spontaneous glutamate release at central synapses caused by the G144W mutation in GOSR2. This result extends previous findings in Drosophila, which showed that the equivalent G147W mutation in the GOSR2 orthologue, Membrin, causes a reduction in the frequency of spontaneous miniature excitatory end-plate potentials at the NMJ (Praschberger et al., 2017). The mechanisms underlying reductions in spontaneous release are likely to be highly complex because there are a multitude of ways by which early changes in the secretory pathway could impact upon neurotransmission. For instance, the ER-Golgi trafficking ‘bottleneck’ conferred by GOSR2 loss-of-function is likely to have a downstream impact upon the trafficking of cargo to the synaptic terminals, which in turn, is likely to alter the steady-state levels of a number of presynaptic proteins. Furthermore, many presynaptic proteins undergo extensive post-translational modifications, such as palmitoylation, during transport through the GA, which are important for subcellular targeting and protein-protein interactions. Thus, the reduction in spontaneous release that I observe here, and at the fly NMJ, could be caused by steady-state changes in the molecular components of the presynaptic release machinery, mis-targeting of proteins (including ion channels) to the presynaptic terminal or indeed, by structural changes within the terminal itself, not limited to alterations in the size or dynamics of functionally distinct pools of synaptic vesicles. However, I have not ruled out the possibility that the reduction that I observed in spontaneous neurotransmission is due to post-synaptic changes.

It is useful, still, however, to consider whether the mechanisms underlying the reduction in spontaneous release are the same for both the fly NMJ, a model glutamatergic synapse, and mammalian glutamatergic central synapses (Broadie & Bate, 1995). My finding of reduced spontaneous release frequency is consistent across species, including in mammalian neurons where redundancy would be expected to increase. Furthermore, mechanisms of synaptogenesis and synaptic transmission have been extensively studied at the fly NMJ and have been shown to be highly conserved through evolution. It is possible, therefore, that the reduction in spontaneous neurotransmitter release that I observe is caused by changes in highly conserved molecular components of the release machinery. Interestingly, my results reveal a trend towards a reduction in the proportion of SNAP-25 associated complexes, which could correspond to SDS-resistant quaternary SNARE complexes of ~64 kDa (Hayashi et al., 1994b; Söllner et al., 1993).

The assembly and disassembly of SNARE complexes is essential for synaptic vesicle trafficking. A reduction in the proportion of ternary SNARE complexes could be due to a reduction in the formation or stability of trans-SNARE complexes (fusion competent) or an upregulation of the recycling of cis-SNARE complexes (fusion incompetent, remaining in the plasma membrane after vesicle fusion). I probed for quaternary SNARE complexes by immunoblotting for one of its core components, SNAP-25, which forms a complex with syntaxin1 and synaptobrevin2 (or Vesicle-associated membrane protein 2, VAMP2). A reduction in the formation of SNARE complexes could be due to a reduction in the levels of individual SNARE proteins, however, I found no overall reduction in SNAP-25 levels in neurons. These findings are consistent with data from Membrin-G147W expressing flies that showed, using immunocytochemistry, that there was no reduction in the total levels of SNAP-25 in presynaptic terminals at the NMJ (Praschberger et al., 2017). Unchanged levels of SNAP-25 in Membrin-G147W presynaptic terminal was perhaps surprising given the fact that the authors detected a significant reduction in the presynaptic levels of the co-chaperone, CSPα, which is known to regulate SNAP-25 levels by preventing its ubiquitination and degradation (Sharma et al., 2012). CSPα, however, also acts a co-chaperone for the incorporation of SNAP-25 into SNARE complexes and so it is possible that its reduction (by ~20%) in this case specifically leads to impaired SNARE complex formation - this was not investigated in the fly (Sharma et al., 2011). A presynaptic reduction in CSPα, resulting from GOSR2 induced secretory trafficking defects, may therefore represent one mechanism by which SNARE complexes are reduced, however this has yet to be investigated in mammalian neurons. For example, a reduction in SNARE complex assembly could also be due to a reduction in the level of a different presynaptic chaperone, such as α-synuclein, that does not directly chaperone SNAP-25 (Burre et al., 2010).

Alternatively, a reduction in SNAP-25 containing SNARE complexes could be due to an upregulation of the disassembly of cis-SNARE complexes, which in turn requires an upregulation of ATPase N-ethylmaleimide-sensitive fusion protein (NSF) (Littleton et al., 2001). However, upregulation of NSF following GOSR2 mutation is contraindicated in the scenario of CSPα deficiency (as indicated in the fly models) as CSPα deficiency has been shown to result in a reduction in the level of NSF as well as a reduction in other proteins involved in endocytosis, such as dynamin1 (Sharma et al., 2012).

The impairment of spontaneous neurotransmission in neurons expressing GOSR2-G144W may not, however, be directly attributed to a reduction in the proportion of exocytotic quaternary SNARE complexes. Whilst the mechanisms of spontaneous release continue to be elucidated and refined, it is increasingly recognised that evoked and spontaneous release are differentially regulated (Kavalali, 2015). In particular, it has been found that whilst the selective knock-out of core SNARE proteins severely affects evoked release, spontaneous release remains largely preserved, leading some to suggest that the core components of the release machinery vary for the different modes of neurotransmission (Kavalali, 2015). I have not determined the molecular identity of the ternary SNARE complexes identified in my immunoblots, but it is likely that they correspond to mixed population of SNARE complexes that contain SNAP-25. However, it is also likely that, whilst distinctly regulated, the core machinery for evoked and spontaneous release partially overlap, such that both processes may be impaired by a reduction in SNARE complexes.

5.7.5 Excitatory synapse number is unchanged for GOSR2-G144W

In Drosophila, dramatic morphological changes were observed at the NMJ, including evidence of synaptic retraction and smaller, misshapen terminal boutons, which likely perturb the necessarily strict juxtaposition of presynaptic active zones and post-synaptic glutamate receptors (Praschberger et al., 2017). It is possible, therefore, that the disorganisation and reduction in the number of functional excitatory synapses at the fly NMJ accounts for a reduction in spontaneous release.

In my work, however, I did not observe a reduction in the number of excitatory synaptic contacts along the dendrites of neurons in culture expressing GOSR2 mutants, suggesting that reduction in synapse number does not account for the reduction in spontaneous release that I observed. However, I cannot rule out the contribution of post-synaptic effects of GOSR2 mutation. For example, mutation of GOSR2 may result in a reduction in the number of synapses expressing AMPARs (active synapses). Indeed, immunolabelling for the excitatory synaptic markers VGLUT1 and HOMER1 did not allow for me to distinguish between active and silent synapses in cultures expressing GOSR2 mutants.

5.8 Conclusions and new perspectives

I have shown using an overexpression model in cortical neuronal cultures that the G144W mutation in GOSR2 results in a reduction in GOSR2 protein levels (presumably contributing to loss-of-function phenotypes in patients) and impacts upon presynaptic physiology, presumably by conferring reduced rates of vesicle trafficking from the ER-Golgi, and through the Golgi stack. I have identified a possible reduction in SNARE complexes required for neurotransmitter exocytosis caused by GOSR2 mutation. I suggest a possible role for CSPα in the reduction of fusion competent SNARE complexes, but this has not been experimentally determined, nor has the identity of SNAP-25 associated complexes as SNARE complexes been validated.

It remains unclear as to how exactly an impairment in ER-Golgi trafficking would result in the reduction of selected synaptic cargoes such as CSPα. Recently, however, it has been shown, using fly models and murine hippocampal neuronal cultures, that certain active zone components and synaptic vesicle proteins are delivered to terminal synaptic boutons via anterograde axonal transport in presynaptic lysosome-related vesicles (PLVs) (Vukoja et al., 2018). PLVs are lysosomal structures that express LAMP1, a well-characterised lysosomal associated protein, but are distinct from their mature and acidic counterparts that are involved in protein degradation, and are trafficked along axonal microtubules by the kinesin adaptor protein, Arl8 (Vukoja et al., 2018). At the fly NMJ, the specific presynaptic knockdown of Arl8 was found to result in the reduction of specific exocytotic presynaptic proteins including, synaptotagmin 1, VGLUT1, synapsin and CSPα. It appears therefore that CSPα and VGLUT1 are transported within the same trafficking vesicles that could explain the reduction in both VGLUT1 and CSPα that was observed in Drosophila expressing Membrin mutants. Given that the GA is required for the formation of lysosomes, it is possible that ER-Golgi trafficking deficits have a downstream effect on the formation or composition of PLVs or rates of PLV trafficking (Hsu et al., 2009).

5.9 Future directions

5.9.1 Dendritic outgrowth

The work presented in this chapter has focused on the impact of early secretory trafficking defects, conferred by GOSR2 mutation, on presynaptic physiology. I have not explored the effect of overexpressing GOSR2-G144W on dendritic outgrowth, which has previously been shown to be profoundly affected in the Drosophila models of NS-PME (**Figure 5.1**), in mammalian neurons. One reason why I did not do this as an early, initial experiment in neuronal cultures is because I anticipated a high degree of cell-type and dendritic tree variability for neurons in culture, especially as I were not using cell-type specific promoters to reduce this variability. Whilst significant results were observed by Jepson & Praschberger following overexpression of Membrin mutants on a WT background in Drosophila (**Figure 5.1**), the observed dendritic phenotype was milder than that observed for expression on a null background (Praschberger et al., 2017). Furthermore, variability in dendritic architecture was minimized by studying the effects of Membrin mutants on the exact same sensory neuron (ddaC, abdominal section 5 of L3 larva) (Grueber et al., 2002; Praschberger et al., 2017). Future experiments will aim to investigate neurite outgrowth in culture at an early developmental age, and potentially in a restricted neuronal population, using sparse labelling.

5.9.2 Investigating the effects of GOSR2 mutation on Purkinje cell development

In this chapter I presented a strategy for targeting the expression of GOSR2 transgenes to cerebellar Purkinje cells. There were a number of factors that dictated this choice of experiment:

1. I predicted secretory pathway deficits to exert a selective effect on neurons with complex dendritic trees *in vivo*.
2. Purkinje cells are a highly relevant cell type in Ataxia, one of the major disease phenotypes in NS-PME.
3. The restricted expression of GOSR2 transgenes would allow for the separation of the pre- and post-synaptic effects of GOSR2 mutations.

With respect to point 3, I wanted to investigate whether the previously observed deficits in dendritic outgrowth are cell-autonomous, i.e. mostly affected by impaired trafficking and delivery of biosynthetic materials required for building neuronal processes. Furthermore, by recording from neurons of the deep cerebellar nuclei, I could take advantage of the high levels of Purkinje cell spontaneous activity to investigate the effects of GOSR2 mutants on evoked release, without the potential confounding factor of post-synaptic changes caused by GOSR2 mutations.

Unfortunately, I was unable to observe effective transduction of Purkinje cells using commercially synthesised AAV9 pseudotyped virus. Instead, a new AAV-PCP2-GFP virus of the PhP.eb serotype was recently synthesized by a collaborator. PhP.eb viruses have been shown to have a good tropism for the Purkinje cells (transduction of >75% of Purkinje cells) and higher rates of neuronal transduction than AAV9 (Challis et al., 2018, 2019). I will assess the efficiency of Purkinje cell transduction using tail vein injection of AAV into adult mice and immunofluorescent analysis of cerebellar slices (Challis et al., 2019). I will also consider changing the PCP2 promoter to a stronger promoter.

5.9.3 Validation of findings related to alterations in exocytotic SNARE complexes

I have observed a trend towards a reduction in the proportion of quaternary exocytotic SNARE complexes caused by GOSR2-G144W overexpression. The next step would be to repeat this experiment a 4th time in order to see whether this is a significant trend. It is also important to confirm the identity of the higher order SNAP-25 immunoreactive bands as SDS-resistant SNARE complexes. This could be done by validating the specificity of the SNAP-25 antibody on in cultures derived from SNAP-25 knock-out mice. Alternatively, different protocols for the preparation of protein lysates could be used in order to show the conditions under which the ternary complex breaks down – to help confirm specificity of the band. It would also be informative to perform an immunoblot for other components of the core SNARE complex such as syntaxin1 and synaptobrevin2. If a reduction in exocytotic SNARE complexes is validated, it would be interesting to see what effect this has on evoked neurotransmission. In the future Synaptophluorin (genetically encoded indicator of vesicle release) experiments could be performed in order to calculate the probability of release at single synapses using fluorescence variation. Increase of fluorescence is associated with Synaptophluorin exposure to the extracellular space and is therefore a readout of vesicle fusion and exocytosis. I would use extracellular stimulation at 40 Hz/100 Hz to estimate the readily releasable pool (RRP) and combined with the single stimulus release, the probability of release would be calculated as the ratio between single stimulus and RRP (Ariel, 2010).

Finally, in order to test the hypothesis that the reduction in quaternary SNARE complexes is due to a reduction in CSPα, a next step could also be to perform an immunoblot for CSPα levels. A synaptosomal preparation may be required for this, as the reduction in CSPα may be specifically presynaptic. Alternatively, an immunocytochemical investigation of CSPα signal at presynaptic terminals could be performed.

Chapter 6

General Discussion

The Progressive Myoclonic Epilepsies (PME) are a highly heterogeneous population of rare and severe genetic epilepsies that are characterised by the core symptoms of myoclonus and epilepsy. PME also features ataxia and dementia, comorbidities that are driven by progressive neurodegeneration. The severity of the epilepsy and the extent of neurodegeneration varies considerably across the different forms of PME, spurring the subdivision of PME with or without dementia. Recently, however, it is being increasingly recognized that some forms of PME feature ataxia more prominently than dementia or epilepsy, leading to a newly proposed subdivision of Progressive Myoclonus Ataxia (PMA). At the beginning of this thesis I hypothesised that by studying gene mutations underlying a more homogenous group of disorders, classified as PMA, I would be more likely to uncover common disease mechanisms. Here, I summarise my main findings for MEAK and NS- PME and suggest that they might indeed share common pathological endpoints. These points of mechanistic convergence are represented by dendritic dysfunction in parallel with alterations in presynaptic function, which may contribute towards the degenerative nature of PME.

6.1 Results summary

This thesis has focused on characterising the neuronal effects two different gene mutations known to cause PMA. The first gene mutation I studied was the recurrent c.959G>A point mutation in *KCNC1*, which results in a p.R320H transition in the VSD of K_V3.1. Patients are heterozygous for this mutation (which displays an autosomal dominant form of inheritance) and are described as having a distinct form of PME; myoclonus epilepsy and ataxia caused by potassium channel mutation (MEAK). The second gene mutation I studied was the p.G144W mutation in GOSR2 that occurs in the highly conserved SNARE domain of the protein and induce a partial-loss-of-function. Mutations in GOSR2 cause North-Sea PME, which has an autosomal recessive mode of inheritance and prominently features early-onset ataxia. Prior to this thesis, the neuronal effects of mutation in K_V3.1 had not been studied, nor had the effects of mutation in GOSR2 been studied in mammalian neurons or at central synapses. Here, I summarise my main findings for the expression of these mutant proteins in cortical neurons *in vitro*.

6.1.1 MEAK might represent a neurodevelopmental disorder

VGKCs are key regulators of neuronal excitability and loss-of-function mutations in potassium channels are frequently associated with hyperexcitability disorders, such as epilepsy (Köhling & Wolfart, 2016). In this thesis, and previously, it has been confirmed that the R320H mutation $K_V3.1b$ is a partial loss-of-function with a dominant negative effect of WT channel function (Munch et al., 2018). $K_V3.1$ is important for the rapid repolarization of the action potential and is highly expressed in neurons that fire at high frequencies, such as PV^+ interneurons and neurons of the cerebellum (Rudy & McBain, 2001). Therefore, $K_V3.1b$ loss-of-function is predicted to result in hyperexcitability phenotypes by selectively impairing the ability of fast-spiking neurons to convey signals at high frequencies, resulting in cortical disinhibition and dysregulated of the cerebellar circuitry. In this thesis, I have confirmed that $K_V3.1b^{R320H}$, compared to $K_V3.1b^{WT}$, cannot support high frequency firing of interneurons, however, I have also revealed unexpected effects of this mutant channel on neuronal development (**Chapter 3**).

Firstly, I have found this mutation to induce a reduction in dendritic and axonal length when expressed at high levels during development, changes that may contribute to cell loss. Although the mechanisms by which this occurs are unclear, I speculate that cell death is initiated by a reduction in dendritic length, which in turn is caused by dendritic hyperexcitability due to the loss of local potassium conductances. Expression of $K_V3.1^{R320H}$ at lower levels does not result in such severe neuronal phenotypes, however I do observe significant alterations in the input-output properties of interneurons at 14 DIV, suggesting that the channel induces morphological alterations, or other compensatory changes involving other ion channels, which impair the ability of the neuron to fire more frequent action potentials upon increasing depolarising stimulus. Indeed, alterations in the input-output properties of interneurons expressing $K_V3.1^{R320H}$ do not appear to be due to alterations in single AP properties as I do not observe any changes in AP parameters that I would expect to be influenced by the expression of fast-delayed rectifier conductances. Therefore, it seems that $K_V3.1b^{R320H}$ channels do not have a dominant negative effect on endogenous K_V3 channels at the level of the membrane, as might have been predicted from biophysical studies.

The potential effects of $K_V3.1b^{R320H}$ channels on neuronal development are unexpected and need to be confirmed by further experiments. However, our results are exciting as they reveal a potentially novel role for K_V3 channels in neuronal development, particularly in the development of the dendrites. I have found overexpression of mutant $K_V3.1b$

channels to result in severe neuronal phenotypes and so models of MEAK where the mutation is expressed at physiological levels, such as those outlined in **Chapter 4** of this thesis, promise to provide important insights into disease mechanisms. However, I still predict severe functional impairment of neurons that express high levels $K_V3.1$ channels, given the severe neurological phenotypes exhibited by patients with MEAK. Indeed, channelopathies that disproportionately affect the functioning of one particular neuronal subtype usually result in some of the most severe forms of epilepsy due to a severe offset of excitatory-inhibitory imbalance (Jiang et al., 2016; Rossignol et al., 2013).

6.1.2 NS- PME may represent a synaptopathy

Mutations in in the cis Golgi SNARE protein, GOSR2, result in partial loss-of-function of the SNARE domain and reduced rates of vesicle fusion in the early secretory pathway. In fly models of North-Sea PME, reduced rates of flux through the early secretory pathway result in impaired dendritic outgrowth and alterations in presynaptic structure and function (Praschberger et al., 2017). In this thesis (**Chapter 5**) I focused on characterising the effects of GOSR2 mutation on presynaptic function in mammalian neurons.

In Membrin-G147W flies, a reduction in the frequency of spontaneous neurotransmission was observed at the NMJ. I have also found a reduction in the frequency of excitatory spontaneous neurotransmitter release at central synapses resulting from a suspected presynaptic deficit. The mechanism by which this occurs is as yet unknown, however it is likely to represent a conserved mechanism given the replication of this finding across species. I have also found a trend towards a reduction in the proportion of SNARE complexes resulting from mutation in GOSR2, which may contribute towards the reduction in spontaneous release or may have an as of yet unconfirmed effect on evoked release. The reduced proportion of SNARE complexes observed upon the expression of GOSR2 mutant protein may be due to a presynaptic reduction in CSPα, as suggested by findings from the fly model of the disorder, however this has yet to be confirmed (Praschberger et al., 2017). Thus, I demonstrate for the first time in mammalian central synapses downstream effects of early secretory pathway trafficking deficits on presynaptic function.

6.2 Dendritic dysfunction in PME with ataxia

Perturbations that affect the structure of the dendrites can have a significant impact on synaptic integration, plasticity and excitability and can lead to disease (Johnston et al., 2015). The morphological changes induced by $K_V3.1b^{R320H}$ channels suggest that structural changes in the dendrites may a role in the disease pathogenesis of MEAK. Previous findings for mutations in GOSR2 report profound dendritic growth defects, suggesting that dendritic changes also contribute towards disease symptoms in NS-PME. Here I discuss the possibility that dendritic dysfunction is a common pathological endpoint in PME, that likely contributes towards the ataxic phenotypes of these patients.

6.2.1 Dysregulation of dendritic K^+ channels in Epilepsy and Ataxia

I have seen that the developmental expression of mutant Kv3.1 channels results in a reduction in dendritic length under circumstances of high expression, revealing a potential role for Kv3(.1) channels in dendritic development and function. Interestingly, despite the pervasiveness of ion channel mutations in epilepsy, only one other VGKC gene, KCND2 ($K_V4.2$), has been clearly associated with dendritic pathophysiology in epileptogenesis (Bernard et al., 2004; Johnston et al., 2015). $K_V4.2$ has been implicated as an inherited and acquired channelopathy in temporal lobe epilepsy (TLE) as well as in epilepsy with autism (Bernard et al., 2004; Lin et al., 2018; Singh et al., 2006). In experimental TLE, $K_V4.2$ was found to be dramatically reduced at both the transcriptional and translational level in chronically epileptic rats (Bernard et al., 2004). The consequence of a dendritic loss of $K_V4.2$ function was an enhancement of back propagating action potentials (bAPs), increased dendritic excitability and increased burst firing that may contribute towards seizure generation (Bernard et al., 2004).

Interestingly, in the last few years, novel loss-of-function mutations have been identified in the closely related KCND3 gene ($K_V4.3$) as causative for autosomal dominant spinocerebellar ataxia 19/22 (SCA19/22) (Kurihara et al., 2018; Lee et al., 2012; Smets et al., 2015). SCA19/22 is characterised by progressive ataxia, epilepsy, myoclonus (depending on the specific mutation) and intellectual disability (Kurihara et al., 2018; Lee et al., 2012; Smets et al., 2015). $K_V4.3$ is also expressed in dendrites but has a different expression pattern to $K_V4.2$ in the brain - being highly expressed in the cerebellum as well as in GABAergic interneurons (Rhodes et al., 2004). It is therefore likely that dendritic hyperexcitability caused by loss-of-function of A-type K^+ currents, as has been observed for $K_V4.2$ in TLE, is also the main disease mechanism in SCA19/22. The overlapping PMA-like disease phenotypes of a dendritic channelopathy ($K_V4.3$) and MEAK ($K_V3.1$) supports the way in which I have interpreted our data to suggest that dendritic dysfunction plays a pivotal role in MEAK.

Further in support of our hypothesis is the observation that loss of K_V3-mediated channel conductances are also implicated in spinocerebellar ataxia. Mutations in $K_V3.3$ have been shown to cause SCA13, which is characterised by progressive cerebellar atrophy, ataxia, occasionally seizures and neurodevelopmental features (Zhang & Kaczmarek, 2016). K_V3 channels may also represent an 'acquired channelopathy' in other forms of spinocerebellar ataxia caused by different gene mutations. For example, it has been shown in SCA1 and 2 that the expression $K_V3.2$ and 3.3, as well as some other VGKCs, is significantly reduced in Purkinje cell dendrites, resulting in increased bAPs and dendritic calcium spikes (Chopra et al., 2018; Dell'Orco et al., 2017). These changes, albeit secondary to the initial genetic insult, likely drive disease pathogenesis, as it has been shown that normalising potassium conductances improves motor performance and abates Purkinje cell degeneration (Chopra et al., 2018). Targeting potassium channels is now being proposed as a valid treatment strategy for the cerebellar ataxias (Bushart et al., 2018).

6.2.2.1 Dysregulation of dendritic K^+ conductances and dendritic degeneration

Changes in dendritic excitability can impact dendritic development and lead to abnormalities in dendritic structure. I have observed that when expressed at high levels, mutant $K_V3.1$ channels induce reductions in dendritic length and neuronal loss. While neurodevelopmental defects may contribute to disease pathogenesis in MEAK, disease symptoms do not appear until an average of ten years of age, implying that compensatory mechanisms maintain excitatory balance in the interim (Oliver et al., 2017). Indeed, the progressive nature of PME likely reflects the eventual failure or overload of neuronal compensatory mechanisms that have been activated in order to regulate dendritic excitability.

It is possible that over time, some of these compensatory changes become maladaptive and eventually contribute to disease pathogenesis. In mouse models of spinocerebellar ataxia, it has been shown that dendritic retraction precedes Purkinje cell degeneration, suggesting that structural changes in dendrites are an early event in the neuropathological progression of the disease (Koeppen, 2005). Interestingly, dendritic atrophy has been purported as a compensatory mechanism that helps to maintain repetitive Purkinje cell firing in the face of unopposed Ca^{2+} currents resulting from reduced BK and A-type potassium channel expression (Dell'Orco et al., 2015). Maladaptive remodelling could explain the dramatic reduction in dendritic length that I observed upon mutant $K_V3.1$ channel expression in young cortical interneurons. I likely observed an accelerated and severe effect of dendritic atrophy due to the fact that I expressed the channel at very high levels that the cell struggled to compensate for. As a result, I saw a very early ‘developmental’ phenotype in culture. In patients, the effects of maladaptive remodelling are likely to be much delayed (i.e. clinical presentation at ~10 years) because the channel is expressed at a much lower level and at different developmental time-points, such that neuronal compensatory mechanisms are able to maintain neuronal function within normal limits. MEAK may still represent a neurodevelopmental disorder, however, because the cerebellum shows a protracted development into young adolescence (Tiemeier et al., 2010).

6.2.2 Secretory pathway deficits preferentially impact dendrites

In MEAK dendritic hyperexcitability induced by mutation in a potassium channel might cause dendritic defects due to compensatory mechanisms involving sacrifice of the dendritic membrane surface area in an attempt to maintain intrinsic excitability. Interestingly, a similar compensatory principle may apply in NS-PME. In NS-PME, secretory pathway deficits conferred by mutation in GOSR2 have been shown to lead to reduced complexity of the dendritic tree (Praschberger et al., 2017). The shrinkage of the dendritic tree is likely due to sacrifice of the dendritic plasma membrane due to a limited supply of biosynthetic materials, such as lipids, required to expand and maintain the plasmalemma. Indeed, multiple lines of evidence suggest that dendritic and axonal trafficking is differentially regulated and that dendrites are preferentially pruned under conditions of secretory pathway stress (Horton et al., 2005; Horton & Ehlers, 2003; Ye et al., 2007). This is somewhat unsurprising given that dendrites constitute the majority of the surface membrane of a pyramidal neuron. While I have yet to confirm these dendritic defects in mammalian neurons, I envisage that neurons with particularly large and complex dendritic trees, such as Purkinje cells, will be disproportionately affected by GOSR2 mutations.

It is interesting to consider the extent to which the principles that apply for NS-PME and possibly MEAK may also broadly apply to other forms of PME. For example, sacrifice of dendritic membrane, or impairments in neurite outgrowth, may also occur as a maladaptive compensatory mechanism in the neuronal ceroid lipofuscinoses (NCLs) due to a limiting supply of membrane lipids. The NCLs are a group of PMEs with dementia that have broad biochemical aetiologies and yet are collectively characterised by an accumulation of neuronal lipopigments within the lysosome (Nita et al., 2016). The accumulation of lipids in the lysosome implies that defects in lipid trafficking and/or metabolism contribute towards disease pathology. Indeed, most CLN variants manifest dysregulated sphingolipid metabolism. Sphingolipid biosynthesis has been shown to be essential for dendrite growth and survival of cerebellar Purkinje cells *in vitro* (Furuya et al., 1995; Persaud-Sawin et al., 2007).

Specific examples of lipid dysregulation in NCLs and other PMEs further our argument. Deficits in ER-Golgi lipid transport has been reported for CLN8 that has a distinctive PME phenotype (Nita et al., 2016). A role for CLN8 has been suggested in the biosynthesis and transport of lipids such as ceramide synthesis and glycosphingolipid trafficking (Furuya et al., 1995; Jalanko & Braulke, 2009). Furthermore, in SCARB2-based PME, LIMP2 (the protein product of SCARB2) has been shown to play a role in lipid transport and is required for trafficking of β-glucocerebrosidase through the secretory pathway (Neculai et al., 2013; Reczek et al., 2007). Interestingly, mutations in β-glucocerebrosidase cause Gaucher's disease, a lysosomal storage disorder, where a subset of patients have PME. It therefore appears that a large proportion of PME genes impact lipid metabolism or trafficking, which may have knock-on impacts on dendritic development and maintenance (Zunke et al., 2016).

6.2.3 Dendritic vulnerability in PME

A concept of the preferential vulnerability of the dendrites over the axon in PME thus emerges. This hypothesis appears to be supported by histopathological findings for other forms of PME such as LBD. LBD has a distinctive pathology, where insoluble polyglucosans accumulate to form aggregates termed, Lafora Bodies (LBs) (Turnbull et al., 2016). LBs are found exclusively in the dendrites and soma of neurons, with a particularly striking deposition of LBs found in the dendrites of Purkinje cells and Stellate neurons of the cerebellum (Chan et al., 2004; Minassian, 2001; Turnbull et al., 2016). Interestingly, when polyglucosan bodies are deposited in the axons of neurons as a result of glycogen-branching enzyme deficiency (and not mutations in laforin or malin) it results in a completely different disease: adult-onset motor neuron disease (Bruno et al., 1993). These markedly dissimilar clinical symptoms resulting from a very similar molecular pathology (involving the glycogen metabolic pathway) suggests that it is the very specific location of the polyglucosan bodies that determine the disease phenotypes and suggests that the localisation of LBs in the dendrites contributes directly towards hyperexcitability and ataxia in PME.

6.3 Presynaptic dysfunction in PME

I have seen that postsynaptic deficits are implied for many PME mutations, particularly relating to changes in the structure of the dendritic tree. However, ours and previous findings relating to NS-PME suggest that presynaptic deficits also contribute to disease pathogenesis. In fly models of NS-PME, reduced rates of vesicular transport and fusion in the early secretory pathway were found to impact upon neurotransmitter release and the delivery of presynaptic cargo to terminals. In this thesis, I have found that mutation in GOSR2 impairs spontaneous neurotransmission at central glutamatergic synapses via a presynaptic mechanism and also found a reduction in fusogenic exocytotic SNARE complexes. Interestingly, data from fly models of NS-PME found a presynaptic reduction in the levels of CSPα, a SV-associated presynaptic chaperone protein, and so I speculate that the possible trend towards a reduction in fusogenic SNARE complexes that I observe in mammalian central synapses is due to impaired complex formation, possibly due to presynaptic reductions in the levels of CSPα (Praschberger et al., 2017).

It is interesting to note that a role for CSPα has been implicated in lysosomal storage disorders, such as the NCLs – a group of PMEs with dementia. In lysosomal storage disorders it has been found that lysosomal dysfunction disrupts presynaptic maintenance due to a cytosolic accumulation of α-synuclein and enhanced proteasomal degradation of CSPα (Sambri et al., 2017). As a consequence, there is a reduced availability of presynaptic chaperones, which results in inhibition of SNARE complex assembly and synaptic vesicle cycling (Sambri et al., 2017). In addition to this, mutations in CSPα have been shown to cause the adult-onset form of PME, CLN4 (Benitez et al., 2011; Nosková et al., 2011; Velinov et al., 2012). These mutations occur within the cysteine string domain of the protein, resulting in decreased palmitoylation of this domain, with mistargeting and aggregation of the protein as a functional consequence (Greaves et al., 2012; Nosková et al., 2011). It is possible that alterations in palmitoylation and mis-sorting of CSPα also occurs to some extent in NS-PME given the central role that the Golgi plays in post-translational modification of secretory cargoes.

Presynaptic deficits are significant in the CLNs and may contribute towards neurodegeneration (Cooper, 2010; Cooper et al., 2015). Whilst neurodegeneration is not as much of a prominent feature in NS-PME, synaptic instability is suggested by the fact that motor neuron denervation is observed (van Egmond et al., 2014). Motor neurons are likely to be particularly vulnerable to defects in axonal trafficking because they have very long axons and rely more heavily upon distantly regulated synaptic homeostasis (Ikenaka et al., 2012). Interestingly, CLN8 is caused by a mutation in an ER/ERGIC localized transmembrane protein, which likely impacts on the early secretory pathway, and features a motorneuron disease phenotype when naturally mutated in mice (Ranta et al., 1999). Whilst anecdotal, these findings lend further evidence towards early secretory pathway perturbations causing presynaptic deficits in PME.

6.4 PME as a neurodegenerative disorder

Progressive neurodegeneration occurs in many different forms of PME, however, neurodegeneration features much less prominently in NS-PME and MEAK. The exact mechanisms leading to neurodegeneration are not well understood, however they are proposed to feature a combination of synapse loss, lysosomal dysfunction and impaired autophagy (Bhat & Ganesh, 2018; Polajnar & Erovnik, 2011). Whilst I cannot rule out these processes in PMA, I propose that dendritic atrophy, as well as presynaptic dysfunction, contributes towards neuronal loss. As the disease progresses, the compensatory sacrifice of dendritic membrane and the loss of synaptic inputs becomes detrimental to neuronal survival, leading to the loss of vulnerable cell types. These sorts of processes are proposed for the closely related spinocerebellar ataxias, which are neurodegenerative conditions largely affecting the Purkinje cells of the cerebellum (Chopra et al., 2018). Progressive dendritic retraction need not to be incompatible with the activation of cell death pathways however. Indeed, I observed cell death following the expression of mutant K_V3.1 channels in young cortical neurons in culture that appeared to be related to neurite dystrophy (**Chapter 3**). In the absence of apoptotic markers, it is possible these neurons were lost as a result of overactive autophagy mechanisms. Future experiments will need to rule out aggregation of Kv3.1 as a cause of the pathological processes I observe. It is worth noting that prominent cerebellar atrophy is observed for MEAK and NS-PME on patient MRI scans, suggesting mechanistic overlaps with the ataxias (Oliver et al., 2017).

6.5 Conclusions

In this thesis I studied two very distinct gene mutations that are causative for PME with ataxia and have gained insights into the specific disease mechanisms underlying these disorders. By considering gene mutations that are causative for a more homogeneous ‘PMA’ phenotype, I found evidence to suggest that these diseases share structural alterations of the dendritic tree as a common pathological endpoint. Interestingly, MEAK appears to share clinical and mechanistic overlaps with the spinocerebellar ataxias, such that lessons learnt from this group of disorders may inform future experiments into this specific channelopathy.

For NS-PME, I found that mutation in GOSR2 results in alterations in presynaptic function. If such alterations were found to be due to changes in CSPα, this would reveal exciting mechanistic overlaps with the CLNs. Defects in dendritic outgrowth have previously been observed in fly models of NS- PME and so it appears that pre- and post-synaptic deficits co-exist within this disorder. Indeed, presynaptic deficits are also likely to be uncovered for MEAK because $K_V3.1$ is expressed in presynaptic terminals.

Often it can be difficult when studying neurological diseases to separate the pre- and post-synaptic effects of a mutation on neuronal function, a problem that seems to be highly relevant for PME. I went some way to addressing this dilemma by developing an optogenetic screen that would allow for the presynaptic effects of a mutation to be isolated, yet found this approach to be practically challenging. The principles of such an approach, however, can be taken forwards to address the hypothesis that interneurons are particularly vulnerable to PME mutations. I did not look at cell type specific effects for GOSR2 mutations, however certain cell-types are likely to be particularly vulnerable to its effects such as Purkinje cells of the cerebellum, with their highly complex dendritic architecture. Cell type vulnerability is already suggested for MEAK, because $K_V3.1$ is only expressed in restricted neuronal populations. Our proposed conditional knock-in mouse model of MEAK promises to help dissect the varying contributions of different neuronal subtypes to disease phenotypes and to provide further insights into disease mechanisms. Overall, the data presented in this thesis supports the hypothesis that common disease mechanisms underlie PME with ataxia and I envisage that the further elucidation of these mechanisms may help to direct the development of rational treatments for this devastating, often fatal, group of disorders.

Bibliography

Airaksinen, E. M. & Leino, E. (1982). Decrease of GABA in the cerebrospinal fluid of patients with progressive myoclonus epilepsy and its correlation with the decrease of 5HIAA and HVA. *Acta Neurologica Scandinavica*, **66**(6), 666–672.

Alakurtti, K. et al. (2005). Loss of lysosomal association of cystatin B proteins representing progressive myoclonus epilepsy, EPM1, mutations. *European Journal of Human Genetics*, **13**(2), 208–215.

Allen, A. S. et al. (2017). Ultra-rare genetic variation in common epilepsies: a case-control sequencing study. *The Lancet Neurology*, **16**(2), 135–143.

Marseille Consensus Group. (1990). Classification of progressive myoclonus epilepsies and related disorders. *Annals of Neurology*, **28**(1), 113–116.

Andreae, L. C. & Burrone, J. (2015). Spontaneous Neurotransmitter Release Shapes Dendritic Arbors via Long-Range Activation of NMDA Receptors. *Cell Reports*, **10**(6), 873–882.

Angulo, E. et al. (2004). Up-regulation of the Kv3.4 potassium channel subunit in early stages of Alzheimer's disease. *Journal of Neurochemistry*, **91**(3), 547–557.

Antonin, W. et al. (2002). Crystal structure of the endosomal SNARE complex reveals common structural principles of all SNAREs. *Nature Structural Biology*, **9**(2), 107–111.

Appenzeller, S. et al. (2014). De Novo Mutations in Synaptic Transmission Genes Including DNM1 Cause Epileptic Encephalopathies. *The American Journal of Human Genetics*, **95**(4), 360–370.

Ariel, P. & Ryan, T. A. (2010). Optical mapping of release properties in synapses. *Frontiers in Neural Circuits,* **4**, 18.

Armstrong, C. M. & Bezanilla, F. (1973). Currents related to movement of the gating particles of the sodium channels. *Nature*, **242**(5398), 459–61.

Ashizawa, T. & Xia, G. (2016). Ataxia. *Continuum*, **22**(4, Movement Disorders), 1208–1226.

Asinof et al. (2015). Independent Neuronal Origin of Seizures and Behavioral Comorbidities in an Animal Model of a Severe Childhood Genetic Epileptic Encephalopathy. *PLoS Genetics* **11**(6): e1005347.

Atasoy, D. et al. (2008). A FLEX Switch Targets Channelrhodopsin-2 to Multiple Cell Types for Imaging and Long-Range Circuit Mapping. *Journal of Neuroscience*, **28**(28), 7025–7030.

Avanzini, G. et al. (2016). Neurophysiology of myoclonus and progressive myoclonus epilepsies. *Epileptic Disorders*, **18**(Suppl. 2), S11–S27.

Azizieh, R. et al. (2011). Progressive myoclonic epilepsy-associated gene KCTD7 is a regulator of potassium conductance in neurons. *Molecular Neurobiology*, **44**(1), 111–121.

Bannykh, S. I., Rowe, T., & Balch, W. E. (1996). The organization of endoplasmic reticulum export complexes. *Journal of Cell Biology*, **135**(1), 19–35.

Bassuk, A. G. et al. (2008). A homozygous mutation in human PRICKLE1 causes an autosomal-recessive progressive myoclonus epilepsy-ataxia syndrome. *American Journal of Human Genetics*, **83**(5), 572–581.

Benitez, B. A. et al. (2011). Exome-sequencing confirms DNAJC5 mutations as cause of adult neuronal ceroid-lipofuscinosis. *PLoS ONE*, **6**(11), e26741.

Bezanilla, F. (2005). Voltage-gated ion channels. *NanoBioscience, IEEE Transactions on*, **4**(1), 34-48.

Berkovic, S. F. et al. (1988). Kufs' disease: a critical reappraisal. *Brain: A Journal of Neurology*, **111**(1), 27–62.

Berkovic, S. F. et al. (2008). Array-based gene discovery with three unrelated subjects shows SCARB2/LIMP-2 deficiency causes myoclonus epilepsy and glomerulosclerosis. *American Journal of Human Genetics*, **82**(3), 673–84.

Bernard, C. et al. (2004). Acquired dendritic channelopathy in temporal lobe epilepsy. *Science Reports,* **305** (5683), pp. 532-553.

Bhat, S. & Ganesh, S. (2018). New discoveries in progressive myoclonus epilepsies: a clinical outlook. *Expert Review of Neurotherapeutics*, **18**(8), 649–667.

Boda, E. et al. (2012). Brain expression of Kv3 subunits during development, adulthood and aging and in a murine model of alzheimer's disease. *Journal of Molecular Neuroscience*, **46**(3), 606–615.

Boillot, M. et al. (2014). Glutamatergic neuron-targeted loss of LGI1 epilepsy gene results in seizures. *Brain,* **137**, 2984-2996.

Boillot, M. et al. (2016). LGI1 acts presynaptically to regulate excitatory synaptic transmission during early postnatal development. *Scientific Reports*, **6**, 21769.

Boissé Lomax, L. et al. (2013). "North Sea" progressive myoclonus epilepsy: phenotype of subjects with GOSR2 mutation. *Brain*, **136**(4), 1146–1154.

Bolte, S. & Cordelieres, F. P. (2006). A guided tour into subcellular colocalization analysis in light microscopy. *Journal of Microscopy*, **224**(3), 213–232.

Bonten, E. et al. (1996). Characterization of human lysosomal neuraminidase defines the molecular basis of the metabolic storage disorder sialidosis. *Genes and Development*, **10**(24), 3156–3169.

Boscia, F. et al. (2017). The expression and activity of KV3.4 channel subunits are precociously upregulated in astrocytes exposed to Aβ oligomers and in astrocytes of Alzheimer's disease Tg2576 mice. *Neurobiology of Aging*, **54**, 187–198.

Broadie, K. & Bate, M. (1995). The drosophila NMJ: a genetic model system for synapse formation and function. *Seminars in Developmental Biology*, **6**(3), 221–231.

Broker, L. E., Kruyt, F. A. E., & Giaccone, G. (2005). Cell Death Independent of Caspases: A Review. *Clinical Cancer Research*, **11**(9), 3155–3162.

Brooke, R. E. et al. (2004). Association of potassium channel Kv3.4 subunits with pre- and post-synaptic structures in brainstem and spinal cord. *Neuroscience*, **126**(4), 1001–1010.

Brooke, R. E. et al. (2004). Kv3 voltage-gated potassium channels regulate neurotransmitter release from mouse motor nerve terminals. *The European Journal of Neuroscience*, **20**(12), 3313–21.

Brunklaus, A., & Zuberi, S. M. (2014). Dravet syndrome - from epileptic encephalopathy to channelopathy. *Epilepsia*, **55**(7), 979–984.

Bruno, C. et al. (1993). Glycogen branching enzyme deficiency in adult polyglucosan body disease. *Annals of Neurology*, **33**(1), 88–93.

Burgoyne, R. D. & Morgan, A. (2015). Cysteine string protein (CSP) and its role in preventing neurodegeneration. *Seminars in Cell & Developmental Biology*, **40**, 153–9.

Burre, J. et al. (2010). α-Synuclein promotes SNARE-complex assembly in vivo and in vitro. *Science*, **329**(5999), 1663–1667.

Bushart, D. D. et al. (2018). Targeting potassium channels to treat cerebellar ataxia. *Annals of Clinical and Translational Neurology*, **5**(3), 297–314.

Buzzi, A., et al. (2012). Loss of cortical GABA terminals in Unverricht-Lundborg disease. *Neurobiology of Disease*, **47**(2), 216–224.

Callaway, E. M. et al. (2009). Short promoters in viral vectors drive selective expression in mammalian inhibitory neurons , but do not restrict activity to specific inhibitory cell-types, **3**, 1–24.

Canafoglia, L. et al. (2004). Sensorimotor cortex excitability in Unverricht-Lundborg disease and Lafora body disease. *Neurology*, **63**(12), 2309–2315.

Canafoglia, L. et al. (2010). Short and long interval cortical inhibition in patients with Unverricht-Lundborg and Lafora body disease. *Epilepsy Research*, **89**(2–3), 232–237.

Canafoglia, L. et al. (2017). Variable course of Unverricht-Lundborg disease. *Neurology*, **89**(16), 1691–1697.

Canafoglia, L. et al. (2011). Characterization of severe action myoclonus in sialidoses. *Epilepsy Research*, **94**(1–2), 86–93.

Canafoglia, L. et al. (2014). Expanding sialidosis spectrum by genome-wide screening:

NEU1 mutations in adult-onset myoclonus. *Neurology*, **82**(22), 2003–2006.

Cannon, S. C. (2010). Voltage-sensor mutations in channelopathies of skeletal muscle. *Journal of Physiology*, **588**(11), 1887–1895.

Carpenter, J. C. & Schorge, S. (2018). The voltage-gated channelopathies as a paradigm for studying epilepsy-causing genes. *Current Opinion in Physiology*, **2**, 71–76.

Carpenter, S. & Karpati, G. (1981). Sweat gland duct cells in Lafora disease: diagnosis by skin biopsy. *Neurology*, **31**(12), 1564–1568.

Carr, J. (2011). Classifying myoclonus: a riddle, wrapped in a mystery, inside an enigma. *Parkinsonism and Realted Disorders*, **18**(S1), S174–S176.

Cassim, F. & Houdayer, E. (2006). Neurophysiology of myoclonus. *Neurophysiologie Clinique/ Clinical Neurophysiology*, **36**(5–6), 281–291.

Catterall, W. A. (2010). Ion channel voltage sensors: structure, function, and pathophysiology. *Neuron*, **67**(6), 915–928.

Challis, R. C. et al. (2019). Systemic AAV vectors for widespread and targeted gene delivery in rodents. *Nature Protocols*, **14**(2), 379–414.

Chan, E. M. et al. (2004). Laforin preferentially binds the neurotoxic starch-like polyglucosans, which form in its absence in progressive myoclonus epilepsy. *Human Molecular Genetics*, **13**(11), 1117–1129.

Chan, E. M. et al. (2003). Mutations in NHLRC1 cause progressive myoclonus epilepsy. *Nature Genetics*, **35**(2), 125–127.

Chan, K. Y. et al. (2017). Engineered AAVs for efficient noninvasive gene delivery to the central and peripheral nervous systems. *Nature Neuroscience*, **20**, 1172-1179.

Chandra, S. et al. (2005). α-Synuclein cooperates with CSPα in preventing neurodegeneration. *Cell*, *123*(3), 383–396.

Chang, S. Y. et al. (2007). Distribution of Kv3.3 potassium channel subunits in distinct neuronal populations of mouse brain. *The Journal of Comparative Neurology*, **502**(6), 953–72.

Cheng, A. et al. (2007). A role for AGL ubiquitination in the glycogen storage disorders of Lafora and Cori's disease. *Genes and Development*, **21**(19), 2399–2409.

Chopra, R., Bushart, D. D., & Shakkottai, V. G. (2018). Dendritic potassium channel dysfunction may contribute to dendrite degeneration in spinocerebellar ataxia type 1. *PloS One*, **13**(5), e0198040.

Chow, A. et al. (1999). K+ channel expression distinguishes subpopulations of parvalbumin- and somatostatin-containing neocortical interneurons. *Journal of Neuroscience*, **19**(21), 9332–9345.

Clements, J. D. & Bekkers, J. M. 1997. Detection of spontaneous synaptic events with an optimally scaled template. *Biophysical Journal*, **73**, 220-229.

Coetzee, W. A. et al. (1999). Molecular diversity of K+ channels. *Annals of the New York Academy of Sciences*, **868**, 233–285.

Cohen, F. S. & Melikyan, G. B. (2004). The energetics of membrane fusion from binding, through hemifusion, pore formation, and pore enlargement. *Journal of Membrane Biology*, **199**(1), 1–14.

Cooper, J. D. (2010). The neuronal ceroid lipofuscinoses: the same, but different? *Biochemical Society Transactions*, **38**(6), 1448–52.

Cooper, J. D., Tarczyluk, M. A., & Nelvagal, H. R. (2015). Towards a new understanding of NCL pathogenesis. *Biochimica et Biophysica Acta - Molecular Basis of Disease*, **1852**(10), 2256–2261.

Cooper, J. et al. (1999). Apparent loss and hypertrophy of interneurons in a mouse model of neuronal ceroid lipofuscinosis: evidence for partial response to insulin-like growth factor-1 treatment. *The Journal of Neuroscience*, **19**(7), 2556–67.

Coppola, G. et al. (2005). Autosomal recessive progressive myoclonus epilepsy with ataxia and mental retardation. *Journal of Neurology*, **252**(8), 897–900.

Corbett, M. A. et al. (2011). A mutation in the Golgi Qb-SNARE gene GOSR2 causes progressive myoclonus epilepsy with early ataxia. *American Journal of Human Genetics*, **88**(5), 657–63.

Crespel, A. et al. (2017). Perampanel in 12 patients with Unverricht-Lundborg disease. *Epilepsia*, **58**(4), 543–547.

D'Amato, E. et al. (2000). Seizures induce widespread upregulation of cystatin B, the gene mutated in progressive myoclonus epilepsy, in rat forebrain neurons. *European Journal of Neuroscience*, **12**(5), 1687–1695.

Dancourt, J. & Barlowe, C. (2010). Protein sorting receptors in the early secretory pathway. *Annual Review of Biochemistry*, **79**(1), 777–802.

De Leeuw, C. N. et al. (2016). RAAV-compatible MiniPromoters for restricted expression in the brain and eye. *Molecular Brain*, **9**(1), 1–13.

De Marco Garcia, N. V. & Fishell, G. (2014). Subtype-selective electroporation of cortical interneurons. *Journal of Visualized Experiments:* (90), e51518.

Dell'Orco, J. M., Pulst, S. M., & Shakkottai, V. G. (2017). Potassium channel dysfunction underlies Purkinje neuron spiking abnormalities in spinocerebellar ataxia type 2. *Human Molecular Genetics*, **26**(20), 3935–3945.

Dell'Orco, J. M. et al. (2015). Neuronal atrophy early in degenerative ataxia is a compensatory mechanism to regulate membrane excitability. *Journal of Neuroscience*, **35**(32), 11292–11307.

Depienne, C. et al. (2010). Mechanisms for variable expressivity of inherited SCN1A mutations causing Dravet syndrome. *Journal of Medical Genetics*, **47**(6), 404–410.

Devinsky, O. et al. (2018). Epilepsy. *Nature Reviews Disease Primers*, **4**, 18024.

Di Giaimo, R. et al. (2002). New insights into the molecular basis of progressive myoclonus epilepsy: a multiprotein complex with cystatin B. *Human Molecular Genetics*, **11**(23), 2941–50.

Dibbens, L. et al. (2016). SCARB2/LIMP2 deficiency in action myoclonus-renal failure syndrome. *Epileptic Disord*, **18**, 63–72.

Dibbens, L. M. et al. (2009). SCARB2 mutations in progressive myoclonus epilepsy (PME) without renal failure. *Annals of Neurology*, **66**(4), 532–536.

DiMauro, S. (2004). Mitochondrial diseases. *Biochimica et Biophysica Acta - Bioenergetics*, **1658**(1–2), 80–88.

Dimidschstein, J. et al. (2016). A viral strategy for targeting and manipulating interneurons across vertebrate species. *Nature Neuroscience*, **19**(12), 1743–1749.

Ding, D. et al. (2018). Engineering introns to express RNA guides for Cas9- and Cpf1-mediated multiplex genome editing. *Molecular Plant*, **11**(4), 542–552.

Dong, F. et al. (2017). Polycistronic tRNA and CRISPR guide-RNA enables highly efficient multiplexed genome engineering in human cells. *Biochemical and Biophysical Research Communications*, **482**(4), 889–895.

Donnelier, J. & Braun, J. E. A. (2014). CSPα chaperoning presynaptic proteins. *Frontiers in Cellular Neuroscience*, **8**, 1–6.

Dragos, N., Mole, S. & Minassian, B. (2016). Neuronal ceroid lipofuscinoses. *Epileptic Disorders*, **126**(15), 1908–1910.

Du, J. et al. (1996). Developmental expression and functional characterization of the potassium-channel subunit Kv3.1b in parvalbumin-containing interneurons of the rat hippocampus. *The Journal of Neuroscience*, **16**(2), 506–518.

Duarri, A. et al. (2015). Functional analysis helps to define KCNC3 mutational spectrum in Dutch ataxia cases. *PLoS ONE*, **10**(3), 1–11.

Dull, T. O. M. et al. (1998). A third-generation lentivirus vector with a conditional packaging system, **72**(11), 8463–8471.

Dur-e-Ahmad, M., Crook, S. & Baer, S. (2007). A model of activity-dependent changes in dendritic spine density and spine structure. *BMC Neuroscience*, **8**(S2), 91.

Duran, J. et al. (2014). Glycogen accumulation underlies neurodegeneration and autophagy impairment in lafora disease. *Human Molecular Genetics*, **23**(12), 3147–3156.

Dutton, S. B. et al. (2013). Preferential inactivation of SCN1A in parvalbumin interneurons increases seizure susceptibility. *Neurobiology of Disease,* **49***,* 211-220.

Eberhardt, O. & Topka, H. (2017). Myoclonic disorders. *Brain Sciences*, **7**(8), 103.

El-Brolosy, M. A. et al. (2019). Genetic compensation triggered by mutant mRNA degradation. *Nature,* **568***,* 193-197.

Epi4K Consortium, Epilepsy Phenome/Genome Project, et al. (2013). De novo mutations in epileptic encephalopathies. *Nature*, **501**(7466), 217–221.

Escayg, A. et al. (2000). Mutations of SCN1A, encoding a neuronal sodium channel, in two families with GEFS+. *Nature Genetics*, **24**(4), 343–345.

Espinosa, F. et al. (2004). Increased motor drive and sleep loss in mice lacking Kv3-type potassium channels. *Genes, Brain and Behavior*, **3**(2), 90–100.

Espinosa, F. et al. (2001). Alcohol hypersensitivity, increased locomotion, and spontaneous myoclonus in mice lacking the potassium channels Kv3.1 and Kv3.3. *The Journal of Neuroscience*, **21**(17), 6657–6665.

EuroEPINOMICS-RES Consortium, Epilepsy Phenome/Genome Project & Epi4K Consortium. (2014). De novo mutations in synaptic transmission genes including DNM1 cause epileptic encephalopathies, *American Journal of Human Genetics*, **95**, 360–370.

Fasshauer, D. (2003). Structural insights into the SNARE mechanism. *Biochimica et Biophysica Acta*, **1641**(2–3), 87–97.

Fasshauer, D. et al. (1998). Conserved structural features of the synaptic fusion complex: SNARE proteins reclassified as Q- and R-SNAREs. *Proceedings of the National Academy of Sciences of the United States of America*, **95**(26), 15781–6.

Faught, E. (2003). Clinical Presentations and Phenomenology of Myoclonus. *Epilepsia*, **44**(11), 7–12.

Ferlazzo, E. et al. (2017). Update on pharmacological treatment of Progressive Myoclonus Epilepsies. *Current Pharmaceutical Design*, **23**(37), 5662–5666.

Figueroa, K. P. et al. (2010). KCNC3: phenotype, mutations, channel biophysics - a study of 260 familial ataxia patients. *Human Mutation*, **31**(2), 191–196.

Fisher, R. S. et al. (2014). ILAE Official Report: a practical clinical definition of epilepsy. *Epilepsia*, **55**(4), 475–482.

Fisher, R. S. et al. (2017). Instruction manual for the ILAE 2017 operational classification of seizure types. *Epilepsia*, **58**(4), 531–542.

Fisher, R. S., Elger, C. E. & Engel, J. (2013). An operational clinical definition of epilepsy. *International League Against Epilepsy*.

Franceschetti, S. & Canafoglia, L. (2016). Sialidoses. *Epileptic Disorders*, **18**(S2), 89–93.

Franceschetti, S. et al. (2007). A pathogenetic hypothesis of Unverricht-Lundborg disease onset and progression. *Neurobiology of Disease*, **25**(3), 675–685.

Fremeau, R. T. et al. (2004). VGLUTs define subsets of excitatory neurons and suggest novel roles for glutamate. *Trends in Neurosciences*, **27**(2), 98–103.

Fukuda, R. et al. (2000). Functional architecture of an intracellular membrane t-SNARE. *Nature*, **407**(6801), 198–202.

Fusella, A. et al. (2013). Segregation of the Qb-SNAREs GS27 and GS28 into Golgi vesicles regulates intra-Golgi transport. *Traffic*, **14**(5), 568–584.

Gaborit, N. et al. (2007). Regional and tissue specific transcript signatures of ion channel genes in the non-diseased human heart. *Journal of Physiology*, **582**(2), 675–693.

Gallego-Iradi, C. et al. (2014). KCNC3^{R420H}, a K^+ channel mutation causative in spinocerebellar ataxia 13 displays aberrant intracellular trafficking. *Neurobiology of Disease*, **71**, 270–279.

Gamp, A.C. et al. (2003). LIMP-2/LGP85 deficiency causes ureteric pelvic junction obstruction, deafness and peripheral neuropathy in mice. *Human Molecular Genetics*, **12**(6), 631–46.

Gao, Y. et al. (2012). Single reconstituted neuronal SNARE complexes zipper in three distinct stages. *Science*, **337**(6100), 1340–1344.

Gataullina, S. & Dulac, O. (2017). From genotype to phenotype in Dravet disease. *Seizure*, **44**, 58–64.

Gaudelli, N. M. et al. (2017). Programmable base editing of A • T to G • C in genomic DNA without DNA cleavage. *Nature Publishing Group*, **551**(7681), 464–471.

Gavrieli Y., Sherman Y. & Ben-Sasson S. A. (1992) Identification of programmed cell death in situ via specific labeling of nuclear DNA fragmentation. *Journal of Cell Biology*, **119** (3), 493–501.

Genton, P. & Gelisse, P. (2004). Antimyoclonic use of levetiracetam. *Epileptic Disorders*, **45**(6), 678–681.

Genton, P., Striano, P. & Minassian, B. A. (2016). The history of progressive myoclonus epilepsies. *Epileptic Disorders*, **18**, 3–10.

Gentry, M. S., Worby, C. A. & Dixon, J. E. (2005). Insights into Lafora disease: Malin is an E3 ubiquitin ligase that ubiquitinates and promotes the degradation of laforin. *Proceedings of the National Academy of Sciences*, **102**(24), 8501–8506.

Glick, B. S. et al. (2013). Models for Golgi traffic: a critical assessment models for Golgi traffic, a critical assessment. *Cold Spring Harbor Perspectives in Biology*, **60637**, 1–15.

Goldberg, E. M. (2005). Specific functions of synaptically localized potassium channels in synaptic transmission at the neocortical GABAergic fast-spiking cell synapse. *Journal of Neuroscience*, **25**(21), 5230–5235.

Goldberg, E. M. & Coulter, D. A. (2013). Mechanisms of epileptogenesis: a convergence on neural circuit dysfunction. *Nature Reviews. Neuroscience*, **14**(5), 337–49.

Goldsmith, D. & Minassian, B. A. (2016). Efficacy and tolerability of perampanel in ten patients with Lafora disease. *Epilepsy and Behavior*, **62**, 132–135.

Greaves, J. et al. (2012). Palmitoylation-induced aggregation of cysteine-string protein mutants that cause neuronal ceroid lipofuscinosis. *The Journal of Biological Chemistry*, **287**(44), 37330–9.

Grosse, P., Cassidy, M. J. & Brown, P. (2002). EEG-EMG, MEG-EMG and EMG-EMG frequency analysis: physiological principles and clinical applications. *Clinical Neurophysiology*, **113**(10), 1523–1531.

Grueber, W. B., Jan, L. Y. & Jan, Y. N. (2002). Tiling of the Drosophila epidermis by multidendritic sensory neurons. *Development*, **129**(12), 2867–78.

Gu, Y. et al. (2012). Alternative splicing regulates Kv3.1 polarized targeting to adjust maximal spiking frequency. *Journal of Biological Chemistry*, **287**(3), 1755–1769.

Gu, Y. et al. (2012). Alternative splicing regulates Kv3.1 polarized targeting to adjust maximal spiking frequency. *Journal of Biological Chemistry*, **287**(3), 1755–1769.

Gu, Y. et al. (2018). Balanced activity between Kv3 and Nav channels determines fast-spiking in mammalian central neurons. *Science*, **9**, 120–137.

Guellerin, J. et al. (2012). Low-frequency photoparoxysmal response in adults: an early clue to diagnosis. *Journal of Clinical Neurophysiology*, **29**(2), 160–164.

Hallett, M. (1985). Myoclonus: relation to epilepsy. *Epilepsia*, **26**, S67–S77.

Haltia, M. & Goebel, H. H. (2013). The neuronal ceroid-lipofuscinoses: a historical introduction. *Biochimica et Biophysica Acta - Molecular Basis of Disease*, **1832**(11), 1795–1800.

Han, I. et al. (2010). Differential vulnerability of neurons in Huntington's disease: the role of cell type-specific features. *Journal of Neurochemistry,* **113**(5), 1073-1091.

Hardy, J. (2016). Catastrophic cliffs: a partial suggestion for selective vulnerability in neurodegenerative diseases. *Biochemical Society Transactions*, **44**, 659-661.

Hay, J. C. et al. (1997). Protein interactions regulating vesicle transport between the endoplasmic reticulum and Golgi apparatus in mammalian cells. *Cell*, **89**(1), 149–158.

Hay, J. C. et al. (1998). Localisation, dynamics, and protein interactions reveal distinct roles for ER and Golgi SNAREs. *Journal of Cell Biology,* **141**(7), 1489–1502.

Hayashi, T. et al. (1994). Synaptic vesicle membrane fusion complex: action of clostridial neurotoxins on assembly. *The EMBO Journal*, **13**(21), 5051–61.

Ho, C. S., Grange, R. W. & Joho, R. H. (1997). Pleiotropic effects of a disrupted K+ channel gene: reduced body weight, impaired motor skill and muscle contraction, but no seizures. *Proceedings of the National Academy of Sciences of the United States of America*, **94**(4), 1533–8.

Hodgkin, A. L. & Huxley, A. F. (1952). A quantitative description of membrane current and its application to conduction and excitation in nerve. *The Journal of Physiology*, **117**(4), 500–44.

Honda, A. et al. (2005). Targeting of Arf-1 to the early Golgi by Membrin, an ER-Golgi SNARE. *Journal of Cell Biology*, **168**(7), 1039–1051.

Horton, A. C. & Ehlers, M. D. (2003). Neuronal polarity and trafficking. *Neuron*, **40**(2), 277–95.

Horton, A. C. et al. (2005). Polarized secretory trafficking directs cargo for asymmetric dendrite growth and morphogenesis. *Neuron*, **48**(5), 757–771.

Houseweart, M. K. et al. (2003). Cathepsin B but not cathepsins L or S contributes to the pathogenesis of Unverricht-Lundborg progressive myoclonus epilepsy (EPM1). *Journal of Neurobiology*, **56**(4), 315–327.

Hoxha, E. et al. (2018). Purkinje cell signaling deficits in animal models of ataxia. *Frontiers in Synaptic Neuroscience*, **10**, 1–17.

Hsu, V. W., Lee, S. Y. & Yang, J.S. (2009). The evolving understanding of COPI vesicle formation. *Nature Reviews Molecular Cell Biology*, **10**(5), 360–364.

Hu, H., Martina, M. & Jonas, P. (2010). Dendritic mechanisms underlying rapid synaptic activation of fast-spiking hippocampal interneurons. *Science*, **327**(5961), 52–58.

Hu, J. H. et al. (2018). Evolved Cas9 variants with broad PAM compatibility and high DNA specificity. *Nature*, **556**(7699), 57–63.

Hu, S. C. et al. (2018). Seizure remission and improvement of neurological function in sialidosis with perampanel therapy. *Epilepsy and Behavior Case Reports*, **10**, 32–34.

Hu, H., Gan, J. & Jonas, P. (2014). Fast-spiking, parvalbumin+ GABAergic interneurons: from cellular design to microcircuit function. *Science,* **327**(5961)*,* 52-58.

Huang, C.Y. et al. (2017). K+ channel Kv3.4 is essential for axon growth by limiting the influx of Ca2+ into growth cones. *The Journal of Neuroscience,* **37**(17), 4433–4449.

Huang, S. & Wang, Y. (2017). Golgi structure formation, function, and post-translational modifications in mammalian cells. *F1000 Research*, **6**, 2050.

Iffland, P. H. & Crino, P. B. (2017). Focal Cortical Dysplasia: gene mutations, cell signaling, and therapeutic implications. *Annual Review of Pathology: Mechanisms of Disease*, **12**(1), 547–571.

Iivanainen, M. & Himberg, J. J. (1982). Valproate and clonazepam in the treatment of severe progressive myoclonus epilepsy. *Archives of Neurology*, **39(**4), 236–8.

Ikeda, A. et al. (1990). Cortical tremor: a variant of cortical reflex myoclonus. *Neurology*, **40**(10), 1561–1565.

Ikenaka, K. et al. (2012). Disruption of axonal transport in motor neuron diseases.

International Journal of Molecular Sciences, **13**(1), 1225–38.

Irie, T. et al. (2014). Kv3.3 channels harbouring a mutation of spinocerebellar ataxia type 13 alter excitability and induce cell death in cultured cerebellar Purkinje cells. *Journal of Physiology*, **592**(1), 229–247.

Islas, L. D. (2016). Functional diversity of potassium channel voltage-sensing domains. *Channels*, **10**(3), 202–213. https://doi.org/10.1080/19336950.2016.1141842

Islas, L. D. & Sigworth, F. J. (1999). Voltage sensitivity and gating charge in Shaker and Shab family potassium channels. *The Journal of General Physiology*, **114**(5), 723–741.

Jahn, R. & Scheller, R. H. (2006). SNAREs — engines for membrane fusion. *Nature Reviews Molecular Cell Biology*, **7**(9), 631–643.

Jalanko, A. & Braulke, T. (2009). Neuronal ceroid lipofuscinoses. *Biochimica et Biophysica Acta (BBA) - Molecular Cell Research*, **1793**(4), 697–709.

Jan, Y. N. & Jan, L. Y. (2010). Branching out: mechanisms of dendritic arborization. *Nature Reviews Neuroscience*, **11**(5), 316–328.

Jensen, C. S., Rasmussen, H. B. & Misonou, H. (2011). Neuronal trafficking of voltage-gated potassium channels. *Molecular and Cellular Neuroscience*, **48**(4), 288–297.

Jensen, M. et al. (2012). Mechanism of voltage gating in potassium channels. *Science*, **336**(6078), 229–233.

Jiang, X., Lachance, M. & Rossignol, E. (2016). Involvement of cortical fast-spiking parvalbumin-positive basket cells in epilepsy. *Progress in Brain Research*, **226**, 81-126.

Joensuu, T., Lehesjoki, A.-E. & Kopra, O. (2008). Molecular background of EPM1—Unverricht–Lundborg disease. *Epilepsia*, **49**(4), 557–563.

Joensuu, T. et al. (2014). Gene expression alterations in the cerebellum and granule neurons of Cstb-/-mouse are associated with early synaptic changes and inflammation. *PLoS ONE*, ***9***(2).

Johnston, D., Frick, A., & Poolos, N. (2015). Dendrites and disease. In: *Dendrites*, 3 Edition (Stuart G., Spruston, N. & Hausser M., eds). New York, NY: Oxford University Press.

Joho, R. H. & Hurlock, E. C. (2009). The role of Kv3-type potassium channels in cerebellar physiology and behavior. *Cerebellum*, **8**(3), 323–333.

Jurkat-Rott, K., Groome, J. & Lehmann-Horn, F. (2012). Pathophysiological role of omega pore current in channelopathies. *Frontiers in Pharmacology*, **3**, 1–19.

Jurkat-Rott, K. et al. (2009). K+-dependent paradoxical membrane depolarization and Na+ overload, major and reversible contributors to weakness by ion channel leaks. *Proceedings of the National Academy of Sciences*, **106**(10), 4036–4041.

Kälviäinen, R. et al. (2008). Clinical picture of EPM1-Unverricht-Lundborg disease. *Epilepsia*, **49**(4), 549–556.

Kamada, S. et al. (2005). Nuclear translocation of caspase-3 is dependent on its proteolytic activation and recognition of a substrate-like protein(s). *The Journal of Biological Chemistry*, **280**(2), 857–60.

Kavalali, E. T. (2015). The mechanisms and functions of spontaneous neurotransmitter release. *Nature Reviews Neuroscience*, **16**(1), 5–16.

Keynes, R. D. & Rojas, E. (1974). Kinetics and steady-state properties of the charged system controlling sodium conductance in the squid giant axon. *The Journal of Physiology*, **239**(2), 393–434.

Khan, A. & Sergi, C. (2018). Sialidosis: a review of morphology and molecular biology of a rare pediatric disorder. *Diagnostics*, **8**(2), 29.

Khare, S. et al. (2018). C-terminal proline deletions in KCNC3 cause delayed channel inactivation and an adult-onset progressive SCA13 with spasticity. *Cerebellum*, **17**(5), 692–697.

Khiari, H. M. et al. (2009). Death in Unverricht–Lundborg disease. *Neurological Sciences*, **30**(4), 315–318.

Kim, H. et al. (2018). Familial cases of progressive myoclonic epilepsy caused by maternal somatic mosaicism of a recurrent KCNC1 p.Arg320His mutation. *Brain and Development*, **40**(5), 429–432.

Kim, J. Y. et al. (2013). Viral transduction of the neonatal brain delivers controllable genetic mosaicism for visualising and manipulating neuronal circuits in vivo. *European Journal of Neuroscience*, **37**(8), 1203–1220.

Kloepper, T. H., Kienle, C. N. & Fasshauer, D. (2007). An elaborate classification of SNARE proteins sheds light on the conservation of the eukaryotic endomembrane system. *Molecular Biology of the Cell*, **18**(9), 3463–71.

Klumperman, J. (2011). Architecture of the mammalian Golgi. *Cold Spring Harbor Perspectives in Biology*, **3**(7), 1–19.

Koeppen, A. (2005). The pathogenesis of spinocerebellar ataxia. *The Cerebellum*, **4**(1), 62–73.

Köhling, R. & Wolfart, J. (2016). Potassium channels in epilepsy. *Cold Spring Harbor Perspectives in Medicine*, **6**(5), 24.

Kojovic, M., Cordivari, C. & Bhatia, K. (2011). Myoclonic disorders: a practical approach for diagnosis and treatment. *Therapeutic Advances in Neurological Disorders*, **4**(1), 47–62.

Komor, A. C. et al. (2016). Programmable editing of a target base in genomic DNA without double-stranded DNA cleavage. *Nature*, **533**(7603), 420–424.

Komuro, H. & Rakic, P. (1996). Intracellular Ca2+ fluctuations modulate the rate of neuronal migration. *Neuron*, **17**(2), 275–85.

Konur, S. & Ghosh, A. (2005). Calcium Signaling and the Control of Dendritic Development. *Neuron*, **46**(3), 401–405.

Kousi, M. et al. (2012). Novel mutations consolidate *KCTD7* as a progressive myoclonus epilepsy gene. *Journal of Medical Genetics*, **49**(6), 391–399.

Krabichler, B. et al. (2012). Novel mutation in potassium channel related gene KCTD7 and Progressive Myoclonic Epilepsy. *Annals of Human Genetics*, **76**(4), 326–331.

Krokan, H. E., Drabløs, F. & Slupphaug, G. (2002). Uracil in DNA – occurrence, consequences and repair. *Oncogene*, **21**(58), 8935–8948.

Kullmann, D. M. (2002). The neuronal channelopathies. *Brain*, **125**, 1177-1195.

Kurihara, M. et al. (2018). Novel de novo KCND3 mutation in a Japanese patient with intellectual disability, cerebellar ataxia, myoclonus, and dystonia. *Cerebellum*, **17**(2), 237–242.

Labro, A. J. et al. (2015). Kv3.1 uses a timely resurgent K(+) current to secure action potential repolarization. *Nature Communications*, **6**, 10173.

League Against Epilepsy Consortium on Complex Epilepsies. (2014). Genetic determinants of common epilepsies: a meta-analysis of genome-wide association studies International League Against Epilepsy Consortium on Complex Epilepsies. *The Lancet Neurology*, **13**, 893–903.

Lee, M. C. S. et al. (2004). Bi-directional protein transport between the ER and Golgi. *Annual Review of Cell and Developmental Biology*, **20**(1), 87–123.

Lee, Y.C. et al. (2012). Mutations in *KCND3* cause spinocerebellar ataxia type 22. *Annals of Neurology*, **72**(6), 859–869.

Lehtinen, M. K. et al. (2009). Cystatin B deficiency sensitizes neurons to oxidative stress in Progressive Myoclonus Epilepsy, EPM1. *Journal of Neuroscience*, **29**(18), 5910–5915.

Lenz, S. et al. (1994). GABA-ergic interneurons of the striatum express the Shaw-like potassium channel Kv3.1. *Synapse*, **18**(1), 55–66.

Li, M. et al. (2010). Optimal promoter usage for lentiviral vector-mediated transduction of cultured central nervous system cells. *Journal of Neuroscience Methods*, **189**(1), 56–64.

Lien, C.C. & Jonas, P. (2003). Kv3 potassium conductance is necessary and kinetically optimized for high-frequency action potential generation in hippocampal interneurons. *The Journal of Neuroscience,* **23**(6), 2058–2068.

Lin, M. A., Cannon, S. C. & Papazian, D. M. (2018). Kv4.2 autism and epilepsy mutation enhances inactivation of closed channels but impairs access to inactivated state after opening. *Proceedings of the National Academy of Sciences*, **115**(15), 3559–3568.

Littleton, J. T. et al. (2001). SNARE-complex disassembly by NSF follows synaptic-vesicle fusion. *Proceedings of the National Academy of Sciences of the United States of America*, **98**(21), 12233–8.

Liu, C. et al. (2013). Prickle1 is expressed in distinct cell populations of the central nervous system and contributes to neuronal morphogenesis. *Human Molecular Genetics*, **22**(11), 2234–2246.

Liu, C. et al. (2017). Loss of the golgin GM130 causes Golgi disruption, Purkinje neuron loss, and ataxia in mice. *Proceedings of the National Academy of Sciences*, **114**(2), 346–351.

Liu, S. J. & Kaczmarek, L. K. (1998). The expression of two splice variants of the Kv3.1 potassium channel gene is regulated by different signaling pathways. *J.Neurosci.*, ***18***(0270–6474), 2881–2890.

Liu, Z. et al. (2017). Systematic comparison of 2A peptides for cloning multi-genes in a polycistronic vector. *Scientific Reports*, **7**(1), 2193.

Lonka, L. et al. (2000). The neuronal ceroid lipofuscinosis CLN8 membrane protein is a resident of the endoplasmic reticulum. *Human Molecular Genetics*, **9**(11), 1691–1697.

Lonka, L. et al. (2004). Localization of wild-type and mutant neuronal ceroid lipofuscinosis CLN8 proteins in non-neuronal and neuronal cells. *Journal of Neuroscience Research*, **76**(6), 862–871.

Lowe, S. L. et al. (1997). A SNARE involved in protein transport through the Golgi apparatus. *Nature*, **389**(6653), 881–4.

Luneau, C. J. et al. (1991). Alternative splicing contributes to K+ channel diversity in the mammalian central nervous system. *Proceedings of the National Academy of Sciences of the United States of America*, **88**(9), 3932–6.

Ma, Z. et al. (2019). PTC-bearing mRNA elicits a genetic compensation response via Upf3a and COMPASS components. *Nature,* **568**(7751), 259-263.

Magaudda, A. et al. (2006). Unverricht-Lundborg disease, a condition with self-limited progression: Long-term follow-up of 20 patients. *Epilepsia*, **47**(5), 860–866.

Maresca, M. et al. (2013). Obligate ligation-gated recombination (ObLiGaRe): custom-designed nuclease-mediated targeted integration through nonhomologous end joining. *Genome Research*, **23**(3), 539–46.

Marsden, C. D. & Hallett, M. (1981). The nosology and pathophysiology of myoclonus. *Movement Disorders*, 196–248.

Martina, M. et al. (1998). Functional and molecular differences between voltage-gated

K+ channels of fast-spiking interneurons and pyramidal neurons of rat hippocampus. *The Journal of Neuroscience*, **18**(20), 8111–25.

Martins da Silva, A. & Leal, B. (2017). Photosensitivity and epilepsy: current concepts and perspectives, a narrative review. *Seizure*, **50**, 209–218.

Mashal, R. D., Koontz, J. & Sklar, J. (1995). Detection of mutations by cleavage of DNA heteroduplexes with bacteriophage resolvases. *Nature Genetics*, **9**(2), 177–183.

Matsumoto, R. R. et al. (2000). Involvement of GABA(A) receptors in myoclonus. *Movement Disorders,* **15**(1), 47–52.

Mattis, J. et al. (2011). Principles for applying optogenetic tools derived from direct comparative analysis of microbial opsins. *Nature Methods*, **9**(2), 159–172.

McNew, J. A. et al. (2000). Compartmental specificity of cellular membrane fusion encoded in SNARE proteins. *Nature*, **407**(6801), 153–159.

Minassian, B. A. (2001). Lafora's disease: towards a clinical, pathologic, and molecular synthesis. *Pediatric Neurology*, **25**(1), 21–29.

Minassian, B. A. (2014). The progressive myoclonus epilepsies. *Progress in Brain Research* (1st edVol. 213). Elsevier B.V. , 113--122

Minassian, B. A. et al. (1998). Mutations in a gene encoding a novel protein tyrosine phosphatase cause progressive myoclonus epilepsy. *Nature Genetics*, **20**(2), 171–174.

Minassian, N. A., Lin, M. C. A. & Papazian, D. M. (2012). Altered Kv3.3 channel gating in early-onset spinocerebellar ataxia type 13. *Journal of Physiology*, **590**(7), 1599–1614.

Moen, M. N. et al. (2016). Pathogenic variants in *KCTD7* perturb neuronal K $^+$ fluxes and glutamine transport. *Brain*, **139**(12), 3109–3120.

Mole, S. E. & Cotman, S. L. (2015). Genetics of the neuronal ceroid lipofuscinoses (Batten disease). *Biochimica et Biophysica Acta - Molecular Basis of Disease*, **1852**(10), 2237–2241.

Moreau, A. et al. (2018). A leaky voltage sensor domain of cardiac sodium channels causes arrhythmias associated with dilated cardiomyopathy. *Scientific Reports*, **8**(1), 1–12.

Mukhopadhyay, A. et al. (2009). Differential effects of BMP signaling on parvalbumin and somatostatin interneuron differentiation. *Development*, **136**(15), 2633–2642.

Munch, A. S. et al. (2018). Pharmacological rescue of mutated Kv3.1 ion-channel linked to progressive myoclonus epilepsies. *European Journal of Pharmacology*, **833**, 255–262.

Muñoz-Ballester, C. et al. (2016). Homeostasis of the astrocytic glutamate transporter GLT-1 is altered in mouse models of Lafora disease. *Biochimica et Biophysica Acta*,

1862(6), 1074–83.

Muona, M. et al. (2014). A recurrent de novo mutation in KCNC1 causes progressive myoclonus epilepsy. *Nature Genetics*, **47**(1), 39–46.

Myers, C. T. & Mefford, H. C. (2015). Advancing epilepsy genetics in the genomic era. *Genome Medicine,* **7**, *91*.

Nakamura, N., Wei, J. H. & Seemann, J. (2012). Modular organization of the mammalian Golgi apparatus. *Current Opinion in Cell Biology*, **24**(4), 467–474.

Nardone, R. et al. (2018). Transcranial magnetic stimulation in myoclonus of different aetiologies. *Brain Research Bulletin*, **140**, 258–269.

Neculai, D. et al. (2013). Structure of LIMP-2 provides functional insights with implications for SR-BI and CD36. *Nature*, **504**(7478), 172–176.

Ngugi, A. K. et al. (2010). Estimation of the burden of active and life-time epilepsy: A meta-analytic approach. *Epilepsia*, **51**(5), 883–890.

Noebels, J. (2015). Pathway-driven discovery of epilepsy genes. *Nature Neuroscience*, **18**(3), 344–350.

Nosková, L. et al. (2011). Mutations in DNAJC5, encoding Cysteine-string protein alpha, cause autosomal-dominant adult-onset neuronal ceroid lipofuscinosis. *The American Journal of Human Genetics*, **89**(2), 241–252.

Oliver, K. L. et al. (2017). Myoclonus epilepsy and ataxia due to KCNC1 mutation: Analysis of 20 cases and K+channel properties. *Annals of Neurology*, **81**(5), 677–689.

Ortolano, S. et al. (2014). Loss of GABAergic cortical neurons underlies the neuropathology of Lafora disease. *Molecular Brain*, **7**(1), 1–17.

Oyrer, J. et al. (2018). Ion channels in genetic epilepsy: from genes and mechanisms to disease-targeted therapies. *Pharmacological Reviews*, **70**(1), 142–173.

Ozaita, A. et al. (2002). Differential subcellular localization of the two alternatively spliced isoforms of the Kv3.1 potassium channel subunit in brain. *Journal of Neurophysiology*, **88**(1), 394–408.

Packer, A. M., Roska, B. & Häusser, M. (2013). Targeting neurons and photons for optogenetics. *Nature Neuroscience*, **16**(7), 805–15.

Pannaccione, A. et al. (2007). Up-regulation and increased activity of Kv3.4 channels and their accessory subunit MinK-related peptide 2 induced by amyloid peptide are involved in apoptotic neuronal death. *Molecular Pharmacology*, **72**(3), 665–673.

Parlati, F. et al. (2000). Topological restriction of SNARE-dependent membrane fusion. *Nature*, *407*(6801), 194–198.

Perney, T. M. et al. (1992). Expression of the mRNAs for the Kv3.1 potassium channel gene in the adult and developing rat brain. *J.Neurophysiol.*, **68**, 756–766.

Perozo, E. et al. (1993). Gating currents from a nonconducting reveal open-closed conformations in Shaker K+ channels, **11**, 353–358.

Poduri, A. et al. (2013). Somatic mutation, genomic variation, and neurological disease. *Science*, **341**(6141), 1237758–1237758.

Poirier, K. et al. (2017). Loss of function of KCNC1 is associated with intellectual disability without seizures. *European Journal of Human Genetics*, **25**, 560–564.

Polajnar, M. & Erovnik, E. Z. (2011). Impaired autophagy: a link between neurodegenerative diseases and progressive myoclonus epilepsies. *Trends in Molecular Medicine*, **17**, 293–300.

Powell, S. K., Rivera-Soto, R. & Gray, S. J. (2015). Viral expression cassette elements to enhance transgene target specificity and expression in gene therapy. *Discovery Medicine*, **19**(102), 49–57.

Prange, O. & Murphy, T. H. (1999). Correlation of miniature synaptic activity and evoked release probability in cultures of cortical neurons. *The Journal of Neuroscience,* **19**(15), 6427–38.

Praschberger, R. et al. (2015). Expanding the phenotype and genetic defects associated with the *GOSR2* gene. *Movement Disorders Clinical Practice*, **2**(3), 271–273.

Praschberger, R. et al. (2017). Mutations in Membrin/GOSR2 reveal stringent secretory pathway demands of dendritic growth and synaptic integrity. *Cell Reports*, **21**(1), 97–109.

Pratt, J. A. et al. (2008). Modelling prefrontal cortex deficits in schizophrenia: Implications for treatment. *British Journal of Pharmacology*, **153**(1), 465–470.

Pshezhetsky, A. V. & Potier, M. (1996). Association of N-acetylgalactosamine-6-sulfate sulfatase with the multienzyme lysosomal complex of β-galactosidase , cathepsin A, and neuraminidase. *The Journal of Biological Chemistry*, **271**(45), 28359–28365.

Qin, J. Y. et al. (2010). Systematic comparison of constitutive promoters and the doxycycline-inducible promoter. *PloS One*, **5**(5), e10611.

Ramachandran, N. et al. (2009). The autosomal recessively inherited progressive myoclonus epilepsies and their genes. *Epilepsia*, **50** *(5)*, 29–36.

Ranta, S. et al. (1999). The neuronal ceroid lipofuscinoses in human EPMR and mnd mutant mice are associated with mutations in CLN8. *Nature Genetics*, **23**(2), 233–236.

Rapin, I. et al. (1978). The cherry-red spot-myoclonus syndrome. *Annals of Neurology*, **3**(3), 234–242.

Reczek, D. et al. (2007). LIMP-2 is a receptor for lysosomal mannose-6-phosphate-independent targeting of β-glucocerebrosidase. *Cell*, **131**(4), 770–783.

Redmond, L., Kashani, A. H. & Ghosh, A. (2002). Calcium regulation of dendritic growth via CaM kinase IV and CREB-mediated transcription. *Neuron*, **34**(6), 999–1010.

Reid, C. A., Berkovic, S. F. & Petrou, S. (2009). Mechanisms of human inherited epilepsies. *Progress in Neurobiology,* **87**, 41–57.

Renger, J. J., Egles, C. & Liu, G. (2001). A developmental switch in neurotransmitter flux enhances synaptic efficacy by affecting AMPA receptor activation. *Neuron*, **29**(2), 469–84.

Reutens, D. C., Puce, A. & Berkovic, S. F. (1993). Cortical hyperexcitability in progressive myoclonus epilepsy: a study with transcranial magnetic stimulation. *Neurology*, **43**(1), 186–92.

Rhodes, K. J. et al. (2004). KChIPs and Kv4 subunits as integral components of A-type potassium channels in mammalian brain. *Journal of Neuroscience*, **24**(36), 7903–7915.

Rinne, R. et al. (2002). Reduced cystatin B activity correlates with enhanced cathepsin activity in progressive myoclonus epilepsy. *Annals of Medicine*, **34**(5), 380–5.

Ritter, L. M. et al. (2016). Lentiviral expression of GAD67 and CCK promoter-driven opsins to target interneurons in vitro and in vivo. *The Journal of Gene Medicine*, **18**(1–3), 27–37.

Roivainen, R., Karvonen, M. K. & Puumala, T. (2014). Seizure control in Unverricht-Lundborg disease: a single-centre study. *Epileptic Disorders*, **16**(2), 191–195.

Rossignol, E. et al. (2013). CaV2.1 ablation in cortical interneurons selectively impairs fast-spiking basket cells and causes generalized seizures. *Annals of Neurology,* **74**(2), 209-222.

Rouet, P., Smih, F. & Jasin, M. (1994). Introduction of double-strand breaks into the genome of mouse cells by expression of a rare-cutting endonuclease. *Molecular and Cellular Biology*, **14**(12), 8096–106.

Rubboli, G. et al. (2011). Clinical and neurophysiologic features of progressive myoclonus epilepsy without renal failure caused by SCARB2 mutations. *Epilepsia*, **52**(12), 2356–2363.

Rubinstein, M. et al. (2015). Dissecting the phenotypes of Dravet syndrome by gene deletion. *Brain*, **138**(8), 2219–2233.

Rudy, B. et al. (1999). Contributions of Kv3 channels to neuronal excitability. *Annals of the New York Academy of Sciences*, **868**, 304–343.

Rudy, B. et al. (1999). Contributions of Kv3 channels to neuronal excitability. *Annals of the New York Academy of Sciences*, **868**, 304–343.

Rudy, B. et al. (2011). Three groups of interneurons account for nearly 100% of neocortical GABAergic neurons. *Developmental Neurobiology*, **71**(1), 45–61.

Rudy, B. & McBain, C. J. (2001). Kv3 channels: voltage-gated K+ channels designed for high-frequency repetitive firing. *Trends in Neurosciences*, **24**(9), 517–526.

Sambri, I. et al. (2017). Lysosomal dysfunction disrupts presynaptic maintenance and restoration of presynaptic function prevents neurodegeneration in lysosomal storage diseases. *EMBO Molecular Medicine*, **9**, 112–132.

Saunders, A. et al. (2018). Molecular diversity and specializations among the cells of the adult mouse brain. *Cell*, **174**(4), 1015–1030.e16.

Saxena, S. & Caroni, P. (2007). Mechanisms of axon degeneration: from development to disease. *Progress in Neurobiology*, **83**(3), 174–191.

Saxena, S. & Caroni, P. (2011). Selective neuronal vulnerability in neurodegenerative diseases: from stressor thresholds to degeneration. *Neuron,* **71**(1), 35-48.

Scheffer, I. E. et al. (2017). ILAE classification of the epilepsies: position paper of the ILAE commission for classification and terminology. *Epilepsia*, **58**(4), 512–521.

Schene, I. F. et al. (2016). Pitfalls in diagnosing neuraminidase deficiency: psychosomatics and normal sialic acid excretion. *JIMD Reports*, **25**, 9–13.

Schnütgen, F. et al. (2003). A directional strategy for monitoring Cre-mediated recombination at the cellular level in the mouse. *Nature Biotechnology*, **21**(5), 562–565.

Schutte, B. et al. Annexin V binding assay as a tool to measure apoptosis in differentiated neurons. *Journal of Neuroscience Methods*, **86**(1), 63-69

Segal, M., Korkotian, E. & Murphy, D. D. (2000). Dendritic spine formation and pruning: common cellular mechanisms? *Trends in Neurosciences*, **23**(2), 53–57.

Sekirnjak, C. et al. (1997). Subcellular localization of the K+ channel subunit Kv3.1b in selected rat CNS neurons. *Brain Research*, **766**(1–2), 173–187.

Shahwan, A., Farrell, M. & Delanty, N. (2005). Progressive myoclonic epilepsies: a review of genetic and therapeutic aspects. *The Lancet Neurology*, **4**(4), 239-248.

Shanmugarajah, P. D. et al. (2018). Phenytoin-related ataxia in patients with epilepsy: clinical and radiological characteristics. *Seizure*, **56**, 26–30.

Shannon, P. et al. (2002). Neuropathological changes in a mouse model of progressive myoclonus epilepsy: cystatin B deficiency and Unverricht-Lundborg disease. *Journal of Neuropathology and Experimental Neurology*, **61**(12), 1085–91.

Sharma, J. et al. (2013). Neuronatin-mediated aberrant calcium signaling and endoplasmic reticulum stress underlie neuropathology in Lafora disease. *Journal of Biological Chemistry*, **288**(13), 9482–9490.

Sharma, M. et al. (2012). CSPα knockout causes neurodegeneration by impairing SNAP-25 function. *EMBO Journal*, **31**(4), 829–841.

Sharma, M., Burré, J. & Südhof, T. C. (2011). CSPα promotes SNARE-complex assembly by chaperoning SNAP-25 during synaptic activity. *Nature Cell Biology*, **13**(1), 30–39.

Shaw, P. & Eggett, C. (2000). Molecular factors underlying selective vulnerability of motor neurons to neurodegeneration in amyotrophic lateral sclerosis. *Journal of Neurology*, **247**, 17-27.

Shibasaki, H. & Kuroiwa, Y. (1975). Electroencephalographic correlates of myoclonus. *Electroencephalography and Clinical Neurophysiology*, **39**(5), 455–63.

Shibasaki, H. & Thompson, P. D. (2011). Milestones in myoclonus. *Movement Disorders*, **26**(6), 1142–1148.

Shibasaki, H. et al. (1985). Pathogenesis of giant somatosensory evoked potentials in progressive myoclonic epilepsy. *Brain*, **108**(1), 225–240.

Shibata, R. et al. (1999). Expression of Kv3.1 and Kv4.2 genes in developing cerebellar granule cells. *Developmental Neuroscience*, **21**(2), 87–93.

Shim, J., Newman, A. P. & Ferro-Novick, S. (1991). The BOS1 gene encodes an essential 27-kD putative membrane protein that is required for vesicular transport from the ER to the Golgi complex in yeast. *Journal of Cell Biology*, **113**(1), 55–64.

Shiraishi, H. et al. (2017). Efficacy of perampanel for controlling seizures and improving neurological dysfunction in a patient with dentatorubral-pallidoluysian atrophy (DRPLA). *Epilepsy and Behavior Case Reports*, **8**, 44–46.

Simons, M. & Mlodzik, M. (2008). Planar cell polarity signaling: from fly development to human disease. *Annual Review of Genetics*, **42**(1), 517–540.

Singh, B. et al. (2006). A Kv4.2 truncation mutation in a patient with temporal lobe epilepsy. *Neurobiology of Disease*, **24**(2), 245–253.

Smets, K. et al. (2015). First de novo KCND3 mutation causes severe Kv4.3 channel dysfunction leading to early onset cerebellar ataxia, intellectual disability, oral apraxia and epilepsy. *BMC Medical Genetics*, **16**(1), 51.

Snowball, A. et al. (2019). Epilepsy gene therapy using an engineered potassium channel. *The Journal of Neuroscience,* **39**(16), 3159-3169.

Soares, D. et al. (2017). Expression of Kv3.1b potassium channel is widespread in macaque motor cortex pyramidal cells: a histological comparison between rat and macaque. *Journal of Comparative Neurology*, **525**(9), 2164–2174.

Sokolov, S., Scheuer, T. & Catterall, W. A. (2007). Gating pore current in an inherited ion channelopathy. *Nature*, **446**(7131), 76–78.

Söllner, T. et al. (1993). SNAP receptors implicated in vesicle targeting and fusion. *Nature*, **362**(6418), 318–324.

Staley, K. (2015). Molecular mechanisms of epilepsy. *Nature Neuroscience*, **18**(3), 367–72.

Starace, D. M. & Bezanilla, F. (2001). Histidine scanning mutagenesis of basic residues of the S4 segment of the Shaker K^+ channel, **117**(5), 469-490.

Starace, D. M., Stefani, E. & Bezanilla, F. (1997). Voltage-dependent proton transport by the voltage sensor of the Shaker K+ channel. *Neuron*, **19**(6), 1319–1327.

Staropoli, J. F. et al. (2012). A homozygous mutation in KCTD7 links neuronal ceroid lipofuscinosis to the ubiquitin-proteasome system. *The American Journal of Human Genetics*, **91**(1), 202–208.

Struyk, A. F. & Cannon, S. C. (2007). A Na^+ channel mutation linked to hypokalemic periodic paralysis exposes a proton-selective gating pore. *The Journal of General Physiology*, **130**(1), 11–20.

Südhof, T. C. & Rothman, J. E. (2009). Membrane fusion: grappling with SNARE and SM proteins. *Science*, **323**(5913), 474–7.

Sutton, G. G. & Mayer, R. F. (1974). Focal reflex myoclonus. *Journal of Neurology Neurosurgery and Psychiatry*, **37**(2), 207–217.

Sutton, R. B. et al. (1998). Crystal structure of a SNARE complex involved in synaptic exocytosis at 2.4 Å resolution. *Nature*, **395**(6700), 347–353.

Suzuki, K. et al. (2016). In vivo genome editing via CRISPR/Cas9 mediated homology-independent targeted integration. *Nature*, **540**(7631), 144–149.

Symonds, J. D. & Zuberi, S. M. (2018). Genetics update: monogenetics, polygene disorders and the quest for modifying genes. *Neuropharmacology*, **132**, 3–19.

Tagliabracci, V. S. et al. (2007). Laforin is a glycogen phosphatase, deficiency of which leads to elevated phosphorylation of glycogen in vivo. *Proceedings of the National Academy of Sciences*, **104**(49), 19262–19266.

Tait, S. W. G. & Green, D. R. (2008). Caspase-independent cell death: leaving the set without the final cut. *Oncogene*, **27**(50), 6452–6461.

Tauer, U., Knoth, R. & Volk, B. (1998). Phenytoin alters Purkinje cell axon morphology and targeting in vitro. *Acta Neuropathologica*, **95**(6), 583–91.

Terrence F. et al. (2017). Disease model discovery from 3,328 gene knockouts by the international mouse phenotyping consortium, **143**(5), 951–959.

Tiemeier, H. et al. (2010). Cerebellum development during childhood and adolescence: a longitudinal morphometric MRI study. *NeuroImage*, **49**(1), 63–70.

Toledo-Rodriguez, M. et al. (2004). Correlation maps allow neuronal electrical properties to be predicted from single-cell gene expression profiles in rat neocortex. *Cerebral Cortex,* **14**(12), 1310-1327.

Tombola, F., Pathak, M. M. & Isacoff, E. Y. (2005). Voltage-sensing arginines in a potassium channel permeate and occlude cation-selective pores. *Neuron*, **45**, 379–388.

Torkamani, A. et al. (2014). De novo KCNB1 mutations in epileptic encephalopathy. *Annals in Neurology*, **76**(4), 529–540.

Trimmer, J. S. (2015). Subcellular localization of K+ channels in mammalian brain neurons: remarkable precision in the midst of extraordinary complexity. *Neuron*, **85**(2), 238–256.

Tsuji, S. (2012). Dentatorubral–pallidoluysian atrophy. *Handbook of Clinical Neurology*, **103**, 587–594.

Turnbull, J. et al. (2011). PTG depletion removes lafora bodies and rescues the fatal epilepsy of lafora disease. *PLoS Genetics*, **7**(4), 1–10.

Turnbull, J. et al. (2016). Lafora disease. *Epileptic Disorders*, **18**(S2), S38–S62.

Van Bogaert, P. et al. (2007). Mutation of a potassium channel-related gene in progressive myoclonic epilepsy. *Annals of Neurology*, **61**(6), 579–586.

Van der Veen, S. et al. (2018). Progressive myoclonus ataxia: time for a new definition? *Movement Disorders*, **33**(8), 1281–1286.

Van Egmond et al. (2014). Ramsay hunt syndrome: clinical characterization of progressive myoclonus ataxia caused by GOSR2 mutation. *Movement Disorders*, **29**(1), 139–143.

Vantaggiato, C. et al. (2009). A novel CLN8mutation in late-infantile-onset neuronal ceroid lipofuscinosis (LINCL) reveals aspects of CLN8 neurobiological function. *Human Mutation*, **30**(7), 1104–1116.

Velinov, M. et al. (2012). Mutations in the gene DNAJC5 cause autosomal dominant Kufs disease in a proportion of cases: study of the parry family and 8 other families. *PLoS ONE*, **7**(1), e29729.

Vlaskou, D. et al. (2007). Generation of magnetic nonviral gene transfer agents and magnetofection in vitro. **2**(10), 2391–2411.

Volchuk, A. et al. (2004). Countercurrent distribution of two distinct SNARE complexes mediating transport within the Golgi stack. *Molecular Biology of the Cell*, **15**(4), 1506–1518.

Völker, J. M. et al. (2017). Functional assays for the assessment of the pathogenicity of variants of GOSR2, an ER-to-Golgi SNARE involved in progressive myoclonus epilepsies. *Disease Models & Mechanisms*, **10**(12), 1391–1398.

Vossler, D. G. et al. (2008). Zonisamide for the treatment of myoclonic seizures in progressive myoclonic epilepsy: an open-label study. *Epileptic Disorders*, **10**(1), 31–34.

Vukoja, A. et al. (2018). Presynaptic biogenesis requires axonal transport of lysosome-related vesicles. *Neuron*, **99**(6), 1216–1232.

Walsh, J. G. et al. (2011). Caspase-1 promiscuity is counterbalanced by rapid inactivation of processed enzyme. *The Journal of Biological Chemistry*, **286**(37), 32513–24.

Wang, L. Y. et al. (1998). Contribution of the Kv3.1 potassium channel to high-frequency firing in mouse auditory neurones. *The Journal of Physiology*, **509***(1)*, 183–94.

Waters, M. F. et al. (2006). Mutations in voltage-gated potassium channel KCNC3 cause degenerative and developmental central nervous system phenotypes. *Nature Genetics*, **38**(4), 447–451.

Weiser, M. et al. (1995). The potassium channel subunit Kv3.1b is localized to somatic and axonal membranes of specific populations of CNS neurons. *The Journal of Neuroscience*, **15**(6), 4298–4314.

Weiser, M. et al. (1994). Differential expression of Shaw-related K+ channels in the rat central nervous system. *The Journal of Neuroscience,* **14**, 949–972.

Weston, M. et al. (2018). Olanzapine: a full and potent agonist at the hM4D(Gi) DREADD amenable to clinical translation of chemogenetics. *Science Advances,* **5**(4), 477513.

Wheless, J. W. & Sankar, T. (2003). Treatment strategies for myoclonic seizures and epilepsy syndromes with myoclonic seizures. *Epilepsia,* **44**(11), 27-37.

Wilson, N. R. et al. (2005). Presynaptic regulation of quantal size by the vesicular glutamate transporter VGLUT1. *Journal of Neuroscience*, **25**(26), 6221-6234.

Wu, F. et al. (2012). A calcium channel mutant mouse model of hypokalemic periodic paralysis. *Journal of Clinical Investigation*, **122**(12), 4580–4591.

Wykes, R. C. & Lignani, G. (2018). Gene therapy and editing: novel potential treatments for neuronal channelopathies. *Neuropharmacology*, **132**, 108–117.

Xie, K., Minkenberg, B. & Yang, Y. (2015). Boosting CRISPR/Cas9 multiplex editing capability with the endogenous tRNA-processing system. *Proceedings of the National Academy of Sciences*, **112**(11), 3570–3575.

Xie, K., Minkenberg, B. & Yang, Y. (2015). Boosting CRISPR / Cas9 multiplex editing capability with the endogenous tRNA processing system. *Proceedings of the National Academy of Sciences*, **112**(11), 3570-5.

Xu, L. et al. (2017). Empower multiplex cell and tissue-specific CRISPR-mediated gene manipulation with self-cleaving ribozymes and tRNA. *Nucleic Acids Research*, **45**(5), 1–9.

Xu, M. et al. (2007). The axon-dendrite targeting of Kv3 (Shaw) channels is determined by a targeting motif that associates with the T1 domain and ankyrin G. *The Journal of Neuroscience,* **27**(51), 14158–70.

Yanagi, M. et al. (2014). Kv3.1-containing K(+) channels are reduced in untreated schizophrenia and normalized with antipsychotic drugs. *Molecular Psychiatry*, **19**(5), 573–9.

Yang, Y. et al. (2013). Autophagy in axonal and dendritic degeneration. *Trends in Neurosciences*, **36**(7), 418–28.

Yang, Y., Yan, Y., & Sigworth, F. J. (1997). How does the W434F mutation block current in Shaker potassium channels? *The Journal of General Physiology*, **109**(6), 779–89.

Yasuda, T., Cuny, H. & Adams, D. J. (2013). Kv3.1 channels stimulate adult neural precursor cell proliferation and neuronal differentiation. *The Journal of Physiology*, **591**(10), 2579–2591.

Ye, B. et al. (2007). Growing dendrites and axons differ in their reliance on the secretory pathway. *Cell*, **130**(4), 717–729.

Ye, J. et al. (2012). Primer-BLAST: a tool to design target-specific primers for polymerase chain reaction. *BMC Bioinformatics*, **13**(1), 134.

Yeagle, P. L. (2016). *Introduction,* from: *The Membranes of Cells,* Edition 3. *Academic Press*. 1–25.

Yi, J.H. & Hazell, A. S. (2006). Excitotoxic mechanisms and the role of astrocytic glutamate transporters in traumatic brain injury. *Neurochemistry International*, **48**(5), 394–403.

Yu, F. H. & Catterall, W. A. (2004). The VGL-Chanome: a protein superfamily specialized for electrical signaling and ionic homeostasis. *Science Signaling*, ***253***, re15.

Yu, F. H. et al. (2006). Reduced sodium current in GABAergic interneurons in a mouse model of severe myoclonic epilepsy in infancy. Nature Neuroscience, **9**(9), 1142-1149.

Zerucha, T. et al. (2000). A highly conserved enhancer in the Dlx5/Dlx6 intergenic region is the site of cross-regulatory interactions between Dlx genes in the embryonic forebrain. *The Journal of Neuroscience*, **20**(2), 709–721.

Zhang, X. & Wang, Y. (2016). Glycosylation quality control by the Golgi structure. *Journal of Molecular Biology*, **428**(16), 3183–3193.

Zhang, Y. et al. (2018). Plasma membrane changes during programmed cell deaths. *Cell Research*, **28**(1), 9–21.

Zhang, Y. & Kaczmarek, L. K. (2016a). Kv3.3 potassium channels and spinocerebellar ataxia. *Journal of Physiology*, **594**(16), 4677–4684.

Zhao, J., Zhu, J. & Thornhill, W. B. (2013). Spinocerebellar ataxia-13 Kv3.3 potassium channels: arginine-to-histidine mutations affect both functional and protein expression on the cell surface. *Biochemical Journal*, **454**(2), 259–265.

Ziemann, U. (2004). TMS and drugs. *Clinical Neurophysiology*, **115**(8), 1717–1729.

Zorman, S. et al. (2014). Common intermediates and kinetics, but different energetics, in the assembly of SNARE proteins. *ELife*, **3**, 1–21.

Zucker, R. S. & Regehr, W. G. (2002). Short-term synaptic plasticity. *Annual Reviews in Physiology*, **64**, 355–405.

Zunke, F. et al. (2016). Characterization of the complex formed by β-glucocerebrosidase and the lysosomal integral membrane protein type-2. *Proceedings of the National Academy of Sciences of the United States of America*, **113**(14), 3791–6.

Zutt, R. et al. (2018). Electrophysiologic testing aids diagnosis and subtyping of myoclonus. *Neurology*, **90**(8), e647–e657.